

The acoustics of curved and lined cylindrical ducts with mean flow

Edward James Brambley

Pembroke College

Department of Applied Mathematics and Theoretical Physics,

University of Cambridge

August 2007

This dissertation is submitted for the degree of Doctor of Philosophy

Copyright © 2007 Edward James Brambley.

Permission granted to reproduce for personal and educational use only.

The acoustics of curved and lined cylindrical ducts with mean flow

Edward James Brambley

This thesis considers linear perturbations to the steady flow of a compressible inviscid perfect gas along a cylindrical or annular duct. Particular consideration is given to the model of the duct boundary, and to the effect of curvature of the duct centreline.

For a duct with a straight centreline and a locally-reacting boundary, the acoustic duct modes can be segregated into ordinary duct modes and surface modes. Previously-known asymptotics for the surface modes are generalized, and the generalization is shown to provide a distinctly better approximation in aeroacoustically relevant situations.

The stability of the surface modes is considered, and previous stability analyses are shown to be incorrect, as their boundary model is illposed. By considering a metal thin-shell boundary, this illposedness is explained, and stability analysed using the Briggs–Bers criterion. The stability of a cylindrical thin shell containing compressible fluid is shown to differ significantly from the stability for an incompressible fluid, even for parameters for which the fluid would otherwise be expected to behave incompressibly.

The scattering of sound by a sudden hard-wall to thin-shell boundary change is considered, using the Wiener–Hopf technique. The causal acoustic field is derived analytically, without the need to apply a Kutta-like condition or to include an instability wave, as had previously been necessary.

Attention is then turned to a cylindrical duct with a curved centreline and either hard or locally-reacting walls. The centreline curvature (which is not assumed small) and wall radii vary slowly along the duct, enabling an asymptotic multiple scales analysis. The duct modes are found numerically at each axial location, and interesting characteristics are explained using ray theory. This analysis is applied to a hard-walled RAE 2129 duct, and frequency-domain solutions are convolved to give a time-domain example of a pulse propagating along this duct.

Finally, some numerical work on the nonlinear propagation of a large-amplitude pulse along a curved duct is presented. This is aimed at modelling a surge event in an aeroengine with a convoluted intake.

Preface and Acknowledgements

This dissertation is the result of my own work and includes nothing which is the outcome of work done in collaboration except where specifically indicated in the text. The analysis of §2.1 has been published (Brambley & Peake, 2006*a*), and chapters 3 and 4 have been submitted for publication (Brambley & Peake, 2007*c* and Brambley & Peake, 2007*b*, respectively). Parts of chapters 3, 4, and 5 have also been presented at international conferences (Brambley & Peake, 2006*c,b*, 2007*a*).

I would like to thank my supervisor, Prof. N. Peake, for his guidance and support. I would also like to thank Dr P.D. Metcalfe for our discussions and his advice, particularly relating to the idea of illposedness and the related Hille–Yosida theorem which was useful for §2.2, and for his help deciphering the LAPACK numerical library used in chapter 4. My thanks also go to Dr B. Veitch for our discussions on the Wiener–Hopf technique which I found useful for chapter 3.

This work was supported by an EPSRC CASE grant in conjunction with Rolls–Royce plc, both of whom I would like to thank, and was undertaken under the University Gas Turbine Partnership Research Programme. My thanks also go to Pembroke College for funding a significant part of my expenses for attending the AIAA/CEAS aeroacoustics conferences in Boston, MA in May 2006, and in Rome, Italy in May 2007.

Contents

1	Introduction	6
1.1	Governing equations for a straight cylinder	13
1.2	Discussion of modes in a straight cylinder	14
1.3	Asymptotics for high-order modes	15
2	Surface waves and their stability	19
2.1	Surface-mode asymptotics	19
2.1.1	Recovery of Rienstra's asymptotics	20
2.1.2	Number of surface modes	20
2.1.3	Wavenumbers of the surface modes	23
2.1.4	Accuracy of the asymptotics	25
2.2	Stability	27
2.3	Comparison of Briggs–Bers and Rienstra's stability criteria	28
2.3.1	Convective instability	29
2.3.2	Absolute instability	31
3	Thin-shell boundaries	33
3.1	Impedance of a thin-shell boundary	33
3.2	Surface modes	35
3.3	Stability	37
3.3.1	A stable example	38
3.3.2	An example of instability	40

3.3.3	The boundary between stable and unstable behaviour	46
3.3.4	Recovery of the mass–spring–damper boundary for small shell thicknesses	49
3.4	Scattering by a hard-wall to thin-shell boundary transition	50
3.4.1	Solution in the fluid	50
3.4.2	Imposing the thin-shell boundary	52
3.4.3	Factorizing the Wiener–Hopf kernel	53
3.4.4	Asymptotic behaviour of $E(k)$	55
3.4.5	The Wiener–Hopf Solution	56
3.4.6	Determining the constants $C1$ to $C4$	58
3.4.7	Analytic continuation to real frequencies	60
3.4.8	Numerical evaluation	60
3.4.9	Numerical results	60
3.4.10	Further results	61
4	Slowly-varying curved torsionless ducts	68
4.1	Steady flow	68
4.1.1	Small curvature steady flow	70
4.2	Unsteady flow	71
4.3	Numerical solution	75
4.3.1	Computational simplification for a hard-wall boundary	77
4.3.2	Spurious eigenvalues and filtering	78
4.3.3	Code validation	82
4.4	Results	83
4.4.1	Local mode shapes	83
4.4.2	Partially lined boundary	87
4.4.3	Global mode shapes	91
4.4.4	The RAE 2129 inlet diffuser duct	92
4.5	Turning points and wave reflection	95
4.6	Time domain pulse propagation	99

4.7	Raytracing	100
4.7.1	Application of raytracing to curved ducts	102
4.7.2	Localization of fundamental modes	104
4.7.3	Whispering gallery asymptotics	110
4.8	Asymptotics	112
4.8.1	Smallish curvature limit for a hard-wall duct	112
4.8.2	Small curvature limit	116
5	Nonlinear two-dimensional surge propagation	118
5.1	Numerical method	118
5.1.1	The Riemann problem	121
5.1.2	Boundary conditions	122
5.1.3	Properties of the numerical method	127
5.2	Test cases	128
5.3	Surge in a two-dimensional RAE 2129 intake	132
6	Conclusion	136
6.1	Further research	141
A	Bibliography	143
B	Curve-centred coordinate system	149
B.1	Curvature and torsion	149
B.2	Coordinates	149
B.3	Vector calculus	150

Chapter 1

Introduction

One of the main motivations for the work presented here is an analysis of aircraft jet engine intakes, and in particular, long and curved intakes that are commonly found on military aircraft, such as shown in figure 1.1. Within such an intake during flight there is a significant subsonic mean flow, typically of the order of Mach number 0.5. On top of this mean flow are small perturbations, such as sound, and it is predominantly these perturbations that we investigate here. A more detailed understanding of the effects of the intake curvature on sound propagation may lead to new intake designs that are quieter, such as is being considered by the Silent Aircraft Initiative (Law & Dowling, 2006).

Another sort of event that can occur in aircraft engines is known as *surge*. This is when, for whatever reason, the compressor blades in the interior of the jet engine stall, and the engine depressurizes rapidly, both out the back of the engine through the turbines, and through the front of the engine through the fan and the intake. The pressure increase in the intake during such a surge is significant, typically peaking at two or three times the mean flow pressure. This is significant enough that shock waves can form as the surge pulse propagates along the intake. The details of how a surge is affected by the curvature of the intake are at present not well understood. A better understanding could lead to lighter and safer aircraft engine intakes.

Acoustic waves in a straight cylindrical rigid duct are very well understood, with solutions in terms of Bessel's functions of the first kind. If the duct boundary is not rigid but is allowed to oscillate with the flow, as modelled by Myers (1980), the solution becomes more complicated. Rienstra (2003a) noted that for high frequencies, the modes of such a duct could be classified into acoustic modes and surface modes, the latter being localized about the duct boundary and having interesting stability properties. Formally, Rienstra considered asymptotics in the limit $\omega \rightarrow \infty$ with m fixed for modes of the form $f(r) \exp\{i\omega t - ikx - im\theta\}$, where the duct



Figure 1.1: A Lockheed Martin F-16, showing its curved engine intake. Photograph by Kevin Boydston.

cross-section is described in polar coordinates r and θ with x in the axial direction. A good agreement between the asymptotic and exact results was demonstrated even for modest values of ω , but provided $m \lesssim \omega$.

McAlpine & Wright (2006) considered noise in the intakes of high-powered aeroengines with supersonic fan blade tips. They suggested the dominant noise contribution to be the rotor-alone Blade Passing Frequency (BPF) fundamental mode. For the parameters they provided as being representative of a typical aeroengine, ω and m are of comparable order, and the asymptotic predictions of Rienstra are notably inaccurate. In chapter 2, an alternative asymptotic treatment of the surface modes is given in order to deal with such situations.

Rienstra (2003a) went on to predict some of the surface modes to be unstable and exponentially growing, similar in nature to the Kelvin–Helmholtz shear layer instability. In order to perform the stability analysis a model for the boundary mechanics is needed, and Rienstra chose a mass–spring–damper model (also known as the three parameter model, Tam & Auriault, 1996). The response of the duct boundary is characterized by its impedance $Z = p/v$, where a pressure forcing $p \exp\{i\omega t - ikx - im\theta\}$ produces a radial boundary velocity $v \exp\{\dots\}$. A mass–

spring–damper model (effectively a modified Winkler foundation) assumes the radial boundary displacement w to be governed by

$$a \frac{\partial^2 w}{\partial t^2} + R \frac{\partial w}{\partial t} + bw = p, \quad \Rightarrow \quad Z = R + i a \omega - i b / \omega, \quad (1.1)$$

where a , b , and R are positive real constants representing the mass, spring, and damping terms respectively. The lack of x and θ derivatives in this model causes Z to be independent of both k and m , and corresponds to the assumption that the boundary (in Rienstra’s case a thin vortex sheet close to the acoustic lining) is infinitely flexible and locally reacting. However, in chapter 2 the stability analysis performed by Rienstra is shown to be incorrect. The difficulty with analysing the stability of the mass–spring–damper boundary model is that this model turns out to be illposed.

There are various methods by which stability may be analysed. A commonly used and proven stability analysis is the Briggs–Bers criterion (Briggs, 1964; Bers, 1983). As described by Briggs, this involves introducing a harmonic point-forcing term $\delta(x)H(t) \exp\{i\omega_f t\}$, for which it is required that the solution be identically zero for $t < 0$ in order to satisfy causality. For large t , it is hoped the system will have time dependence $\exp\{i\omega_f t\}$; the direction of propagation of each mode is then given by whether the mode occurs in $x < 0$ or $x > 0$. However, Briggs showed that another situation might arise, for which the solution grows exponentially in time with dominant frequency ω_p , termed the *pinch frequency*. This is referred to as *absolute instability*, while a spatially-growing instability at the driving frequency ω_f is referred to as *convective instability*. Technically, the Briggs–Bers criterion is only applicable provided $\text{Im}(\omega(k))$ is bounded below for real k , or in other words, provided the temporal growth rate of the system is bounded for any initial conditions. Unfortunately, the mass–spring–damper boundary model turns out to belong to a class of problems, also including the Kelvin–Helmholtz vortex sheet instability, for which this is not the case, and so the Briggs–Bers criterion is inapplicable.

Various authors have considered systems with unbounded $\text{Im}(\omega(k))$. Jones & Morgan (1972) analysed the stability of a vortex sheet subject to an acoustic line source, and discovered that this problem has an unbounded temporal growth rate which caused problems with imposing causality (Jones & Morgan, 1972, pp. 478–479). For the impulsive forcing $\delta(x)\delta(t)$, they derived an explicit causal solution in terms of ultradistributions. In a later paper, Jones & Morgan (1974, p. 25) stated that the time harmonic solution $\psi(\omega, x)$ is causal if and only if it is an analytic function of ω in the lower half plane and $\psi(\omega) \exp\{(b + id)\omega\} = O(|\omega|^s)$ as $|\omega| \rightarrow \infty$ in the lower half plane, for real constants b , d , and s with $d > 0$. This stability criterion was extensively used at the time (e.g. Morgan, 1975; Munt, 1977). It is correct if only convective

instabilities are present, although neglects the possibility that ψ might have a pole at ω_p in the lower-half ω -plane, leading to an absolute instability while not contradicting causality provided the ω inversion contour is taken below ω_p .

Crighton & Leppington (1974) considered the scattering of an acoustic line source by a semi-infinite plate shedding a vortex sheet. They discovered that by taking the time-harmonic solution with ω purely imaginary and analytically continuing the solution to real ω , a desirable but unproved Kutta condition (Crighton & Leppington, 1974, pp. 394–396) was satisfied at the trailing edge of the plate and the solution was unbounded downstream. They proposed (Crighton & Leppington, 1974, p. 406), although left unproved, that in similar problems to their own, for $\psi(\omega, x)$ to be causal it must be analytic in the lower-half ω -plane and $\psi \rightarrow 0$ as $\text{Im}(\omega) \rightarrow -\infty$ with $\text{Re}(\omega)$ fixed. They went on to consider the impulsive forcing $\delta(x)\delta(t)$, and again derived an explicit causal solution in terms of ultradistributions.

Note that neither Jones & Morgan (1972, 1974) nor Crighton & Leppington (1974) considered the causal solution for a harmonic forcing as was done by Briggs (1964), but rather the Fourier transform of the causal solution to an impulsive forcing, more similar to the analysis of Bers (1983); Bers showed how the two are related. It would be flawed to interpret the Fourier transform of the impulsive forcing solution as the large- t response of the system to harmonic forcing, and indeed both Briggs and Bers showed the dominant large- t response may in fact be at a frequency other than the forcing frequency if absolute instabilities are present.

An alternative stability criterion was used by Rienstra (2003a) to analyse the stability of the surface modes mentioned above. This method, first suggested by Rienstra (1985) as a misinterpretation of Jones & Morgan (1974) and described in detail by Rienstra & Tester (2005) and Rienstra (2007) as the ‘‘Crighton–Leppington’’ criterion, involves analytic continuation for $|\omega|$ fixed with $\arg(\omega)$ running from $-\pi/2$ to 0. However, this method is not universally valid, and additionally does not consider absolute instability (see §2.2).

How does one, therefore, go about analysing the stability of the surface modes? One answer is to regularize the problem, by including some previously neglected phenomenon that bounds the temporal growth rate, while recovering the original problem in a suitable limit. The vortex sheet problem mentioned above was regularized by Jones (1977), by considering a shear layer of finite thickness h . Jones concluded that for h small but nonzero an instability was present that could be represented in terms of conventional functions, which in the limit $h \rightarrow 0$ yielded the previously discovered ultra-distribution result.

A duct boundary model suitable for stability analysis is developed in chapter 3, for which the

duct boundary is modelled as a thin shell using Flügge’s equations. The mass–spring–damper boundary is recovered in the limit of the shell thickness tending to zero. The stability of a cylindrical thin shell bounding an incompressible fluid was analysed by Peake (1997), using the similar Donnell thin-shell equations. Peake built on the flat plate results of Crighton & Oswell (1991), and using the Briggs–Bers criterion, predicted the oscillations of the boundary to be stable, convectively unstable, or absolutely unstable, depending on the mean flow velocity and the thickness of the duct boundary; instabilities of either kind were only possible for exceedingly small shell thicknesses. Here, for compressible flow and the Flügge thin-shell boundary, it is shown that the boundary is either stable or absolutely unstable, and is not found to support only convective instabilities. The parameters that lead to either stable or unstable behaviour are also analysed. By considering the limit of the shell thickness tending to zero, the illposedness of the mass–spring–damper boundary is demonstrated and explained.

Recently, Rienstra (2007) analysed the scattering of a downstream-propagating hard-wall acoustic mode as it encounters a sudden transition at $x = 0$ to a locally-reacting lined duct, using the Wiener–Hopf technique. Assuming all modes to be stable, the surface streamline was found to be $O(x^{1/2})$ as $x \rightarrow 0$, giving a cusp in the boundary at $x = 0$. Treating one surface mode as an instability, an extra degree of freedom became available which could be chosen to satisfy a Kutta-like condition, giving the surface streamline behaviour as $O(x^{3/2})$ at the boundary transition. In chapter 3, this problem is reconsidered using the newly-derived thin-shell model, and the surface streamline is shown to be $O(x^2)$ at the boundary transition, without necessarily including an instability.

Attention is then turned to a duct with a curved centreline. Keefe & Benade (1983) used ideas of impedance matching to study the propagation of very long waves along a curved pipe. Pagneux and coworkers have developed multi-modal techniques to describe propagation in various sorts of curved ducts with zero mean flow (Pagneux *et al.*, 1996*a,b*; Felix & Pagneux, 2001, 2002). Felix & Pagneux (2004) have also studied sound attenuation round a lined bend, including a raytracing explanation of the effects of curvature, although this was still for zero mean flow. More analytically-based studies have tended to use specific limits, including slender curved ducts (Ting & Miksis, 1983) and weakly curved ducts in two and three dimensions (Gridin & Craster, 2003; Adamou, Gridin & Craster, 2005).

In a different direction, including mean flow for a straight duct with a circular cross-section that varies slowly in the axial direction, Rienstra (1999) derived a multiple scales approximation for the unsteady field. This approximation has been validated by Rienstra & Eversman (2001) by comparison against finite element computations. Rienstra’s analysis has been ex-

tended in a number of ways: by Rienstra (2003*b*) to the case of arbitrary duct cross-section; by Cooper & Peake (2001) to the case of swirling mean flow; and by Ovenden (2005) to a uniformly-valid solution that allows modes to undergo cuton–cutoff transition. However, all of this has been for straight ducts. In chapter 4, Rienstra’s analysis is extended to the case of a curved duct with mean flow. In the straight-duct case, the cross-duct differential equation is solvable analytically in terms of Bessel’s functions. In the curved-duct case this is not possible, and a pseudospectral numerical method as described by Khorrami, Malik & Ash (1989) is used instead. Interesting behaviour is discovered for the curved-duct equivalent of a plane wave, which becomes localized on either the inside or the outside of a bend, or possibly both, depending on the mean flow Mach number, the curvature, and whether the mode is propagating upstream or downstream. This is explained, at least for high frequencies, using a raytracing approximation.

Keller & Rubinow (1960) constructed a raytracing method for determining the eigenvalues of eigenmodes in closed chambers at high frequencies. Their procedure was adapted by Babic & Buldyrev (1991, chapter 5) to closed domains of arbitrary shape with a varying wave speed. Two asymptotic extremes of wave modes are studied, termed *bouncing-ball* and *whispering-gallery* modes. Bouncing-ball modes are concentrated about an *extremal ray*, which is a ray that intersects the boundaries at each of its ends at right angles, and effectively consist of rays bouncing backwards and forwards about this extremal ray. Not all extremal rays support bouncing-ball modes; to do so, the geometry of the boundary locally about the points of reflection must satisfy a stability condition. Babic & Buldyrev (1991, chapter 5, p. 107) refer to this as being *stable in the first approximation*. At the other extreme, whispering-gallery modes consist of rays running around the perimeter of the boundary, bouncing a large number of times at very short intervals. They are named after the whispering galleries found in cathedrals, where a whisper close to the wall on one side of the whispering gallery may be heard on the opposite side. In mathematical terms, bouncing-ball modes are modes of high radial order, while whispering gallery modes are modes of high azimuthal order (for example, large m for a mode with $\exp\{im\theta\}$ dependence). As well as using raytracing to explain the localization of plane waves on the inside or outside of a duct bend, the axial wavenumber predictions of Babic & Buldyrev (1991) using raytracing are compared to the numerical wavenumbers in §4.7.

Finally, we begin to consider nonlinear waves in a curved duct, although in this case only in two dimensions. To do this, we use a first-order-accurate conservative shock-capturing Godunov (finite-volume) scheme. The inspiration for using this method comes from Igra *et al.* (2001), who used a similar second-order-accurate Godunov scheme to predict the behaviour of shocks

around a Z-shaped bend with sharp corners. They presented both numerical and experimental results, and demonstrated remarkable similarity between the two.

The history of this scheme starts with attempts to generalize Godunov's first-order-accurate one-dimensional scheme to second-order accuracy (van Leer, 1979; Ben-Artzi & Falcovitz, 1984). In the first-order Godunov scheme, the fluid is divided up into intervals, and the fluid parameters are considered to be constant within each interval. The arbitrary jump between consecutive intervals forms a Riemann problem (see §5.1.1 for a detailed explanation), which is solved exactly for a small time interval during which the disturbances from the neighbouring jumps do not interact. The fluxes of the conserved quantities mass, momentum, and energy are then calculated, and once all of these are known, the conserved quantities within each interval are updated. To generalize this to second-order accuracy, the fluid parameters are considered to be piecewise linear within each interval. This leads to a Generalized Riemann Problem (GRP) at each interval boundary, which must be solved to second-order accuracy in time and space. A monotonicity argument is also necessary to ensure stability, and to allow discontinuities such as shocks to be modelled accurately (van Leer, 1979, §3.3). A detailed scheme encompassing all of this was given by Ben-Artzi & Falcovitz (1984), and it was this scheme that was used so successfully by Igra *et al.* (2001). Their scheme involves some slightly messy changes of frame from Eulerian (static) to Lagrangian (comoving with the fluid) and back, and recently a fully Eulerian scheme was published by Ben-Artzi *et al.* (2006); however, this was probably first derived much earlier by Men'shov (1990). Another approach was taken by Colella & Woodward (1984), who modelled the flow parameters as being piecewise parabolic within each interval and named their scheme the Piecewise Parabolic Method (PPM). A review of these methods, together with some testcases which are reproduced in §5.2, was given by Woodward & Colella (1984).

All these second-order-accurate schemes have been for one-dimensional flows. To generalize them to two dimensions, Strang splitting (Strang, 1968) is almost unanimously used. Generalizing the boundary conditions to two dimensions is more tricky, since oblique boundaries may be present which do not lie along the numerical grid. Oblique boundaries are dealt with only in passing in the literature (see, for example, Ben-Artzi & Falcovitz, 2003), and so are dealt with in detail in §5.1.2.

Since computing power and memory have increased dramatically since these studies, the discretization used here is far finer than that used in the references above, and hence it was found sufficient to use only the first-order-accurate Godunov method. In order that the code could be generalized to second-order accuracy if the need arose, Strang splitting was still used.

This code was then given the task of calculating the flow in a two-dimensional version of the RAE 2129 intake, with a significant disturbance modelling a surge event being introduced at the upstream end of the intake. Results from this calculation are given in §5.3.

1.1 Governing equations and dispersion relation for a straight cylinder

A straight cylindrical duct of radius r_0 and of infinite extent in the x direction is considered. An inviscid steady uniform axial flow of speed U , density D , pressure P , and sound speed C flows down the inside of the duct in the positive x direction. All parameters are nondimensionalized to simplify the notation. Speeds are nondimensionalized by the speed of sound C , so that U becomes the mean flow Mach number, henceforth considered subsonic. Distances are nondimensionalized by the duct radius r_0 , time by r_0/C , densities by D , and pressures by DC^2 . Note that this gives the nondimensionalized mean pressure as $1/\gamma$ for a perfect gas, where γ is the ratio of specific heats.

Neglecting entropic and vortical disturbances, a small potential perturbation $\phi(x, r, \theta, t)$ is considered to the steady state, with corresponding velocity perturbation $\mathbf{u} = \nabla\phi$, pressure p and density ρ . The linearized governing equations given by Goldstein (1978) in this case become

$$\frac{D^2\phi}{Dt^2} - \nabla^2\phi = 0 \quad \text{and} \quad p = \rho = -\frac{D\phi}{Dt},$$

where $D/Dt = \partial/\partial t + U\partial/\partial x$ is the convective derivative with respect to the mean flow. A solution is sought of the form $\phi = f(r) \exp\{i\omega t - ikx - im\theta\}$. With the nondimensionalization above, ω is the Helmholtz number, k is the *axial wavenumber*, and m (an integer) is the *azimuthal wavenumber*. Making this substitution, the radial equation for $f(r)$ is found to be

$$r^2 \frac{d^2f}{dr^2} + r \frac{df}{dr} + (\alpha^2 r^2 - m^2) f = 0, \quad \text{where} \quad \alpha^2 = (\omega - Uk)^2 - k^2. \quad (1.2)$$

This is Bessel's equation, up to a scaling of r . The solution is required to be non-singular at $r = 0$, giving the solution in terms of Bessel's functions of the first kind as $f(r) = AJ_m(\alpha r)$, for some constant amplitude A . This solution satisfies the linearized governing equations in the fluid, although the boundary condition at the duct wall imposes further restrictions on α .

The boundary is modelled as a flexible impermeable surface with impedance $Z(k, \omega, m)$. Rienstra (2003a) used this as a model for an aeroengine acoustic lining, since in the limit of vanishing viscosity the boundary layer along the wall reduces to a vortex sheet, and it is this vortex sheet that is modelled as a flexible impermeable surface. The motion of the boundary

complicates the no-flux boundary condition $\mathbf{u} \cdot \hat{\mathbf{n}} = 0$ applied on the surface, since both the position of the surface and the direction of the surface normal $\hat{\mathbf{n}}$ are unsteady and depend on the flow. For a general geometry and impedance, Myers (1980) derived the first order no-flux boundary condition to be

$$i\omega \mathbf{u} \cdot \mathbf{n} = (i\omega + \mathbf{U} \cdot \nabla - (\mathbf{n} \cdot \nabla \mathbf{U}) \cdot \mathbf{n}) p/Z, \quad (1.3)$$

where \mathbf{n} is the unperturbed surface normal out of the fluid, \mathbf{U} is the mean flow, \mathbf{u} and p are the linearized velocity and pressure, and all quantities are evaluated on the unperturbed boundary. Substituting the solution for ϕ into this yields the dispersion relation

$$1 - \frac{(\omega - Uk)^2}{i\omega Z} \frac{J_m(\alpha)}{\alpha J'_m(\alpha)} = 0. \quad (1.4)$$

Note that since $J_m(-r) = (-1)^m J_m(r)$, it does not matter which branch is chosen for α . For a hard-wall boundary, no flow through the boundary implies the dispersion relation $J'_m(\alpha) = 0$; this may be obtained from (1.4) by taking the limit $Z \rightarrow \infty$.

Following Rienstra (2003a), the *reduced axial wavenumber* σ is introduced,

$$\sigma = U + \frac{\beta^2}{\omega} k, \quad \text{giving} \quad \alpha^2 = \frac{\omega^2}{\beta^2} (1 - \sigma^2), \quad (1.5)$$

where $\beta^2 = 1 - U^2$. This is so as to remove the Doppler effect of the mean flow, and to scale σ to be $O(1)$ irrespective of ω . With this transformation, the dispersion relation (1.4) becomes

$$1 - \frac{\omega}{iZ\beta^4} (1 - U\sigma)^2 \frac{J_m(\alpha)}{\alpha J'_m(\alpha)} = 0. \quad (1.6)$$

1.2 Discussion of modes in a straight cylinder

For a fixed azimuthal wavenumber m and frequency ω , the dispersion relation (1.4) yields an infinite discrete set of solutions for k . In the hard-wall limit $Z \rightarrow \infty$, the dispersion relation simplifies to $J'_m(\alpha) = 0$, with solutions for α along the positive real axis. Figure 1.2(a) plots the axial wavenumbers k for a hard-wall duct (+). It shows a finite number of real wavenumbers corresponding to propagating (*cuton*) modes, and an infinite discrete set of complex wavenumbers corresponding to exponentially decaying (*cutoff*) modes. Also shown are the wavenumbers for an impedance boundary with $Z = 2 - i$ (\times). The boundary damping causes all modes to have complex axial wavenumbers and decay in space, although there is still a structure similar to the cuton–cutoff behaviour of the hard-wall duct. The majority of modes have nearly real radial wavenumbers α , and indeed $\text{Im}(\alpha)$ tends to zero as the modes become more cutoff (see §1.3). However, there are two series of modes, shown in figure 1.2(b), for which α has

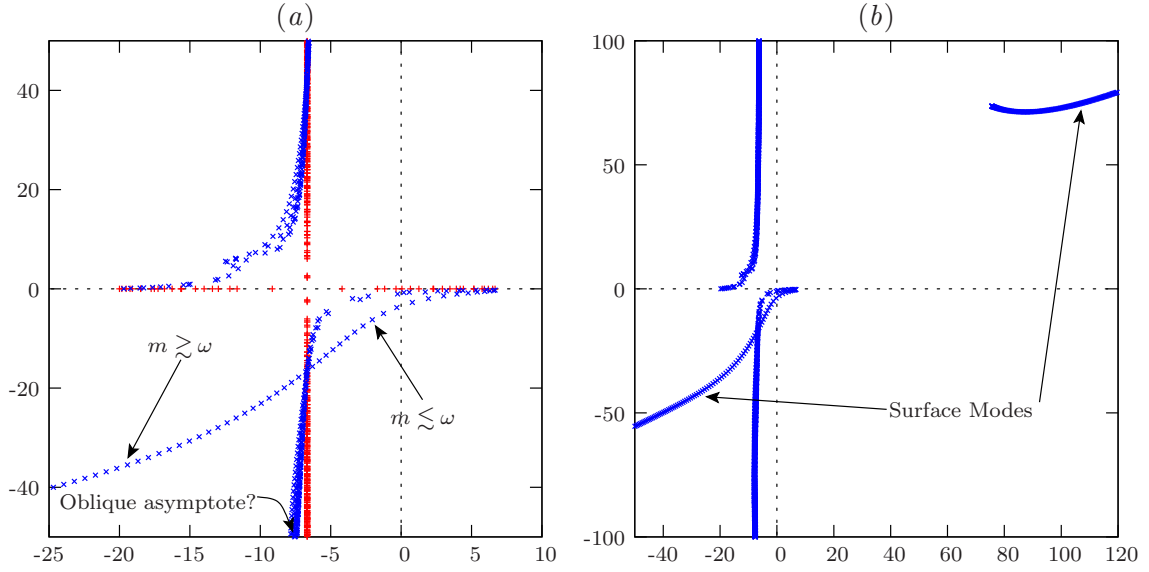


Figure 1.2: Axial wavenumbers k , for $U = 0.5$, $\omega = 10$. (a) Comparison between hard-wall wavenumbers (+) and impedance boundary with $Z = 2 - i$ (x). (b) Larger view showing two surface mode series, for $Z = 2 - i$.

a significant imaginary part. These series, one in the lower left and one in the upper right k -plane, contain one mode for each azimuthal wavenumber m . The leading order asymptotics for Bessel's functions of large complex argument (see e.g. Abramowitz & Stegun, 1964, p. 364) give

$$\frac{|J_m(\alpha r)|}{|J_m(\alpha)|} \sim r^{-1/2} \exp\{-|\text{Im}(\alpha)|(1 - r)\}$$

for large $|\text{Im}(\alpha)|$. Thus, modes for which α has a large imaginary part decay exponentially with distance from the duct wall; these are the *surface modes* discovered by Rienstra (2003a). Other modes for which α is close to the real axis decay at most algebraically with distance from the duct wall, and are termed *acoustic modes*.

1.3 Asymptotics for high-order modes

In figure 1.2, the impedance boundary wavenumbers cross the vertical line of hard-wall wavenumbers, and appear to be tending to an oblique asymptote (as marked). These modes, excluding the surface modes, correspond to large and nearly real values of α , and are termed *high-order modes*. We now develop an asymptotic approximation for these modes in the limit $\alpha \rightarrow \infty$.

In terms of α , the dispersion relation (1.6) is

$$1 - \frac{\omega}{iZ\beta^4} \left(1 \mp U \sqrt{1 - \frac{\beta^2}{\omega^2} \alpha^2} \right)^2 \frac{J_m(\alpha)}{\alpha J'_m(\alpha)} = 0.$$

The branch cut for $\sigma(\alpha)$ is taken along the positive imaginary $(1 - \beta^2 \alpha^2 / \omega^2)$ axis, and the branch is selected to be positive for downstream-propagating modes and negative for upstream-propagating modes, denoted by \pm . This branch cut was selected so as to yield the correct cuton to cutoff behaviour, with propagating modes transitioning into exponentially-decaying modes. Expanding the dispersion relation in powers of α gives

$$1 + \frac{\omega}{iZ\beta^4} \left[\frac{U^2 \beta^2}{\omega^2} \alpha \mp \frac{2iU\beta}{\omega} - (1 + U^2) \alpha^{-1} + O(\alpha^{-2}) \right] \frac{J_m(\alpha)}{J'_m(\alpha)} = 0. \quad (1.7)$$

For the leading order terms to balance, $J_m/J'_m = O(\alpha^{-1})$, so that α must be close to a zero of J_m . Let j_{mn} be the n^{th} zero of J_m . By differentiating Bessel's equation and setting J_m to zero, it is found that

$$\frac{J''_m(j_{mn})}{J'_m(j_{mn})} = -\frac{1}{j_{mn}} \quad \frac{J'''_m(j_{mn})}{J'_m(j_{mn})} = \frac{m^2 + 2}{j_{mn}^2} - 1,$$

so that

$$\frac{J_m(j_{mn} + j)}{J'_m(j_{mn} + j)} = j \left[1 + \frac{1}{2j_{mn}} j + \frac{\mu}{3} j^2 + O(j^3) \right],$$

where $\mu = 1 - (m^2 + 1/2)/j_{mn}^2$. Note that as $m \rightarrow \infty$ for fixed n , $j_{mn} = m + O(m^{1/3})$, so that $\mu = O(j_{mn}^{-2/3})$, while as $n \rightarrow \infty$ for fixed m , $\mu = O(1)$; μ therefore represents the *bouncing ball coefficient*.

By substituting $\alpha = j_{mn} + j$ into (1.7) and equating the leading order coefficients, it is seen that $j = O(j_{mn}^{-1})$. Expanding in powers of j , (1.7) becomes

$$\frac{iZ\beta^4}{\omega} j_{mn}^{-1} = -\frac{U^2 \beta^2}{\omega^2} j \pm \frac{2iU\beta}{\omega} \frac{j}{j_{mn}} + (1 + U^2) \frac{j}{j_{mn}^2} - \frac{3U^2 \beta^2}{2\omega^2} \frac{j^2}{j_{mn}} - \frac{U^2 \beta^2 \mu}{3\omega^2} j^3 + O(j_{mn}^{-4}). \quad (1.8)$$

Solving for j yields

$$\begin{aligned} \alpha &= j_{mn} - \frac{iZ\beta^2 \omega}{U^2} j_{mn}^{-1} \pm \frac{2Z\beta \omega^2}{U^3} j_{mn}^{-2} \\ &\quad + \frac{iZ\omega^2}{U^4} \left[(\beta^2 + 2)\omega - \frac{3}{2}iZ\beta^4 - \frac{Z^2 \beta^6 \omega}{3U^2} \mu \right] j_{mn}^{-3} + O(j_{mn}^{-4}), \\ k &= \mp \frac{i}{\beta} j_{mn} - \frac{\omega U}{\beta^2} \mp \left(\frac{Z\beta \omega}{U^2} - \frac{i\omega^2}{2\beta^3} \right) j_{mn}^{-1} - \frac{2iZ\omega^2}{U^3} j_{mn}^{-2} \\ &\quad \mp \left(\frac{Z\omega^2}{\beta U^4} \left[\frac{3}{2}iZ\beta^4 + \frac{Z^2 \beta^6 \omega}{3U^2} \mu - \frac{3}{2}(1 + \beta^2)\omega \right] - \frac{i\omega^4}{8\beta^5} \right) j_{mn}^{-3} + O(j_{mn}^{-4}). \end{aligned} \quad (1.9)$$

Figure 1.3 shows how the amount by which this solution fails to satisfy the dispersion relation

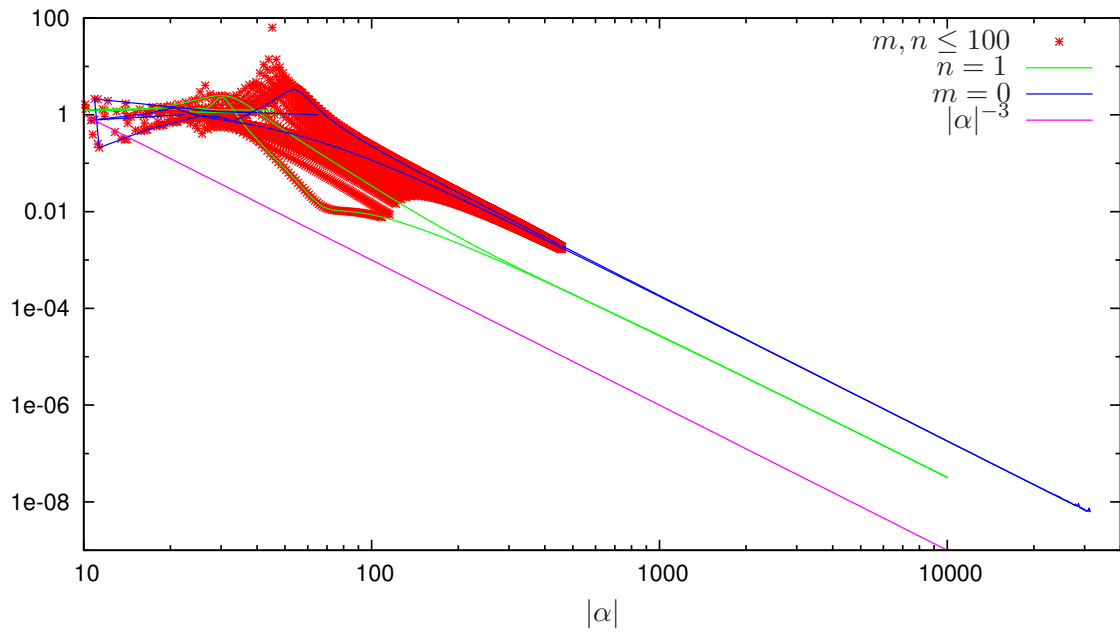


Figure 1.3: Magnitude of the left hand side of the dispersion relation (1.4) for the asymptotics (1.9), with $\omega = 10$, $Z = 2 - i$, and $U = 0.5$.

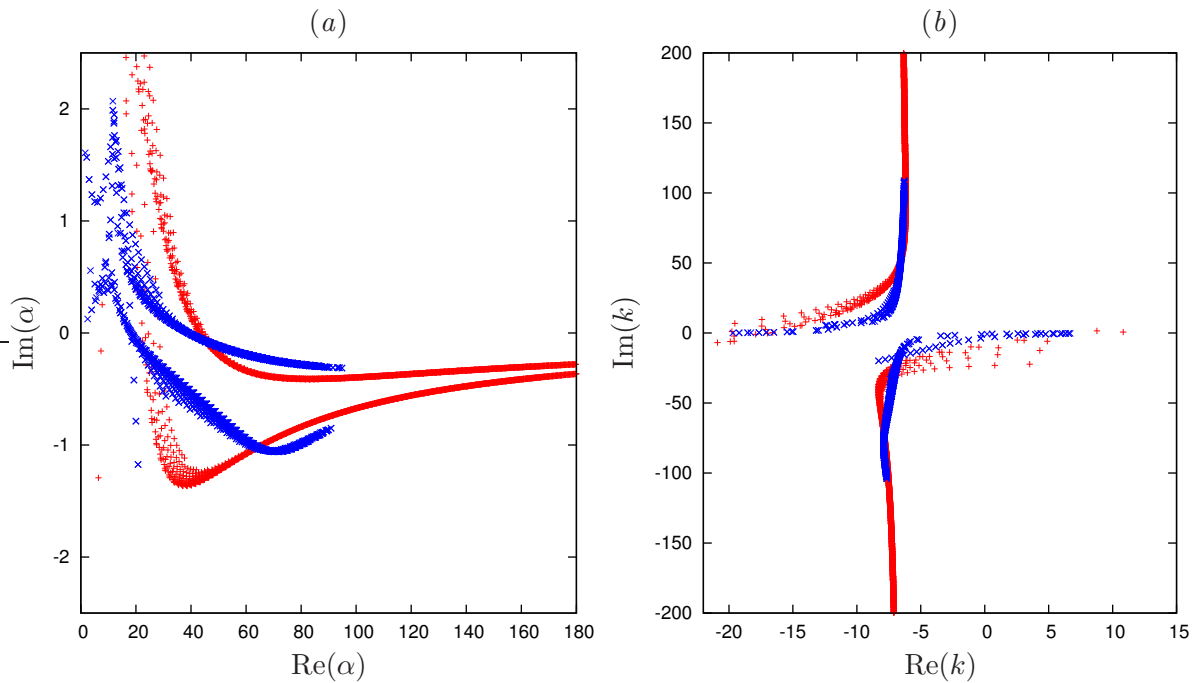


Figure 1.4: Comparison of numerical (\times) and asymptotic ($+$) eigenvalues, for $\omega = 10$, $Z = 2 - i$, and $U = 0.5$.

decreases with $|\alpha|$. It verifies the correctness of the above asymptotics by demonstrating an $O(|\alpha|^{-3})$ error, as is expected from (1.8).

Figure 1.4 compares the values of α and k generated numerically and from the above asymptotics. While the match is far from perfect, the asymptotic results do show the correct characteristics. Since the asymptotic results have been validated by showing they satisfy the dispersion relation to the correct order, it is to be expected that the asymptotic results will match increasingly better for higher order modes. Higher order modes were not computed numerically, owing to the computational cost.

These asymptotics show that the high order modes do not tend to an oblique asymptote, despite what one might have expected from figure 1.2(a). In fact, from (1.9), the high-order modes tend to solutions to the pressure-release boundary $J_m(\alpha) = 0$, obtained from (1.4) in the limit $Z \rightarrow 0$.

Chapter 2

Surface waves and their stability

Analysing acoustic waves in a straight cylindrical duct with an impedance boundary and a mean flow, Rienstra (2003*a*) discovered that the wave modes could be classified into acoustic modes and surface modes, the latter being localized exponentially about the duct boundary; examples of these surface modes are labelled in figure 1.2. Formally, Rienstra considered asymptotics in the limit $\omega \rightarrow \infty$ with m fixed for modes of the form $f(r) \exp\{i\omega t - ikx - im\theta\}$. A good agreement between the asymptotic and exact results was demonstrated even for modest values of ω , provided $m \lesssim \omega$. However, as $m \sim \omega$, the surface mode predicted to be in the lower-right σ -plane shifts over to the lower-left, as labelled in figure 1.2. For rotor-alone noise produced in aeroengines, m is an integer multiple of the number of fan blades B , and typically $B = 24$ and $\omega = 31$ (McAlpine & Wright, 2006), so that $m \sim \omega$.

Rienstra went on to consider the stability of the surface modes, and tentatively identified one surface mode as an instability. The nature of these surface modes is therefore important, and here we generalize Rienstra's surface mode asymptotics to arbitrary azimuthal orders m , before reconsidering the issue of their stability.

2.1 Surface-mode asymptotics

Rienstra (2003*a*) investigated surface modes using asymptotics for large ω . Here, we are interested in both large m and ω , and so we fix $\Omega = \omega/m$ and consider the high-frequency asymptotics in this case. From the definition of reduced axial wavenumber in (1.5), it is expected that $\sigma = O(1)$ and $\alpha = O(\omega)$. This motivates the definitions

$$\omega = m\Omega, \quad \alpha = m\zeta, \quad \lambda = \frac{\Omega}{\beta}, \quad \zeta^2 = \lambda^2(1 - \sigma^2).$$

Note that Ω was used by Rienstra to represent a different quantity.

The high-frequency limit is obtained by taking $m \rightarrow \infty$ with Ω held fixed. The solutions are expected to be surface waves confined to a thin neighbourhood of the duct boundary, and it turns out the distinguished scaling is obtained by substituting $r = 1 - y/m$ into (1.2), with $y = O(1)$, yielding

$$(m - y)^2 \frac{d^2 f}{dy^2} - (m - y) \frac{df}{dy} + m^2 \left(\zeta^2 \left(1 - \frac{y}{m}\right)^2 - 1 \right) f = 0.$$

To leading order in m , the first and third terms balance, giving

$$f(y) = e^{-\mu y}, \quad \mu^2 = 1 - \zeta^2, \quad \text{Re}(\mu) > 0.$$

The boundary condition (1.3) gives the dispersion relation

$$\mu - \frac{\lambda}{iZ\beta^3} (1 - U\sigma)^2 = 0, \quad (2.1)$$

or, in terms of the primitive variables ω and k ,

$$\sqrt{k^2 + m^2 - (\omega - Uk)^2} - \frac{(\omega - Uk)^2}{i\omega Z} = 0. \quad (2.2)$$

2.1.1 Recovery of Rienstra's asymptotics

Rienstra's *reduced radial wavenumber* is $\gamma_R = \zeta/\lambda$, so that the dispersion relation (2.1), on division by λ , may be written

$$\left(\frac{1}{\lambda^2} - \gamma_R^2 \right)^{1/2} - \frac{1}{iZ\beta^3} (1 - U\sigma)^2 = 0.$$

Rienstra defined γ_R such that $\text{Im}(\gamma_R) < 0$, while μ is defined so that $\text{Re}(\mu) > 0$. Hence, multiplying throughout by $-iZ\beta^3$ and letting $\lambda \rightarrow \infty$, the dispersion relation becomes

$$(1 - U\sigma)^2 + \beta^3 Z \gamma_R = 0.$$

This is exactly Rienstra's (2003a, equation 11) dispersion relation, and hence the asymptotic dispersion relation (2.1), or equivalently (2.2), is seen to be a generalization of Rienstra's to the case of finite λ .

2.1.2 Number of surface modes

In this chapter, we consider only impedance boundaries for which Z is independent of k or, equivalently, σ . This simplification was implicitly assumed by Rienstra (2003a), and corresponds to the assumption that the boundary is locally reacting.

$$\begin{array}{ll}
\text{(a)} & \text{Im}(Z) = \frac{2U}{\beta^3} \\
\text{(b)} & Z = \frac{2iU}{\beta^3\sqrt{1+\tau^2}} \\
\text{(c)} & Z = \frac{U}{\beta^3} \frac{5+4\tau^2-3\sqrt{1+8\tau^2}}{\sqrt{2\sqrt{1+8\tau^2}-2-4\tau^2}} \\
\text{(d)} & Z = \frac{U}{\beta^3\tau} \\
\text{(e)} & Z = ((1-\tilde{\tau}^2) + 2i\tilde{\tau})s \\
\text{(f)} & Z = ((\tilde{\tau}^2-1) + 2i\tilde{\tau})s \\
\text{(g)} & Z = \frac{2U}{\beta^3\sqrt{\tilde{\tau}^2-1}} \left((\tilde{\tau}^2-1) + i\sqrt{2\tilde{\tau}^2-1} \right)
\end{array}$$

Table 2.1: Labelled points in figure 2.1. $\tau = U\sqrt{1-\lambda^{-2}}$, and $\tilde{\tau} = U\sqrt{\lambda^{-2}-1}$ are used to simplify the notation. The lines (e) and (f) are parametrized by $s \in [0, \infty)$.

On taking the right hand term of the dispersion relation (2.1) to the right hand side and squaring both sides, a quartic equation for σ is found,

$$\left(\frac{1}{\lambda^2} - 1 \right) + \sigma^2 + \frac{1}{Z^2\beta^6} (1 - U\sigma)^4 = 0. \quad (2.3)$$

There are therefore exactly four solutions counting multiplicity, although some of these solutions may have $\text{Re}(\mu) < 0$ and so must be discounted. Modes satisfying (2.3), but with $\text{Re}(\mu) < 0$, are termed *fake surface modes*. A change in the number of valid roots can therefore only occur when one of the roots crosses the line $\text{Re}(\mu) = 0$. This line corresponds to the surface mode becoming an acoustic mode, no longer being localized about the duct boundary, and hence the asymptotics above breaking down; in other words, the line $\text{Re}(\mu) = 0$ is an anti-Stokes line. Mapping this anti-Stokes line into the complex Z -plane segregates the Z -plane into regions with different numbers of surface modes.

Figure 2.1 shows the anti-Stokes lines mapped into the Z plane for $U = 0.5$. The limit $\lambda = \infty$ corresponds to Rienstra's (2003a) figure 5. For $1 < \lambda < \infty$, Rienstra's results are still qualitatively correct, although quantitatively some variation is seen as λ approaches unity. Specifically, the point (d) approaches positive real infinity as $\lambda \rightarrow 1$. At $\lambda = 1$ a qualitative change is seen, and for $\lambda < 1$ a different regime is entered. As $\tilde{\tau}$ from table 2.1 approaches one, the points (b) tend to $\pm i\infty$, and the boundaries of regions 0 and 4 approach the imaginary axis. This corresponds to λ approaching $\lambda_n \equiv 1/\sqrt{1+U^{-2}}$. For $\lambda < \lambda_n$ a third regime is entered in which regions 0 and 4 are absent, and as $\lambda \rightarrow 0$ region 2 expands to fill the whole of the Z -plane. The numbering of the regions reflects the number of surface modes present for that region. This explains why there are only two surface-mode series seen in figure 1.2(b) for large m , instead of the three predicted by Rienstra, since $Z = 2 - i$ lies in region 2 for sufficiently large m .

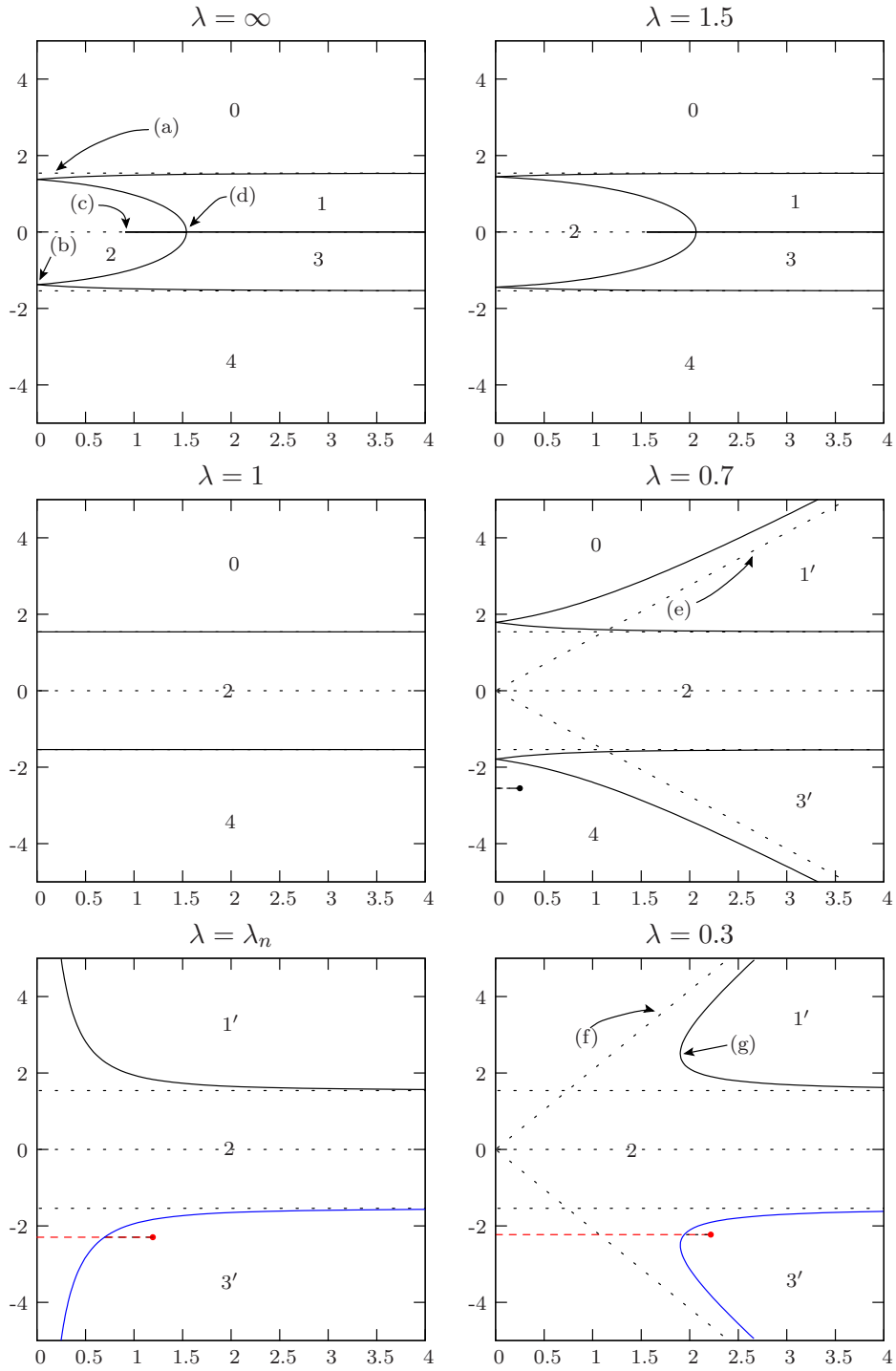


Figure 2.1: The anti-Stokes line $\text{Re}(\mu) = 0$ mapped into the Z -plane for $U = 0.5$, giving $\lambda_n \approx 0.45$. The labelled points are displayed in table 2.1. The dashed line and filled circle are described in §2.1.3.

2.1.3 Wavenumbers of the surface modes

The line $\text{Re}(Z) = 0$ is an important boundary, separating an energy absorbing duct wall ($\text{Re}(Z) > 0$) from an energy producing one ($\text{Re}(Z) < 0$). It was pointed out by Rienstra (2003a) that, since only energy absorbing duct boundaries are considered, no surface mode can cross this boundary, and it turns out that this boundary separates the individual surface modes from one another. Using this, a schematic of the allowable positions in the σ -plane for each of the four surface modes, labelled a, b, c, and d, is shown in figure 2.2. The trajectories of the surface modes in the σ -plane for $\text{Re}(Z) = 0$ give an egg-shaped contour for large enough λ , exactly as described by Rienstra (2003a) in the case $\lambda = \infty$. The egg-shaped contour remains qualitatively correct for all $\lambda > 1$, and indeed a very similar contour is found for λ just less than unity. At $\lambda = 1$ the two branches along the real σ axis meet at the origin, and for $\lambda < 1$ a new double root of (2.3) becomes present on the negative real σ axis. As λ approaches a critical value λ_p (determined below), the two double roots on the negative real σ axis coalesce, and for $\lambda < \lambda_p$ a topological change is seen, with $\text{Re}(Z) = 0$ now mapping to a mushroom-shaped contour. The critical value λ_n discovered earlier is seen to be where the overhang on the underside of the mushroom disappears, along with region 4 of the Z -plane which corresponds to the presence of surface mode c inside the overhang.

As mentioned above, the quartic equation (2.3) for σ permits a double root for certain values of Z ; an obvious quadruple root is given by $\sigma = U^{-1}$, $Z = 0$, corresponding to the right of the egg or the top of the mushroom. A value of Z leading to a double root in σ will be termed a *double root singularity*. A double root is indicated by the derivative (with respect to σ) of (2.3) being zero, in addition to (2.3) being satisfied. Requiring a zero derivative gives

$$\frac{\sigma}{2U} = \frac{1}{Z^2\beta^6}(1 - U\sigma)^3.$$

For $Z \neq 0$, substituting the above into (2.3) to eliminate the Z dependence yields a quadratic equation for σ , giving solutions

$$\sigma_{\pm} = -\frac{1}{2U} \pm \sqrt{\frac{1}{4U^2} + 2\left(1 - \frac{1}{\lambda^2}\right)}, \quad Z_{\pm}^2 = \frac{2U}{\beta^6} \frac{(1 - U\sigma_{\pm})^3}{\sigma_{\pm}},$$

the branch of Z_{\pm} being chosen such that $\text{Re}(\mu) > 0$. The coincidence of the double roots with $Z \neq 0$ occurs when $\sigma_+ = \sigma_-$, implying $\sigma = -1/(2U)$ and $\lambda = \lambda_p \equiv 1/\sqrt{1 + U^{-2}/8}$. For $\lambda < \lambda_p$, Z_+ and Z_- move off the imaginary Z axis; one into the half plane $\text{Re}(Z) > 0$, the other into $\text{Re}(Z) < 0$.

The question of where in the σ -plane the surface modes exist, and which disappear when crossing an anti-Stokes line, may now be attended to. The existence of a double root singularity

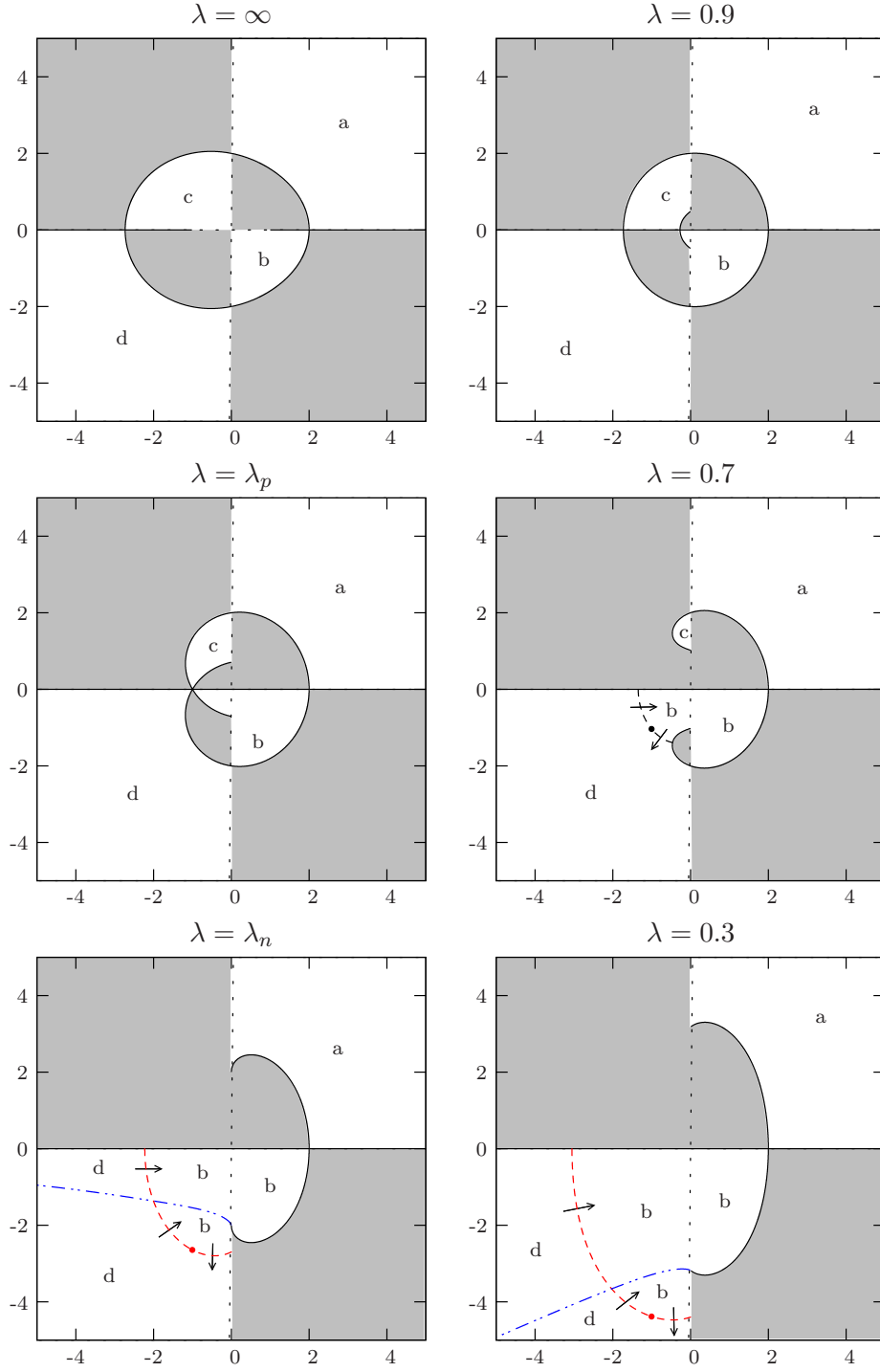


Figure 2.2: Schematic of the σ -plane showing the allowable locations of the surface modes a, b, c, and d. $\text{Re}(Z) = 0$ maps to the solid lines, with the shaded areas corresponding to $\text{Re}(Z) < 0$. The dashed line and filled circle are images of those in figure 2.1. The boundary between regions 2 and 3' maps to the dash-dot line. $U = 0.5$, giving $\lambda_p \approx 0.82$ and $\lambda_n \approx 0.45$.

	a	b	c	d
0				
1	x			
1'		x		
2	x	↑		↓
3	x	x	x	
3'	x	x		x
4	x	x	x	x

Table 2.2: Table showing which surface modes of figure 2.2 are present for each region of figure 2.1. Key: x) present. ↑) present above a branch cut, or with no branch cut. ↓) present only below a branch cut. blank) not present.

in the interior of the half plane $\text{Re}(Z) > 0$ for $\lambda < \lambda_p$ complicates matters, since tracing modes as Z moves in a closed circle around such a singularity would show the b and d surface modes exchanging places. The position of the double root is shown as a filled circle in both figure 2.1 and figure 2.2 (the other double roots having either $\text{Re}(Z) < 0$ or $\text{Re}(\mu) < 0$). Also shown is a dashed line extending from the double root singularity to the imaginary Z axis, and its projection into the σ -plane. Taking this as a branch cut, the image of the branch cut may be used to distinguish between the b and d modes. The arrows shown in figure 2.2 show how the b and d modes would exchange places if Z were allowed to transition upwards across the branch cut. Above the dash-dot line corresponds to Z belonging to region 2 and only one of the b or d modes being present, while below the dash-dot line corresponds to Z belonging to region 3' and both b and d modes being present; it is in the latter case that the modes switch places.

With the branch cut as shown in figure 2.1, the existence of each of the surface modes a, b, c, and d depends on which region Z is in, and is tabulated in table 2.2. The orientation of the branch cut is arbitrary; using a different branch cut would only change the labelling of some b surface modes to d, and vice versa. The branch cut used here was chosen for simplicity.

2.1.4 Accuracy of the asymptotics

Figure 2.3 shows the trajectories of modes in the k -plane as $\text{Im}(Z)$ is varied, with $\text{Re}(Z)$ fixed. Figure 2.3(a) takes $\omega = 5$, $m = 1$, and $U = 0.5$, giving $\lambda \approx 5.8$, and corresponds to the top-left diagram of Rienstra's (2003a) figure 7. For such a relatively small value of ω the asymptotics do not show a perfect match, as the asymptotic results were obtained in the limit

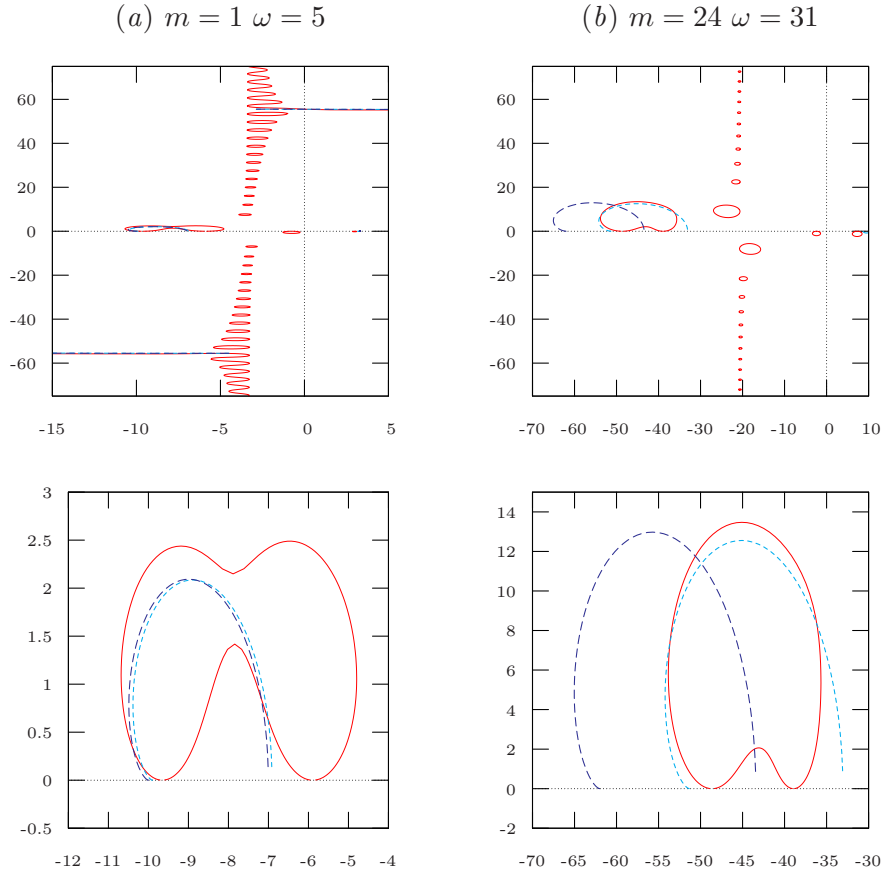


Figure 2.3: Comparison of the new asymptotics (short dashed line), Rienstra's asymptotics (long dashed line) and exact results (solid line) for the axial wavenumber k . $\text{Re}(Z) = 3$, $\text{Im}(Z) \in (-\infty, \infty)$, and $U = 0.5$. The bottom diagrams show some of the modes in more detail.

$\omega \rightarrow \infty$. In particular, both asymptotics switch from approximating one mode to approximating another, missing the fact that these modes are distinct. Nonetheless, both the new asymptotics and those of Rienstra provide a good indication of the exact results. Figure 2.3(a) also shows how the surface modes transition into acoustic modes, with the other acoustic modes switching places to accommodate the new mode. This was discussed by Rienstra (2003a), and since this behaviour is no different in the present case, it is not discussed further here.

Figure 2.3(b) uses $\omega = 31$, $m = 24$, and $U = 0.5$, which are realistic parameters for aeroengine intake noise at takeoff, or sideline (McAlpine & Wright, 2006), and lead to $\lambda \approx 1.5$. The figure shows a very good agreement between the new asymptotic and exact results, while Rienstra's predictions are noticeably less accurate. The other two surface modes are present, although not shown in figure 2.3(b) due to the scale used, and are both accurately predicted by both asymptotic approximations.

2.2 Stability

The Briggs–Bers criterion (Briggs, 1964; Bers, 1983) is commonly used to analyse the stability of linear systems. Consider the linear system

$$\Delta \left(i \frac{\partial}{\partial x}, -i \frac{\partial}{\partial t} \right) G(x, t) = 0.$$

As described by Briggs, a harmonic point-forcing term $\delta(x)H(t) \exp\{i\omega_f t\}$ is introduced on the right hand side, and it is required that the solution be identically zero for $t < 0$ in order to satisfy causality. The equations are Fourier transformed in both space and time, giving $\Delta(k, \omega)\phi(k, \omega) = -i/(\omega - \omega_f)$, where $\phi(k, \omega)$ is the Fourier-transform of $G(x, t)$. Inverting this gives the solution

$$G(x, t) = \frac{1}{4\pi^2} \int_{\mathcal{C}_\omega} \int_{\mathcal{C}_k} \frac{-i \exp\{i\omega t - ikx\}}{(\omega - \omega_f)\Delta(k, \omega)} dk d\omega.$$

The poles of the integrand occur in the ω -plane at ω_f and $\omega(k)$, where the possibly multi-valued function $\omega(k)$ satisfies the *dispersion relation* $\Delta(\omega, k) = 0$. The Briggs–Bers procedure looks at the long-time behaviour of $G(x, t)$, for which it is hoped all transients of the initial sudden start at $t = 0$ will have died away and the system will have a time dependence $\exp\{i\omega_f t\}$. Initially \mathcal{C}_k is taken along the real k axis (as in a standard Fourier transform) and \mathcal{C}_ω is taken below $\text{Im}(\omega(k))$ for any real k (as in a standard Laplace transform), so that for $t < 0$ Jordan’s Lemma may be applied giving $G(x, t) \equiv 0$. The \mathcal{C}_ω contour is then deformed upwards onto the real ω axis to pick up the pole at ω_f in the long-time limit. In so doing, to maintain analytic continuity the \mathcal{C}_k contour must be deformed so that no poles of the integrand cross the contour. This leads to three distinct possibilities:

- (a) Such a deformation of \mathcal{C}_ω is possible, and the \mathcal{C}_k contour need not be deformed. Applying Jordan’s Lemma for the k integral shows that, in the long-time limit, poles in the upper-half k -plane occur in $x < 0$, while poles in the lower-half k -plane are present for $x > 0$, and in both cases the long-time time-dependence is $\exp\{i\omega_f t\}$. There is no exponential growth, and the system is therefore stable.
- (b) The \mathcal{C}_ω contour deformation is possible, but the \mathcal{C}_k contour must be deformed off the real k axis. Similarly to (a), the long-time time-dependence is therefore $\exp\{i\omega_f t\}$, but now there is at least one pole that is either in the upper-half k -plane below \mathcal{C}_k or in the lower-half k -plane above \mathcal{C}_k , which is picked up through Jordan’s Lemma in $x > 0$ or $x < 0$ and so corresponds to a right- or left-propagating instability respectively. Such an instability is referred to as a *convective instability*, since its leading-order long-time behaviour grows exponentially in space but is bounded in time at each spatial location.

(c) The \mathcal{C}_ω contour cannot be deformed onto the real ω axis, since there is a frequency ω_p for which two poles in the k -plane coincide, one originating from above \mathcal{C}_k and the other from below, which *pinch* the \mathcal{C}_k contour. Briggs (1964) showed that in this case a branch cut at ω_p is necessary, and that this frequency, rather than the driving frequency ω_f , is the dominant time dependence of the solution at large times. Since $\text{Im}(\omega_p) < 0$, the long-time solution grows exponentially in time at each point in space, with a spatial distribution $\exp\{-ik_p x\}$, where k_p is the location of the pinch in the k -plane. Such an occurrence is referred to as an *absolute instability*.

The above is obviously only possible provided $\text{Im}(\omega(k))$ is bounded below for real k , or in other words, provided the temporal growth rate is bounded. If this is not the case, the problem is illposed, since the conditions of the Hille–Yosida theorem (Rudin, 1991) are not satisfied; in other words, there are initial conditions for which the solution at $t = 0$ does not match with the solution at $t = \varepsilon$ in the limit $\varepsilon \rightarrow 0$ (i.e. the solution instantly blows up). There may not even be a sensible answer to the question of spatial stability for such systems given a time harmonic forcing, although they are certainly temporally unstable for certain initial conditions.

The mass–spring–damper impedance model considered by Rienstra (2003a) turns out to belong to a class of problems, which also includes the Kelvin–Helmholtz vortex sheet instability, for which $\text{Im}(\omega(k))$ is not bounded below for real k (see §3.3), and so the Briggs–Bers criterion is inapplicable. An alternative stability criterion was used by Rienstra (2003a) to analyse the stability of surface waves. This method, suggested by Rienstra (1985) as a misinterpretation of Jones & Morgan (1974), and described in detail by Rienstra & Tester (2005) and Rienstra (2007) as the “Crighton–Leppington” criterion, involves analytic continuation for $|\omega|$ fixed with $\arg(\omega)$ running from 0 to $-\pi/2$. However, this method is not universally valid, and two examples are provided below for which the method fails to predict the correct stability.

2.3 Comparison of Briggs–Bers and Rienstra’s stability criteria

Here, we consider a simple model which demonstrates that Rienstra’s (1985) method does not, in general, give the (correct) results of the Briggs–Bers procedure.

Consider the self-exciting advection–diffusion equation with harmonic point forcing

$$\frac{\partial G}{\partial t} + u \frac{\partial G}{\partial x} - \frac{\partial^2 G}{\partial x^2} - G = \delta(x)H(t) \exp\{i\omega_f t\}, \quad (2.4)$$

where u is a constant, subject to $G \equiv 0$ for $t < 0$. Upon Fourier-transforming, this gives

$$\Delta(k, \omega) \tilde{G}(k, \omega) = -i/(\omega - \omega_f),$$

where the Fourier-transformed operator $\Delta(k, \omega) = i(\omega - uk) + k^2 - 1$. The zeros of $\Delta(k, \omega)$ in the ω and k -planes occur at

$$\omega = uk - i(1 - k^2) \quad \text{and} \quad k_{\pm} = iu/2 \pm \sqrt{1 - u^2/2 - i\omega}.$$

Inverting the Fourier transform gives the solution

$$G(x, t) = \frac{1}{4\pi^2 i} \int_{\mathcal{C}_\omega} \int_{\mathcal{C}_k} \frac{e^{i\omega t - ikx} dk d\omega}{(\omega - \omega_f) \Delta(k, \omega)},$$

with initially the \mathcal{C}_k contour taken along the real k axis (as in a standard Fourier transform) and the \mathcal{C}_ω contour taken below all poles of the integrand to ensure $G \equiv 0$ for $t < 0$ (as in a standard Laplace transform). Note that $\text{Im}(\omega)$ is bounded below by -1 for any real k and u , so that this may always be achieved.

2.3.1 Convective instability

Figure 2.4 shows the Briggs–Bers criterion applied to (2.4) for $u = 3$. Initially the \mathcal{C}_k contour is along the real k axis, while the \mathcal{C}_ω contour is taken along the real ω axis everywhere but in a finite region approximately $-5 < \omega < 5$, where it is deformed to lie below the image of $\text{Im}(k) = 0$. The \mathcal{C}_ω contour is then deformed upwards onto the real ω axis to pick up the pole contribution at $\omega = \omega_f$. In so doing, the zeros of $\Delta(k, \omega)$ move in the k -plane, and the \mathcal{C}_k contour is deformed upwards to prevent them from crossing the contour in order to maintain analyticity. The dashed arrowed lines show the motion of various parts of the \mathcal{C}_ω contour (for fixed $\text{Re}(\omega)$ as numbered), and their images in the k -plane. The final shape of the \mathcal{C}_k contour is also shown. Zeros of $\Delta(k, \omega)$ (corresponding to poles of the k integrand) above \mathcal{C}_k correspond to left-propagating modes, while zeros of $\Delta(k, \omega)$ below \mathcal{C}_k correspond to right-propagating modes. It can be seen from the dashed arrowed lines that for the range of frequencies $-3 < \omega < 3$, the k_- modes have crossed the real k axis but are below the \mathcal{C}_k contour and therefore represent exponentially-growing right-propagating convective instabilities.

Figure 2.5 shows the same system analysed using Rienstra’s (1985) method. Again, the dashed arrowed lines show the motion of the modes as ω is varied, although this time with $|\omega|$ fixed (as numbered) and $\arg(\omega)$ varied from the negative imaginary ω axis to the real ω axis. Those modes that finish in the upper-half k -plane that started in the lower half are then predicted by this method to be right-propagating instabilities. However, this criterion shows this happening only for $1 < |\omega| < 3$, in contradiction to the Briggs–Bers criterion. Since all the assumptions of the Briggs–Bers criterion are justified for this example, the Briggs–Bers criterion gives the correct results, and hence Rienstra’s criterion incorrectly predicts the instabilities of this system.

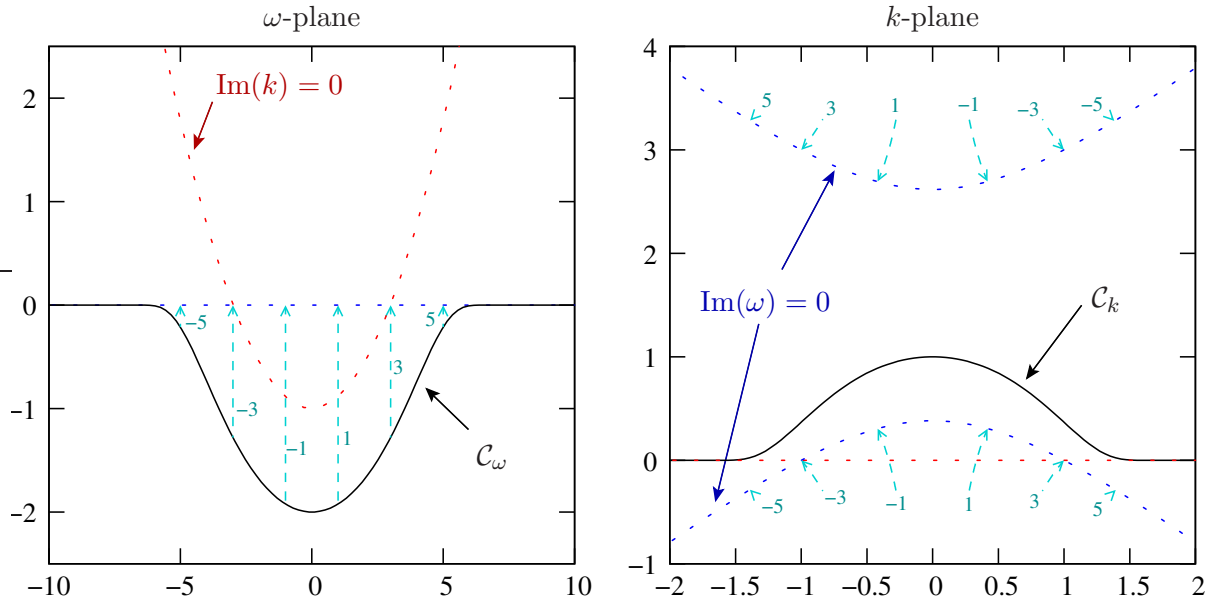


Figure 2.4: The Briggs–Bers method applied to (2.4) with $u \equiv 3$. The C_ω contour shown is the initial ω contour which is deformed onto the real axis. In so doing, the C_k contour is deformed off the real k axis into the contour shown, to avoid poles crossing the contour. The numbers labelling dashed lines refer to the value of $\text{Re}(\omega)$.

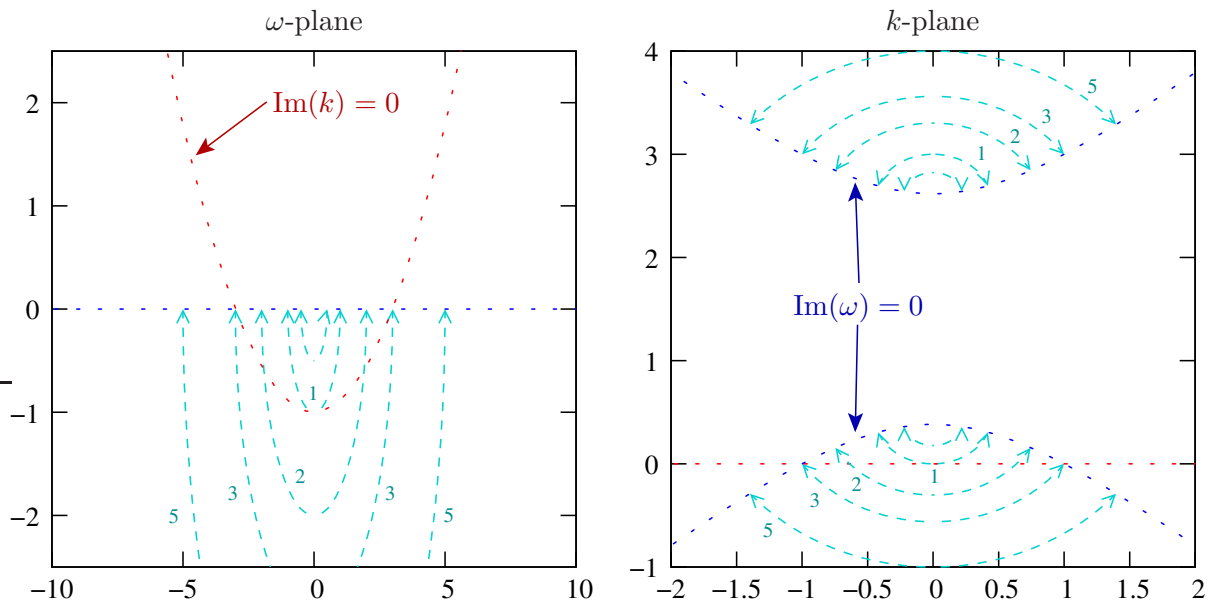


Figure 2.5: Rienstra's (1985) method applied to (2.4) with $u \equiv 3$. The dashed arrowed lines show ω being deformed from purely imaginary to purely real with $|\omega|$ fixed, and the motion of the corresponding poles in the k -plane. The numbers labelling dashed lines refer to the value of $|\omega|$.

2.3.2 Absolute instability

If instead the Briggs–Bers criterion is applied to (2.4) with $u = 1$, as the \mathcal{C}_ω contour is deformed onto the real ω axis, k_+ and k_- coincide at $k_p = i/2$ when $\omega = \omega_p = -3i/4$ and pinch the \mathcal{C}_k contour. Continuing to deform the \mathcal{C}_ω contour onto the real ω axis as far as possible yields the \mathcal{C}_ω' contour shown in figure 2.6. The dominant large-time contribution comes from the part of the \mathcal{C}_ω contour with the most negative $\text{Im}(\omega)$, which is at ω_p , leading to an absolute instability.

Figure 2.7 shows Rienstra’s method applied to (2.4) with $u = 1$. Since no modes end up having crossed the real k axis because of the \mathcal{C}_ω deformation, this method predicts no instabilities at all, in stark contrast to the Briggs–Bers criterion. An erroneous result for this case is unsurprising, since Rienstra’s criterion does not consider the possibility of absolute instability.

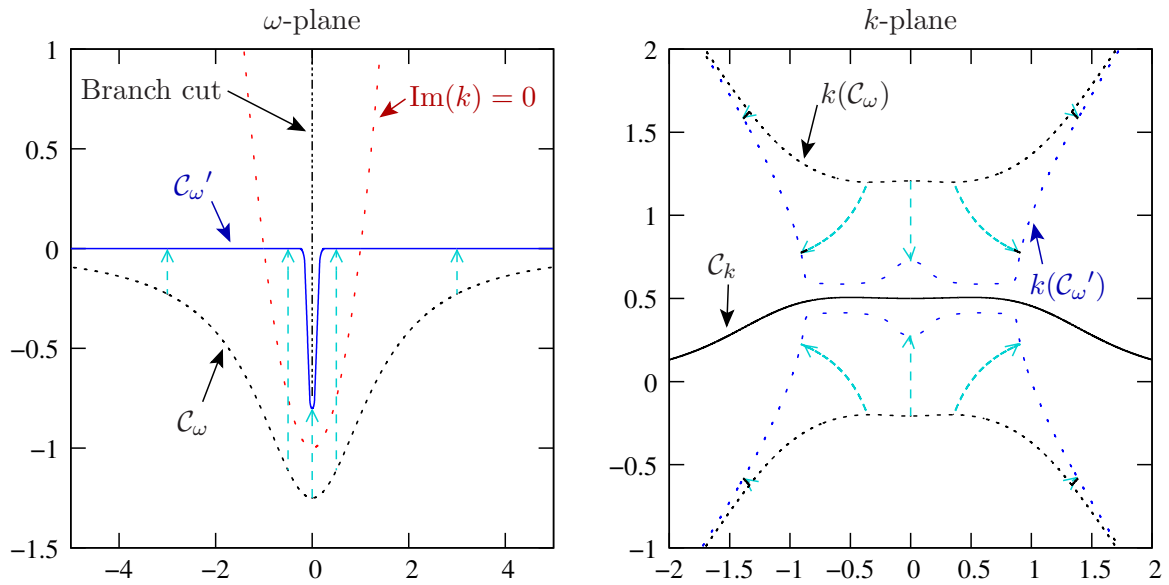


Figure 2.6: The Briggs–Bers method applied to (2.4) with $u \equiv 1$. The C_ω contour shown is the initial ω contour, which is deformed onto the real axis and around the branch cut into the contour C_ω' . In so doing, the C_k contour is deformed off the real k axis into the contour shown, to avoid poles crossing the contour.

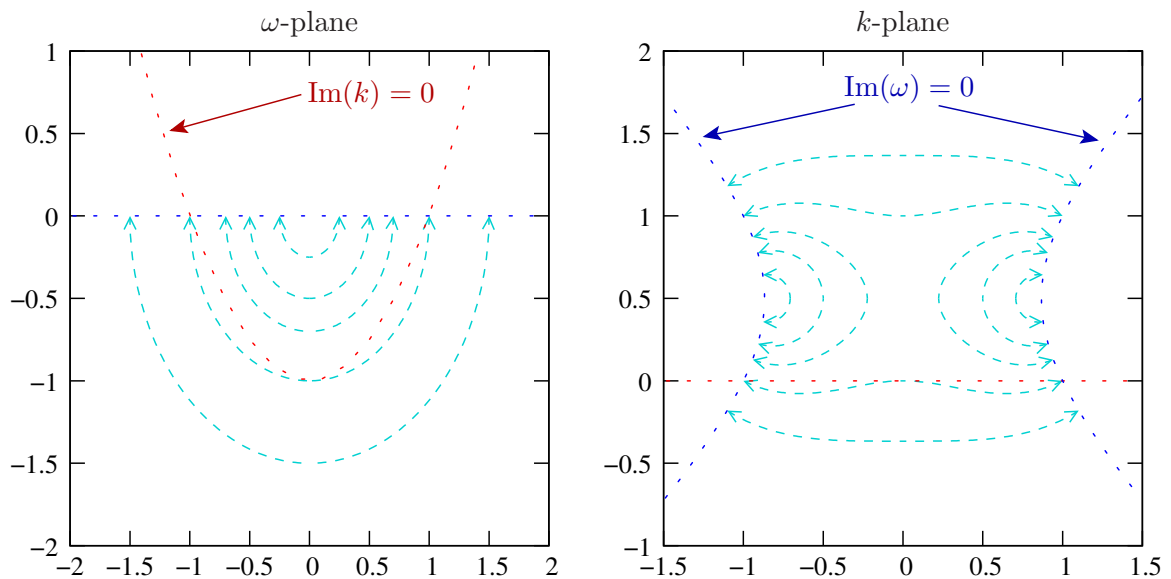


Figure 2.7: Rienstra's (1985) method applied to (2.4) with $u \equiv 1$.

Chapter 3

Thin-shell boundaries

In this chapter, we consider a hollow cylindrical duct with mean axial flow, the boundary of which is a linear-elastic (e.g. metal) damped thin shell. This is considered partly as an interesting problem in its own right, and partly as a possible regularization of the mass–spring–damper boundary model used in chapter 2. After first describing and analysing this model, we will use it to demonstrate how the problems with the mass–spring–damper model arise.

3.1 Impedance of a thin-shell boundary

Consider a straight cylindrical duct with inviscid steady uniform axial flow, exactly as in §1.1. Rather than the simplified mass–spring–damper boundary model, however, the duct boundary is here modelled as a thin shell, the outside of which is sprung and damped. The equations of motion of a Flügge thin shell used here are taken from Païdoussis (2004, p. 576). Let u , v , and w denote the axial, azimuthal and radial displacement of the shell from equilibrium, as shown in figure 3.1, and let $p^* = p - bw - R\partial w/\partial t$ be the net outward force per unit area on the shell. Here, p is the linearized acoustic pressure in the duct at the duct boundary, and b and R represent a spring force and damping respectively, assumed to originate from the exterior of the shell, as in the mass–spring–damper model. All variables p , u , v , and w are taken to have $\exp\{i\omega t - ikx - im\theta\}$ dependence, and the impedance $Z(k, \omega, m)$ is sought, where $Z = p/(\partial w/\partial t)$. We assume that the thin-shell thickness $h \ll 1$. Additionally, we assume that $2m^2 - 1 \ll (k^2 + m^2)^2$, which is almost always true and simplifies the thin-shell equations significantly. The Fourier-transform of Flügge’s equations then give

$$Z = R - i(c_l^2 d + b)/\omega + id\omega - \frac{ic_l^2 d}{\omega} \left(\frac{h^2}{12} (k^2 + m^2)^2 - Q_1 \frac{iu}{w} - Q_2 \frac{iv}{w} \right), \quad (3.1a)$$

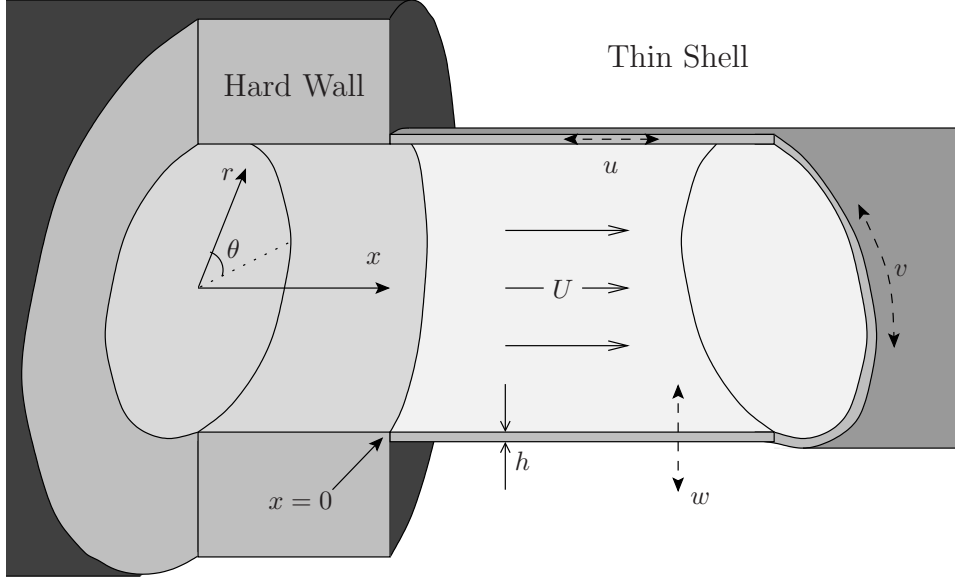


Figure 3.1: Schematic of a cylindrical duct with a sudden change from hard-wall boundary for $x < 0$ to thin-shell boundary for $x > 0$. The small unsteady perturbations to the position of the thin shell are given by u , v , and w .

Fluid	Solid	c_l	ρ_s	ν
Air	Aluminium	15.8	2 200	0.33
Water	Steel	3.6	7.85	0.3

Table 3.1: Nondimensionalized thin-shell parameters for different materials, at standard temperature and pressure (STP).

where

$$\begin{pmatrix} a_{11} & a_{12} \\ a_{12} & a_{22} \end{pmatrix} \begin{pmatrix} iu/w \\ iv/w \end{pmatrix} = \begin{pmatrix} Q_1 \\ Q_2 \end{pmatrix} \quad (3.1b)$$

$$\begin{aligned} a_{11} &= k^2 + \frac{1-\nu}{2}m^2 - \frac{\omega^2}{c_l^2} & a_{12} &= \frac{1+\nu}{2}mk & Q_1 &= k \left[\nu + \frac{h^2}{12} \left(k^2 - \frac{1-\nu}{2}m^2 \right) \right] \\ a_{22} &= m^2 + \frac{1-\nu}{2}k^2 - \frac{\omega^2}{c_l^2} & & & Q_2 &= m \left[1 + \frac{h^2}{12} \frac{3-\nu}{2}k^2 \right], \end{aligned} \quad (3.1c)$$

and $c_l^2 = E/(\rho_s(1-\nu^2))$ is the square of the speed of longitudinal compressive waves in the boundary material, h is the radial shell thickness, $d = \rho_s h$, and the properties of the boundary material ρ_s , E and ν are the density, Young's modulus, and Poisson's ratio respectively. All of these quantities are assumed to be nondimensional, as described in §1.1. Some typical values are given in table 3.1.

If k is large, $m/k \lesssim O(1)$ (of particular interest for stability analysis), and the determinant of (3.1b) is non-zero, then $u/w = O(h^2k)$, $v/w \lesssim O(h^2k)$, and $Q_1u/w + Q_2v/w = O(h^4k^4)$. Neglecting the terms involving Q_1 and Q_2 in (3.1a) is therefore justified in this limit, and the thin-shell impedance takes the form of a modified mass–spring–damper system (c.f. equation 1.1), with the thin shell providing a spring force c_l^2d in addition to that provided by the modified Winkler foundation, together with a bending stiffness $B = c_l^2dh^2/12$.

The determinant of (3.1b) is zero when $k = \pm k_l$ or $k = \pm k_t$, where

$$k_l^2 = \omega^2/c_l^2 - m^2 \quad \text{and} \quad k_t^2 = \omega^2/c_t^2 - m^2 \quad (3.2)$$

and $c_t = c_l\sqrt{(1-\nu)/2}$ is the speed of transverse waves in the duct boundary. The imaginary parts of k_l and k_t are here taken negative, or if zero the real parts are taken positive, so that they represent right-propagating longitudinal and transverse waves in the thin-shell boundary. The zero determinant implies that these boundary waves propagate independently of the radial shell displacement w , and consequently independently of the fluid within the shell.

3.2 Surface modes

As shown in §2.1.2, for a locally-reacting boundary such as the mass–spring–damper boundary, Z is independent of k , and (2.2) may be rearranged to give a quartic equation for k . There would therefore be at most four roots for any given ω and m ; the nature and position of these four surface modes is discussed in §2.1. For the thin-shell impedance (3.1), (2.2) is still valid, only now Z is also a function of k . Rearranging (2.2) gives an 18th order polynomial in k for fixed ω , or a 14th order polynomial in ω for fixed k . For a given frequency, there are therefore a maximum of 18 surface modes, although some of these may be fake surface modes. Figure 3.2 gives an example of these surface modes. Figure 3.2(a) demonstrates the accuracy with which the surface modes are predicted by (2.2); the modes shown as a + alone are acoustic modes, and so are not described by the surface-mode asymptotics (2.2). Figure 3.2(b) shows, as well as can be in a two-dimensional plot, the behaviour of the surface modes in the limit $h \rightarrow 0$.

From considering a large number of plots such as figure 3.2 for different parameters and in different regimes, some interpretation of the nature and physical mechanisms supporting these surface modes may be speculated. Of the 18 potential surface modes, one real surface mode and one fake surface mode tend to each of k_l , k_t , $-k_l$, and $-k_t$ (defined in 3.2), and surface modes of this type are here termed *quasi-solid* surface modes. It should be emphasized, however, that these surface modes are distinct from the solid boundary waves with wavenumbers exactly

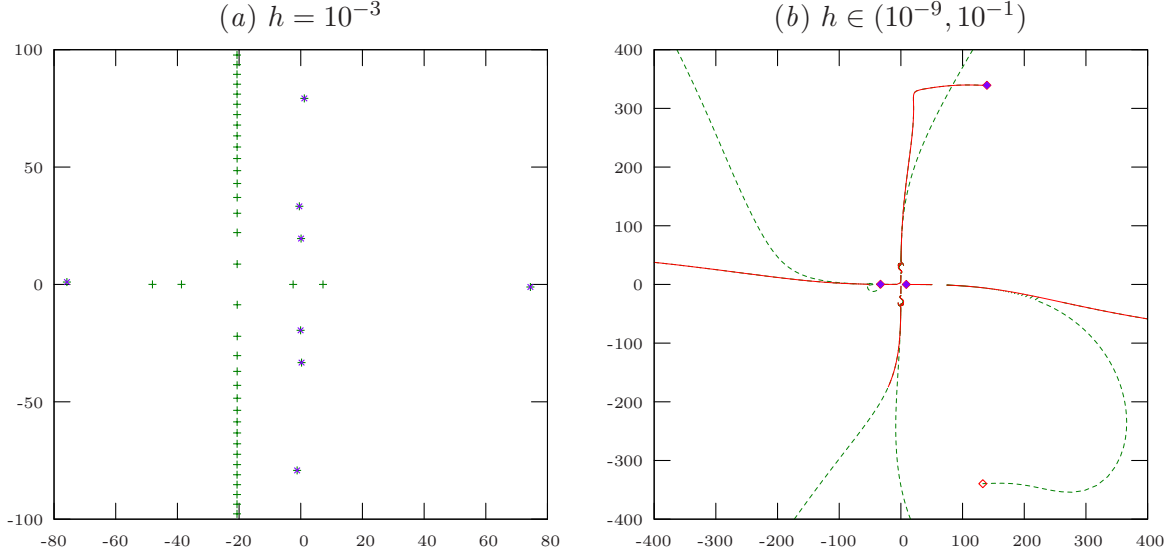


Figure 3.2: Surface modes in the k -plane for air within an aluminium boundary (see table 3.1). $\omega = 31$, $U = 0.5$, $R = 3$, $b = 1$, and $m = 24$. (a) Comparison between analytic modes (+) and solutions to (2.2) (\times), for $h = 10^{-3}$. (b) Surface modes for varying h for thin-shell (lines) and mass-spring-damper (diamonds). Dashed lines and hollow diamonds denote fake surface modes. As $h \rightarrow 0$, modes tend to infinity, to one of the diamonds, or to $\pm k_l$ or $\pm k_t$.

equal to $\pm k_l$ and $\pm k_t$; the quasi-solid modes are fluid modes occurring in the vicinity of the boundary, whereas the solid boundary waves correspond to zeros of the determinant of (3.1b) and therefore produce no disturbance in the fluid. Of the remaining 10 surface modes, four fake and two real surface modes tend to infinity as $h \rightarrow 0$, while the other four tend to the mass-spring-damper values. This suggests that of the 18 potential surface modes, 8 are sustained by compressional and twisting solid mechanisms, 6 are supported by bending solid mechanisms, and four are supported by effectively mass-spring-damper mechanisms.

If the terms involving Q_1 and Q_2 in (3.1a) may be neglected (recall that this is the case when k is large), a considerable simplification is possible. In this case, (2.2) can be rearranged to give

$$(k^2 + m^2 - (\omega - Uk)^2) \left((c_l^2 d + b) + i\omega R - d\omega^2 + B(k^2 + m^2)^2 \right)^2 - (\omega - Uk)^4 = 0. \quad (3.3)$$

This is now a polynomial of 10th order in k , or of 6th order in ω . In the author's experience, this dispersion relation is remarkably accurate, even for modest values of k for which the previous argument for neglecting Q_1 and Q_2 is not appropriate. Of course, this simplification neglects the compressional and twisting components in the solid, and consequently the 8 quasi-solid surface modes are not modelled by (3.3).

3.3 Stability

Having investigated the possible wavemodes supported by our model, we now turn to the question of their stability. To do this, we employ the Briggs–Bers criterion (Briggs, 1964; Bers, 1983), as described in §2.2.

In order for the Briggs–Bers criterion to be applicable, the image of the real k axis mapped into the ω -plane must have its imaginary part bounded below, which is shown below not to be true for the mass–spring–damper model. The validity of the Briggs–Bers criterion is now verified for the thin-shell model. The acoustic modes are stable, being analogous to the stable hard-wall duct modes, and do not therefore preclude the Briggs–Bers criterion from being applied. Utilizing (2.2), and noting from (3.1a) that $|Z| \rightarrow \infty$ as $|k| \rightarrow \infty$, two classifications of surface modes emerge in the limit $|k| \rightarrow \infty$,

$$\omega = Uk \pm \sqrt{k^2 + m^2} + O(k^{-5}),$$

$$\omega = \pm \sqrt{B/d} (k^2 + m^2 + 1/2) + \frac{i}{2d} (R \pm 1) + O(k^{-1}),$$

where the two \pm in the last equation are independent. These have the leading-order large- k behaviour of a hard-wall duct mode and a bending wave in an unforced cylindrical thin shell respectively; these two classifications are therefore termed *fluid* and *bending* surface modes. Although not demonstrated by the above equations, the fluid surface modes and two of the bending surface modes become the four mass–spring–damper surface modes in the limit $h \rightarrow 0$, while the other two bending surface modes tend to infinity as $h \rightarrow 0$, as mentioned in the previous section. Accounting for zeros of the determinant of (3.1b) gives an additional surface mode classification, consisting of eight modes of the form

$$\omega = \pm c_l k + O(k^{-1}) \quad \text{or} \quad \omega = \pm c_t k + O(k^{-1}).$$

These are the quasi-solid surface modes of the previous section.

The regularity of (2.2) when rearranged into a polynomial in ω and k means that $\omega(k)$ is continuous, and consequently $\omega(k)$ is bounded for k in any finite interval, just as for the mass–spring–damper boundary model. However, the benefit of the thin-shell boundary model is that all of the above surface modes have a bounded $\text{Im}(\omega)$ for real k as $|k| \rightarrow \infty$. Hence, the image of the real k axis in the ω -plane has bounded imaginary part, and so the Briggs–Bers criterion can be used.

The boundedness of $\text{Im}(\omega(k))$ for real k as $|k| \rightarrow \infty$ does not hold for the mass–spring–damper system. To see how this is regularized by the inclusion of bending stiffness for $h \neq 0$,

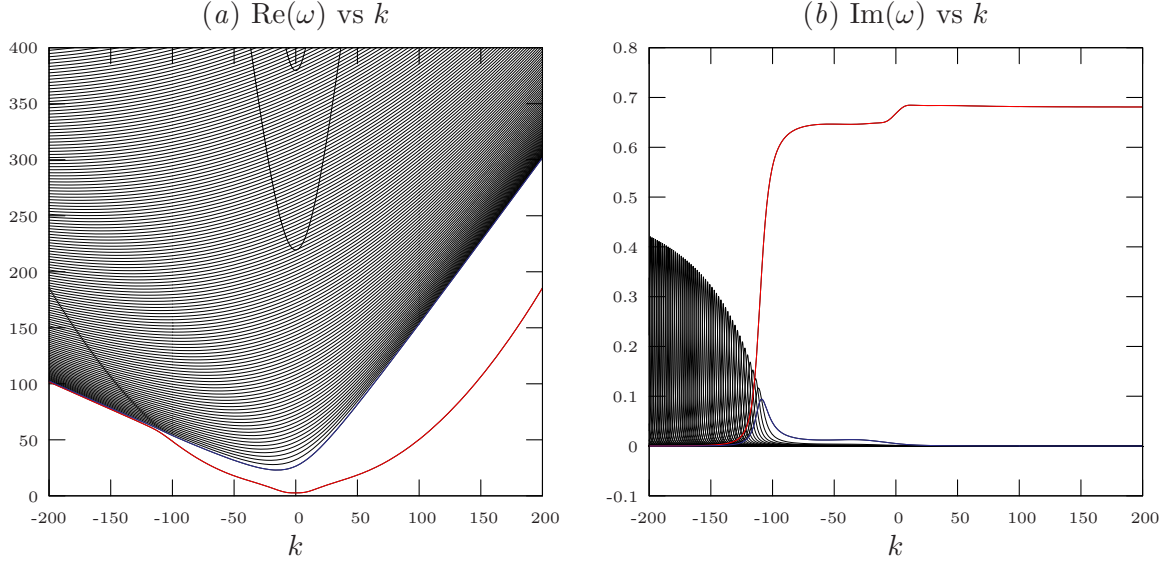


Figure 3.3: Trajectories of $\omega(k)$ for k real. For clarity, only modes with $\text{Re}(\omega) > 0$ are shown; the behaviour for $\text{Re}(\omega) < 0$ may be inferred from $-\bar{\omega}(-\bar{k}) = \omega(k)$, where the bar denotes complex conjugation. The fluid is air at STP and the boundary is aluminium. $h = 10^{-3}$, $U = 0.5$, $R = 3$, $b = 1$, and $m = 24$.

set $\omega = N\sqrt{k}$ in (3.3) to find, to leading order as $|k| \rightarrow \infty$,

$$N^2 = -\frac{U^2}{\beta d} + \frac{B}{d}k^3,$$

where $\beta = \sqrt{1 - U^2}$. The unbounded $\omega = -iU\sqrt{k/(\beta d)}$ behaviour found by Rienstra & Peake (2005) is therefore seen to hold only for moderate values of $|k|$ for which

$$|k| \ll \left(\frac{U^2}{\beta B}\right)^{1/3}, \quad (3.4)$$

giving an estimate of the magnitude of k for which bending stiffness becomes important for stability. An example demonstrating this is given in §3.3.2.

3.3.1 A stable example

Figure 3.3 shows the real k axis mapped into the ω -plane for an air-filled aluminium duct, with $m = 24$, $R = 3$, and $b = 1$. The duct may be thought of as having a 1m radius and a shell thickness of 1mm. The many near-parallel trajectories in figure 3.3(a) correspond to the acoustic modes. The bending surface modes with $\text{Re}(\omega) = O(k^2)$ form the parabola apparently intersecting the acoustic modes (shown in red), while the quasi-solid surface modes with $\text{Re}(\omega) = O(k)$ are the two parabolic-looking trajectories within the region of acoustic

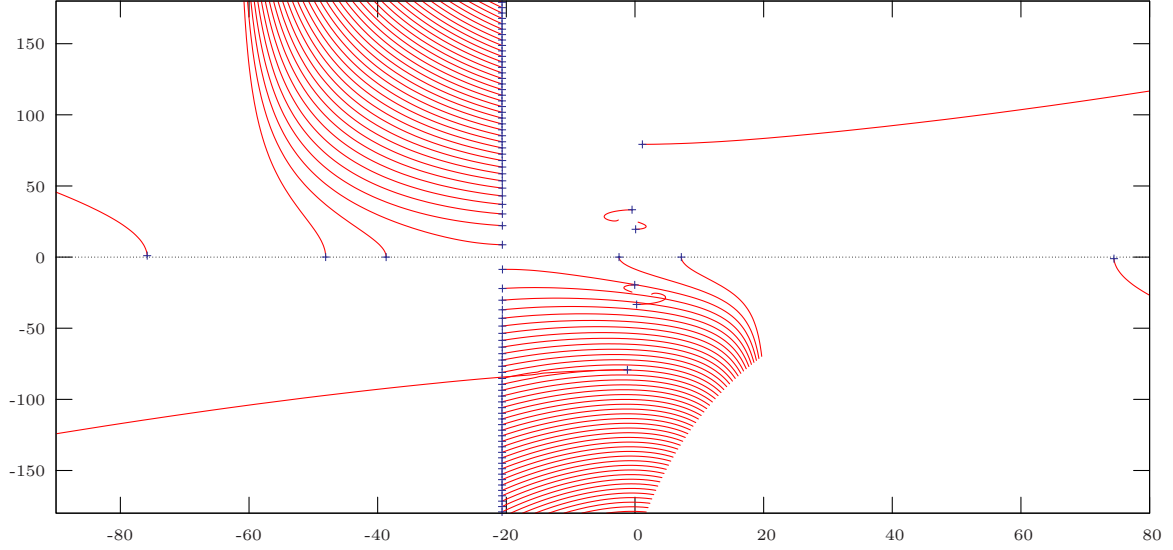


Figure 3.4: Trajectories of modes in the k -plane for $-100 \leq \text{Im}(\omega) \leq 0$ with $\text{Re}(\omega) = 31$ and crosses at $\text{Im}(\omega) = 0$. Parameters are as for figure 3.3.

modes. The fluid surface modes with $\text{Re}(\omega) = O(k)$ correspond to the borders of the region of acoustic modes (shown in blue). As $|k|$ increases, the bending surface modes enter the region of acoustic modes, leading to the trajectories in figure 3.3(b). These consist of acoustic modes jumping order, with an acoustic mode with nearly real ω being displaced by one of its neighbours, transitioning briefly into a bending surface mode with nonzero $\text{Im}(\omega)$, before displacing its other neighbour and once again becoming an acoustic mode. A similar behaviour is seen as the acoustic modes and quasi-solid modes coalesce, although the change in $\text{Im}(\omega)$ during this transition is so small as to be imperceptible in figure 3.3(b). Note that no modes are present with $\text{Im}(\omega) < 0$, so that the temporal inversion contour \mathcal{C}_ω may be taken arbitrarily close to the real ω axis. Hence, any mode with complex $k(\omega)$ corresponds to an exponentially decaying mode, while if $k(\omega)$ is real, the mode is left propagating if $\text{Re}(c_g) < 0$, and right propagating if $\text{Re}(c_g) > 0$, where $c_g = \partial\omega/\partial k$ is the group velocity, and there is no possibility of absolute instability. This is exactly as might have been naively expected without a detailed stability analysis, and shows that for these parameters the system is stable.

As an example of the typical Briggs–Bers treatment given in the literature, figure 3.4 shows the trajectories of modes in the k -plane as $\text{Im}(\omega)$ is varied with $\text{Re}(\omega) = 31$, again for $m = 24$ and $R = 3$ (these parameters were suggested by McAlpine & Wright, 2006 as being realistic parameters for tonal fan-noise in aeroengine intakes). No modes cross the real k axis, and thus all modes are seen to be either exponentially decaying or propagating in the direction of the

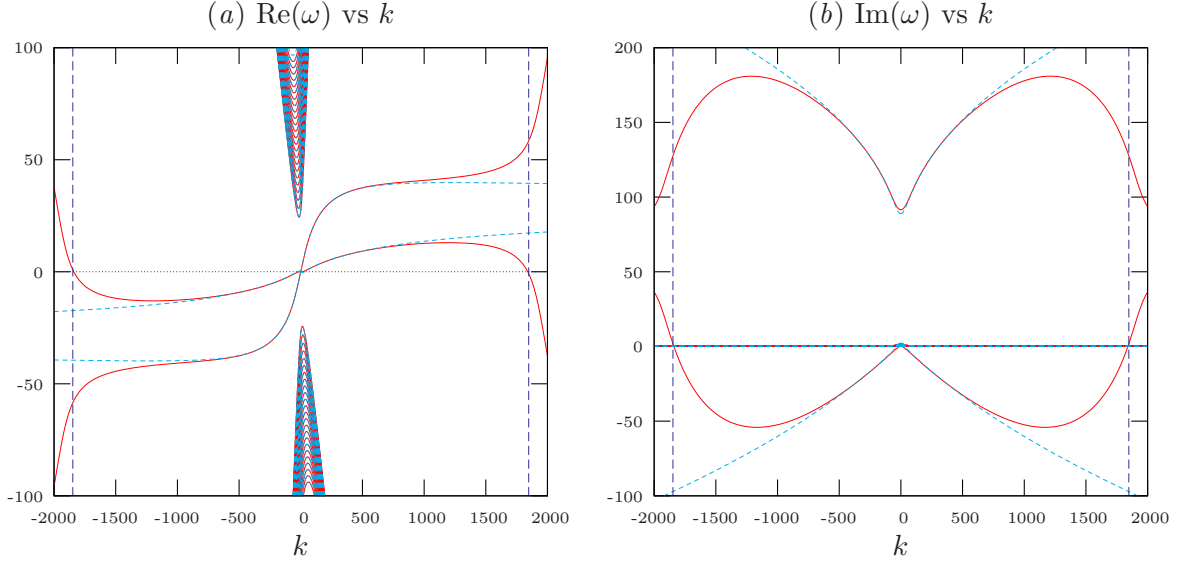


Figure 3.5: Trajectories of $\omega(k)$ for k real. Parameters are as for figure 3.3, but with $h = 10^{-5}$. Solid lines correspond to the thin-shell impedance, while the dashed lines show the equivalent mass–spring–damper trajectories. The value given by (3.4) as when bending stiffness becomes important to stability is $|k| \approx 1850$, shown by the long-dashed vertical lines.

group velocity, as predicted. It should be emphasized that just this analytic continuation alone does not guarantee the stability of the system, without first having ascertained that $\text{Im}(\omega(k))$ is bounded below for real k , and having checked that no absolute instabilities are present.

3.3.2 An example of instability

Using the same parameters as above, but with a very thin shell thickness $h = 10^{-5}$, leads to the situation shown in figure 3.5. In this case, (3.4) suggests that bending stiffness is unimportant provided $|k| \ll 1850$, and indeed for small k the mass–spring–damper model is indistinguishable from the thin-shell model. The two surface modes in the lower-half ω -plane in figure 3.5(b) demonstrate the predicted $\text{Im}(\omega) \propto \sqrt{k}$ behaviour, although for large k this is regularized by the bending stiffness of the thin shell, and $\text{Im}(\omega)$ is bounded below by -100 . This is not the case for the mass–spring–damper impedance, for which these modes continue to arbitrarily negative imaginary values of ω , prohibiting the Briggs–Bers criterion from being applied.

A naive application of the Briggs–Bers criterion would involve, say, analytically continuing from $\text{Im}(\omega) = -100$ to $\text{Im}(\omega) = 0$ with $\text{Re}(\omega) = 1$. Figure 3.6 shows this would cause the upper-right and far-right surface modes to be identified as right- and left-propagating instabilities

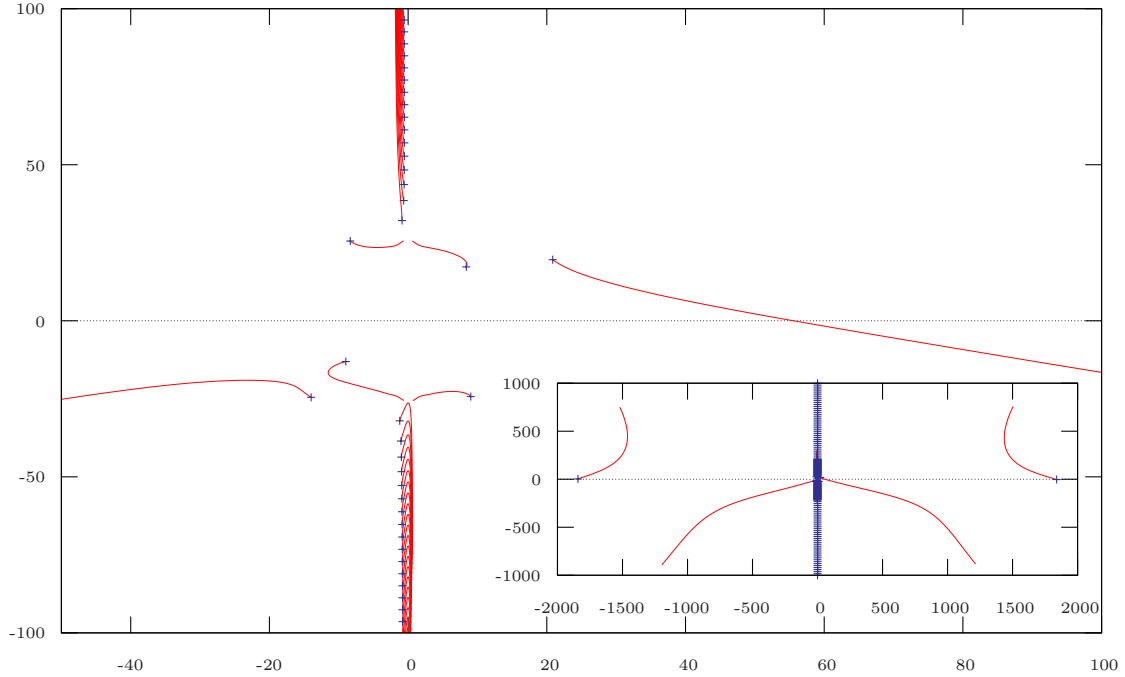


Figure 3.6: Trajectories of modes in the k -plane for $-100 \leq \text{Im}(\omega) \leq 0$ with $\text{Re}(\omega) = 1$ and crosses at $\text{Im}(\omega) = 0$. Parameters are as for figure 3.5.

respectively. This stability analysis is not complete, however, without considering the possibility of absolute instability.

If a pinch frequency ω_p exists, Briggs (1964) showed that this gives rise to an absolute instability, present simultaneously upstream and downstream of the driver, that dominates the solution at large times. Writing the dispersion relation (1.4) as $\Delta(k, \omega) = 0$, a pinch point occurs at a double root, given by $\partial\Delta/\partial k = 0$. The complexity of this dispersion relation means that the pinch points must be found numerically. Satisfying $\Delta(k, \omega) = 0$ gives the possibly multi-valued function $\omega(k)$, and an equivalent condition for a pinch point is that $d\omega/dk = 0$. Peake (1997) used a Newton–Raphson iteration to solve this latter equation, using an analytic result for the absolute instability frequency of a flat plate as a starting point. Using a Newton–Raphson iteration requires knowledge of the second derivative of $\omega(k)$, for which Peake used the Cauchy integral representation, and since $\omega(k)$ is itself calculated numerically using Newton–Raphson iteration, this is numerically expensive. Here, a more simple iteration is used, based directly on $\Delta(k, \omega)$ and without the need to calculate $\omega(k)$ explicitly.

It is required to find values of ω and k for which both $\Delta(k, \omega) = 0$ and $\Delta_k(k, \omega) = 0$, where

the subscript k denotes differentiation with respect to k . For small δk and $\delta\omega$,

$$\begin{pmatrix} \Delta(k + \delta k, \omega + \delta\omega) \\ \Delta_k(k + \delta k, \omega + \delta\omega) \end{pmatrix} = \begin{pmatrix} \Delta \\ \Delta_k \end{pmatrix} + \begin{pmatrix} \Delta_k & \Delta_\omega \\ \Delta_{kk} & \Delta_{k\omega} \end{pmatrix} \begin{pmatrix} \delta k \\ \delta\omega \end{pmatrix} + O(\delta k^2 + \delta\omega^2),$$

the right hand side being evaluated at k and ω . A two-dimensional Newton–Raphson iteration therefore gives

$$\begin{pmatrix} k_{n+1} \\ \omega_{n+1} \end{pmatrix} = \begin{pmatrix} k_n \\ \omega_n \end{pmatrix} - \frac{1}{\Delta_k \Delta_{k\omega} - \Delta_\omega \Delta_{kk}} \begin{pmatrix} \Delta_{k\omega} & -\Delta_\omega \\ -\Delta_{kk} & \Delta_k \end{pmatrix} \begin{pmatrix} \Delta \\ \Delta_k \end{pmatrix},$$

where the right hand side is evaluated at k_n and ω_n . This iteration is performed with starting points located on a grid covering the relevant areas of the k - and ω -planes. The values of ω found are shown in figure 3.7, along with the image $\omega(k)$ of the real k axis, below which the Briggs–Bers temporal inversion contour \mathcal{C}_ω must be initially taken to satisfy causality.

It remains to check which of these are modes originating from $\text{Im}(k) > 0$ on the initial temporal inversion contour \mathcal{C}_ω colliding with modes originating from $\text{Im}(k) < 0$, and that therefore correspond to a pinch point. The majority of the double roots involve the collision of two modes, both of which originate from the same half of the k -plane, and so do not correspond to pinch points. The modes labelled surface mode in figure 3.7 are all caused by the the surface mode in the lower-left of the k -plane interacting with the acoustic duct modes, as shown in figure 3.8. The arrows in figure 3.7 point in the direction of increasing $|\text{Im}(k)|$ for the double root, and show the surface mode interacting with progressively more cutoff acoustic modes. Since all the modes involved in these double roots originate from the lower-half k -plane, none of these correspond to absolute instabilities. The same is true of the double roots located at $\omega_p = \pm 0.9 - 0.5i$ (figure 3.9), $\omega_p = \pm 10.6 - 19.6i$ (figure 3.10), and $\omega_p = \pm 13.3 - 10.0i$ (figure 3.11), so that none of these correspond to absolute instabilities. The dominant double roots that do correspond to pinch points are found to be $\omega_p = \pm 13 - 54i$; the nature of this double-root is demonstrated to be a pinch point in figure 3.12.

The previously identified convective instabilities are still present, in that when excited at a particular axial location at a frequency $\omega_f = 1$, there do exist two unstable modes that, after long times, are seen to grow exponentially in space with the predicted axial wavenumbers. However, these are exponentially small compared to the dominant contribution to the solution at large times, which grows exponentially in time with frequencies $\omega_p = \pm 13 - 54i$, and whose spatial distribution is governed by the axial wavenumbers $k_p = \pm 1170 + 3.69i$. The extreme parameters needed to demonstrate this instability may be thought of as a 1m duct radius with a boundary thickness of 0.01mm and a mean flow Mach number of 0.5, which is not easily realized in practice!

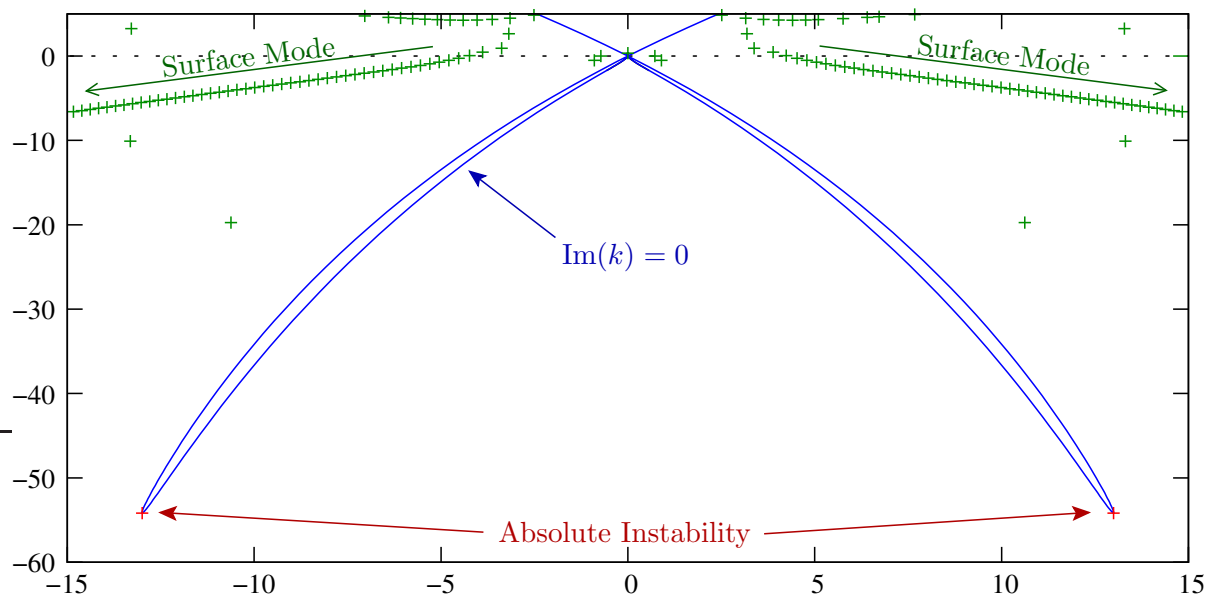


Figure 3.7: Values of ω for which double roots of the dispersion relation occur for some value of k . The solid line is $\omega(k)$ for real k . Parameters are as for figure 3.5.

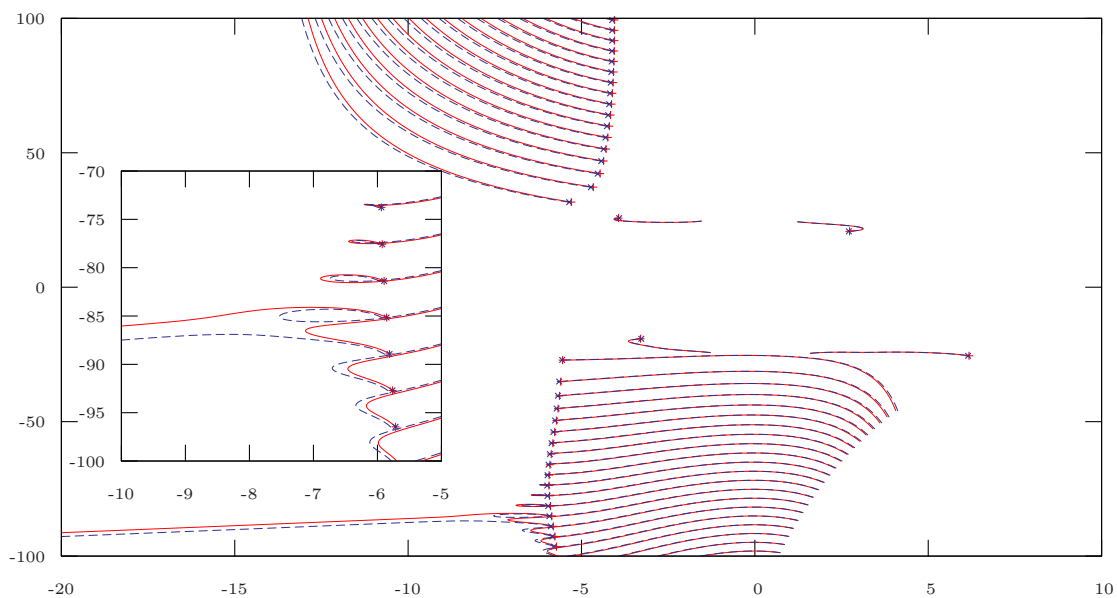


Figure 3.8: Briggs-Bers trajectories in the k plane for $\text{Re}(\omega) = 7.0$ (solid lines) and $\text{Re}(\omega) = 7.1$ (dashed lines). This is the type of double root for all the double roots in figure 3.7 labelled surface mode. Crosses denote $\text{Im}(\omega) = 0$.

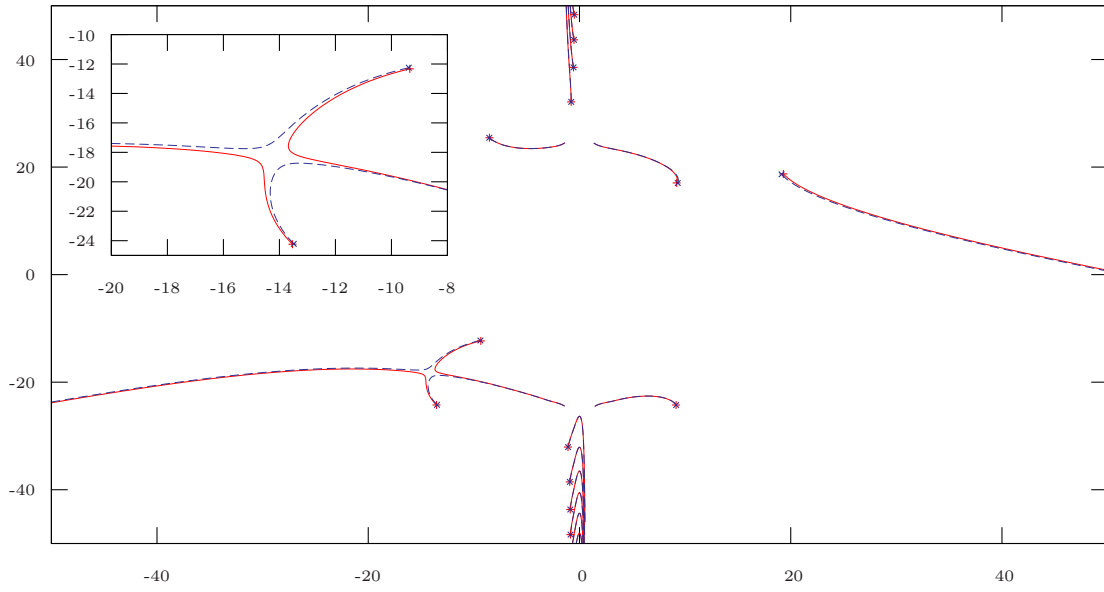


Figure 3.9: Briggs-Bers trajectories in the k plane for $\text{Re}(\omega) = 0.90$ (solid lines) and $\text{Re}(\omega) = 0.89$ (dashed lines). Crosses denote $\text{Im}(\omega) = 0$.

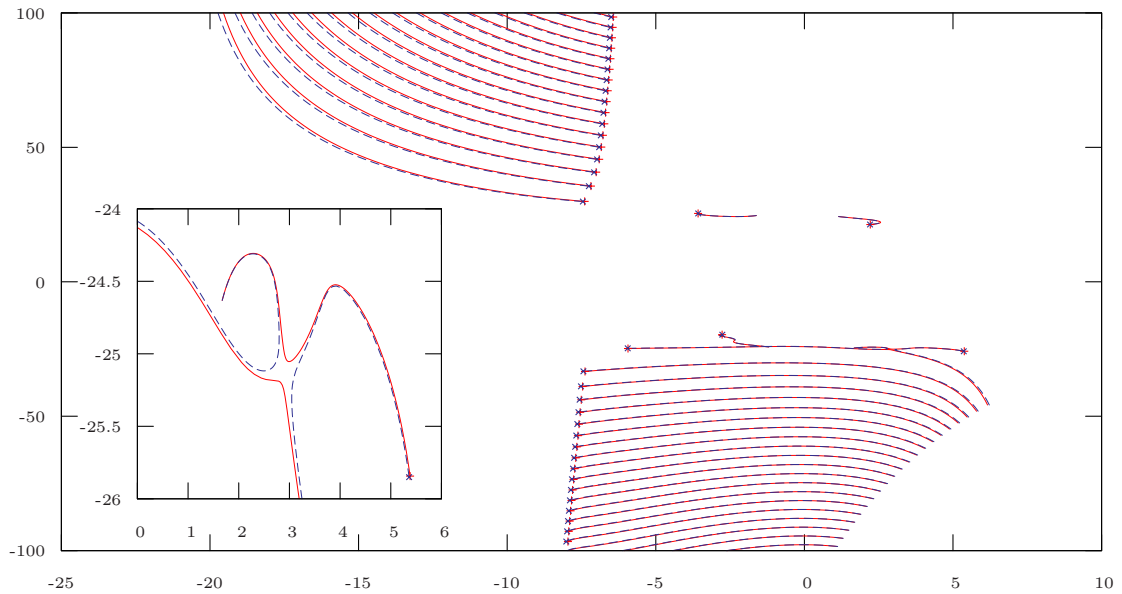


Figure 3.10: Briggs-Bers trajectories in the k plane for $\text{Re}(\omega) = 10.6$ (solid lines) and $\text{Re}(\omega) = 10.7$ (dashed lines). Crosses denote $\text{Im}(\omega) = 0$.

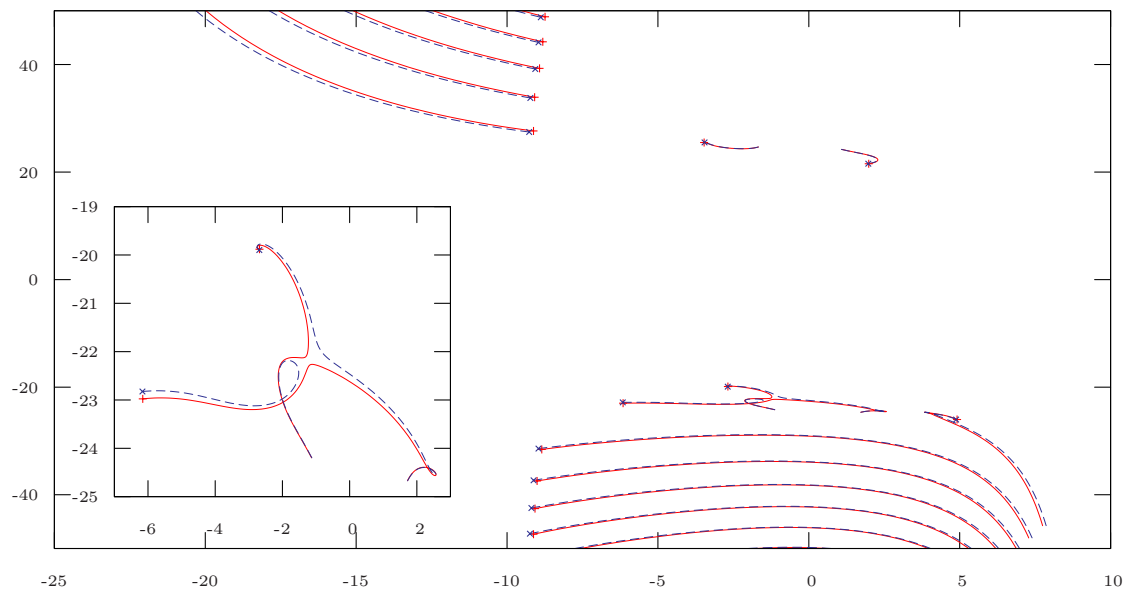


Figure 3.11: Briggs-Bers trajectories in the k plane for $\text{Re}(\omega) = 13.3$ (solid lines) and $\text{Re}(\omega) = 13.5$ (dashed lines). Crosses denote $\text{Im}(\omega) = 0$.

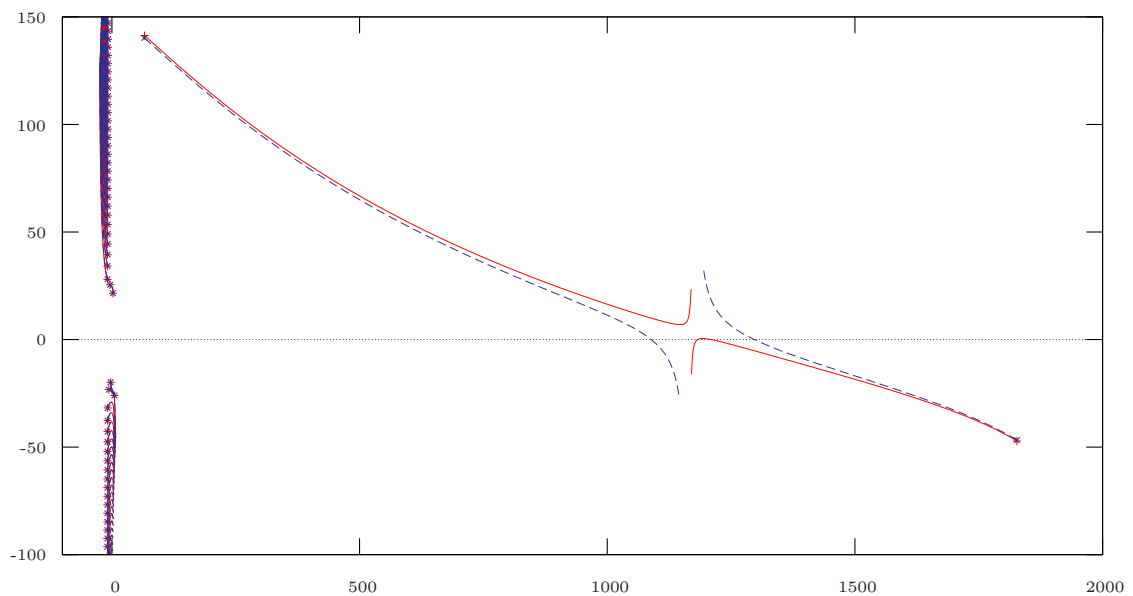


Figure 3.12: Briggs-Bers trajectories in the k plane for $\text{Re}(\omega) = 13.0$ (solid lines) and $\text{Re}(\omega) = 12.9$ (dashed lines). Crosses denote $\text{Im}(\omega) = 0$.

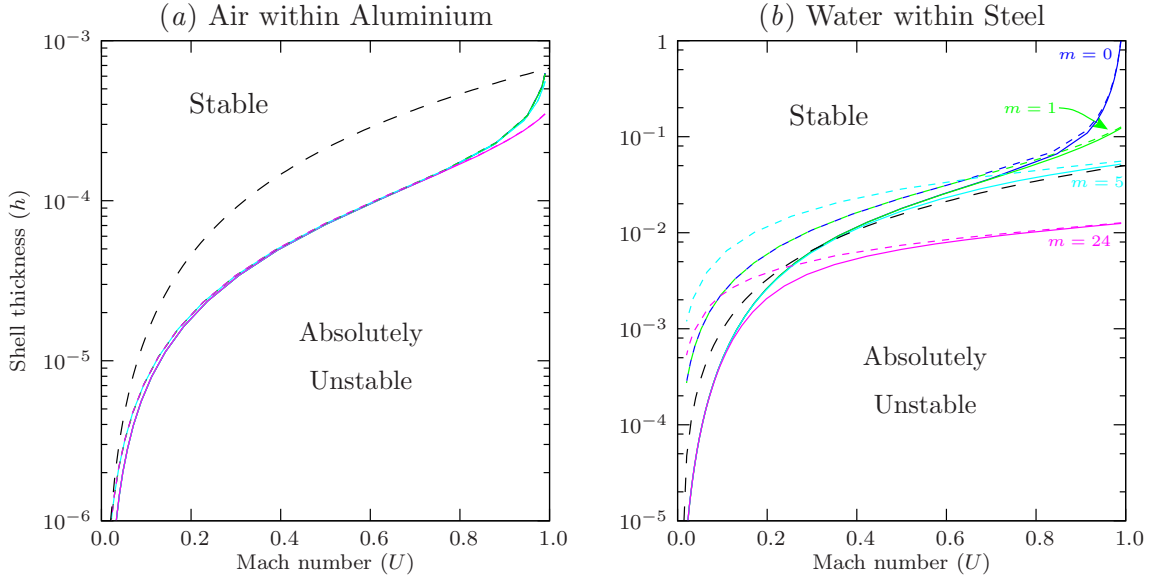


Figure 3.13: Values of h and U giving an absolute instability, for m being 0, 1, 5, and 24. The critical shell thickness h_c is given by short dashed lines for $b = 0$, solid lines for $b = 1$, and long dashed line for the asymptotic incompressible predictions of Peake (1997). The results are independent of R . The material parameters are given in table 3.1.

3.3.3 The boundary between stable and unstable behaviour

The question now arises, how small a shell thickness is needed for there to be an absolute instability? By first finding the dominant pinch frequency ω_p , and then tracking this pinch frequency as h is varied, the critical value $h = h_c$ giving $\text{Im}(\omega_p) = 0$ may be found. For $h < h_c$ we have $\text{Im}(\omega_p) < 0$, giving an absolute instability, while for $h > h_c$ we have $\text{Im}(\omega_p) > 0$, and the \mathcal{C}_ω contour may be deformed onto the real ω axis, so that no absolute instability is present. Figure 3.13 plots these values of h_c for a variety of parameters; the amount of external damping, R , is found to have no effect on the critical shell thickness h_c , and so figure 3.13 only considers $R = 3$. For small U the dominant parameter is the Winkler foundation spring constant b , while the azimuthal order m plays little role. As U approaches unity the situation is reversed, and m becomes the dominant parameter, while b plays little role.

The approximate critical shell thickness found by Peake (1997, equation 3.3) is also plotted in figure 3.13. This result was derived for an incompressible fluid in the small-mean-flow limit, and was shown to give a very accurate approximation to the true critical boundary for an incompressible fluid. Figure 3.13(a) shows that for the light fluid-loading given by air within aluminium, the system is stable for a wider range of shell thicknesses than if the fluid were incompressible. However, figure 3.13(b) shows that for the heavy fluid-loading given by water

within steel, the system may be stable for a wider or smaller range of shell thicknesses than if the fluid were incompressible, depending upon the situation. This is especially true if there is no externally-applied spring forcing, so that $b = 0$.

For a double root to correspond to a pinch, one mode must originate from the upper-half k -plane and one from the lower-half. Hence, at least one of these modes must cross the real k axis, shown as a solid line in figure 3.7 making two fingers in the lower-half ω -plane. As h is increased, these two fingers shrink, until at a certain value of h there are no modes with real k in the lower-half ω -plane, and so there can be no instabilities (either absolute or convective). The dominant pinch frequency ω_p is located towards the ends of these fingers, and the critical shell thickness h_c turns out to be exactly the value of h for which these fingers disappear from the lower-half ω -plane. This implies the interesting result that the system is either absolutely unstable or stable, but never only convectively unstable. Why this should be the case, rather than the pinch point crossing the boundary of one of the fingers and producing convective instability, is unclear. Since the two fingers of $\omega(k)$ for real k shrink down to $\omega = 0$, the critical value of ω_p , defined as $\text{Im}(\omega_p) = 0$, actually occurs at $\omega_p = 0$. Using this, (3.3) tells us that this borderline is given by $\Delta = \partial\Delta/\partial k = 0$, where

$$\Delta \equiv (k^2 + m^2/\beta^2) \left((c_l^2 d + b)/B + (k^2 + m^2)^2 \right)^2 - \frac{U^4 k^4}{B^2 \beta^2} \quad (3.5)$$

and $\beta^2 = 1 - U^2$. These two equations give a simple algebraic expression for h_c and the value of $k = k_p$ for which this occurs, in terms of the parameters $c_l^2 \rho_s$, m , b , and U , assuming of course that the borderline frequency does in fact occur at $\omega_p = 0$. Note that the boundary damping R does not occur in (3.5), explaining why the curves in figure 3.13 are independent of R . However, the general solution of $\Delta = \partial\Delta/\partial k = 0$ involves solving simultaneously a 10th and 8th order polynomial. Progress may be made by considering the case for which $k_p \gg m/\beta$, which will turn out to be valid provided U is sufficiently small. Neglecting the terms involving m^2 in (3.5) then gives

$$\begin{aligned} \frac{1}{k_p^2} \Delta &\equiv k_p^8 + 2\lambda k_p^4 - k_0^6 k_p^2 + \lambda^2 = 0, \\ \frac{1}{2k_p} \frac{\partial\Delta}{\partial k} &\equiv 5k_p^8 + 6\lambda k_p^4 - 2k_0^6 k_p^2 + \lambda^2 = 0, \end{aligned}$$

where $\lambda = (c_l^2 d + b)/B$, and $k_0 = (U^2/(\beta B))^{1/3}$ is the value of k given in (3.4) for which bending becomes important to stability (note that k_0 is the value of k_p for which the k_p^8 and k_p^2 terms of Δ balance). Solving these two equations gives

$$h_c = -\frac{b}{2c_l^2 \rho_s} + \frac{1}{2} \sqrt{\left(\frac{b}{c_l^2 \rho_s} \right)^2 + \left(\frac{9U^4}{(1-U^2)c_l^4 \rho_s^2} \right)^{2/3}}. \quad (3.6)$$

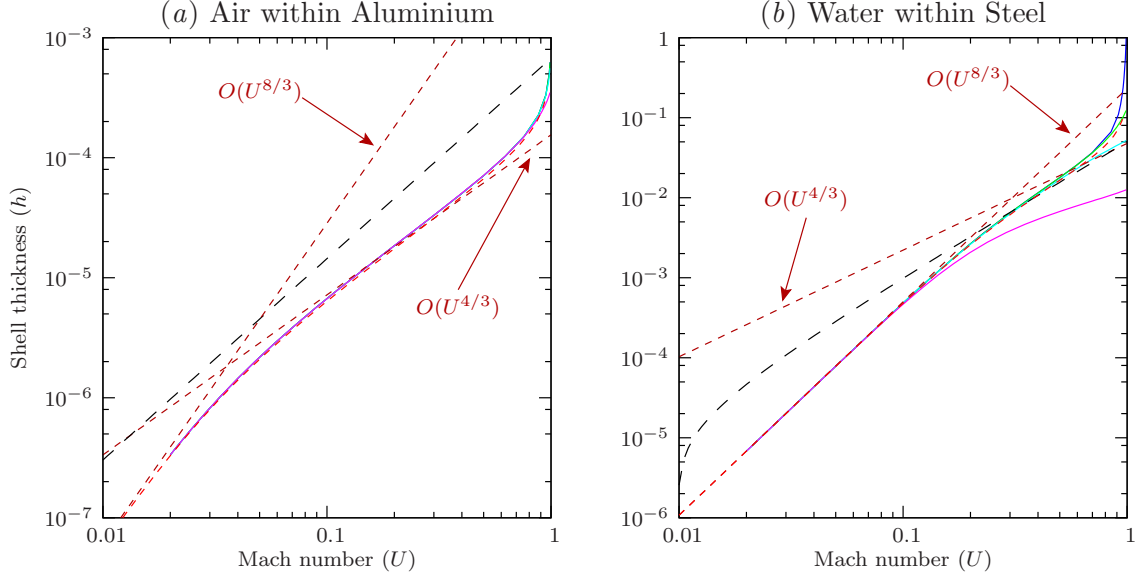


Figure 3.14: Comparison between asymptotic approximations and numerical results for h_c , for $b = 1$ and $m \in \{0, 1, 5, 24\}$. Solid lines give the numerical results, short dashed lines give the asymptotics of (3.6) and the power laws derived from it, and long dashed lines give the incompressible asymptotics.

If $U \ll 1$, this reduces to two cases, depending on whether $U \ll U_c$ or $U \gg U_c$, where

$$U_c = \left(\frac{8b^3}{9c_l^2 \rho_s} \right)^{1/4}.$$

If $U \ll U_c$, the Winkler foundation spring force b dominates the thin-shell spring force $c_l^2 d$, and (3.6) gives an $h_c = O(U^{8/3})$ power law,

$$h_c \simeq \frac{c_l^2 \rho_s}{b} \left(\frac{9U^4}{8c_l^4 \rho_s^2} \right)^{2/3}.$$

Alternatively, if $U \gg U_c$ it is the thin-shell spring force that dominates, and we get an $h_c = O(U^{4/3})$ power law,

$$h_c \simeq \left(\frac{9U^4}{8c_l^4 \rho_s^2} \right)^{1/3}.$$

Note that if $b = 0$, corresponding to no Winkler foundation spring force, the $h_c = O(U^{4/3})$ power law is universally valid for $U \ll 1$.

Figure 3.14 shows these three predictions, and the incompressible predictions, against the numerically found values of h_c . As U approaches unity, the m^2/β^2 factor in (3.5) becomes significant, and the above asymptotics breaks down provided $m \neq 0$. However, for small and moderate U , the asymptotics derived above show a very good agreement to the numerical results, and the $U^{8/3}$ and $U^{4/3}$ scaling laws are clearly demonstrated.

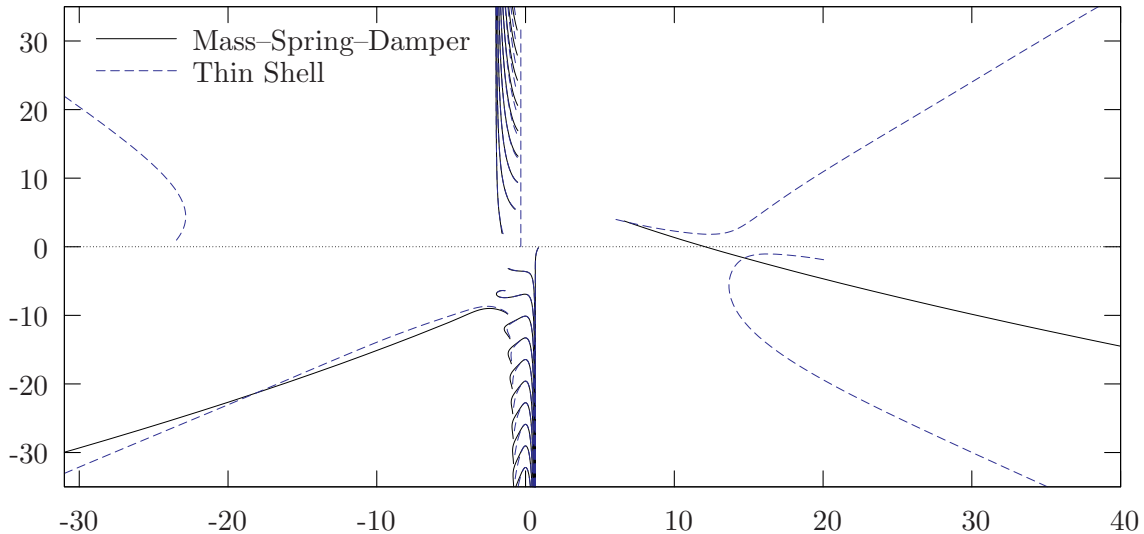


Figure 3.15: Comparison of Briggs–Bers trajectories in the k plane between a mass–spring–damper and thin-shell boundary, for $U = 0.5$, $m = 0$, $\omega = 1$. The mass–spring–damper has $b = 1$, $d = 0.1$, and $R = 1$, and the thin shell has $h = 1.75 \times 10^{-2}$ and $\nu = 0.33$ (and $c_l^2 = 10$, $\rho_s = 5.7$, $b = 0$). These parameters correspond to Rienstra & Peake (2005, figure 4).

3.3.4 Recovery of the mass–spring–damper boundary for small shell thicknesses

We now summarise the stability results of the thin-shell boundary in the limit $h \rightarrow 0$, which we know recovers the mass–spring–damper impedance. From figure 3.13, we know that the thin-shell boundary is absolutely unstable provided h is sufficiently small, with dominant frequency ω_p . As $h \rightarrow 0$, $\text{Im}(\omega_p) \rightarrow -\infty$, so that for arbitrarily small shell thicknesses the absolute instability grows arbitrarily quickly. The pinch leading to this absolute instability occurs because two of the surface modes coincide and pinch the \mathcal{C}_k contour, and one of these surface modes is a surface mode that disappears to infinity as $h \rightarrow 0$, as shown in figure 3.2(b). We therefore conclude that when interpreting the mass–spring–damper as a thin shell of zero thickness, there is an absolute instability present of infinite temporal growth rate, and there are two surface modes that are at $k = \infty$. Of course, we knew already that the mass–spring–damper boundary supported arbitrarily large temporal growth rates, as shown in figure 3.5.

As a comparison between the thin-shell and mass–spring–damper boundaries for a naive Briggs–Bers application, consider figure 3.15. This appears to show the thin shell to be stable at this frequency and the mass–spring–damper boundary to admit a convective instability. However, as we have discovered, one must always consider the possibility of absolute instability

in a Briggs–Bers analysis, and in fact for these parameters the thin shell is absolutely unstable with a dominant frequency $\omega_p = \pm 0.937 - 1.01i$.

3.4 Scattering by a hard-wall to thin-shell boundary transition

Rienstra (2007) considered the scattering of an acoustic duct mode at a transition from a hard-wall to a locally-reacting boundary. As there was some question over the stability of the surface modes, Rienstra considered both stable and unstable cases. We now investigate how this scattering is altered by modelling the boundary as a thin shell.

Consider the duct shown in figure 3.1, which for $x < 0$ has a hard-wall boundary with boundary condition $\partial\phi/\partial r = 0$, while for $x > 0$ the boundary is a thin shell, as described by Flügge’s equations. The thin-shell boundary is clamped to the rigid boundary at the intersection $x = 0$. All quantities are assumed proportional to $\exp\{i\omega t - im\theta\}$. A rigid-wall duct mode with pressure $p_{\text{in}}(x, r) = \exp\{-ik_{\text{in}}x\}J_m(\alpha_{\text{in}}r)/J_m(\alpha_{\text{in}})$ is inbound from upstream, where $\alpha_{\text{in}}^2 = (\omega - Uk_{\text{in}})^2 - k_{\text{in}}^2$ and $J'_m(\alpha_{\text{in}}) = 0$, so that p_{in} satisfies the wave equation and the hard-wall boundary condition for $x < 0$. Since this mode does not satisfy the boundary condition for $x > 0$, as it encounters the boundary transition it scatters into other duct modes, some of which are reflected back upstream. A similar method to Rienstra (2007) is used to solve for the scattered solution using the Wiener–Hopf technique, as described by Noble (1958).

3.4.1 Solution in the fluid

If $w(x)$ is the small unsteady radial deflection of the boundary, as shown in figure 3.1, then the governing equations and boundary condition give

$$\frac{D^2\phi}{Dt^2} - \nabla^2\phi = 0, \quad \text{subject to} \quad \frac{\partial\phi}{\partial r} = \frac{Dw}{Dt} \quad \text{at } r = 1. \quad (3.7)$$

We split the fluid pressure into the sum of the incoming imposed pressure and a scattering pressure, so that the total pressure is $p = -D\phi/Dt = p_{\text{in}} - D\psi/Dt$, where ψ is the potential of the wave scattered by the impedance boundary change at $x = 0$.

In order to achieve a causal solution, and for the convergence of the integrals that follow, it turns out to be convenient to consider $\omega = \omega_r - i\varepsilon$ with ω_r real, and ε positive and chosen such that $\text{Im}(\omega(k)) > -\varepsilon$ for all real k and for both the hard-wall and the thin-shell dispersion relations. Since by definition of ω there are no modes with real k , it is assumed that there exists some positive $\delta(\varepsilon)$ such that the strip \mathcal{S} given by $|\text{Im}(k)| < \delta$ is free of any rigid-wall or

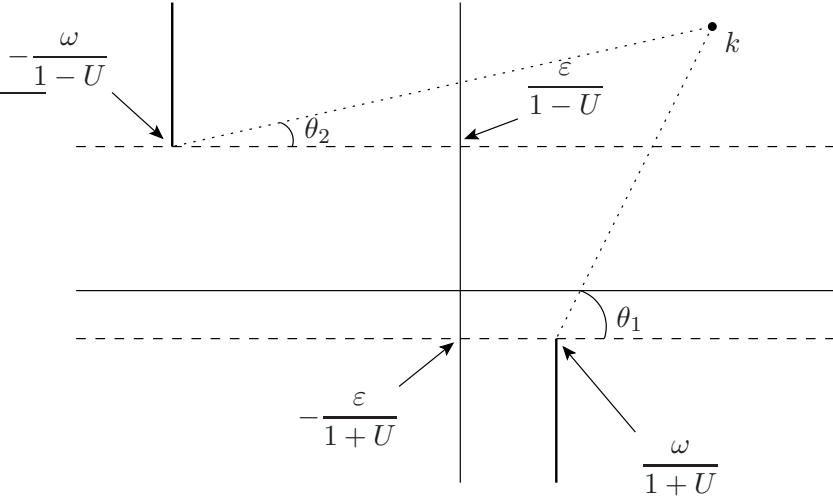


Figure 3.16: Branch cuts (thick lines) of $\alpha(k)$ in the k -plane.

thin-shell modes. The Briggs–Bers criterion then dictates that, for this frequency, all modes that originate at $x = 0$ decay exponentially as $|x| \rightarrow \infty$, and from the definition of \mathcal{S} it follows that they decay at least as fast as $\exp\{-\delta|x|\}$. It will also turn out to be useful to require δ to be small enough so that $\omega/(U \pm 1)$, k_l , and k_t all lie outside \mathcal{S} . Analytic continuity of the solution to $\varepsilon = 0$ will eventually be sought.

The Fourier transform of ψ is given by

$$\tilde{\psi}(k, r) = \int_{-\infty}^{\infty} \psi(x, r) e^{ikx} dx,$$

which, because of the choice of ε , for k in \mathcal{S} converges absolutely and is therefore analytic. The Fourier-transformed differential equation (3.7) is solved as before in terms of Bessel's functions, giving $\tilde{\psi}(k, r) = A(k)J_m(\alpha(k)r)$, where $A(k)$ is an as yet undetermined function representing the spectrum of the scattered wave, and $\alpha(k)^2 = (\omega - Uk)^2 - k^2$. The branch cuts for $\alpha(k)$ are taken parallel to the imaginary axis and away from the real axis, as shown in figure 3.16, and $\alpha(k)$ is defined as

$$\alpha(k) = i\beta \left| k + \frac{\omega}{1-U} \right|^{1/2} \left| k - \frac{\omega}{1+U} \right|^{1/2} \exp \left\{ i \frac{\theta_1 + \theta_2}{2} \right\}$$

so that $\alpha(k)$ is analytic and $\text{Im}(\alpha(k)) > 0$ in a neighbourhood of the real k axis. These branch cuts will turn out to be unnecessary, as before, although this will only become apparent a posteriori.

For $x < 0$ the duct wall is rigid and therefore $w(x) \equiv 0$. The Fourier transform of $w(x)$ is therefore given by the positive-half-range transform

$$H^+(k) = \int_0^{\infty} w(x) e^{ikx} dx,$$

which is an analytic function of k for $\text{Im}(k) > -\delta$. For positive-half-range Fourier transforms, note that

$$\int_0^{\infty} f'(x)e^{ikx} dx = -f(0) - ik \int_0^{\infty} f(x)e^{ikx} dx$$

assuming appropriate decay at infinity (which is ensured in all cases here by taking $k \in \mathcal{S}$). Hence, the boundary condition from (3.7) gives

$$\alpha(k)A(k)J'_m(\alpha(k)) = i(\omega - Uk)H^+(k), \quad (3.8)$$

yielding $A(k)$ in terms of the unknown function $H^+(k)$. Equation (3.7) is now satisfied, for any function $H^+(k)$, or equivalently for any boundary deflection $w(x)$. The physics of the boundary remain to be satisfied.

3.4.2 Imposing the thin-shell boundary

For a thin-shell boundary, the boundary deflection $w(x)$ is related to the fluid pressure $p(x, 1)$ at the boundary by Flügge's equations, the full-range Fourier transforms of which are given in (3.1). Here, we are interested in the positive-half-range Fourier transform of Flügge's equations, in order to derive $H^+(k)$. Since the thin shell is clamped at $x = 0$, so that $w(0) = w'(0) = u(0) = v(0) = 0$, the positive-half-range Fourier transforms of Flügge's equations give

$$\int_0^{\infty} p(x, 1)e^{ikx} dx = i\omega Z_1(k)H^+(k) + i\omega Z_0(k), \quad (3.9)$$

where

$$i\omega Z_1(k) = c_l^2 d + b + i\omega R - d\omega^2 + B(k^2 + m^2)^2 - c_l^2 d \frac{Q_1^2 a_{22} - 2Q_1 Q_2 a_{12} + Q_2^2 a_{11}}{\left(\frac{\omega^2}{c_l^2} - (k^2 + m^2)\right) \left(\frac{\omega^2}{c_l^2} - \frac{1-\nu}{2}(k^2 + m^2)\right)}, \quad (3.10)$$

$$i\omega Z_0(k) = ic_l^2 d \frac{Q_1 C_1 a_{22} - (Q_1 C_2 + Q_2 C_1) a_{12} + Q_2 C_2 a_{11}}{\left(\frac{\omega^2}{c_l^2} - (k^2 + m^2)\right) \left(\frac{\omega^2}{c_l^2} - \frac{1-\nu}{2}(k^2 + m^2)\right)} + iBC_3 k - BC_4, \quad (3.11)$$

$$\begin{aligned} C_1 &= u'(0) - \frac{h^2}{12} w''(0), & C_2 &= \frac{1-\nu}{2} v'(0), \\ C_3 &= \left(1 - \frac{h^2}{12}\right) w''(0) - C_1, & C_4 &= \left(1 - \frac{h^2}{12}\right) w'''(0) + 2imC_2. \end{aligned}$$

The equality $u''(0) = w'''(0)h^2/12 + imv'(0)(1+\nu)/2$, implied by the axial component of Flügge's equations, has been used to write C_4 in the given form. These constants bear a great similarity to the forces and moments exerted on the hard-wall section by the thin shell at the clamp at

$x = 0$. We shall consider these constants later, but for the moment we assume their values to be known.

Since the positive-half-range transform of $p_{\text{in}}(x, 1)$ is $i/(k - k_{\text{in}})$, the positive-half-range transform of $p(x, 1)$ may be manipulated to give

$$\int_0^\infty p(x, 1)e^{ikx} dx = \frac{i}{k - k_{\text{in}}} - i(\omega - Uk)A(k)J_m(\alpha(k)) - P^-(k), \quad (3.12)$$

where $P^-(k)$ is the negative-half-range Fourier transform of the scattered pressure at the boundary,

$$P^-(k) = \int_{-\infty}^0 -\frac{D\psi}{Dt}(x, 1)e^{ikx} dx,$$

and is analytic for $\text{Im}(k) < \delta$. Equating (3.12) and (3.9) gives

$$P^-(k) - i/(k - k_{\text{in}}) + i\omega Z_0(k) = H^+(k)K(k), \quad (3.13)$$

where

$$K(k) = \frac{(\omega - Uk)^2 J_m(\alpha(k))}{\alpha(k) J'_m(\alpha(k))} - i\omega Z_1(k) \quad (3.14)$$

is the Wiener–Hopf kernel. Equations (3.13) and (3.14) form the Wiener–Hopf problem.

3.4.3 Factorizing the Wiener–Hopf kernel

Continuing with the Wiener–Hopf method, in order to solve this problem we would like to factorize $K(k) = K^+(k)/K^-(k)$, where $K^+(k)$ is analytic and nonzero for $\text{Im}(k) > -\delta$, and $K^-(k)$ is analytic and nonzero for $\text{Im}(k) < \delta$. Similarly, we would also like to split $i\omega Z_0(k)K^-(k)$ into $F^-(k) + F^+(k)$. In order to do this, we must first investigate the poles of the Wiener–Hopf kernel. $K(k)$ has poles which are zeros of $J'_m(\alpha(k))$, zeros of $\alpha(k)$, or poles of $i\omega Z_1$. Zeros of $J'_m(\alpha(k))$ correspond to rigid-wall duct modes, while the poles of $i\omega Z_1$ are due to the determinant of (3.1b) being zero, and occur at $\pm k_l$ and $\pm k_t$. The zeros of $K(k)$ are given by the zeros of $\chi(k)$, where

$$\chi(k) = (\omega - Uk)^2 J_m(\alpha(k)) - i\omega Z_1(k) \alpha(k) J'_m(\alpha(k)), \quad (3.15)$$

and hence correspond to duct modes for a duct boundary with impedance Z_1 (c.f. equation 1.6). Hence, by definition of ε , the strip \mathcal{S} defined by $|\text{Im}(k)| < \delta$ contains no poles or zeros of $K(k)$.

The factorization method used here is as described by Noble (1958), and is very similar to the method used by Rienstra (2007). It follows from (3.10) that $K(k) = -B(1 - h^2/12)k^4 + O(k^2)$ as $|k| \rightarrow \infty$. Hence,

$$L(k) \equiv -\frac{K(k)}{B(1 - h^2/12)(k^2 + X^2)^2} = 1 + O(k^{-2}),$$

as $|k| \rightarrow \infty$, where $X > \delta$ is an arbitrary positive constant. Since both $K(k)$ and $(k^2 + X^2)^2$ are analytic and non-zero in the strip \mathcal{S} , so too is $L(k)$, and hence $\log L$ may be defined so as to be analytic in \mathcal{S} . Using Cauchy's integral representation,

$$2\pi i \log(L(k)) = \int_{-Y-i\delta}^{Y-i\delta} + \int_{Y-i\delta}^{Y+i\delta} + \int_{Y+i\delta}^{-Y+i\delta} + \int_{-Y+i\delta}^{-Y-i\delta} \frac{\log(L(\xi))}{\xi - k} d\xi,$$

where the integration contours are straight lines between the endpoints, and k lies inside this closed contour. Since $\log(L(\xi))/(\xi - k) = O(\xi^{-3})$, the end integrals tend to zero as $Y \rightarrow \infty$ and the other two integrals converge, so that

$$\log(L(k)) = \frac{1}{2\pi i} \int_{-\infty-i\delta}^{\infty-i\delta} \frac{\log(L(\xi))}{\xi - k} d\xi - \frac{1}{2\pi i} \int_{-\infty+i\delta}^{\infty+i\delta} \frac{\log(L(\xi))}{\xi - k} d\xi. \quad (3.16)$$

The first integral is analytic for $\text{Im}(k) > -\delta$, and similarly the second integral is analytic for $\text{Im}(k) < \delta$. Calling the first integral $\log(L^+(k))$ and the second integral $\log(L^-(k))$ gives the decomposition $L(k) = L^+(k)/L^-(k)$. Hence

$$K^+(k) = i(B(1 - h^2/12))^{1/2}(k + iX)^2 L^+(k) \quad (3.17a)$$

$$K^-(k) = -i(B(1 - h^2/12))^{-1/2}(k - iX)^{-2} L^-(k) \quad (3.17b)$$

gives the required decomposition $K(k) = K^+(k)/K^-(k)$.

The decomposition of $i\omega Z_0(k)K^-(k)$ into $F^+(k) + F^-(k)$ is more straightforward. The only poles of $i\omega Z_0(k)K^-(k)$ in the lower half plane are the simple poles of $i\omega Z_0$ at k_l and k_t . Hence, $F^-(k) = i\omega Z_0(k)K^-(k) - F^+(k)$, where

$$F^+(k) = \frac{R_l}{k - k_l} + \frac{R_t}{k - k_t}, \quad (3.18)$$

$$\begin{aligned} R_l &= \frac{ic_l^2 dK^-(k_l)}{2k_l \omega^2 / c_l^2} \left(k_l^2 \left(\nu + \frac{h^2 \omega^2}{12c_l^2} \right) + m^2 \right) (k_l C_1 + m C_2), \\ R_t &= \frac{ic_l^2 dK^-(k_t)}{2\omega^2 / c_l^2} m \left(1 - \nu + \frac{h^2 \omega^2}{12c_l^2} \right) (k_t C_2 - m C_1). \end{aligned} \quad (3.19)$$

The above R_l and R_t are the residues of $i\omega Z_0(k)K^-(k)$ at k_l and k_t , and hence $F^-(k)$ has removable singularities at these points.

Substituting these factorizations into (3.13) yields

$$P^-(k)K^-(k) - \frac{i(K^-(k) - K^-(k_{\text{in}}))}{k - k_{\text{in}}} + F^-(k) = H^+(k)K^+(k) + \frac{iK^-(k_{\text{in}})}{k - k_{\text{in}}} - F^+(k). \quad (3.20)$$

The left hand side is analytic for $\text{Im}(k) < \delta$, while the right hand side is analytic for $\text{Im}(k) > -\delta$. Hence, (3.20) defines an entire function $E(k)$.

3.4.4 Asymptotic behaviour of $E(k)$

The asymptotic behaviour of $E(k)$ for large k is now considered. Noble (1958, p. 15, theorem C) states that L^+ and L^- found using the method above remain bounded as $|k| \rightarrow \infty$ provided $\log L = O(k^{-q})$ as $|k| \rightarrow \infty$ for $q > 0$, although no proof is given. Here, we prove the slightly stronger result that L^+ and L^- tend to unity as $|k| \rightarrow \infty$ under the more restrictive condition that $\log L(k) = O(k^{-1})$, as is certainly the case for the problem considered here (in fact, $\log L(k) = O(k^{-2})$, as already mentioned). Defining $f(\xi) = \log(L(\xi - i\delta))/(2\pi i)$, $L^+(k)$ may be cast into the form

$$\log(L^+(k - i\delta)) = \int_{-\infty}^{\infty} \frac{f(\xi)}{\xi - k} d\xi,$$

and with similar definitions $L^-(k)$ may also be cast into this form. In both cases $f(\xi)$ is bounded for real ξ , $f(\xi) = O(\xi^{-1})$ as $\xi \rightarrow \pm\infty$, and it is required to show that the integral tends to zero as $|k| \rightarrow \infty$.

Lemma *Let $f : \mathbb{R} \rightarrow \mathbb{C}$ be bounded, and $f(\xi) = O(\xi^{-1})$ as $\xi \rightarrow \pm\infty$. Then the integral*

$$F(k) = \int_{-\infty}^{\infty} \frac{f(\xi)}{\xi - k} d\xi$$

tends to zero as $|k| \rightarrow \infty$ provided $\text{Im}(k) \neq 0$.

Proof. Let $k = x + iy$, with x and y real and $y \neq 0$. Since $f(\xi) = O(\xi^{-1})$ as $|\xi| \rightarrow \infty$, there exist positive constants R and C such that $|f(\xi)| < C|\xi|^{-1}$ for $|\xi| \geq R$. Since $f(\xi)$ is also bounded, there exists a positive constant M such that $|f(\xi)| < M$ for $|\xi| \leq R$. Thus

$$|F(k)| \leq \int_{-R}^R \frac{M}{\sqrt{(\xi - x)^2 + y^2}} d\xi + \int_R^{\infty} \frac{2C}{\xi \sqrt{(\xi - |x|)^2 + y^2}} d\xi$$

The second integral may be integrated to give

$$\int_R^{\infty} \frac{2C}{\xi \sqrt{(\xi - |x|)^2 + y^2}} d\xi = \frac{4C}{\sqrt{x^2 + y^2}} \tanh^{-1} \left(\frac{\sqrt{x^2 + y^2}}{R + \sqrt{(R - |x|)^2 + y^2}} \right).$$

Let $x = r \cos \theta$ and $y = r \sin \theta$. In the limit $r \rightarrow \infty$ with $\theta \neq 0$, leading order asymptotics and a trivial bound on the first integral give

$$|F(k)| \leq \frac{2RM}{r|\sin \theta|} + \frac{2C \log r}{r} + O(r^{-1}).$$

For the case $\theta = 0$, the limit $|x| \rightarrow \infty$ with $y \neq 0$ fixed is taken. Assuming $|x| > R$ gives a trivial bound on the first integral, and the leading order asymptotics for the second integral give

$$|F(k)| \leq \frac{2RM}{|R - |x||} + \frac{6C \log |x|}{|x|} + O(|x|^{-1}).$$

Hence, in both limits $|F(k)|$ is seen to tend to zero at least as quickly as $\log(|k|)/|k|$. \square

Thus, $L^+(k)$ and $L^-(k)$ both tend to unity as $|k| \rightarrow \infty$ provided k remains in their regions of analyticity. The large k behaviour of K^+ and K^- is therefore seen to be

$$\begin{aligned} K^+(k) &= ik^2 \sqrt{B(1 - h^2/12)} + O(k \log(k)), \\ K^-(k) &= -ik^{-2} / \sqrt{B(1 - h^2/12)} + O(k^{-3} \log(k)). \end{aligned}$$

Requiring $K^+/K^- = K$ with K^+ and K^- analytic and non-zero in their respective half planes determines K^+ and K^- up to multiplication by an arbitrary analytic non-zero function. Since the asymptotic behaviour of these specific K^+ and K^- is known, they are in fact specified up to multiplication by an arbitrary constant. This is the degree of freedom provided by the arbitrary constant X above. However, it will turn out that this degree of freedom has no effect on the final solution (see equation 3.22).

The large k behaviour of F^+ and F^- is easily derived from (3.11), (3.18), and the asymptotic behaviour of $K^-(k)$, giving $F^+(k) = O(k^{-1})$ and $F^-(k) = O(k^{-1})$ as $|k| \rightarrow \infty$. Using integration by parts, if $g(x) = O(x^n)$ as $x \rightarrow 0$ then the half-range Fourier transform of g is $O(k^{-(n+1)})$ as $|k| \rightarrow \infty$. Assuming the fluid pressure at the duct boundary at $x = 0$ to be finite, $P^-(k) = O(k^{-1})$, while the clamped boundary conditions $w(0) = w'(0) = 0$ imply $H^+(k) = O(k^{-3})$.

Putting this all together, both the left and right hand sides of (3.20) are $O(k^{-1})$ as $|k| \rightarrow \infty$. By Liouville's theorem, we deduce the entire function $E(k) \equiv 0$.

3.4.5 The Wiener–Hopf Solution

Since $E(k) \equiv 0$, both the left and right hand sides of (3.20) are zero. Equating the right hand side to zero gives

$$H^+(k) = \frac{-i}{K^+(k)} \left[\frac{K^-(k_{\text{in}})}{k - k_{\text{in}}} + \frac{iR_l}{k - k_l} + \frac{iR_t}{k - k_t} \right]. \quad (3.21)$$

This is an equation for $H^+(k)$ in terms of known functions and involving only the constants C_1 and C_2 (through R_l and R_t). From this, (3.8) gives the scattering wave spectrum $A(k)$, and hence the total pressure field is

$$p(x, r) = p_{\text{in}}(x, r) + \frac{1}{2\pi i} \int_{-\infty}^{\infty} \frac{(\omega - Uk)^2 J_m(\alpha(k)r)}{\alpha(k) J'_m(\alpha(k)) K^+(k)} \left[\frac{K^-(k_{\text{in}})}{k - k_{\text{in}}} + \frac{iR_l}{k - k_l} + \frac{iR_t}{k - k_t} \right] e^{-ikx} dk, \quad (3.22)$$

where R_l and R_t given in (3.19) are from $F^+(k)$. Note that multiplying K^+ and K^- by the same arbitrary constant has no effect on this solution, as mentioned above. Since the integrand is $O(k^{-2})$ as $|k| \rightarrow \infty$, for $x < 0$ the integration contour may be closed in the upper half plane and Jordan's lemma applied. Technically, the contour is deformed around the branch cut of α in the upper half plane, but since $J_m(\alpha r)/(\alpha J'_m(\alpha))$ is a meromorphic function of α^2 , the integrand is identical on either side of the branch cut and the contribution from integrating around the branch cut vanishes. The singularity at $\alpha = 0$ corresponds to a removable singularity for $m \neq 0$, while for $m = 0$ it is included in the following analysis provided it is taken that $m^2/\alpha^2 = 0$. The integral is therefore $2\pi i$ times the sum of the residues of the integrand in the upper half plane. These poles are given by $J'_m(\alpha(k)) = 0$ and correspond to rigid-wall duct modes. Denoting the j^{th} positive root of $J'_m(\alpha) = 0$ by $\alpha_{jm} = \alpha(k_{jm})$ with $\text{Im}(k_{jm}) > 0$, for $x < 0$ the total pressure is given by

$$p(x, r) = \frac{J_m(\alpha_{\text{in}} r)}{J_m(\alpha_{\text{in}})} \exp\{-ik_{\text{in}}x\} + \sum_{j=1}^{\infty} R_{jm} \frac{J_m(\alpha_{jm} r)}{J_m(\alpha_{jm})} \exp\{-ik_{jm}x\}, \quad (3.23)$$

$$R_{jm} = \frac{(\omega - Uk_{jm})^2}{(U\omega + \beta^2 k_{jm})(1 - m^2/\alpha_{jm}^2)K^+(k_{jm})} \left[\frac{K^-(k_{\text{in}})}{k_{jm} - k_{\text{in}}} + \frac{iR_l}{k_{jm} - k_l} + \frac{iR_t}{k_{jm} - k_t} \right].$$

Similarly, for $x > 0$ the integration contour in (3.22) may be closed in the lower half plane and Jordan's lemma applied. Writing $\alpha J'_m(\alpha)K^+(k)$ as $K^-(k)\chi(k)$, where $\chi(k)$ is given in (3.15), the poles of the integrand of (3.22) are given by zeros of $\chi(k)$, and therefore correspond to duct modes for a duct boundary with impedance Z_1 . The pole at k_{in} exactly cancels the incoming pressure p_{in} . The two poles at k_l and k_t correspond to zeros of the determinant (3.1b), so are also poles of $\chi(k)$; the integrand therefore has removable singularities at these points. Denoting the j^{th} zero of $\chi(k)$ by τ_{jm} with $\text{Im}(\tau_{jm}) < 0$, the pressure for $x > 0$ is given by

$$p(x, r) = \sum_{j=1}^{\infty} T_{jm} \frac{J_m(\alpha(\tau_{jm}) r)}{J_m(\alpha(\tau_{jm}))} \exp\{-i\tau_{jm}x\}, \quad (3.24)$$

$$T_{jm} = -\frac{(\omega - U\tau_{jm})^2 J_m(\alpha(\tau_{jm}))}{K^-(\tau_{jm})\chi'(\tau_{jm})} \left[\frac{K^-(k_{\text{in}})}{\tau_{jm} - k_{\text{in}}} + \frac{iR_l}{\tau_{jm} - k_l} + \frac{iR_t}{\tau_{jm} - k_t} \right].$$

The solution within the fluid has now been derived as a sum of duct modes, with reflection coefficients R_{jm} and transmission coefficients T_{jm} , in terms of the constants C_1 and C_2 .

The thin-shell deflection $w(x)$, which is also the surface streamline, may also be expressed as a sum of modes. Again using $\alpha J'_m(\alpha)K^+(k) = K^-(k)\chi(k)$ and inverting the half-range Fourier transform (3.21) gives

$$w(x) = \frac{1}{2\pi i} \int_{-\infty}^{\infty} \frac{\alpha(k)J'_m(\alpha(k))}{K^-(k)\chi(k)} \left[\frac{K^-(k_{\text{in}})}{k - k_{\text{in}}} + \frac{iR_l}{k - k_l} + \frac{iR_t}{k - k_t} \right] e^{-ikx} dk,$$

where the integration contour is taken above all poles so that $w(x) \equiv 0$ for $x < 0$. As in (3.24), the two poles at k_l and k_t correspond to poles of $\chi(k)$, and so are removable singularities of the integrand. This time, the pole at k_{in} is cancelled by a zero of $J'_m(\alpha(k))$ (since k_{in} satisfies the hard-wall dispersion relation), and so k_{in} also corresponds to a removable singularity of the integrand. Hence, the only poles that contribute to $w(x)$ are the zeros of $\chi(k)$, giving

$$w(x) = \sum_{j=1}^{\infty} \frac{\alpha(\tau_{jm}) J'_m(\alpha(\tau_{jm})) T_{jm}}{(\omega - U\tau_{jm})^2 J_m(\alpha(\tau_{jm}))} \exp\{-i\tau_{jm}x\}. \quad (3.25)$$

3.4.6 Determining the constants C_1 to C_4

By examining (3.22), the dependence of the solution on the constants C_1 to C_4 occurs only through R_l and R_t , which themselves depend only on C_1 and C_2 and are independent of C_3 and C_4 . In fact C_3 and C_4 may be calculated (in terms of C_1 and C_2) from our solution for H^+ , since by integrating by parts

$$H^+(k) = -iw''(0)/k^3 + w'''(0)/k^4 + O(k^{-5}) \quad \text{as } k \rightarrow \infty, \quad (3.26)$$

giving $w''(0)$ and $w'''(0)$, and hence C_3 and C_4 . This is possible because, in determining H^+ , we required the pressure to be bounded at $x = 0$, implying $P^-(k) = O(k^{-1})$ as $|k| \rightarrow \infty$. In general, however, setting the left hand side of (3.20) to zero gives $P^-(k) = O(k)$. Satisfying the finite pressure assumption therefore requires the constants C_3 and C_4 to be chosen such that

$$-\frac{iK^-(k_{\text{in}})}{k - k_{\text{in}}} + F^+(k) = i\omega Z_0 K^-(k) + O(k^{-3}),$$

and this can be shown to give the same condition as (3.26). This may be interpreted as the shell bending at $x = 0$ in the only way that does not necessitate an infinite pressure in the fluid at the boundary. As C_3 and C_4 do not appear in the solution (3.22), it is never necessary to solve the above equations to calculate C_3 and C_4 , and we may now forget about C_3 and C_4 completely.

We now turn our attention to the constants C_1 and C_2 , which we determine by imposing causality. The inversion contour in (3.22) is chosen along the real k axis within the strip \mathcal{S} . By definition of ε , the Briggs–Bers criterion shows that this gives the causal solution to a disturbance in the fluid originating at $x = 0$. However, the solid waves in the boundary with axial wavenumbers $\pm k_l$ and $\pm k_t$ are decoupled from w and produce no disturbance in the fluid for $x > 0$. It is therefore necessary to impose a further condition that no solid waves are inbound in the boundary from $x = +\infty$. The positive-half-range Fourier transforms of the axial and

azimuthal boundary displacements $u(x)$ and $v(x)$ for $x > 0$ are denoted $U^+(k)$ and $V^+(k)$, and are given by the half-range version of (3.1b) as

$$\begin{pmatrix} U^+ \\ V^+ \end{pmatrix} = \frac{1}{a_{11}a_{22} - a_{12}^2} \begin{pmatrix} a_{22} & -a_{12} \\ -a_{12} & a_{11} \end{pmatrix} \begin{pmatrix} -iQ_1H^+ - C_1 \\ -iQ_2H^+ - C_2 \end{pmatrix}. \quad (3.27)$$

This shows that $U^+(k)$ and $V^+(k)$ are $O(k^{-2})$ as $|k| \rightarrow \infty$. Taking the inversion contours for $u(x)$ and $v(x)$ above all poles of U^+ and V^+ , Jordan's lemma may be applied to give $u \equiv v \equiv 0$ for $x < 0$, while for $x > 0$, u and v are given as a sum of residues. In general, the poles of U^+ and V^+ are those of H^+ . The zeros of the determinant $a_{11}a_{22} - a_{12}^2$, which occur when $k = \pm k_l$ or $k = \pm k_t$, lead to four additional poles of U^+ and V^+ which correspond to two inbound and two outbound solid boundary waves. In order that there be no incoming waves, it is required that the poles of U^+ and V^+ at both $-k_l$ and $-k_t$ have zero residue (recall that k_l and k_t were chosen so as to represent downstream-propagating waves). While this would appear to be four conditions, the singularity of the matrix at these points reduces this requirement to two independent conditions,

$$\begin{aligned} k_l (iQ_1(-k_l)H^+(-k_l) + C_1) - m (iQ_2(-k_l)H^+(-k_l) + C_2) &= 0, \\ m (iQ_1(-k_t)H^+(-k_t) + C_1) + k_t (iQ_2(-k_t)H^+(-k_t) + C_2) &= 0. \end{aligned}$$

Since $H^+(k)$ is a linear function of C_1 and C_2 , so too are the above two equations. Satisfying them specifies the constants C_1 and C_2 (which in turn specifies $u'(0)$ and $v'(0)$), and ensures that the only permissible solid boundary waves are those that propagate outward from $x = 0$.

It is interesting to note that outward-propagating solid boundary waves, corresponding to the other two zeros of the determinant in (3.27) at $k = k_l$ and $k = k_t$, also both have zero residue for any choice of C_1 and C_2 . This may be seen by evaluating H^+ at k_l and k_t to give

$$H^+(k_l) = i \frac{k_l C_1 + m C_2}{k_l Q_1(k_l) + m Q_2(k_l)} \quad \text{and} \quad H^+(k_t) = i \frac{m C_1 - k_t C_2}{m Q_1(k_t) - k_t Q_2(k_t)},$$

and substituting this into (3.27). The poles at k_l and k_t therefore correspond to removable singularities, and once C_1 and C_2 have been chosen as above so that the poles at $-k_l$ and $-k_t$ also correspond to removable singularities, the only poles of U^+ and V^+ are those of H^+ . The wave scattering is therefore seen to excite none of the solid waves in the thin shell, although it can and in general will excite the quasi-solid surfaces modes in the fluid.

The values of all four constants C_1 to C_4 have now been specified, giving a unique solution, with the only assumptions being bounded pressure and causality. Since the thin shell was assumed clamped at $x = 0$, $w(0) = w'(0) = 0$, and hence the deflection of the surface streamline is $O(x^2)$ as $x \rightarrow 0$.

3.4.7 Analytic continuation to real frequencies

So far, $\text{Im}(\omega) = -\varepsilon$ has been taken, with the results for real ω to be inferred by analytic continuation in the limit $\varepsilon \rightarrow 0$. In this limit the rigid-wall modes approach the real k axis, and the factorizing contour and the strip \mathcal{S} must therefore be deformed around such modes to maintain analyticity. This is exactly the same situation as for the Briggs–Bers criterion; in other words, in choosing the position of the contours and the strip \mathcal{S} , it is necessary to consider the stability of the modes. It is also necessary for k_l and k_t to lie below and $-k_l$ and $-k_t$ to lie above \mathcal{S} , since $H^+(-k_l)$, $H^+(-k_t)$, $K^-(k_l)$ and $K^-(k_t)$ appear in the solution, and H^+ is only defined above the factorizing contour, while K^- is only defined below it. From a Briggs–Bers point of view, this may be seen as requiring k_l and k_t to be right-propagating and $-k_l$ and $-k_t$ to be left propagating.

3.4.8 Numerical evaluation

Our first task is to compute the locations of the poles k_{jm} and τ_{jm} , as defined in §3.4.5. The values of k_{jm} were obtained using a Newton–Raphson iteration to find the (real) roots α_{jm} of $J'_m(\alpha) = 0$, using asymptotics from Abramowitz & Stegun (1964, p. 371) as starting points for the iteration. The values of τ_{jm} were obtained using a Newton–Raphson iteration to find the roots of $\chi(k) = 0$, using k_{jm} and the surface mode asymptotics of §2.1 as starting points. In addition, a grid of starting points was used to discover any other thin-shell modes not close to these starting points.

The factorization of $K(k)$ into $K^+(k)/K^-(k)$ was done by numerically integrating (3.16) along a contour $k(\xi)$ with $\xi \in \mathbb{R}$ (see equations 3.28 and 3.29), using a change of variables $\xi = s/(1 - s^2)$ to get a finite integration range. Care must be taken to ensure that the numerically calculated $\log(L(\xi))$ remains analytic along the contour, and does not jump by a multiple of $2\pi i$ at any point. The coefficients R_{jm} and T_{jm} were then calculated, and finally the modes were summed to give the total pressure. The summations were truncated once the magnitude of the coefficients became sufficiently small.

3.4.9 Numerical results

Figure 3.17 shows the numerically calculated hard-wall and thin-shell poles in the k -plane for an air-filled aluminium duct (see table 3.1) of 1m radius and 1mm shell thickness, with ω and m as suggested by McAlpine & Wright (2006) as being representative of rotor-alone fan

noise in aeroengine intakes. The boundary change at $x = 0$ may be interpreted as a model of the transition from a hard fan casing to a thin-shell nacelle casing for rearward-propagating tonal fan noise in an aeroengine, although in reality such a configuration would have an annular, rather than cylindrical, duct cross-section. A model of an aeroengine intake is obtained by taking U negative, since nowhere has it been assumed that $U > 0$; the results for $U = -0.5$ are very similar to those presented here. The majority of thin-shell modes are almost identical to their hard-wall counterparts. There are, however, eight thin-shell modes for which there is no hard-wall equivalent, and the four below the contour are labelled SM. The Briggs–Bers stability analysis of figure 3.4 has been superimposed on figure 3.17, showing the motion of the thin-shell modes as ε is varied, and consequently the stability of these modes may be verified; it was shown in §3.3.1 that the Briggs–Bers criterion is valid in this case, and that no absolute or convective instabilities are present. The factorizing contour and the inversion contour coincide and are labelled \mathcal{C}_k , which has been chosen both to give the correct stability and also with regard to k_l and k_t . The equation of this curve (following Rienstra, 2007) is

$$k = \frac{\omega}{1 - U^2} \left(\xi - U + iY \frac{4(\xi/q)}{3 + (\xi/q)^4} \right), \quad \xi \in \mathbb{R}, \quad (3.28)$$

with in this case $Y = 0.5$ and $q = 1.0$.

Figure 3.18 shows the numerically evaluated scattering response to an inbound 1st radial order mode for the parameters used in figure 3.17. The 1st radial order mode is the hard-wall duct mode with the most positive $\text{Re}(k)$ shown in figure 3.17, and nearly coincides with a thin-shell mode. Figures 3.18(a) and 3.18(b) show that the response to the inbound wave is dominated by this thin-shell mode, with little scattering or reflection taking place. Figure 3.18(b) also shows how the reflection and transmission coefficients decay as $|\text{Im}(k)|$ increases, justifying the numerical truncation of the infinite summation. Figure 3.18(c) plots contours of the pressure perturbation amplitude. The x -range of this plot is very large, as the dominant thin-shell mode has $\text{Im}(k)$ so small that the mode is seen to decay only over large distances. The thin-shell is seen to act almost exactly as a rigid duct, with very little scattering taking place.

3.4.10 Further results

The example above used realizable parameters, and found the thin-shell to act almost exactly as a rigid duct, with very little scattering taking place. As another example, for what follows the parameters used are $U = 0.5$, $R = 0.5$, $b = 0$, $m = 1$, and $\omega = 16$, for a 1m radius aluminium duct with boundary thickness 0.1mm. The thinner shell, smaller damping, lower azimuthal

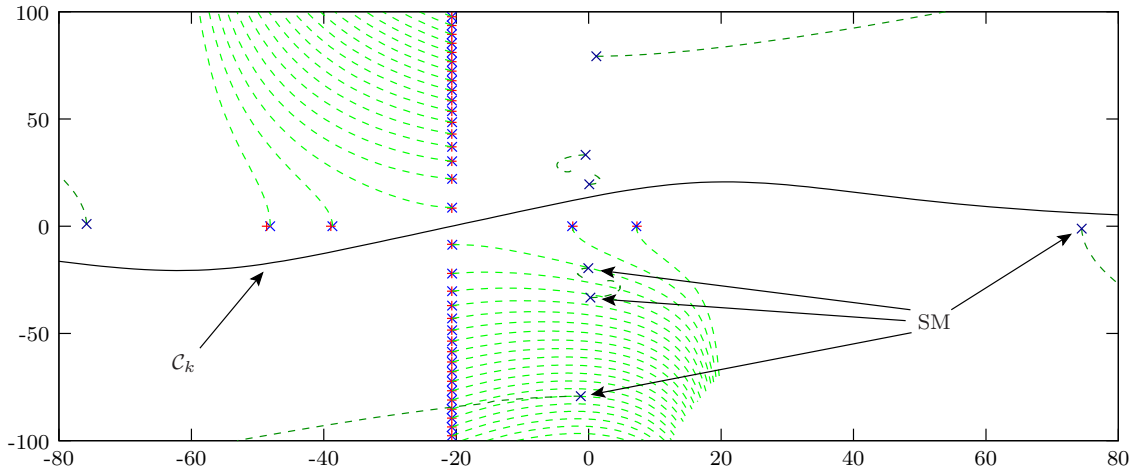


Figure 3.17: Duct modes in the k -plane for hard-wall (+) and thin-shell (\times) boundaries. Surfaces modes present for $x > 0$ are labelled SM. The dashed lines show the Briggs-Bers trajectories of the modes. Parameters are as for figure 3.4.

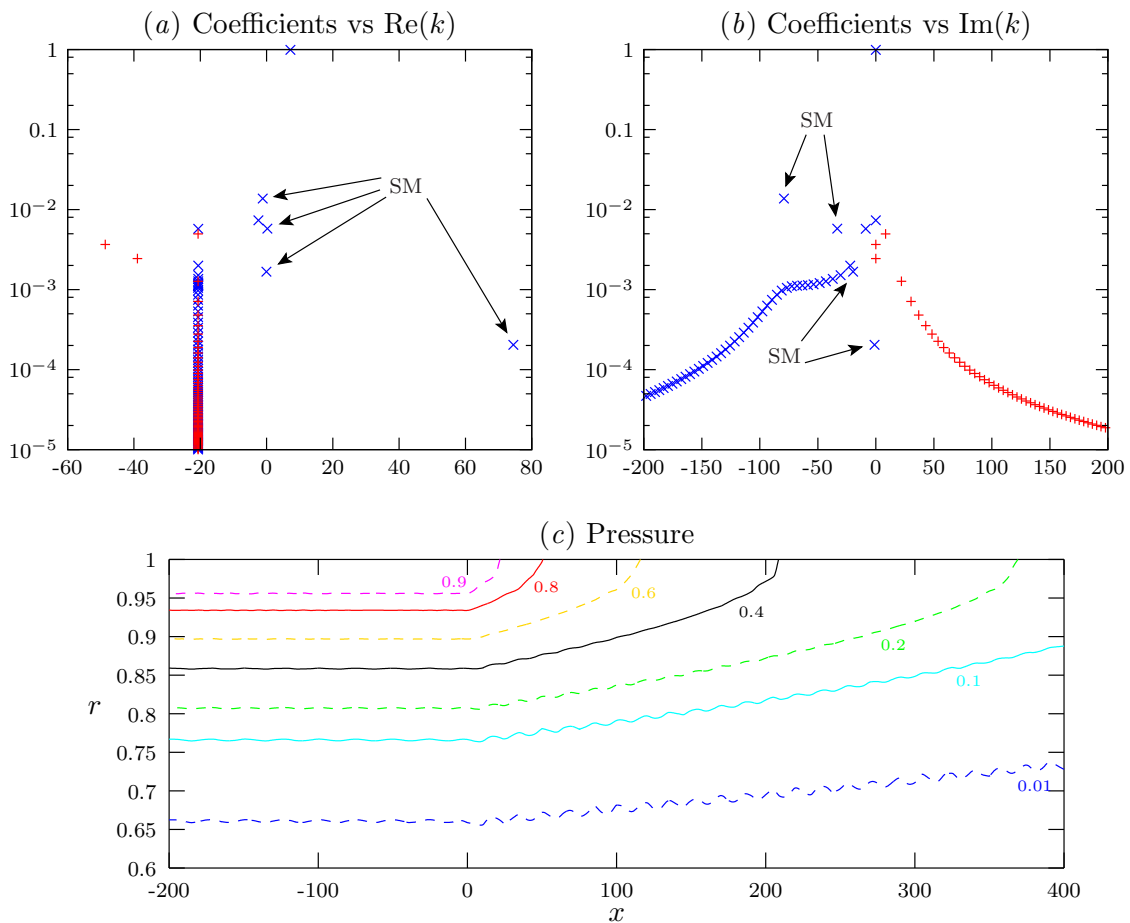


Figure 3.18: Scattering response to an inbound 1st radial order mode. (a) and (b) plot the scattering coefficients $|R_{jm}|$ (+) and $|T_{jm}|$ (\times) against $\text{Re}(k)$ and $\text{Im}(k)$. (c) shows the contours of the acoustic amplitude $|p(x, r)|$. Parameters are as for figure 3.17.

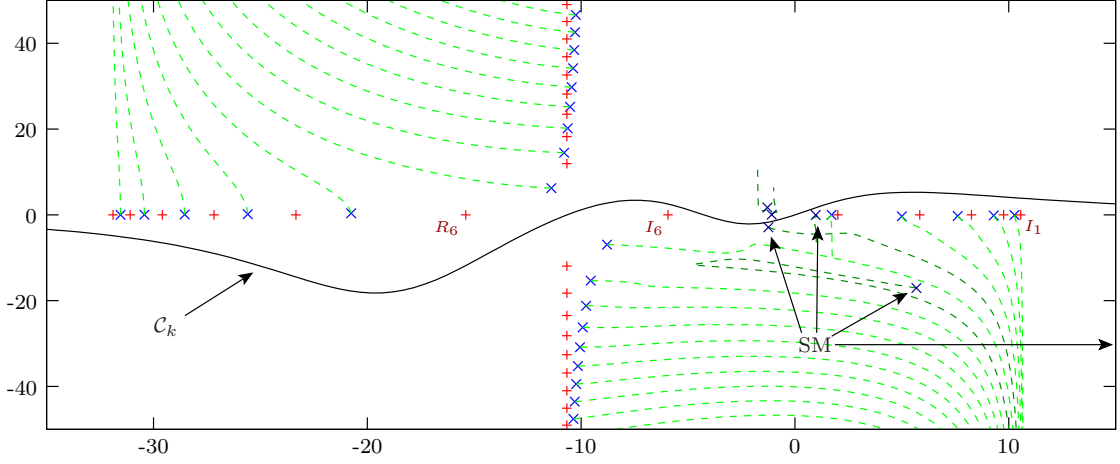


Figure 3.19: Duct modes in the k -plane for hard-wall (+) and thin-shell (x) boundaries, together with the Briggs–Bers trajectories (dashed lines) for the thin-shell modes. One surface mode is not shown owing to the scale used. The 1st and 6th radial order incoming (right-propagating) hard-wall modes and the 6th radial order reflected (left-propagating) hard-wall mode are labelled I_1 , I_6 , and R_6 respectively. Parameters are for an air-filled aluminium duct (see table 3.1) with $R = 0.5$, $b = 0$, $h = 10^{-4}$, $\omega = 16$, $U = 0.5$, and $m = 1$.

order and different frequency all contribute to give rise to more scattering by making the thin-shell modes distinctly different from their hard-wall counterparts. Referring to figure 3.13, no convective or absolute instabilities are present for these parameters. Figure 3.19 shows the hard-wall and thin-shell modes in the k -plane in a similar fashion to figure 3.17, with the Briggs–Bers trajectories showing the \mathcal{C}_k contour to have been chosen to give the correct stability. The simple \mathcal{C}_k contour in (3.28) does not provide enough flexibility to do this, and the more general contour given by

$$k = \frac{\omega}{1 - U^2} \left[\xi - U + iY \frac{4(\xi/q)}{3 + (\xi/q)^4} \left(1 - \frac{1 + g}{1 + g(\xi/f + 1 - U/f)^2} \right) \right], \quad \xi \in \mathbb{R} \quad (3.29)$$

was used, with $Y = 1.0$, $q = 0.4$, $f = 0.1$, and $g = 0.1$.

Figure 3.20 shows the scattering response for the incoming 1st radial order mode labelled I_1 in figure 3.19. The surface modes play a major role near $x = 0$ in order to match the hard-wall and thin-shell solutions smoothly, although for large x these modes still have a negligible effect owing to their large $\text{Im}(k)$ and corresponding fast exponential decay. For large positive x the dominant mode is the 1st radial order thin-shell mode. However, note also the comparably large coefficient for the 6th radial order reflected (left-propagating) mode labelled R_6 , showing that both transmission and reflection are important in this situation.

Figure 3.21(a) shows the amplitude of pressure oscillations, obtained from summing the

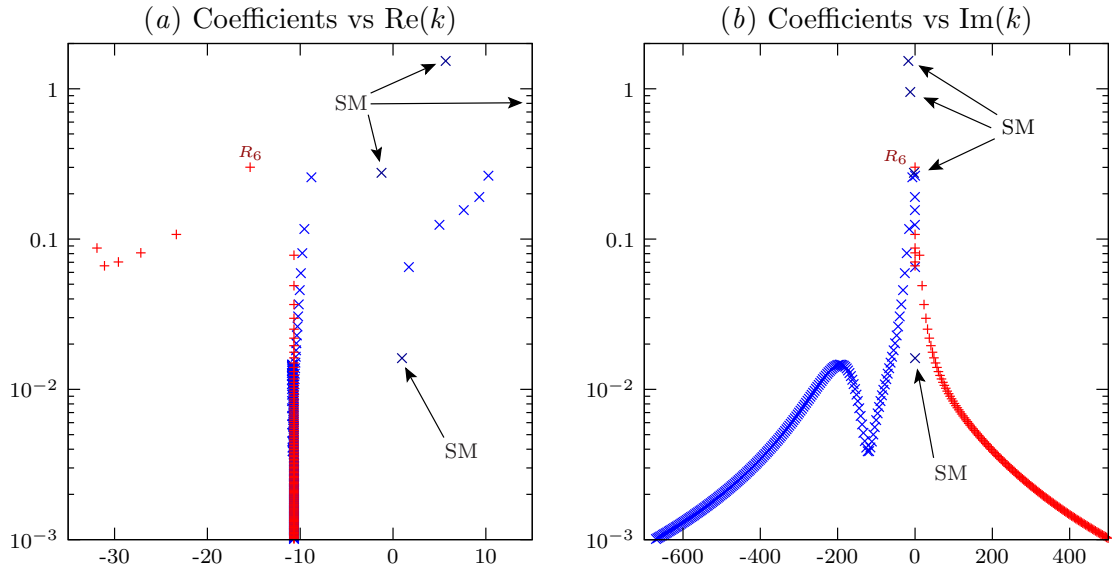


Figure 3.20: Scattering coefficients $|R_{jm}|$ (+) and $|T_{jm}|$ (x) due to an incoming 1st radial order hard-wall mode I_1 . Parameters are as for figure 3.19.

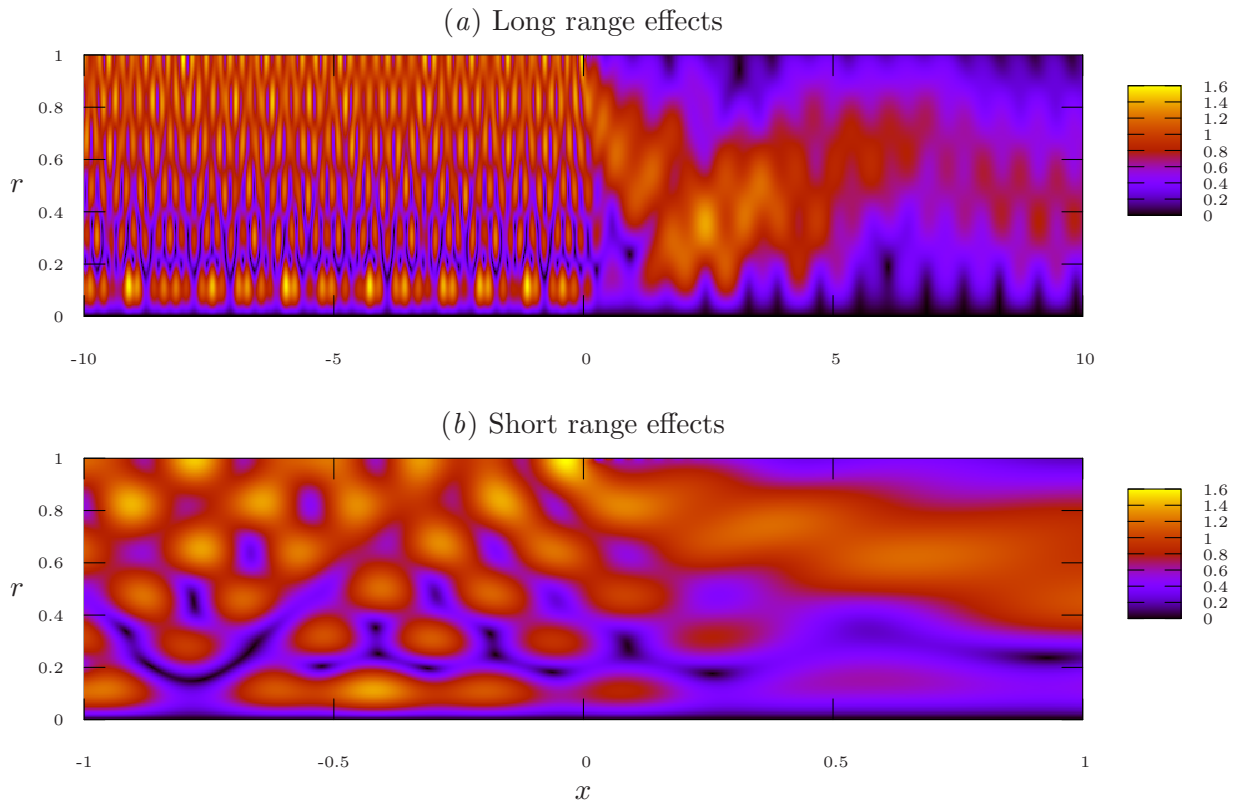


Figure 3.21: Amplitude of pressure oscillations $|p(r, x)|$ due to an inbound I_1 mode. (b) is a more detailed plot of (a). Parameters are as for figure 3.19.

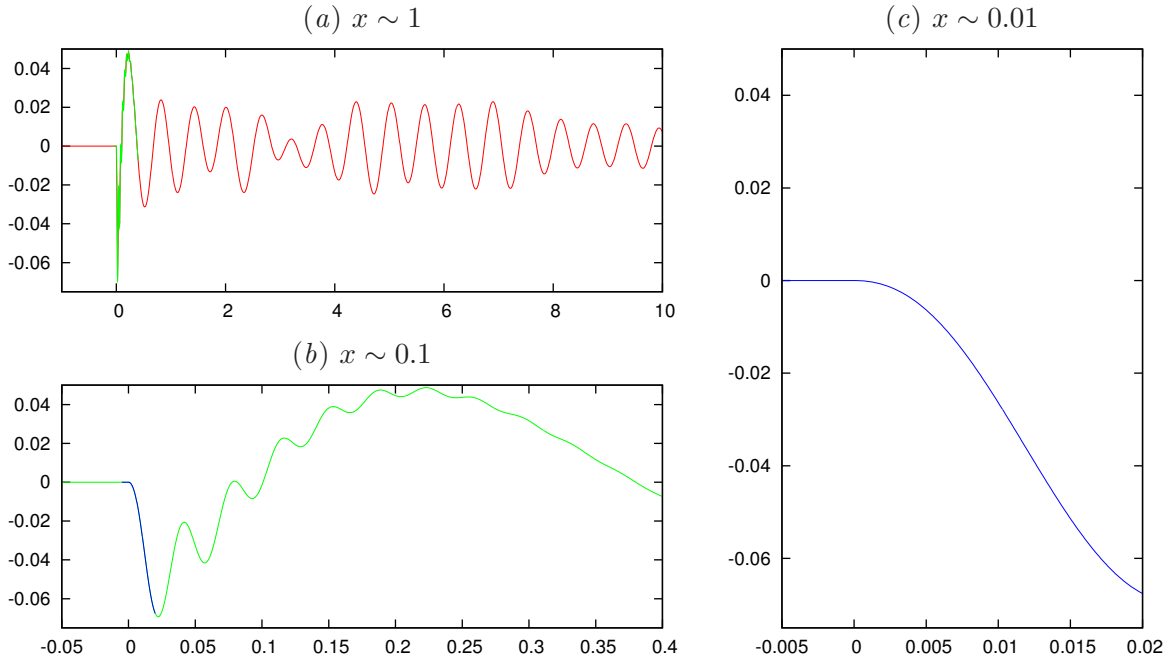


Figure 3.22: The surface streamline near the boundary transition from hard wall to thin shell, for an incoming 1st radial order mode. (c) demonstrates the predicted $O(x^2)$ behaviour. Parameters are as for figure 3.21.

above coefficients. In $x < 0$, the sum of two modes is prominently seen: the inbound 1st radial order I_1 mode (maximum amplitude at $r = 1$ and zero amplitude at $r = 0$), and the 6th radial order R_6 reflected mode (visible as six horizontal bands). Figure 3.21(b) shows a more detailed view around the boundary transition at $x = 0$ where the surface modes are important, and demonstrates the continuity between $x < 0$ and $x > 0$ which is less apparent in figure 3.21(a). Since solutions for $x < 0$ and $x > 0$ are calculated by summing two different series, (3.23) and (3.24), this continuity provides a good check on the numerical results.

The surface streamline was also calculated for this example, by numerically summing (3.25). The streamline is shown over several different scales in figure 3.22 and shows the predicted $O(x^2)$ behaviour at $x = 0$, providing a further check on the validity of the numerical results.

The above is for an inbound 1st radial order mode I_1 . If instead the 6th radial order hard-wall mode, labelled I_6 in figure 3.19, is incident, the transmitted pressure disturbance almost completely disappears. Figure 3.23 shows the reflection and transmission coefficients for this case. Once again the surface modes are important in matching the solutions for $x < 0$ and $x > 0$, although their influence for large x is once again small. The dominant transmitted and reflected modes are both the 6th radial order modes, although the thin-shell one of these

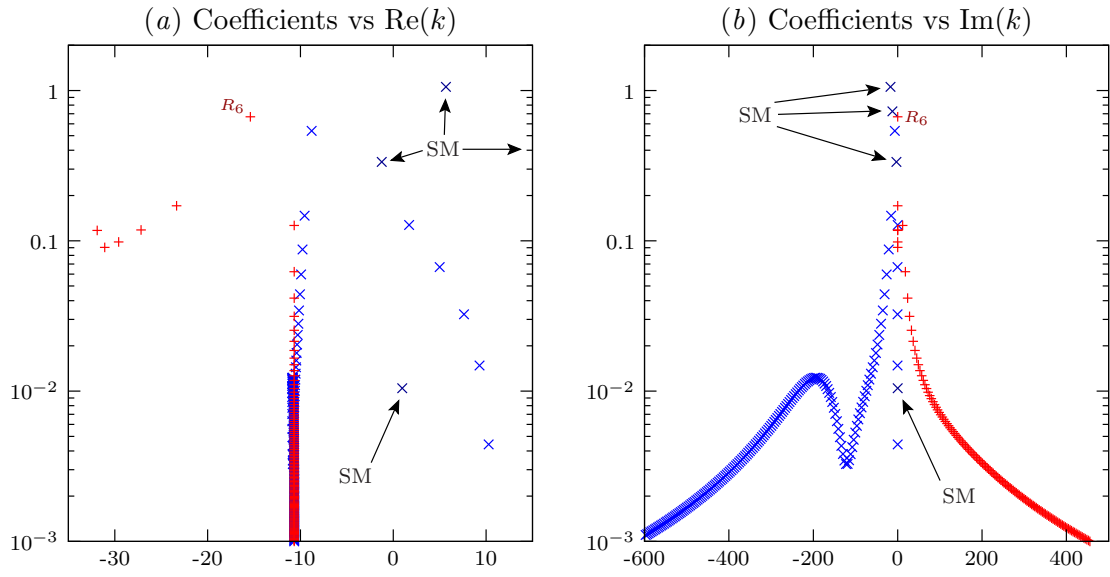


Figure 3.23: Scattering coefficients $|R_{jm}|$ (+) and $|T_{jm}|$ (x) due to an incoming 6th radial order hard-wall mode I_6 . Parameters are as for figure 3.19.

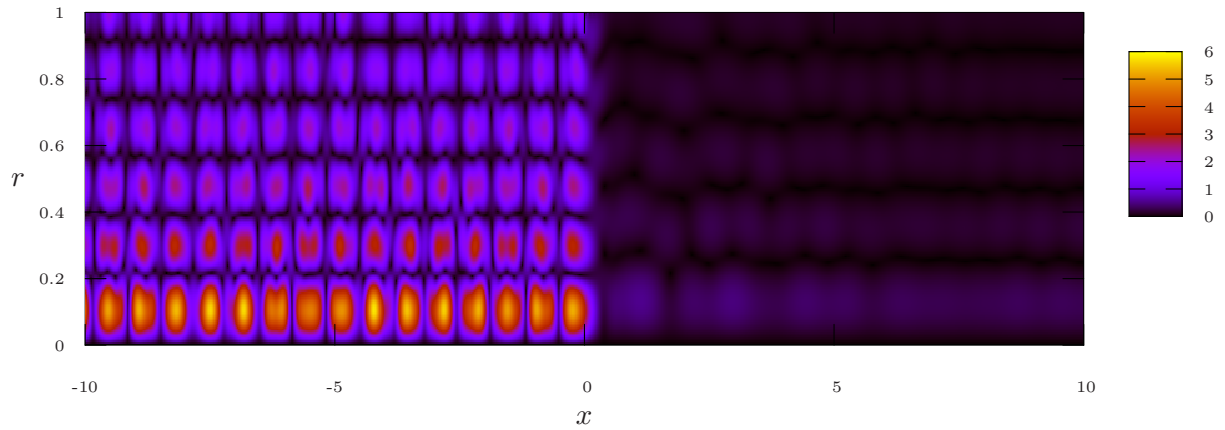


Figure 3.24: Amplitude of pressure oscillations $|p(r, x)|$ due to an inbound I_6 mode. Parameters are as for figure 3.19.

is strongly damped. This is also evident from figure 3.24, which plots the amplitude of the pressure oscillations, and shows a 6th radial order standing wave for $x < 0$ and virtually no transmitted wave in $x > 0$.

Chapter 4

Slowly-varying curved torsionless ducts

We now consider the case of a curved cylindrical duct. After deriving and solving the relevant equations, we apply them to a standard testcase, the RAE 2129 Inlet Diffuser duct. This duct is a typical example of the sort of curved intake that might be found on a military aircraft. It is similar in shape to the F-16 intake shown in figure 1.1, although the RAE 2129 intake remains cylindrical, whereas the F-16's intake has a slowly deforming cross-section that becomes oval towards the intake lip.

4.1 Steady flow

We consider a duct, as shown in figure 4.1, whose centreline possesses nonzero curvature but zero torsion (i.e. the centreline lies in a plane). The duct has a circular cross-section in planes normal to the centreline, and can be either hollow or annular. We pick out two lengthscales for such a duct. The first, ℓ^* (* denotes dimensional variables), is the lengthscale associated with the geometry of the duct at a given axial location, so that the inner and outer duct radii $a_{1,2}^*$ are of order ℓ^* and the duct curvature κ^* is of order $1/\ell^*$. The second lengthscale, L^* , is the shortest lengthscale along the duct centreline over which these parameters vary. These scalings mean the radius of curvature is on the same scale as the duct radius; were these two of different scales some asymptotic simplification becomes possible, but here we deal with the full generality. The cases of a slender curved duct or a straight duct of varying radius then follow as special cases.

Let us now be more specific. Let s^* be the arc-length along the duct centreline. Far

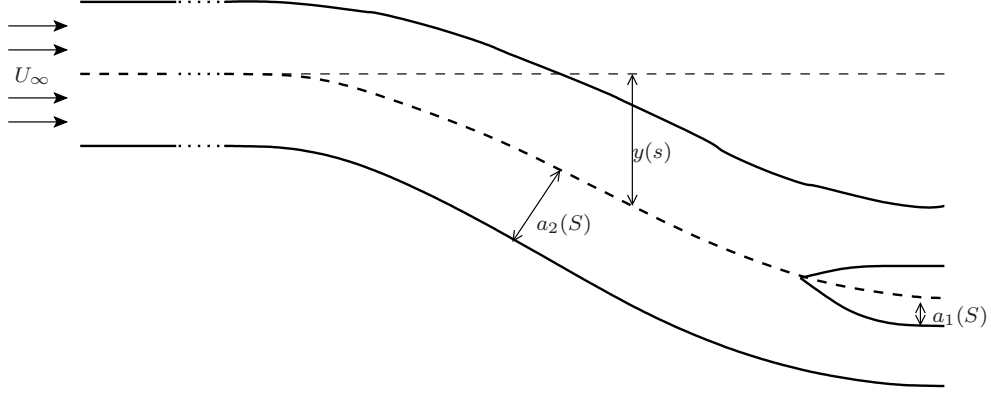


Figure 4.1: Schematic of the duct geometry.

upstream ($s^* \rightarrow -\infty$) the duct is assumed to be straight and of uniform outer radius ℓ^* . The radii of the inner and outer walls and the centreline curvature then vary along the duct on the lengthscale L^* , so that the inner and outer radii $a_{1,2}^*$ and the centreline curvature κ^* are functions of $S \equiv s^*/L^*$. The requirement of slow variation along the axis is then equivalent to $\epsilon \equiv \ell^*/L^* \ll 1$. The duct carries a mean flow, which far upstream has uniform density D_∞^* , speed U_∞^* and sound speed C_∞^* . In what follows speeds are non-dimensionalized by C_∞^* , densities by D_∞^* , distances by ℓ^* , times by ℓ^*/C_∞^* , and pressures by $(C_\infty^*)^2 D_\infty^*$. We introduce the duct-centred coordinate system (s, r, θ) , where r, θ are polar coordinates in planes normal to the duct centreline, and s is the arc-length along the centreline. The duct inner and outer radii are $a_{1,2}(S)$ and the centreline curvature is $\kappa(S)$, where $S = \epsilon s$ is the nondimensionalized slow coordinate over which the duct geometry varies.

The curvilinear coordinates and vector calculus identities used here are detailed in appendix B. The steady velocity in the duct is written $\mathbf{U} = U\mathbf{e}_s + V\mathbf{e}_r + W\mathbf{e}_\theta$, and it is assumed that all steady mean flow variables are functions of r, θ, S , i.e. vary slowly down the duct. The geometric factor associated with the curvilinear coordinate s is $h_s = 1 - \kappa(S)r \cos \theta$. We assume an inviscid irrotational perfect gas with ratio of specific heats γ . We apply the steady continuity condition $\nabla \cdot (D\mathbf{U}) = 0$,

$$\frac{\epsilon}{h_s} \frac{\partial}{\partial S} (D\mathbf{U}) + \frac{1}{rh_s} \frac{\partial}{\partial r} (rh_s DV) + \frac{1}{rh_s} \frac{\partial}{\partial \theta} (h_s DW) = 0,$$

together with the condition for irrotational mean flow, $\nabla \wedge \mathbf{U} = 0$,

$$\frac{1}{r} \frac{\partial}{\partial r} (rW) - \frac{1}{r} \frac{\partial V}{\partial \theta} = 0, \quad \frac{1}{rh_s} \frac{\partial}{\partial \theta} (h_s U) - \frac{\epsilon}{h_s} \frac{\partial W}{\partial S} = 0, \quad \frac{\epsilon}{h_s} \frac{\partial V}{\partial S} - \frac{1}{h_s} \frac{\partial}{\partial r} (h_s U) = 0,$$

and the irrotational form of Bernoulli's equation,

$$\frac{1}{2} U^2 + \frac{1}{\gamma - 1} D^{\gamma-1} = H, \quad (4.1)$$

where the enthalpy $H = U_\infty^2/2 + 1/(\gamma - 1)$ is a constant which has been determined at upstream infinity. For the steady flow, the duct walls are considered perfectly hard and impenetrable, with the corresponding boundary conditions

$$V - \frac{\varepsilon}{h_s} \frac{da_j}{dS} U = 0 \quad \text{at } r = a_j(S) \quad j = 1, 2. \quad (4.2)$$

We assume no leading-order potential swirl, so that W vanishes to leading order. Putting all these assumptions together, we find that

$$D = D_0 + O(\varepsilon^2), \quad U = U_0 + O(\varepsilon^2), \quad V = \varepsilon V_1 + O(\varepsilon^3), \quad W = \varepsilon W_1 + O(\varepsilon^3),$$

where

$$U_0(S, r, \theta) = \frac{U_\dagger(S)}{h_s(r, \theta, S)}, \quad D_0 = \left[(\gamma - 1) \left(H - \frac{1}{2} U_0^2 \right) \right]^{1/\gamma - 1}.$$

The quantity U_\dagger may be found in terms of U_∞ by applying conservation of mass at different axial locations, to yield the implicit equation

$$\mathcal{M}(U_\dagger, S) \equiv \int_0^{2\pi} \int_{a_1}^{a_2} U_0 D_0 r \, dr d\theta = \pi U_\infty (1 - a_1(-\infty))^2. \quad (4.3)$$

In general, (4.3) is not solvable for U_\dagger in closed form. \mathcal{M} has a maximum when

$$\frac{\partial \mathcal{M}}{\partial U_\dagger} \equiv \int_0^{2\pi} \int_{a_1}^{a_2} \frac{D_0}{h_s} \left(1 - \frac{U_0^2}{C_0^2} \right) r \, dr d\theta = 0,$$

where $C_0^2 = D_0^{\gamma - 1}$. If $U_\dagger = 0$ then $\mathcal{M} = 0$, and similarly $\mathcal{M} = 0$ when $D_0 = 0$ in the zero curvature case. However, with nonzero curvature U_\dagger cannot be bigger than the smallest value for which $D_0 = 0$ at some point across the duct. The shape of $\mathcal{M}(U_\dagger, S)$ is shown in figure 4.2. Equation (4.3) therefore has two, zero, or in special cases one root. In the case of two roots, the roots are “subsonic” and “supersonic”, in the sense that they are either side of $\partial \mathcal{M} / \partial U_\dagger = 0$. Equation (4.3) was therefore solved numerically by first finding the maximum of $\mathcal{M}(U_\dagger, S)$, and then using Newton-Raphson iteration on each side of the maximum.

In what follows, it turns out that the value of the radial velocity V_1 is only required on the walls, and can be found simply from the $O(\varepsilon)$ terms in the boundary condition (4.2). The value of the $O(\varepsilon)$ tangential velocity W_1 will not be required at all in our final answer for the unsteady flow.

4.1.1 Small curvature steady flow

Suppose that κ is small. Then

$$U_0 D_0 = U_\dagger D_\dagger + \kappa r \cos(\theta) U_\dagger (D_\dagger - U_\dagger^2 / C_\dagger^2) + O(\kappa^2),$$

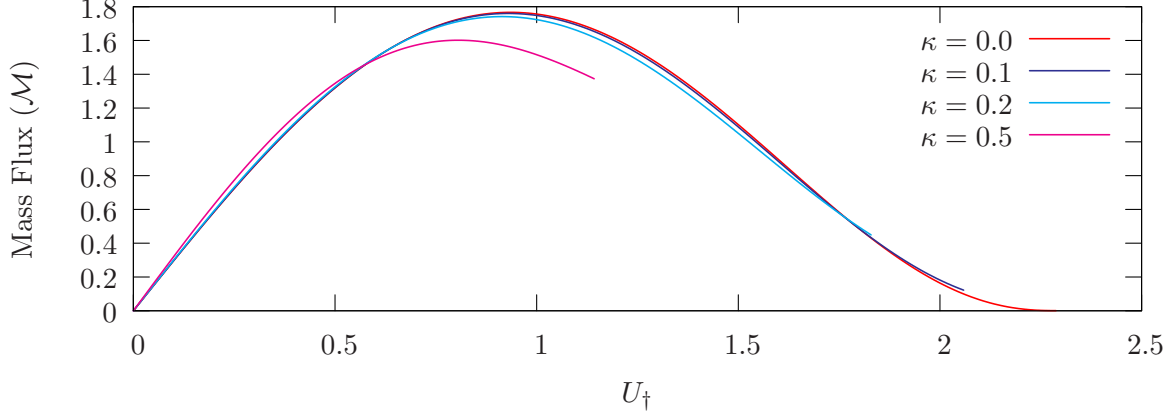


Figure 4.2: Mass flux in a curved annular duct with $U_\infty = 0.5$, $a_1 = 0.4$, and $a_2 = 1.0$.

where D_\dagger is D_0 evaluated with $\kappa = 0$ (and is therefore independent of r and θ), and $C_\dagger^2 = D_\dagger^{\gamma-1}$. Hence, (4.3) becomes

$$\pi(a_2^2 - a_1^2)U_\dagger D_\dagger = \pi(1 - a_1(-\infty)^2)U_\infty + O(\kappa^2),$$

since the $O(\kappa)$ term in $U_0 D_0$ integrates to give zero by symmetry. If the duct cross-sectional area is the same as far upstream, then setting $U_\dagger = U_\infty + u_\dagger$ and dividing through by the cross-sectional area gives

$$U_\infty + u_\dagger(1 - U_\infty^2) + O(u_\dagger^2) = U_\infty + O(\kappa^2),$$

so that $u_\dagger = O(\kappa^2)$. Hence, provided the duct cross-sectional area is the same as far upstream, $U_\dagger = U_\infty + O(\kappa^2)$. This result is used in §4.7.2.

4.2 Unsteady flow

Consider a small time-dependent perturbation (\mathbf{u}, p, ρ) with time dependence $\exp\{i\omega t\}$ to the mean flow (\mathbf{U}, P, D) . Introducing a scalar potential $\mathbf{u} = \nabla\phi$, and neglecting vortical and entropic perturbations, the equations for the unsteady linearized flow due to Goldstein (1978) reduce to

$$\frac{D}{Dt} \left(\frac{1}{C^2} \frac{D\phi}{Dt} \right) - \frac{1}{D} \nabla \cdot (D \nabla \phi) = 0, \quad p = C^2 \rho = -D \frac{D\phi}{Dt}, \quad (4.4)$$

where $D/Dt = i\omega + \mathbf{U} \cdot \nabla$ is the convective derivative with respect to the mean flow, and $C^2 = D^{\gamma-1}$ is the square of the wave speed. This equation is to be solved subject to the usual Myers (1980) boundary condition for a lined duct, namely

$$i\omega \mathbf{n} \cdot \nabla \phi = \left\{ i\omega + \mathbf{U} \cdot \nabla - [(\mathbf{n} \cdot \nabla) \mathbf{U}] \cdot \mathbf{n} \right\} (p/Z_j) \quad \text{on } r = a_j(S) \text{ for } j = 1, 2, \quad (4.5)$$

where $Z_{1,2}(S)$ are the wall impedances and \mathbf{n} is the corresponding wall normal pointing out of the fluid.

In order to account for the slowly-varying duct geometry and mean flow we follow Rienstra (1999) and pose the multiple scales WKB ansatz (see for instance Hinch, 1991, chapter 7)

$$\phi = A(S, r, \theta) \exp \left\{ i\omega t - \frac{i}{\varepsilon} \int_0^S k(S') dS' \right\}. \quad (4.6)$$

For brevity, define the linear operators

$$\tilde{\Lambda} = \omega - \frac{kU}{h_s} \quad \tilde{\mathcal{D}} = \frac{U}{h_s} \frac{\partial}{\partial S} + \frac{V}{\varepsilon} \frac{\partial}{\partial r} + \frac{W}{\varepsilon r} \frac{\partial}{\partial \theta},$$

so that $D/Dt = i\tilde{\Lambda} + \varepsilon\tilde{\mathcal{D}}$. Note that, since V and W are $O(\varepsilon)$, $\tilde{\mathcal{D}}$ is an $O(1)$ operator. Substituting (4.6) into (4.4) gives

$$\begin{aligned} & \frac{1}{h_s D} \left[\frac{1}{r} \frac{\partial}{\partial r} \left(r h_s D \frac{\partial A}{\partial r} \right) + \frac{1}{r^2} \frac{\partial}{\partial \theta} \left(h_s D \frac{\partial A}{\partial \theta} \right) \right] + \left(\frac{\tilde{\Lambda}^2}{C^2} - \frac{k^2}{h_s^2} \right) A \\ &= \frac{i\varepsilon}{h_s D A} \left[h_s D \tilde{\mathcal{D}} \left(\frac{A^2 \tilde{\Lambda}}{C^2} \right) + \frac{\partial}{\partial S} \left(\frac{D k A^2}{h_s} \right) \right] + \varepsilon^2 \left[\tilde{\mathcal{D}} \left(\frac{1}{C^2} \tilde{\mathcal{D}} A \right) - \frac{1}{h_s D} \frac{\partial}{\partial S} \left(\frac{D}{h_s} \frac{\partial A}{\partial S} \right) \right], \end{aligned} \quad (4.7)$$

subject to the boundary conditions (from 4.5)

$$\begin{aligned} \pm \frac{\partial A}{\partial r} - \frac{\tilde{\Lambda}^2 D}{i\omega Z_j} A &= -i\varepsilon \left[\pm \frac{k}{h_s^2} \frac{da_j}{dS} A + \frac{1}{A} \tilde{\mathcal{D}} \left(\frac{\tilde{\Lambda} D A^2}{i\omega Z_j} \right) + \frac{D \tilde{\Lambda}}{i Z_j \omega} \left(\frac{da_j}{dS} \frac{\partial}{\partial r} \left(\frac{U}{h_s} \right) - \frac{\partial(V/\varepsilon)}{\partial r} \right) A \right] \\ &+ \varepsilon^2 \left[\pm \frac{1}{h_s^2} \frac{da_j}{dS} \left(\frac{\partial A}{\partial S} + \frac{1}{2} \frac{da_j}{dS} \frac{\partial A}{\partial r} \right) - \left(\frac{da_j}{dS} \frac{\partial}{\partial r} \left(\frac{U}{h_s} \right) - \frac{\partial(V/\varepsilon)}{\partial r} + \tilde{\mathcal{D}} \right) \left(\frac{D}{i\omega Z_j} \tilde{\mathcal{D}} A \right) \right] + O(\varepsilon^3) \end{aligned} \quad (4.8)$$

at $r = a_j$, where the positive sign is taken for $j = 2$ and the negative sign for $j = 1$.

Define the first order linear operators

$$\Lambda = \omega - \frac{kU_0}{h_s} \quad \mathcal{D} = \frac{U_0}{h_s} \frac{\partial}{\partial S} + V_1 \frac{\partial}{\partial r} + \frac{W_1}{r} \frac{\partial}{\partial \theta},$$

so that $\tilde{\Lambda} = \Lambda + O(\varepsilon^2)$ and $\tilde{\mathcal{D}} = \mathcal{D} + O(\varepsilon^2)$. Expanding $A = A_0 + \varepsilon A_1 + O(\varepsilon^2)$ in (4.7) gives, to leading order,

$$\mathcal{L}A_0 \equiv \frac{1}{h_s D_0} \left[\frac{1}{r} \frac{\partial}{\partial r} \left(r h_s D_0 \frac{\partial A_0}{\partial r} \right) + \frac{1}{r^2} \frac{\partial}{\partial \theta} \left(h_s D_0 \frac{\partial A_0}{\partial \theta} \right) \right] + \left(\frac{\Lambda^2}{C_0^2} - \frac{k^2}{h_s^2} \right) A_0 = 0, \quad (4.9)$$

subject to the boundary conditions (from 4.8)

$$\frac{\partial A_0}{\partial r} = \pm \frac{\Lambda^2 D_0}{i\omega Z_j} A_0 \quad \text{at } r = a_j, \quad j = 1, 2. \quad (4.10)$$

Equations (4.9) and (4.10) are the leading order equations that we will solve numerically in the next section. One crucial difference here from the case of a straight circular duct is the

highly nontrivial dependence of A_0 on θ . When $\kappa = 0$, (4.9) and (4.10) can be solved using separation of variables, as in §1.1, to yield solutions proportional to $\exp\{-im\theta\}$ for integer m and depending on Bessel functions in the radial direction. But when $\kappa \neq 0$, (4.9) is no longer separable. Equations (4.9) and (4.10) must therefore be solved numerically to determine the axial wavenumber $k(S)$ and the corresponding wave function $A_0(S, r, \theta)$. For definiteness, we normalize the solution so that

$$A_0(S, r, \theta) = N(S)\hat{A}_0(S, r, \theta), \quad \int_0^{2\pi} \int_{a_1}^{a_2} \frac{D_0 U_0 \omega}{C_0^2} \hat{A}_0^2 r \, dr \, d\theta = 1. \quad (4.11)$$

The reason for this strange-looking normalization is that it becomes much more natural when we consider turning points in §4.5. The unknown amplitude $N(S)$ is determined by a solvability condition following the procedure given by Rienstra (1999), which we now derive.

At $O(\varepsilon)$, (4.7) gives

$$\mathcal{L}A_1 = \frac{i}{h_s D_0 A_0} \left[h_s D_0 \mathcal{D} \left(\frac{A_0^2 \Lambda}{C_0^2} \right) + \frac{\partial}{\partial S} \left(\frac{D_0 k A_0^2}{h_s} \right) \right], \quad (4.12)$$

where \mathcal{L} is the operator defined in (4.9), subject to the boundary conditions (from 4.8)

$$\pm \frac{\partial A_1}{\partial r} - \frac{\Lambda^2 D_0}{i\omega Z_j} A_1 = \mp \frac{ik}{h_s^2} \frac{da_j}{dS} A_0 - \frac{1}{A_0} \mathcal{D} \left(\frac{\Lambda D_0 A_0^2}{\omega Z_j} \right) - \frac{D_0 \Lambda}{Z_j \omega} \left(\frac{da_j}{dS} \frac{\partial}{\partial r} \left(\frac{U_0}{h_s} \right) - \frac{\partial V_1}{\partial r} \right) A_0 \quad (4.13)$$

at $r = a_j$, with \pm being $+$ at $r = a_2$ and $-$ at $r = a_1$ (this convention will be assumed from here on). Note that, by using integration by parts to move derivatives from A_1 onto A_0 and the fact that $\mathcal{L}A_0 = 0$,

$$\int_0^{2\pi} \int_{a_1}^{a_2} A_0 \mathcal{L}(A_1) h_s D_0 r \, dr \, d\theta = \left[\int_0^{2\pi} \left(A_0 \frac{\partial A_1}{\partial r} - A_1 \frac{\partial A_0}{\partial r} \right) r h_s D_0 \, d\theta \right]_{a_1}^{a_2}, \quad (4.14)$$

where the $[\dots]_0^{2\pi}$ terms that would also have appeared on the right hand side of (4.14) above are zero owing to 2π periodicity. Multiplying (4.12) by $A_0 h_s D_0 r$ and integrating over r and θ , and then substituting for $\partial A_0 / \partial r$ and $\partial A_1 / \partial r$ using the boundary conditions (4.10) and (4.13) therefore gives

$$\begin{aligned} -i \int_0^{2\pi} \left[\left(\frac{k}{h_s^2} \frac{da_j}{dS} A_0^2 \pm \mathcal{D} \left(\frac{\Lambda D_0 A_0^2}{i\omega Z_j} \right) \pm \frac{D_0 \Lambda A_0^2}{i\omega Z_j} \left(\frac{da_j}{dS} \frac{\partial}{\partial r} \left(\frac{U_0}{h_s} \right) - \frac{\partial V_1}{\partial r} \right) \right) r h_s D_0 \right]_{a_1}^{a_2} d\theta \\ = i \int_0^{2\pi} \int_{a_1}^{a_2} r h_s D_0 \mathcal{D} \left(\frac{A_0^2 \Lambda}{C_0^2} \right) + r \frac{\partial}{\partial S} \left(\frac{D_0 k A_0^2}{h_s} \right) dr \, d\theta. \end{aligned} \quad (4.15)$$

Note that, since $\nabla \cdot (DU) = 0$, for any function $f(S, r, \theta)$, $\nabla \cdot (DUf) = \varepsilon D\mathcal{D}f$, and hence

$$r h_s D_0 \mathcal{D}f = r \frac{\partial}{\partial S} (D_0 U_0 f) + \frac{\partial}{\partial r} (r h_s D_0 V_1 f) + \frac{\partial}{\partial \theta} (h_s D_0 W_1 f).$$

Using this to eliminate the \mathcal{D} operator from (4.15), substituting $V_1 = (da_j/dS)(U_0/h_s)$ from the mean flow boundary conditions at $r = a_j$ and rearranging gives

$$Q_1 + Q_2 + \int_0^{2\pi} \int_{a_1}^{a_2} \frac{\partial}{\partial S} \left(\frac{D_0 k A_0^2}{h_s} + \frac{A_0^2 D_0 U_0 \Lambda}{C_0^2} \right) r dr d\theta + \int_0^{2\pi} \left[r \frac{da_j}{dS} \left(\frac{D_0 k A_0^2}{h_s} + \frac{A_0^2 D_0 U_0 \Lambda}{C_0^2} \right) \right]_{a_1}^{a_2} d\theta = 0, \quad (4.16)$$

where, setting $f_j = \Lambda D_0^2 A_0^2 r / (i\omega Z_j)$,

$$Q_j = \int_0^{2\pi} \left[\frac{\partial}{\partial S} (U_0 f_j) + \frac{\partial}{\partial r} (h_s V_1 f_j) + h_s f_j \left(\frac{da_j}{dS} \frac{\partial}{\partial r} \left(\frac{U_0}{h_s} \right) - \frac{\partial V_1}{\partial r} \right) \right] d\theta \Big|_{r=a_j},$$

and a term involving W_1 integrates to give zero owing to 2π periodicity. Expanding out the $\partial/\partial r$ terms and again using $V_1 = (da_j/dS)(U_0/h_s)$ gives

$$Q_j = \int_0^{2\pi} \left[\frac{\partial}{\partial S} (U_0 f_j) + \frac{da_j}{dS} \frac{\partial}{\partial r} (U_0 f_j) \right] d\theta \Big|_{r=a_j} = \frac{d}{dS} \left(\underbrace{\int_0^{2\pi} \frac{U_0 \Lambda D_0^2 A_0^2}{i\omega Z_j} r d\theta \Big|_{r=a_j}}_{I_j(S)} \right). \quad (4.17)$$

Hence, (4.16) may be rearranged, moving the $\partial/\partial S$ derivative to the other side of the integrals as we just have done for Q_j above, to finally get

$$\frac{d}{dS} \left(I_1 + I_2 + \underbrace{\int_0^{2\pi} \int_{a_1}^{a_2} D_0 A_0^2 \left(\frac{\omega U_0}{C_0^2} + \frac{k}{h_s} \left(1 - \frac{U_0^2}{C_0^2} \right) \right) r dr d\theta}_{F(S)} \right) = 0,$$

with $I_{1,2}$ defined in (4.17). Using the normalization (4.11) and using \hat{A}_0 rather than A_0 in $I_{1,2}$ and F gives the final secularity condition

$$\frac{d}{dS} \left\{ (F(S) + I_1(S) + I_2(S)) N(S)^2 \right\} = 0. \quad (4.18)$$

Notice that (4.18) involves \hat{A}_0^2 , rather than $|\hat{A}_0|^2$, which has arisen from the non-self-adjoint nature of \mathcal{L} (in fact the adjoint solution is the complex conjugate of A_0). In the case of rigid walls, (4.18) reduces to the condition that $F(S)N(S)^2$ is constant along the duct, which for cuton modes can be interpreted as conservation of energy. Rienstra & Hirschberg (2001, chapter 2, p39–40) give the energy flux for a linearized perturbation to a steady base flow as

$$\mathbf{I} = (D\mathbf{u} + \rho\mathbf{U})((C^2/D)\rho + \mathbf{U} \cdot \mathbf{u})$$

In this case, the axial component of the energy flux is

$$I_s = \text{Re} \left[-\frac{1}{2} \omega D_0 A_0^2 \left(\frac{\omega U_0}{C_0^2} + \frac{k}{h_s} \left(1 - \frac{U_0^2}{C_0^2} \right) \right) \exp \left\{ 2i\omega t - \frac{2i}{\varepsilon} \int_0^S k(S') dS' \right\} + \frac{1}{2} \omega D_0 |A_0|^2 \left(\frac{\omega U_0}{C_0^2} + \frac{k}{h_s} \left(1 - \frac{U_0^2}{C_0^2} \right) \right) \right]$$

The first term is oscillatory with a time-average of zero. The second term is therefore the time-averaged axial energy flux. When k is real, it is the conservation of this quantity and continuity of phase that is implied by the secularity condition (4.18).

Putting all this together, we now have the leading-order solution (4.11) for the unsteady flow, in which the local axial wavenumber and mode shape are determined by numerical solution of (4.9) and (4.10) and the slowly varying amplitude is then given by (4.18).

4.3 Numerical solution

Our task is to solve the leading-order eigenvalue problem (4.9) and (4.10) so as to determine the local axial wavenumbers k and corresponding eigenfunctions as functions of the slow arc length S . The leading-order equation for A_0 and k is recast, by introducing $B_0 = kA_0$, as the generalized eigenvalue problem

$$\begin{pmatrix} \mathcal{Q} & 0 \\ 0 & 1 \end{pmatrix} \begin{pmatrix} A_0 \\ B_0 \end{pmatrix} = k \begin{pmatrix} \frac{2\omega U_0}{h_s C_0^2} & \frac{1}{h_s^2} \left(1 - \frac{U_0^2}{C_0^2}\right) \\ 1 & 0 \end{pmatrix} \begin{pmatrix} A_0 \\ B_0 \end{pmatrix}, \quad (4.19)$$

where

$$\mathcal{Q}A_0 = \frac{1}{h_s D_0} \left[\frac{1}{r} \frac{\partial}{\partial r} \left(r h_s D_0 \frac{\partial A_0}{\partial r} \right) + \frac{1}{r^2} \frac{\partial}{\partial \theta} \left(h_s D_0 \frac{\partial A_0}{\partial \theta} \right) \right] + \frac{\omega^2}{C_0^2} A_0,$$

subject to the boundary conditions

$$\pm \frac{\partial A_0}{\partial r} + \frac{i\omega D_0}{Z_{1,2}} A_0 = k \left(\frac{2iU_0 D_0}{h_s Z_{1,2}} A_0 - \frac{iD_0 U_0^2}{h_s^2 \omega Z_{1,2}} B_0 \right), \quad (4.20)$$

where the negative sign is taken for the inner boundary (if one is present), and the positive sign for the outer boundary.

We use a pseudospectral method with Chebyshev polynomials as the radial basis (see for example Khorrami, Malik & Ash, 1989; Boyd, 2001, chapter 18.6) and trigonometric polynomials in the azimuthal direction. The number of collocation points in the radial and azimuthal directions are denoted by n_r and n_θ respectively (note that n_θ must be odd, since all trigonometric polynomials have an odd number of degrees of freedom). The numerical domain will consist of collocation points

$$(r_j, \theta_\ell) = \left(\frac{a_1 + a_2}{2} + \frac{a_1 - a_2}{2} \cos \left(\frac{j\pi}{n_r - 1} \right), \frac{2\ell\pi}{n_\theta} \right) \quad \begin{array}{l} j = 0, \dots, n_r - 1, \\ \ell = 0, \dots, n_\theta - 1. \end{array}$$

For a hollow duct, a_1 is replaced by a small nonzero constant, typically of the order of the spacing between neighbouring collocation points at the centre, $a_1 \approx a_2 \pi^2 / (2n_r - 2)^2$. This

allows both annular and hollow cases to be calculated using the same numerical code, and offers the potential to treat a hollow-to-annular transition (as pointed out by Rienstra, 1999). Alternative discretizations are known for a hollow duct that give cleaner numerical results (see Boyd, 2001, chapter 18.5, pp386–391), although the annular and hollow cases would then need treating separately.

Since this is a pseudospectral method, the computational values stored are the values of functions at these collocation points, $b_{j\ell} = f(r_j, \theta_\ell)$, which represent the unique interpolating function of the form

$$f(r, \theta) = \sum_{j=0}^{n_r-1} \sum_{\ell=\frac{n_\theta-1}{2}}^{\frac{n_\theta-1}{2}} a_{j\ell} T_j(r) e^{i\ell\theta} \quad (4.21)$$

where $a_{j\ell}$ are the spectral coefficients, and the Chebyshev polynomials are

$$T_j \left(\frac{a_1 + a_2}{2} + \frac{a_1 - a_2}{2} \cos \theta \right) = \cos(j\theta).$$

Hence, multiplication of two functions simply multiplies their stored values pointwise, while differentiation by r and θ is represented by the matrices D_r and D_θ respectively, where

$$D_{\theta(\ell,m)(j,k)} = \begin{cases} \frac{(-1)^{m+k}}{2 \sin \left(\frac{\pi(m-k)}{n_\theta} \right)} & \text{if } m \neq k \text{ and } \ell = j \\ 0 & \text{otherwise} \end{cases},$$

$$D_{r(\ell,m)(j,k)} = \frac{-2}{a_2 - a_1} \delta_{mk} A_{\ell j},$$

and

$$A_{\ell j} = \frac{c_\ell (-1)^{\ell+j}}{c_j \xi_\ell - \xi_k} \quad \text{if } \ell \neq j$$

$$A_{jj} = \frac{-\xi_j}{2(1 - \xi_j^2)}$$

$$A_{00} = \frac{2(n_r - 1)^2 + 1}{6} = -A_{(n_r-1)(n_r-1)},$$

where $c_j = 2$ if j is 0 or $n_r - 1$, and $c_j = 1$ otherwise.

Our system is discretized for an annular duct by requiring the boundary conditions (4.20) to be satisfied at collocation points $(0, \ell)$ and $(n_r - 1, \ell)$ for $\ell = 0, \dots, n_\theta - 1$, and (4.19) to be satisfied at collocation points (j, ℓ) for $\ell = 0, \dots, n_\theta - 1$ and $j = 1, \dots, n_r - 2$. For a hollow duct, equation (4.19) is also required to be satisfied at collocation points $(0, \ell)$ for $\ell = 0, \dots, n_\theta - 1$, and the inner boundary condition is dropped. This gives a generalized eigenvalue problem which is $2n_\theta n_r$ square. This was solved using the QZ algorithm, as implemented in the LAPACK library routine ZGGEV (Anderson *et al.*, 1999).

4.3.1 Computational simplification for a hard-wall boundary

If the boundary is hard-walled, so that the boundary condition is simply $\partial A_0/\partial r = 0$ at $r = a_{1,2}$, then some substantial computational simplifications are possible. First of all, a hard-wall boundary implies that all the components of the discretized matrices are real, and so the LAPACK library routine `DGGEV` (Anderson *et al.*, 1999) may be used. This reduces the memory required by half.

Let Q be the matrix obtained by discretizing \mathcal{Q} (using the D_r and D_θ matrices and pointwise multiplication) at the interior collocation points, and let G_1 and G_2 be the matrices representing multiplication by $(2\omega U_0)/(h_s C_0^2)$ and $(1 - U_0^2/C_0^2)/h_s^2$ at the interior collocation points. Let D_{bound} be the matrix evaluating the radial derivatives on the boundaries, derived from D_r . Then the hard-wall discretized problem may be written

$$\underbrace{\begin{pmatrix} D_{\text{bound}} & 0 \\ & Q & 0 \\ 0 & & I \end{pmatrix}}_F \begin{pmatrix} b_{j\ell} \\ \\ b_{j\ell}^* \end{pmatrix} = k \underbrace{\begin{pmatrix} 0 & 0 \\ G_1 & G_2 \\ I & 0 \end{pmatrix}}_G \begin{pmatrix} b_{j\ell} \\ \\ b_{j\ell}^* \end{pmatrix}, \quad (4.22)$$

where $b_{j\ell}$ are the values of A_0 at the (j, ℓ) collocation points, and $b_{j\ell}^* = kb_{j\ell}$. The values of $b_{j\ell}^*$ are only needed at the interior points, and not at points where the boundary condition is being enforced. Hence, if d is the number of boundaries (so $d = 2$ for an annular duct, and $d = 1$ for a cylindrical duct), then the first column is $n_\theta n_r$ wide, the second column is $n_\theta(n_r - d)$ wide, the first row is dn_θ deep, and the second and third rows are $n_\theta(n_r - d)$ deep. $b_{j\ell}$ contains one value for every collocation point, and $b_{j\ell}^*$ contains one value for every interior collocation point.

Note that G is singular, since its top dn_θ rows are zero to enforce the boundary conditions. Using column operations, the first dn_θ rows of F may be diagonalized. Letting H denote the matrix of column operations, this may be represented as

$$FH\mathbf{v} = kGH\mathbf{v},$$

where the top dn_θ rows of FH are diagonal. Since only column operations were used, the top dn_θ rows of GH are still zero. This implies $v_j = 0$ for $j = 0, \dots, dn_\theta - 1$. Let F^* and G^* be formed from FH and GH by throwing away the first dn_θ rows and dn_θ columns, and let \mathbf{v}^* be formed from \mathbf{v} by deleting the first dn_θ elements. Then an equivalent problem to (4.22) is

$$F^*\mathbf{v}^* = kG^*\mathbf{v}^*. \quad (4.23)$$

Once this has been solved, the solution to (4.22) may be recovered by

$$\begin{pmatrix} b_{j\ell} \\ b_{j\ell}^* \end{pmatrix} = H \begin{pmatrix} 0 \\ \mathbf{v}^* \end{pmatrix}.$$

The generalized eigenvalue problem (4.23) is now $2n_\theta(n_r - d)$ square. While this reduction in size does not save any significant computational time, it yields a non-singular matrix G^* , and hence the results are numerically more robust.

4.3.2 Spurious eigenvalues and filtering

It is well known (e.g. Boyd, 2001, chapter 7) that pseudospectral methods are prone to giving spurious eigenvalues and eigenfunctions that are numerical artifacts. That is, because of the numerical resolution, it is possible that highly-oscillatory functions which are badly resolved at a chosen resolution do satisfy the discretized problem, without satisfying the underlying eigenvalue problem (4.19).

In order to avoid spurious eigenvalues, two filtering processes were used. The first, based loosely on the description by Boyd (2001, pp137–139), attempts to remove any eigenvalues which vary significantly with the discretization used. Let the numerical eigenvalues calculated with n_r and n_θ be λ_j , and the numerical eigenvalues calculated with a slightly different resolution be μ_ℓ . Define the *eigenvalue continuity* of an eigenvalue λ_m to be

$$\text{continuity} = \frac{\inf_\ell |\lambda_m - \mu_\ell|}{\sqrt{(d_1^2 + d_2^2)/2}},$$

where d_i is the distance between λ_m and the i^{th} nearest λ_j with $j \neq m$. That is, the eigenvalue continuity is the distance moved by an eigenvalue between the two resolutions, normalized by the distance to the next closest eigenvalue so as to be scale free. The reason for the averaging over d_1 and d_2 is to deal with doubly-degenerate eigenvalues. A small eigenvalue continuity indicates the eigenvalue is stable under small changes to the discretization, and hence that it is a good candidate for a physical eigenvalue.

Figure 4.3 shows how continuity varies with the imaginary part of the eigenvalue. The regions of large continuity correspond to the well cutoff modes, as these modes are the most oscillatory, and are therefore the poorest resolved and most susceptible to numerical errors. A threshold of 0.01 is shown, which is typical of the threshold used for the results below. Also plotted in figure 4.3 is the continuity of the same results, having first been filtered using the resolvedness test described below with a threshold of 0.01. As can be seen, both tests yield very similar decisions for which modes to keep and which to remove.

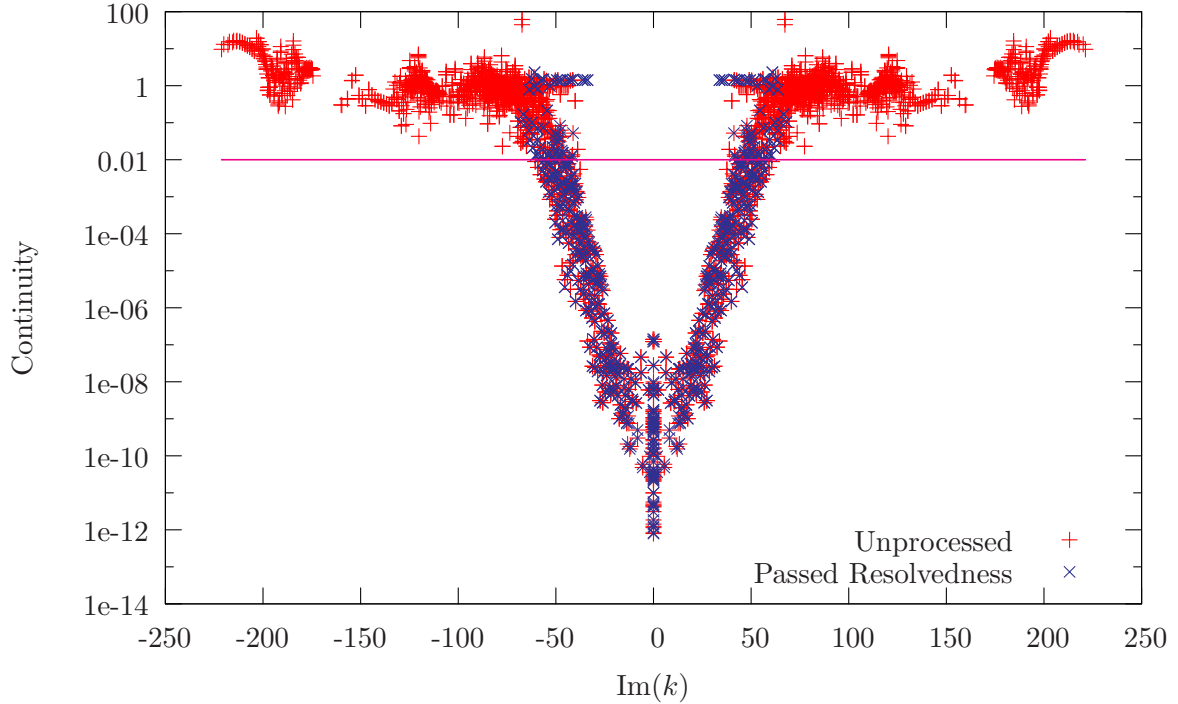


Figure 4.3: Graph showing the continuity of eigenvalues for $U_\infty = 0.5$, $\kappa = 0.1$, $a_1 = 0.4$, $a_2 = 1.0$, $\gamma = 1.4$, $\omega = 10$, $n_r = 21$, $n_\theta = 81$, compared against $n_r = 25$, $n_\theta = 75$ with the same settings.

A continuity based on $\inf_\ell |\lambda_m - \mu_\ell|/|\lambda_m|$, the absolute change in the eigenvalue between discretizations, was also considered. However, when the two were used in conjunction, the absolute continuity made no discernible difference. Either continuity could have been used on its own, and the former was selected, since it depends only on the relative distribution of eigenvalues and therefore does not make a biased choice based on where in the complex plane the eigenvalues occur.

The second filtering attempts to remove eigenvectors for which n_r or n_θ are not large enough to properly resolve the true eigenfunction. In order to do this, the eigenvector is decomposed into its spectral representation a_{pq} , given in (4.21). This decomposition is performed via a discrete cosine transform in the r direction and a discrete Fourier transform in the θ direction, implemented using the FFTW library's `dft_2d` transform (Frigo & Johnson, 2005). Figures 4.4 and 4.5 show the spectral coefficients for two numerical eigenfunctions, one of which is well resolved, and one of which is not. For the well resolved eigenfunction, the outlying spectral coefficients are of the order of the machine precision (2×10^{-16}), whereas for the unresolved mode the outlying spectral coefficients are significant. Motivated by this figure, for a well resolved eigenvector, the spectral coefficients a_{pq} should be small for $n_r - b_r \leq p < n_r$ for some

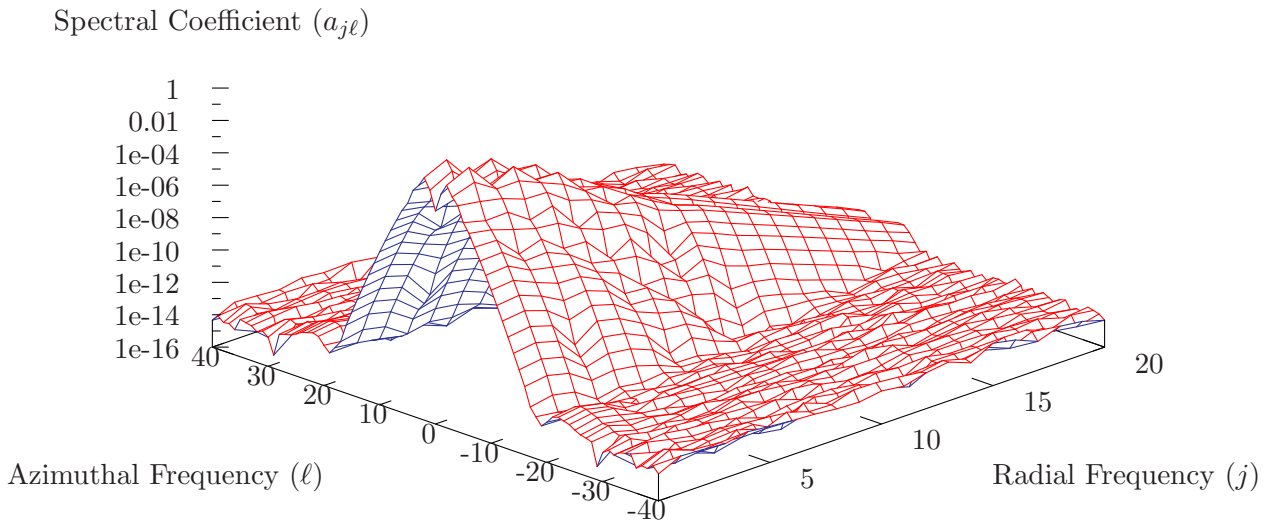


Figure 4.4: The spectral coefficients for a well resolved eigenfunction with eigenvalue $k = -17.77$. $U_\infty = 0.5$, $\kappa = 0.1$, $a_1 = 0.4$, $a_2 = 1.0$, $\gamma = 1.4$, $\omega = 10$, $n_r = 21$, $n_\theta = 81$.

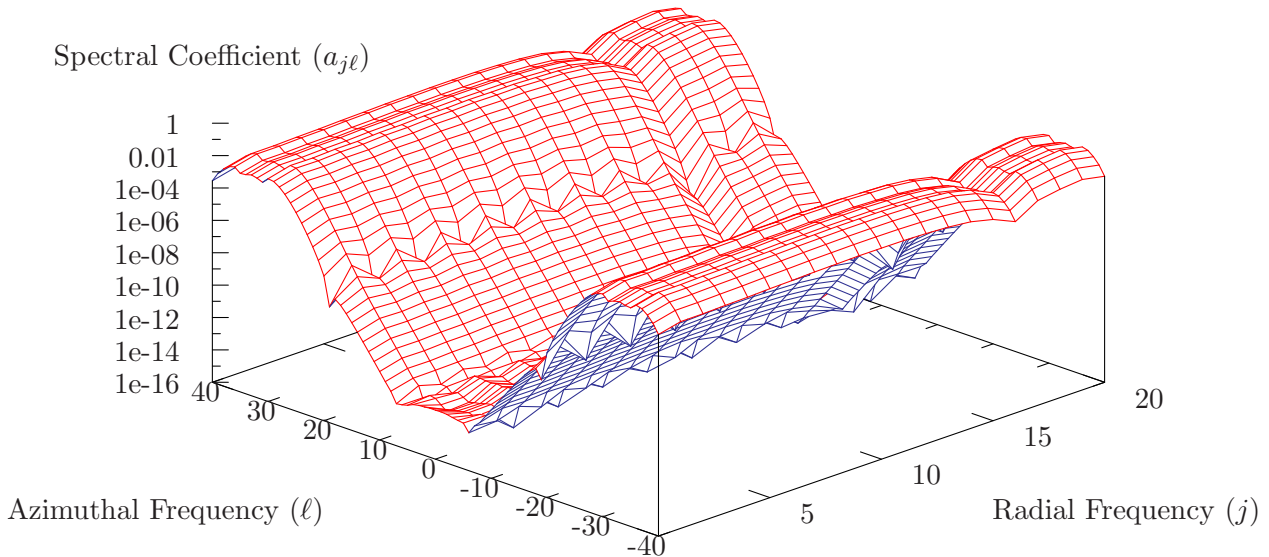


Figure 4.5: The spectral coefficients for a badly resolved eigenfunction with eigenvalue $k = 208.0 - 6.649i$. $U_\infty = 0.5$, $\kappa = 0.1$, $a_1 = 0.4$, $a_2 = 1.0$, $\gamma = 1.4$, $\omega = 10$, $n_r = 21$, $n_\theta = 81$.

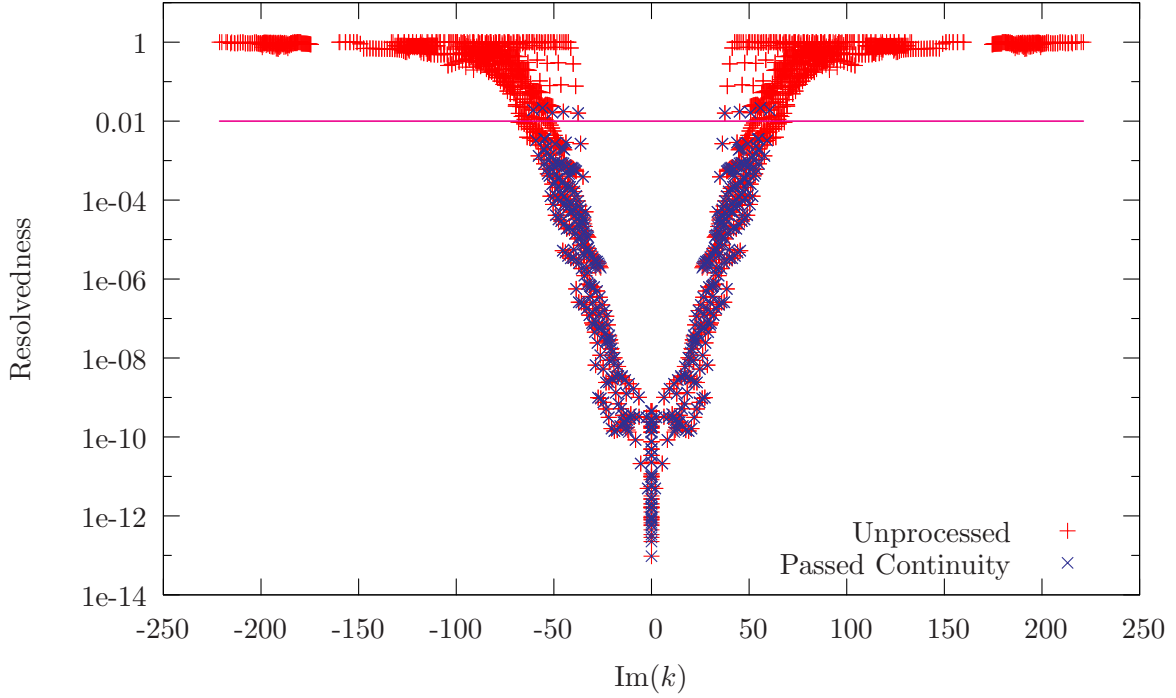


Figure 4.6: Graph showing the resolvedness of eigenfunctions for $U_\infty = 0.5$, $\kappa = 0.1$, $a_1 = 0.4$, $a_2 = 1.0$, $\gamma = 1.4$, $\omega = 10$, $n_r = 21$, $n_\theta = 81$, $b_r = 2$, $b_\theta = 4$.

border width b_r , and for $(n_\theta + 1)/2 - b_\theta \leq |q| < (n_\theta + 1)/2$ for some border width b_θ . Calling these borders \mathcal{B} , the *resolvedness* of an eigenvector with spectral coefficients a_{pq} is defined to be

$$\text{resolvedness} = \frac{\sup_{(p,q) \in \mathcal{B}} |a_{pq}|}{\sup_{\text{all } p,q} |a_{pq}|}.$$

Using $b_r = 2$ and $b_\theta = 4$, the eigenfunction of figure 4.4 has a resolvedness of 2.021×10^{-12} , and the eigenfunction of figure 4.5 has a resolvedness of 0.9344.

Figure 4.6 shows how the resolvedness varies with the imaginary part of the eigenvalue; note the similarity with figure 4.3. Also plotted on the same graph is the resolvedness of the eigenvalues that pass the continuity test with a threshold of 0.01. As can be seen, the two test are very similar in which eigenvalues they exclude and include. A threshold line of 0.01 is also shown on figure 4.6, which was a typical threshold used for the results below.

Since the resolvedness depends only on the shape of the eigenfunction, it is unaffected by any previous filtering. However, since the continuity depends on which other eigenvalues are present, filtering based on resolvedness affects the continuity. This means the order in which the filtering is performed affects the outcome. However, in practice it seems there is little difference

between the two different filtering orders. It may be argued that the continuity filtering is most useful when performed directly on the raw data. Hence, for the results below, the continuity filtering was applied before the resolvedness filtering. While this involves more computational time, the total time for all filtering processes was negligible compared with the time taken by LAPACK to solve the generalized eigenvalue problem.

4.3.3 Code validation

In the case of a straight duct with hard walls it is well known (for example, see Rienstra, 1999) that (4.9) can be solved analytically in a similar manner to §1.1, with solutions in terms of Bessel's functions $A(r, \theta) = (PJ_m(\alpha r) + QY_m(\alpha r))e^{-im\theta}$. Requiring a non-trivial solution satisfying the boundary conditions $\partial A/\partial r = 0$ yields the dispersion relation

$$J_m'(\alpha a_1)Y_m'(\alpha a_2) - J_m'(\alpha a_2)Y_m'(\alpha a_1) = 0, \quad (4.24)$$

with solutions $\alpha = \alpha_{mn}$ for $n = 1, 2, \dots$. Since Bessel's equation is self-adjoint, with weight function $w(r) = r$, and since the trigonometric polynomials are orthogonal, each of these solutions are orthogonal to one another with respect to the inner product

$$\langle \phi, \psi \rangle = \int_0^{2\pi} \int_{a_1}^{a_2} \overline{\phi(r, \theta)} \psi(r, \theta) r \, dr \, d\theta, \quad (4.25)$$

where the overbar denotes the complex conjugate. As a means of validation, the numerically generated solutions for a straight duct with hard walls were compared with the analytic solutions. For eigenvalues, the measure of accuracy was taken to be the eigenvalue continuity defined in the previous section. For eigenvectors, the numerical solutions were separated into a component in the direction of the analytic solution and an orthogonal component, with respect to the above inner product, and the error was taken to be the norm of the orthogonal component.

The numerical solutions were calculated at varying values of (n_r, n_θ) from (21, 21) to (41, 81). These were compared to all the analytic modes that passed the resolvedness test at the (21, 21) resolution. Figure 4.7 shows the accuracy of the eigenvalues and eigenvectors. Since the analytic modes have $e^{-im\theta}$ dependence, which are also the azimuthal basis functions for the pseudospectral method, all analytic modes considered were well resolved in the azimuthal direction and so little variation was seen beyond $n_\theta = 21$. For small values of n_r some modes were not accurately resolved, explaining the initial plateau. For large values of n_r computational rounding errors become apparent. In the intermediate region, an exponential decrease in error is seen,

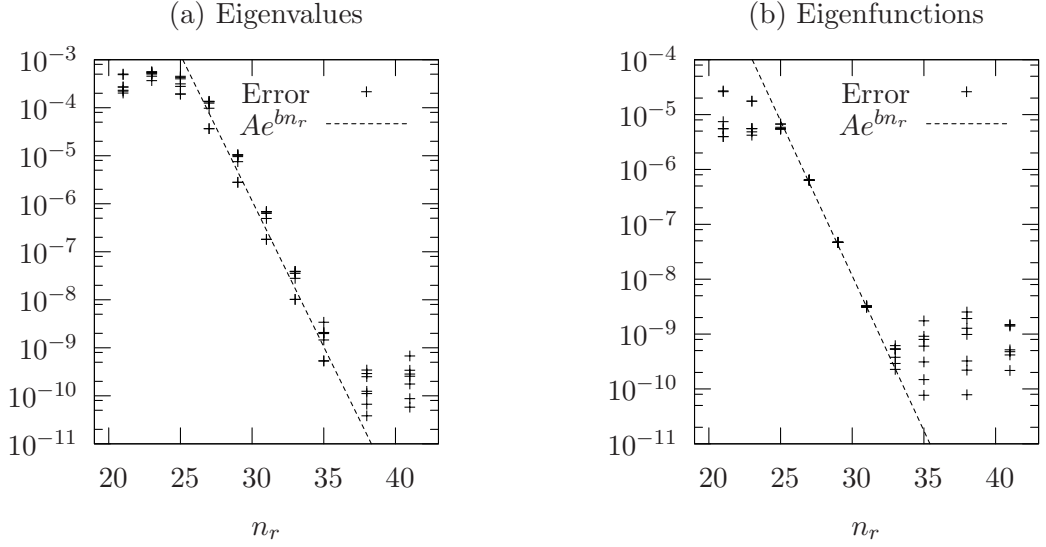


Figure 4.7: Mean numerical error. $U_\infty = 0.5$, $a_1 = 0.4$, and $a_2 = 1.0$, $\omega = 10$. The line shown has slope (a) $b = -1.4$, (b) $b = -1.3$.

as is expected from a pseudospectral method. While the arithmetic mean error for all modes is plotted, similar results were obtained from taking the geometric mean and the maximum error.

The numerical method was verified for an impedance boundary by computing the duct modes for a straight duct, and verifying the results satisfied the analytic dispersion relation (1.4), or its annular equivalent. The value of m to use for this was obtained from each numerically calculated eigenfunction by using a discrete Fourier transform and then averaging the azimuthal orders. Figure 4.8 plots the amount by which the dispersion relation is not satisfied for a numerically generated solution with $n_r = 31$ and $n_\theta = 61$, against the imaginary part of the eigenvalue k . The errors for modes close to the real k axis are only a few orders of magnitude larger than machine precision, while the errors increase with the magnitude of the imaginary part of k as these higher-order modes are less well resolved, although remain small compared with unity.

4.4 Results

4.4.1 Local mode shapes

The numerics above were first applied to a hypothetical duct, with upstream conditions $U_\infty = 0.5$ and $\gamma = 1.4$. The curvature of the duct was considered to vary slowly from $\kappa = 0$ upstream to $\kappa = 0.1$, at which point the wave modes were calculated for $\omega = 10$.

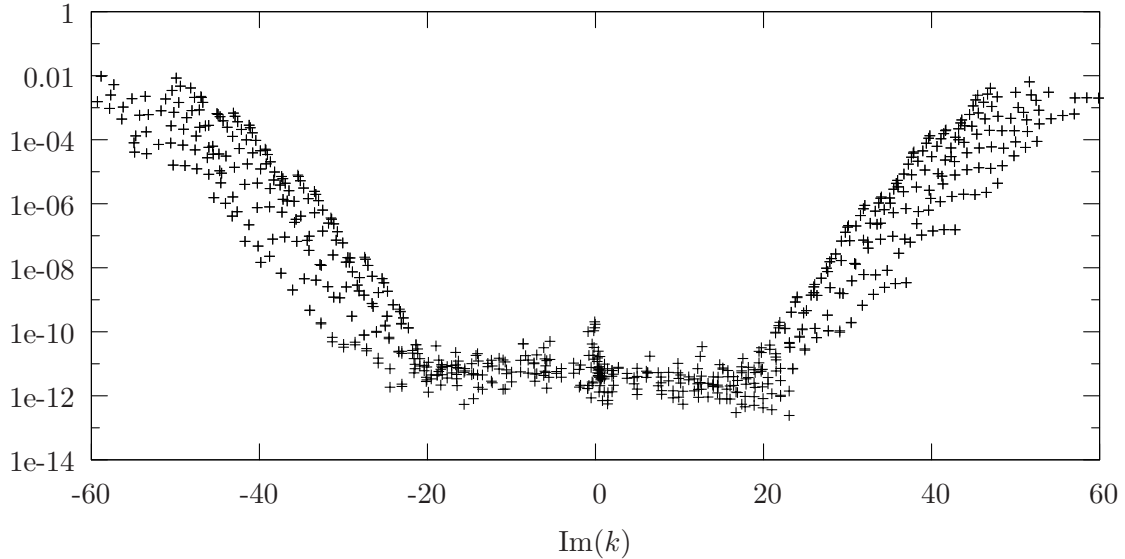


Figure 4.8: Magnitude of the left hand side of the analytic dispersion relation (1.4) for a straight lined duct. $n_r = 31$, $n_\theta = 61$, $U_\infty = 0.5$, $Z = 2 - i$, and $\omega = 10$.

The numerically-generated eigenvalues for an annular duct with this geometry and $a_1/a_2 = 0.4$ are shown in figure 4.9(a,b). Figures 4.9(c,d) show examples of cross-sectional modal shapes. Both of these are upstream propagating modes, and the fundamental mode (the curved-duct equivalent of a plane-wave mode) in figure 4.9(c) is seen to be localized in the inside of the bend. The downstream propagating modes have similar shapes, but are localized on the outside of the bend. Figures 4.9(e,f) show typical higher order modes, both of which are cutoff modes. These modal shapes are termed *bouncing ball* and *whispering gallery* type modes respectively, in light of the ray-tracing approximations in §4.7.

One interesting feature of the spectrum is the diagonal vanes of eigenvalues occurring periodically across the usual line of cutoff modes in figure 4.9(a), shown in close-up in figure 4.9(b). This only seems to appear in the presence of both non-zero mean flow and non-zero curvature, and can perhaps be associated with the asymmetric mean flow and asymmetric mode shapes leading to slightly different Doppler shifts experienced by each mode.

These vanes are also present for a cylindrical duct geometry, although with real parts in a far smaller range than for the annular case, as shown in figure 4.10(a). Figures 4.10(c,d,e,f) give the hollow duct equivalents of figures 4.9(c,d,e,f). Hollow and annular cases are very similar with the exception that the hollow bouncing ball mode in figure 4.10(e) is not localized on the inside of the duct bend, but is free to explore the whole duct.

We now consider a lined ($Z = 2 - i$) curved ($\kappa = 0.1$) hollow duct with mean flow ($U_\infty = 0.5$),

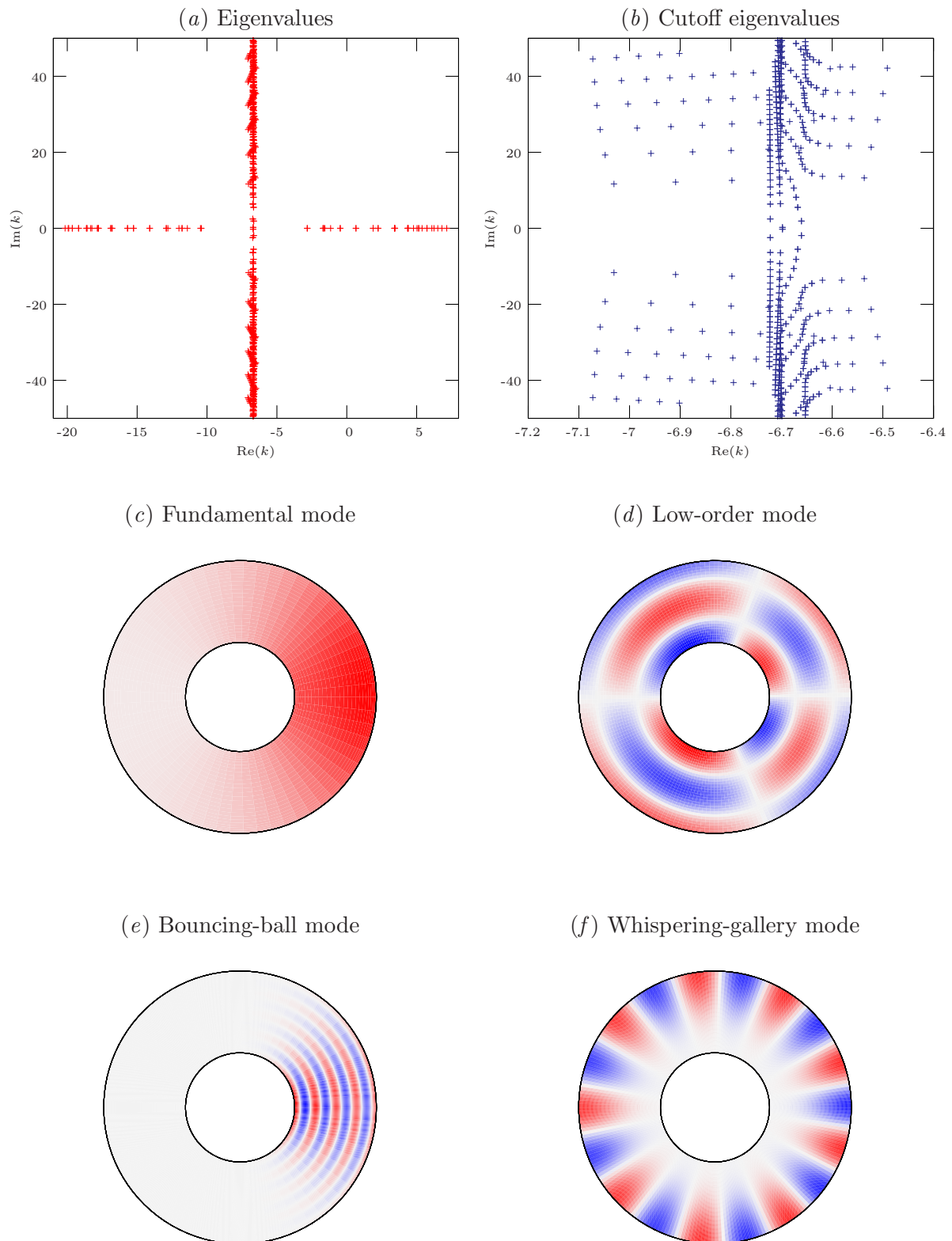


Figure 4.9: Results for a hard-walled annular duct, (b) being a close-up of the cutoff modes in (a). The modes in (c–f) are all downstream propagating, with the inside of the bend on the right. $U_\infty = 0.5$, $\omega = 10$, $a_1/a_2 = 0.4$, and $\kappa = 0.1$.

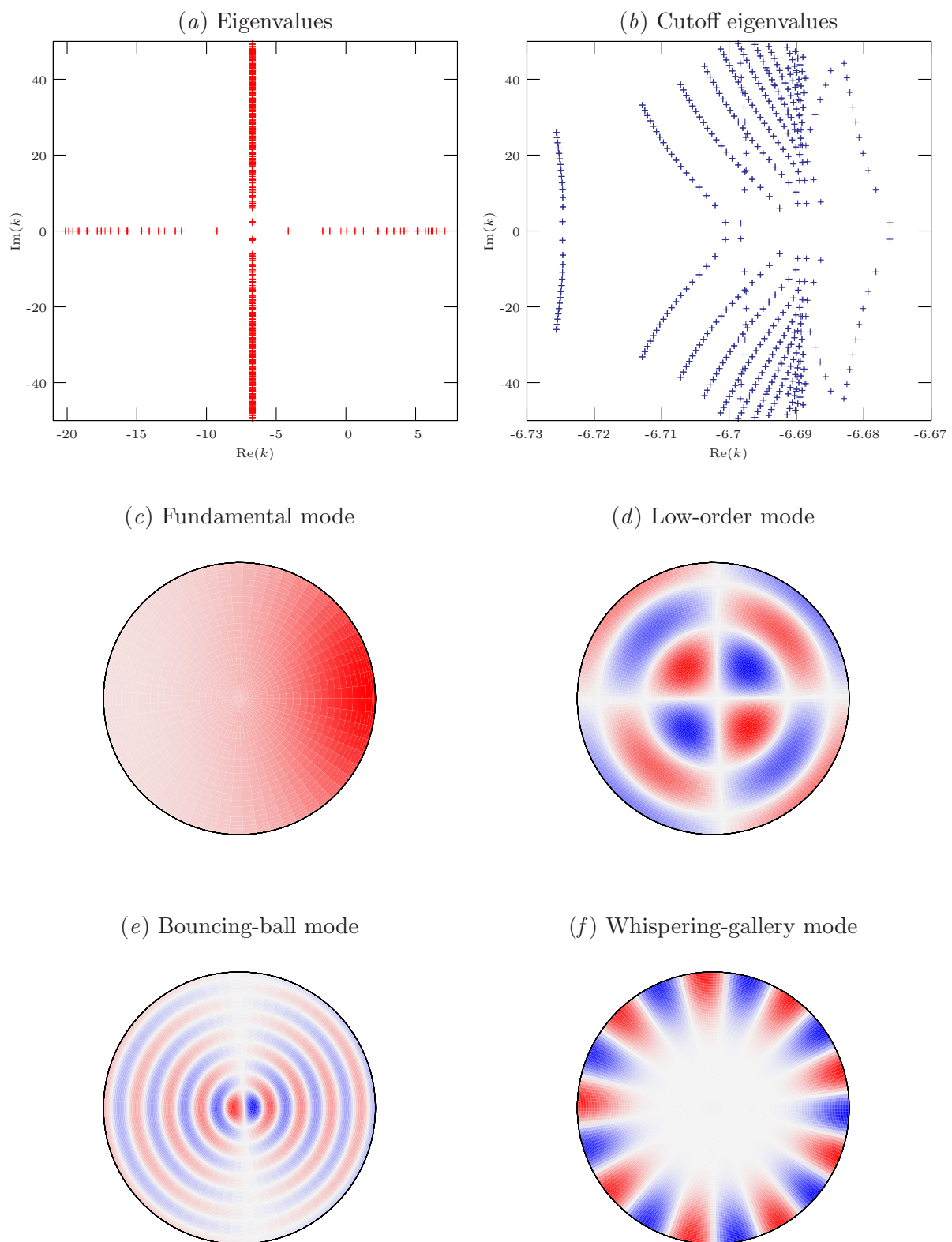


Figure 4.10: Results for a hard walled, cylindrical duct. $U_\infty = 0.5$, $\omega = 10$, and $\kappa = 0.1$.

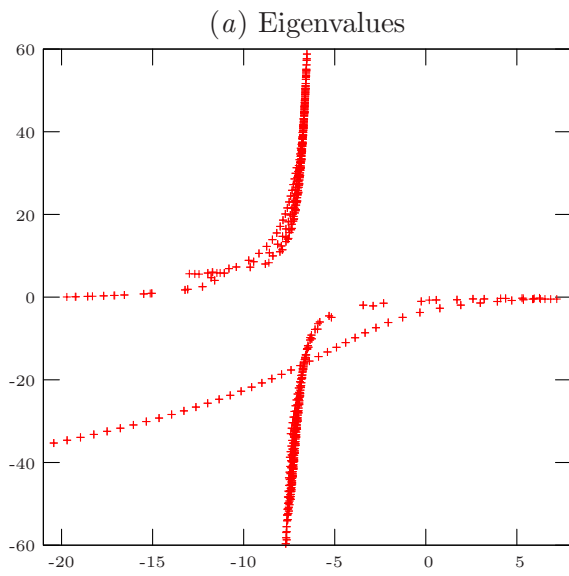
some results for which are presented in figure 4.11. The additional series of eigenvalues in the lower-half k -plane corresponds to a series of surface modes, exactly as for surface modes in a straight duct described in chapter 2. Figure 4.11(*d*) shows how such modes are strongly localised near the boundary, while figure 4.11(*c*) shows the upstream-propagating acoustic mode of the same order. This latter mode is a whispering gallery mode, and while still being localised close to the outer boundary is noticeably more pervasive into the duct than the surface mode. (The true difference is that 4.11*c* decays algebraically away from the boundary, while 4.11*d* decays exponentially.) At the other extreme is the bouncing-ball mode shown in figure 4.11(*b*). These modes are similar to the high-order modes in a hard-wall duct, except that for the lined duct there is very little oscillation at the duct wall. Figures 4.11(*e*) and 4.11(*f*) show the fundamental duct modes, and illustrate the dramatic asymmetry between upstream- and downstream-propagating modes. The upstream-propagating mode is removed from the boundary, similar to a mode with a pressure-release boundary condition, while the curvature biases the mode slightly to the inside of the bend (the right hand side). The downstream-propagating mode, in contrast, is strongly localised on the outside of the bend, and is oscillating significantly on the duct boundary; it is very similar in form to a hard-wall duct mode.

Figure 4.12 shows how the axial wavenumbers k vary with the curvature κ . Note that owing to the left–right symmetry for $\kappa = 0$, two distinct modes with $\kappa \neq 0$ may merge into a double mode as $\kappa \rightarrow 0$. As the curvature increases from zero, the first few downstream modes (on the right of figure 4.12*b*) become more damped, as do the first few upstream modes. In contrast, the surface modes (i.e. the lower branch in the right half plane) for $k \lesssim 5$ become less damped, while most of the well cutoff acoustic modes maintain the same rate of decay, although their phase speed shifts slightly towards upstream.

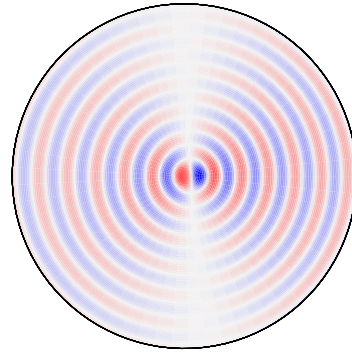
4.4.2 Partially lined boundary

The numerics described in §4.3 above do not require the impedance Z to be azimuthally constant, or even continuous. Since the results in figure 4.11 suggest that different modes are localized in different sections of the duct cross-section, a natural generalization is to only line part of the boundary, leaving the remainder hard walled. Figure 4.13 demonstrates this, for a lining of impedance $Z = 2 + i$ that extends 35 degrees either side of the inside of the duct bend, the rest of the duct wall being rigid.

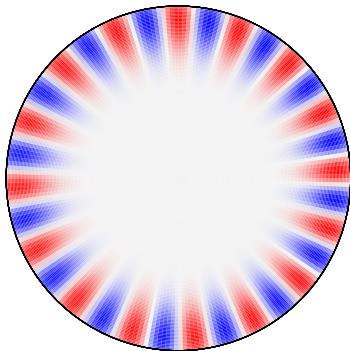
Figure 4.13, and a number of similar results for different impedances, curvatures, frequencies, and lining angles, give the conclusion that a considerable improvement in sound attenuation



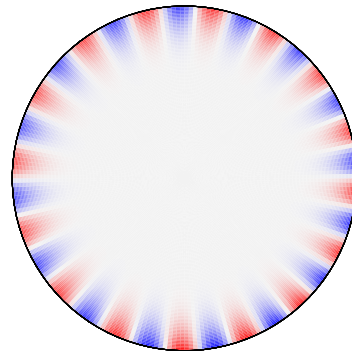
(b) A bouncing-ball mode



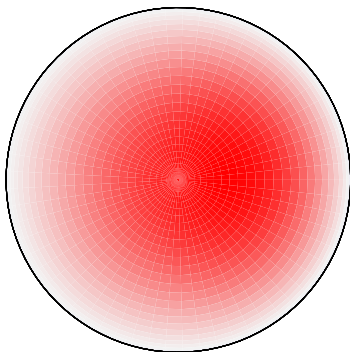
(c) A whispering-gallery mode



(d) A surface mode



(e) The upstream fundamental mode



(f) The downstream fundamental mode

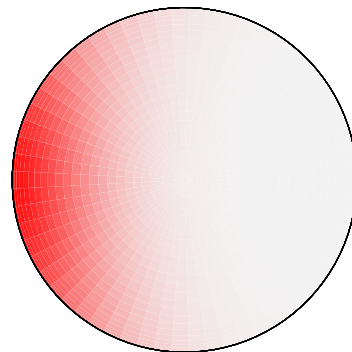


Figure 4.11: Results for a lined curved duct. $U_\infty = 0.5$, $\kappa = 0.1$, $Z = 2 - i$, and $\omega = 10$.

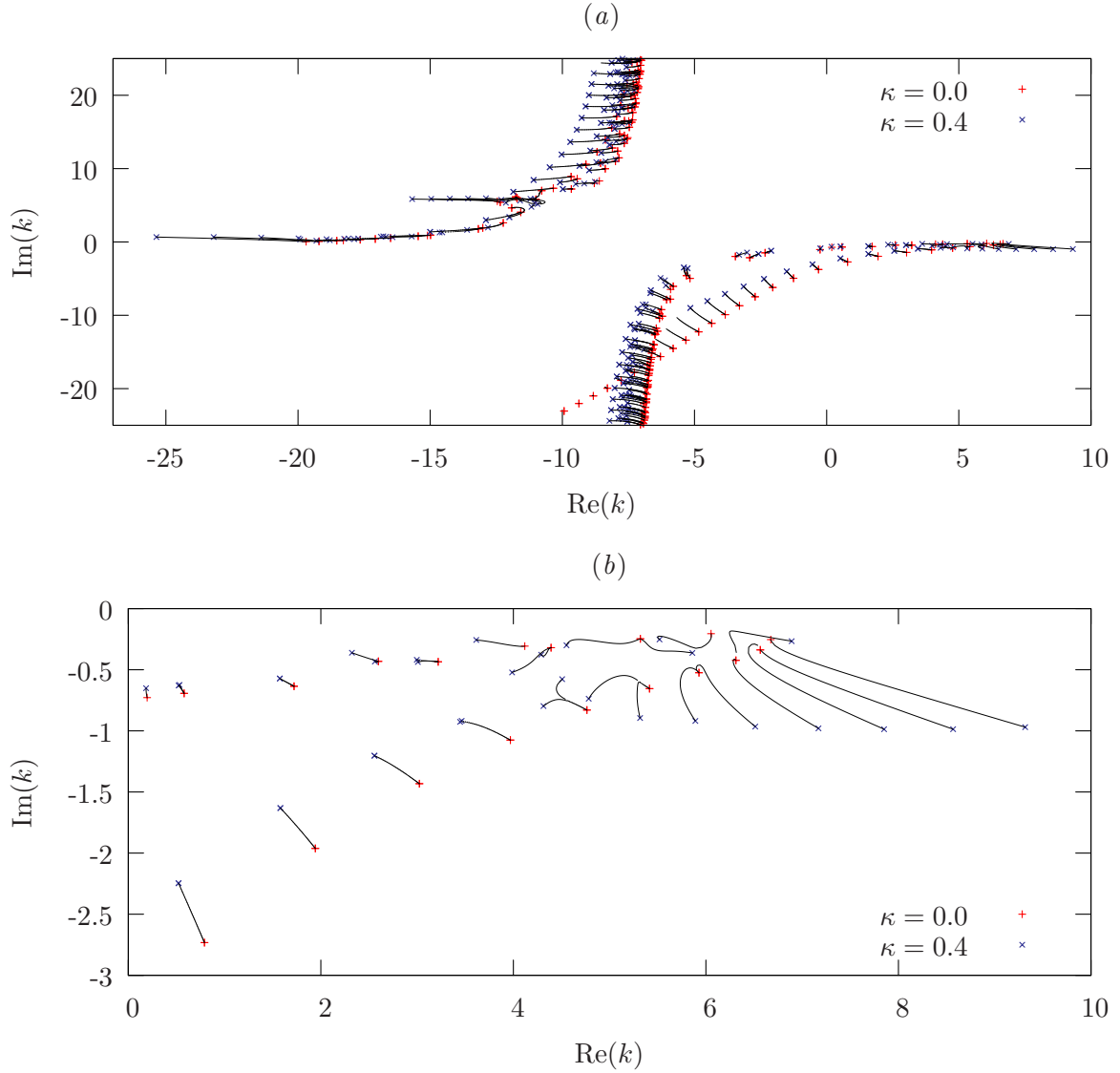


Figure 4.12: The motion of eigenvalues in the k -plane from $\kappa = 0.0$ (+) to $\kappa = 0.4$ (x). $Z = 2 - i$, $U_\infty = 0.5$, and $\omega = 10.0$. (b) shows a close up of the nearly cuton modes in (a).

is given by lining the entire duct; even for a mode localized on the inside of the bend, only lining the duct on the inside of the bend gives a considerably lower attenuation than lining the entire duct. An explanation of this is that the curvature leads to certain modes being algebraically large on the inside of the bend compared with the outside, while the wall lining leads to exponential decay. Therefore, a mode that would have been localized on the inside of the bend had the entire duct been lined becomes localized on the outside if only the inside of the bend is lined; the inner part of the mode being exponentially damped by the boundary. For example, figure 4.13(c) is localized on the outside of the bend, but would have been localized on the inside (similarly to figure 4.11e) had the entire duct been lined.

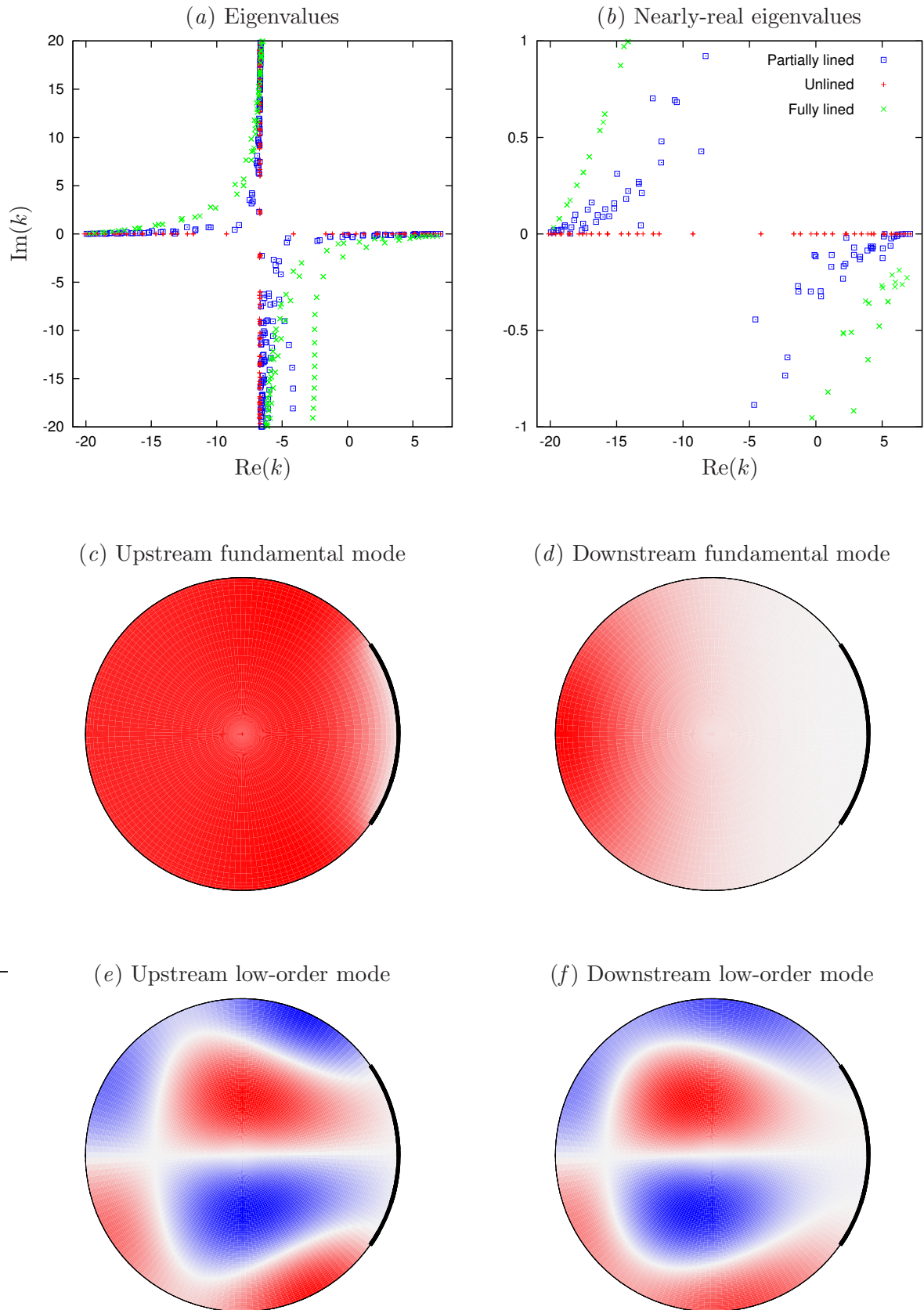


Figure 4.13: Modes for a partially-lined duct; the lined section is the thicker boundary shown in (c)–(f). $Z = 2 + i$, $\omega = 10$, $U = 0.5$, and $\kappa = 0.1$.

The pseudospectral method described in §4.3 is not best suited to discontinuous boundary impedance changes, such as in figure 4.13. This is because the eigenmodes tend to change rapidly in the neighbourhood of impedance discontinuities, and so a far larger number of azimuthal modes n_θ are needed than in the uniform boundary case. In fact, it may well be that the spectral accuracy is lost in the neighbourhood of the impedance discontinuities, with the solution only converging algebraically fast. One method to alleviate these problems would be to smoothly vary the boundary from lined to hard; however, this was considered unrealistic and was therefore not attempted here.

Another partially-lined situation that was considered was that of liner splices. A typical aeroengine liner is manufactured in sections that are then fitted together; along the join is a *liner splice*, which is a thin hard-walled section that runs axially along the duct. Typically, two or four splices are present, each covering less than 0.06 radians azimuthally (McAlpine & Wright, 2006). Since this impedance discontinuity is so localized, an extremely large number of azimuthal modes n_θ would be needed to accurately resolve the effects of the splices. This is computationally impractical using the pseudospectral code developed in §4.3, and so no results are presented here for liner splices. Some suggestions for modifications that would allow liner splices to be investigated are given in §6.1.

4.4.3 Global mode shapes

The results given above in §4.4.1 are for one particular axial location. In a slowly varying geometry, the axial wavenumber $k(S)$ and the mode shape $A_0(S; r, \theta)$ will vary slowly along the duct. In order to compute numerically the global mode shape along the entire duct, the above local analysis must be performed at a number of different axial locations, and then modes in one axial location must be matched to the same mode at the neighbouring axial locations.

Suppose we have a mode with eigenvalue λ and eigenfunction $\phi(r, \theta)$ at one axial location, and we have calculated numerically the eigenvalues μ_i and $\psi_i(r, \theta)$ at a neighbouring axial location. We require the eigenvalue μ and eigenfunction $\psi(r, \theta)$ at the new axial location that correspond to the original eigenvalue λ and eigenfunction $\phi(r, \theta)$.

There are four threshold values we will use in deciding on this matching. The first is the *partner threshold*, T_p , which determines whether two eigenfunctions span an eigenspace of dimension two. Suppose that the closest eigenvalue to μ_1 is μ_2 , and the second closest is μ_3 . Define $d_1 = |\mu_1 - \mu_2|$ and $d_2 = |\mu_1 - \mu_3|$. Then the eigenfunctions ψ_1 and ψ_2 are considered to

be part of the same eigenspace (i.e. ψ_1 and ψ_2 span an eigenspace of dimension two) if

$$\frac{d_1}{\sqrt{(d_1^2 + d_2^2)/2}} < T_p.$$

We try in turn to match ϕ with the eigenfunctions ψ_i , trying the ψ_i with the smallest $|\lambda - \mu_i|$ first, and then proceeding in order of $|\lambda - \mu_i|$. First, we determine if ψ_i has a partner eigenfunction ψ_j using the partner threshold test above. If so, we decompose $\phi = a\psi_i + b\psi_j + \zeta$, with ζ being a function orthogonal to ψ_i and ψ_j according to the inner product (4.25). If ψ_i has no partner, so that it corresponds to an eigenspace of dimension one, the decomposition is, as would be expected, $\phi = a\psi_i + \zeta$ where ζ is orthogonal to ψ_i . The *residual* is then defined to be $\text{res} = \sqrt{\langle \zeta, \zeta \rangle / \langle \phi, \phi \rangle}$.

We then proceed as follows. If $\text{res} < T_s$, where T_s is the *sort threshold*, then we have found a match so good that we need try no more, and we terminate the search. Otherwise, we proceed until $|\lambda - \mu_i| > T_d$, where T_d is the *distance threshold*, in which case the eigenvalues differ by so much that we consider them not to match. In this case, we just pick the match that had the smallest value of res we have found so far. Finally, if $\text{res} > T_f$, where T_f is the *function threshold*, then the match still is not good enough, and we discard this axial location and move on to the next closest neighbour in search of a matching eigenfunction.

Typically, for the results that follow, $T_f = 0.25$, $T_d = 4$, $T_p = 10^{-2}$, and $T_s = 10^{-3}$ were used.

4.4.4 The RAE 2129 inlet diffuser duct

The RAE 2129 Inlet Diffuser duct is a much studied reference duct geometry (as considered by Menzies, 2002). It is a curved cylindrical duct with varying diameter. A cross-section along the RAE 2129 duct centreline is shown in figure 4.14, along with the mean flow for a uniform inlet Mach number $U_\infty = 0.5$. The duct geometry is defined in terms of the lateral offset of the centreline, y^* , from its position at the intake $s^* = 0$ (as shown in figure 4.1), with

$$y^*(s^*) = -\frac{h^*}{2} \left(1 - \cos\left(\frac{\pi s^*}{L^*}\right) \right) \quad \Rightarrow \quad \kappa^*(s^*) = \frac{\frac{\pi}{L^*} \cos\left(\frac{\pi s^*}{L^*}\right)}{\sqrt{\frac{4L^{*2}}{\pi^2 h^{*2}} - \sin^2\left(\frac{\pi s^*}{L^*}\right)}}, \quad (4.26)$$

where the formula for κ^* is given in (B.1). The lateral offset at the downstream exit ($s^* = L^*$) is then $-h^*$. The duct itself is hollow, with outer radius varying quartically between upstream

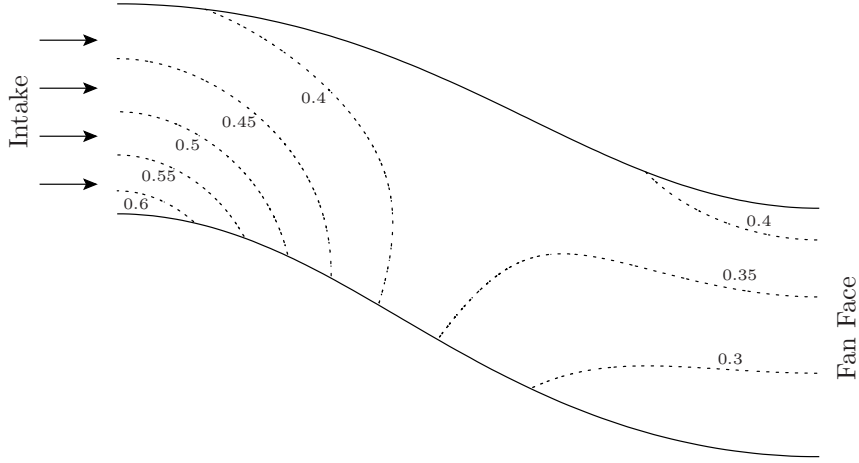


Figure 4.14: Contours of axial mean flow Mach number in the RAE 2129 Inlet Diffuser. Far upstream is a uniform inlet Mach number of 0.5.

(radius ℓ^*) and downstream (radius a_f^*) as

$$\frac{a^*(s^*) - \ell^*}{a_f^* - \ell^*} = 3 \left(1 - \frac{s^*}{L^*}\right)^4 - 4 \left(1 - \frac{s^*}{L^*}\right)^3 + 1.$$

For the RAE 2129 duct,

$$L^*/\ell^* = 7.1, \quad h^*/L^* = 0.3, \quad (a_f^*/\ell^*)^2 = 1.4.$$

This leads to a value of ε based on the duct length of $\varepsilon = 1/7.1$, for which it is reasonable to suppose that the small- ε asymptotics will work well. In fact, since $\max|d\kappa/dS| \approx 0.24$ and $\max|da/dS| \approx 0.33$, the lengthscale over which the slow parameters vary by order 1 is really $\sim 20\ell^*$, giving $\varepsilon \sim 0.05$, for which the small- ε asymptotics can be expected to give fairly accurate results.

The cuton eigenvalues for the RAE 2129 intake are plotted against the position along the duct centreline in figure 4.15, for a realistic aeroengine rotor-alone frequency. As can be seen, many modes which are cuton at the fan face ($s = 7.1$) will propagate all the way to the intake ($s = 0$). In figure 4.16 we plot the sound pressure level (SPL) of one such cuton mode (in the initial straight portion of the duct this corresponds to the $m = 24$ first radial order mode, a typical aeroengine rotor-alone mode), and in this case the amplitude varies rather little along the duct and the mode is concentrated close to the duct wall all the way along. The curvature does give an amplification of 4dB to the mode, occurring on the inside of the left-most bend.

For these parameters, there are also several duct modes which transition from cuton to cutoff within the duct (e.g. four around $s \approx 2$ etc). These transitions correspond to wave reflection by

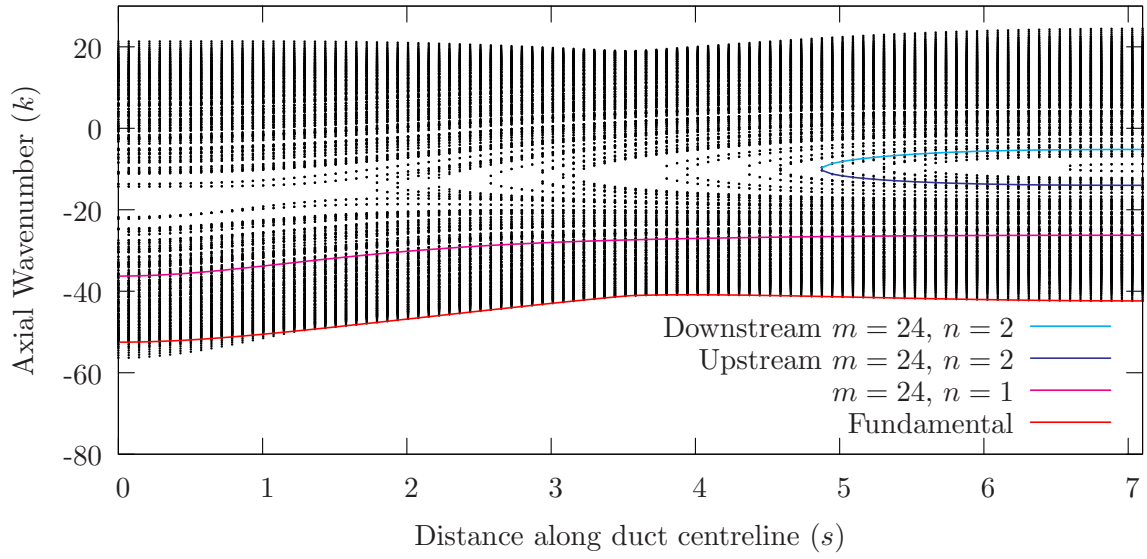


Figure 4.15: Real eigenvalues in the (hard-walled) RAE 2129 Inlet Diffuser shown in figure 4.14, for $\omega = 26.2$, giving $a_2^* \omega^* / C_\infty^* = 31.0$ at the fan face ($s = 7.1$). The mean flow has Mach number 0.5 at the intake ($s = 0$).

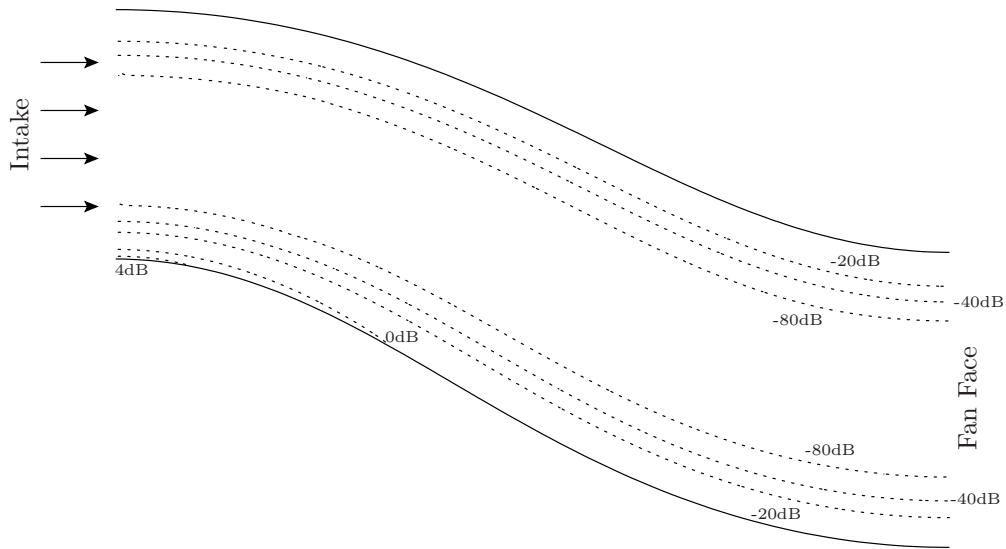


Figure 4.16: SPL for the first radial order, 24th azimuthal order mode propagating from right to left. The axial wavenumber k for this mode is shown in figure 4.15 as the middle solid line.

the changing geometry and flow, and will be described in detail in the next section. The cutoff transition confines these modes to the fan end of the duct. The amplitude of one of the reflected modes is shown in figure 4.17, using the analysis of the next section, and shows a standing-wave pattern formed by the mode and its reflection. In the initial straight portion of the duct, this mode corresponds to the $m = 24$ second radial order mode, a harmonic of a typical aeroengine rotor-alone mode. This suggests the possibility of acoustic resonance, in which acoustic modes are trapped upstream of the fan by the cutoff transition and are prevented from propagating downstream by the swirl in the rotor-stator gap (see Cooper & Peake, 2000).

4.5 Turning points and wave reflection

For a hard-walled duct, the secularity condition (4.18) represents continuity of axial energy flux. Since a cuton mode has a non-zero energy flux and a cutoff mode has no energy flux, it is to be expected that the secularity condition breaks down in the neighbourhood of a cuton–cutoff transition. The secularity condition (4.18) becomes singular when $F(S)$ becomes zero, a so-called *turning point*. This is well understood in straight ducts (see, for example, Rienstra, 2003b), and here we now derive the turning point behaviour incorporating curvature.

Define

$$G(S) = \int_0^{2\pi} \int_{a_1}^{a_2} \frac{D_0}{h_s} \hat{A}_0^2 \left(1 - \frac{U_0^2}{C_0^2}\right) r \, dr \, d\theta,$$

so that $k = (F(S)-1)/G(S)$. Since $G(S)$ varies little over the transition region, $F(S)$ transitions from real when the mode is cuton to complex when the mode is cutoff. For example, figure 4.18 shows the variation in $F(S)^2$ for a mode in the RAE 2129 intake that undergoes a cuton–cutoff transition; in the neighbourhood of the cutoff region, $F(S)^2$ is seen to be a linear function of S , and goes through zero as the mode transitions from cuton to cutoff.

The problem stems from the fact that there is a $\varepsilon d^2/dS^2$ term in the secularity condition (4.18) that has been neglected. This is justified provided the d/dS term in (4.18) is non-zero, which is not true at a turning point. These missing terms come from the fact that the right hand side of (4.12) has an $O(\varepsilon)$ term coming from the $O(\varepsilon^2)$ terms in (4.7). Including only higher order terms involving d^2/dS^2 and following the same procedure to derive the secularity condition as in §4.2, the secularity condition becomes

$$\frac{d}{dS} (FN^2) + i\varepsilon GN \frac{d^2N}{dS^2} = 0. \quad (4.27)$$

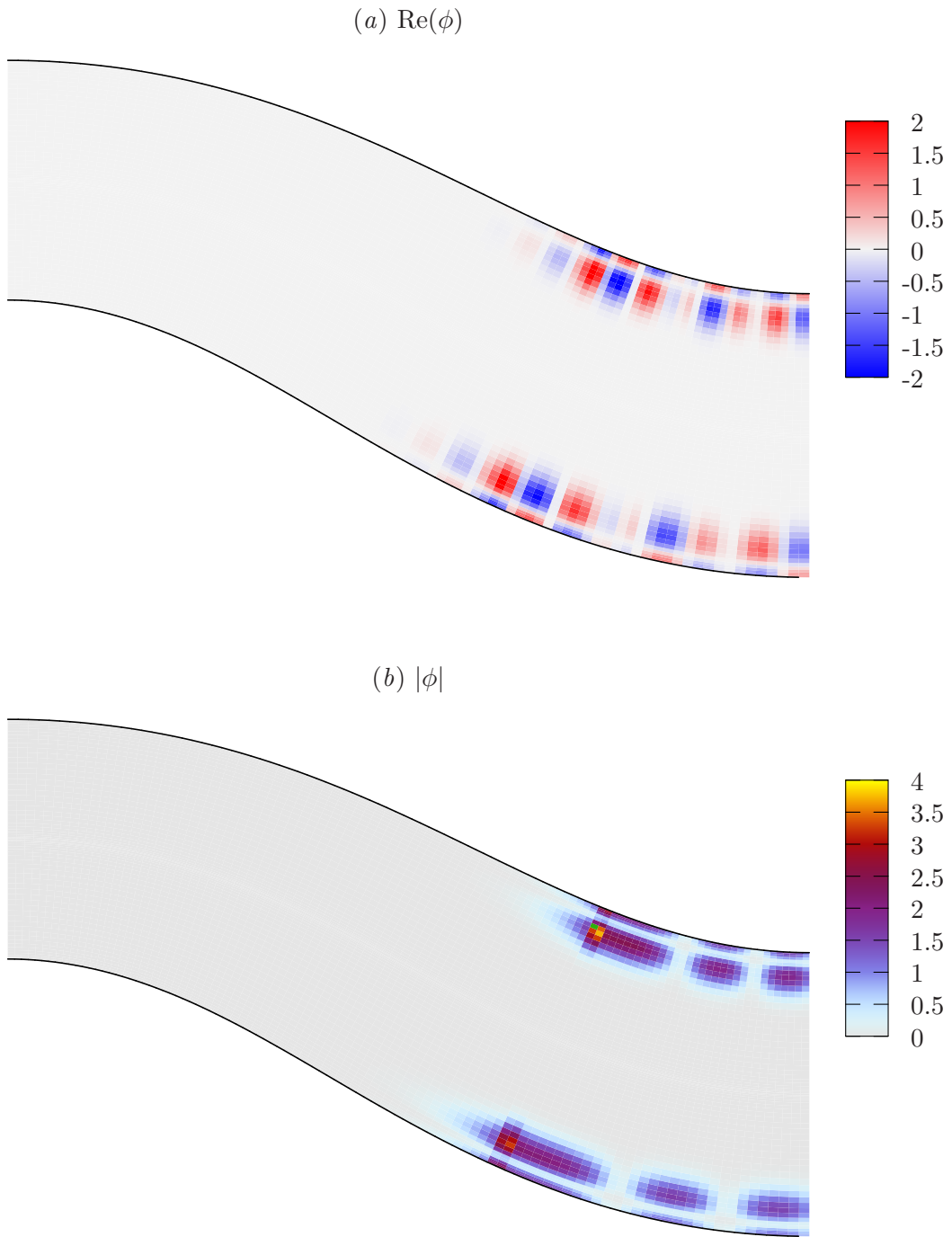


Figure 4.17: The second radial order, 24th azimuthal order mode propagating from the fan face (on the right) towards the intake (on the left), before being reflected by the duct geometry and propagating back towards the fan face. The axial wavenumbers k for these modes are shown as the upper solid lines in figure 4.15. (a) shows the real part of the wavefunction $\phi = A_0 \exp\{\int ik(S')/\varepsilon dS'\}$, while (b) shows the modulus of the wavefunction $|\phi|$.

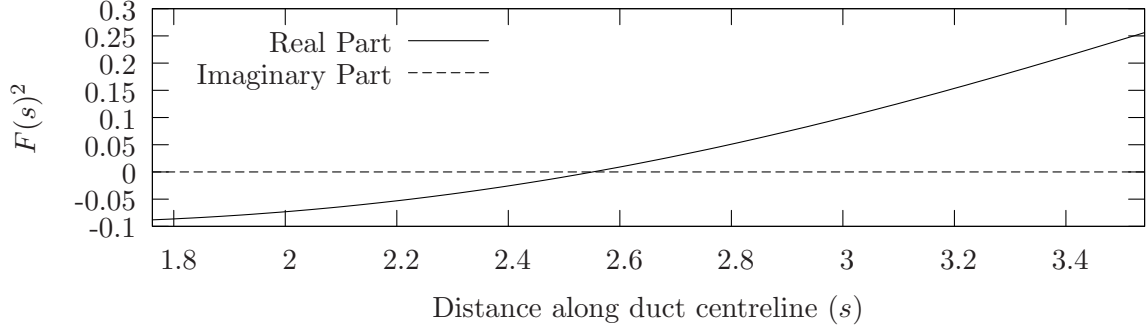


Figure 4.18: Graph showing $F(S)^2$ over a cutoff to cuton transition in the RAE 2129 Inlet Diffuser.

Let the turning point be at S_0 , so that

$$F(S_0 + \Delta S) = \sqrt{a\Delta S} + O(\Delta S), \quad G(S_0 + \Delta S) = G(S_0) + O((\Delta S)^{1/2})$$

for some a . The correct branch cut for the square root is along the positive imaginary axis. For an inbound downstream propagating mode, the branch is chosen so that $\sqrt{1} = 1$; for an inbound upstream propagating mode (as in the RAE 2129 duct), the correct branch is $\sqrt{1} = -1$. For simplicity of algebra, in what follows an inbound downstream propagating mode is considered, although the same analysis is valid for an upstream propagating inbound mode. Note that in the case considered, a is negative. By introducing the inner variable

$$x = \Delta S \varepsilon^{-2/3} G(S_0)^{-2/3} a^{1/3},$$

(4.27) becomes

$$N'' + 2i\sqrt{x}N' + \frac{iN}{2\sqrt{x}} = O(\varepsilon^{1/3}),$$

with leading order solution

$$N = (AAi(-x) + BBi(-x)) \exp\left\{-\frac{2i}{3}x^{3/2}\right\}.$$

Using asymptotic expansions of Airy function for large $|x|$ (see Abramowitz & Stegun, 1964, pp448–449), N has the large- x behaviour

$$\begin{aligned} N &\sim \frac{e^{i\pi/4}}{2\sqrt{\pi}x^{1/4}} \left[(A - iB) \exp\left\{-\frac{4i}{3}x^{3/2}\right\} - i(A + iB) \right] && \text{as } x \rightarrow \infty, \\ N &\sim \frac{1}{2\sqrt{\pi}|x|^{1/4}} \left[A + 2B \exp\left\{\frac{4}{3}|x|^{3/2}\right\} \right] && \text{as } x \rightarrow -\infty. \end{aligned}$$

The outer solution to (4.18) about the singular point S_0 is

$$N = \begin{cases} \frac{N_0}{(a\Delta S)^{1/4}} & \text{for } S < S_0 \\ \frac{TN_0 e^{i\pi/4}}{|a\Delta S|^{1/4}} & \text{for } S > S_0 \end{cases}$$

Expanding in terms of the inner variable x and matching with the inner solution gives $B = 0$ and $T = 1$. However, there is still an unmatched term as $x \rightarrow \infty$. This term is

$$\frac{Ae^{i\pi/4}}{2\sqrt{\pi}x^{1/4}} \exp\left\{-\frac{4i}{3}x^{3/2}\right\} \sim \frac{iN_0}{\sqrt{F(S)}} \exp\left\{\frac{2i}{\varepsilon} \int_{S_0}^S \frac{F(S')}{G(S')} dS'\right\}.$$

The inbound downstream propagating mode has $k = (F(S) - 1)/G(S)$. The corresponding upstream propagating mode would have $\tilde{k} = (-F(S) - 1)/G = k - 2F(S)/G(S)$. Hence, the upstream propagating mode from the singular point would have the form

$$\frac{RN_0}{\sqrt{F(S)}} \exp\left\{-\frac{i}{\varepsilon} \int_{S_0}^S \tilde{k}(S') dS'\right\} = \frac{N_0}{\sqrt{F(S)}} \exp\left\{-\frac{i}{\varepsilon} \int_{S_0}^S k(S') dS'\right\} \times R \exp\left\{\frac{2i}{\varepsilon} \int_{S_0}^S \frac{F(S')}{G(S')} dS'\right\}$$

This is exactly the solution needed to match with the extra term in the inner solution, provided $R = i$.

The inbound mode therefore gives rise to a reflected outbound propagating mode with reflection coefficient $R = i$, and an evanescent wave with transmission coefficient $T = 1$, exactly as if the duct were straight. This is perhaps surprising, since the inner region over which the mode transitions from cuton to cutoff occurs over an $O(\varepsilon^{-1/3})$ range of values of s , and hence the duct is significantly curved over this region, albeit with a constant curvature. It might therefore have been expected that the curvature would cause a significantly different cuton–cutoff behaviour.

An example of the results of this matching behaviour is shown in figure 4.17, as previously discussed. Note that only the outer solution for ϕ is plotted in figure 4.17, and therefore a singularity at the reflection point is shown. This singularity is not physical, and is smoothed over by the inner Airy function solution. A method for obtaining a uniformly valid solution, incorporating both the inner and outer solutions, is given by Ovenden (2005), motivated by investigating cuton–cutoff transition near the ends of the duct (especially for civilian aeroengines, where the ducts are very short). This was not investigated further here, as the reflection points for a curved duct tend to occur in the centre of the duct, and away from this reflection point the accuracy of the outer solution is unaffected by the singularity. In particular, the reflection and transmission coefficients derived above, which are arguably the most important result of this section, are correct without needing to resort to a uniformly valid solution.

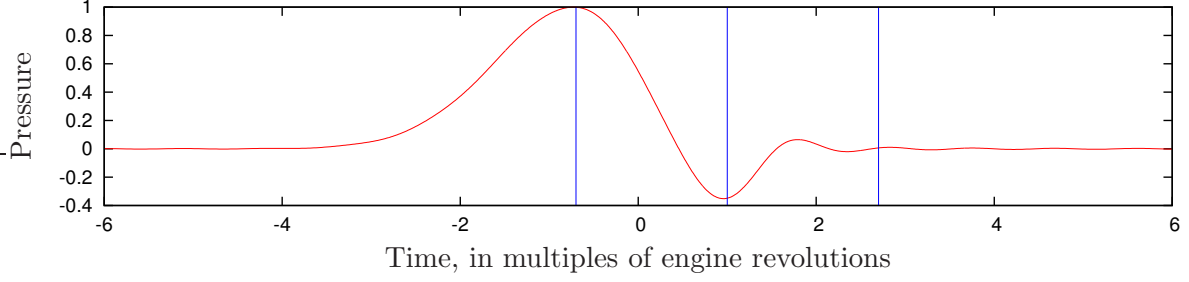


Figure 4.19: The pressure difference from steady state, introduced as a plane wave at the fan face. The vertical lines show the times of the snapshots in figures 4.20–4.22.

4.6 Time domain pulse propagation

All the derivation above has been at a single fixed frequency. By taking a periodic signal and decomposing it into its frequency components, each of these frequencies may be analysed as above, and then summed to give a time-domain solution for the propagation of that signal through a curved duct.

As an example, consider the pressure signal given in figure 4.19. This signal was suggested by J. Longley (2006, private communication) as being representative of the pressure at the engine fanface for a surge event. Note that the time axis has been given in terms of the number of engine revolutions, as this is how the surge signal is thought to scale. A surge event is a strong pressure disturbance that breaks the linearized small disturbance assumptions of the derivation above. The surge signal is used here to demonstrate the time-domain synthesis from the frequency-domain analysis above, as it is a less artificial signal than a purely hypothetical pulse.

The surge signal is initiated in a straight section of duct as a plane-wave that does not vary across the duct cross-section. This straight section of duct is then smoothly curved to fit onto the downstream end of the RAE 2129 intake, and the upstream end of the RAE 2129 intake is similarly connected to a section of duct that smoothly curves to become straight again. This is so that both ends of the duct are straight and the curvature varies smoothly along the duct. These extra duct sections are given in terms of their lateral offset $y(s)$. They are required to satisfy $y(0) = y'(0) = 0$ to fit smoothly onto the RAE 2129 intake, and $y''(0) = \kappa_0$ and $y''(d) = 0$ to smoothly vary the curvature from κ_0 to zero over a distance d (see equation B.1). Here, $d = L/8$ is chosen, and the function used is

$$y(s) = \kappa_0 \left(\frac{1}{2}s^2 - \frac{1}{6d}s^3 \right). \quad (4.28)$$

The propagation of a surge pulse through this modified RAE 2129 intake, with a nondimensionalized engine blade-tip speed of unity, is shown in figures 4.20–4.22. These figures plot the pressure difference from steady state. As shown in figure 4.21, the curvature and narrowing of the intake cause a peak pressure on the intake wall of 1.6 times the peak pressure at the fan face. This peak pressure is highly localized on the inside of the bend closest to the intake lip. The peak underpressure also occurs at the same position, as shown in figure 4.22, and reaches -0.6 , while the peak underpressure at the fan face was only -0.4 .

4.7 Raytracing

Consider the Helmholtz equation

$$\nabla^2 \psi + \alpha(\mathbf{x})^2 \psi = 0.$$

If α is large, say $\alpha = O(1/\delta)$ for $\delta \ll 1$, then the variation in α is small on the length scale of a wavelength. This motivates the raytracing ansatz (a special case of Multiple Scales), introducing a *slow vector* $\mathbf{X} = \mathbf{x}$ and a *fast scalar* $\theta(\mathbf{x})$ with $\nabla\theta = \mathbf{S}(\mathbf{X})/\delta$, for some function $\mathbf{S}(\mathbf{x})$ to be specified below. Then, with ∇ denoting differentiation with respect to \mathbf{X} , the Helmholtz equation becomes

$$\frac{1}{\delta^2} \|\mathbf{S}\|^2 \frac{\partial^2 \psi}{\partial \theta^2} + \frac{2}{\delta} \mathbf{S} \cdot \nabla \frac{\partial \psi}{\partial \theta} + \frac{1}{\delta} (\nabla \cdot \mathbf{S}) \frac{\partial \psi}{\partial \theta} + \nabla^2 \psi + \alpha^2 \psi = 0.$$

As for a standard multiple scales analysis, the wavefunction ψ is expanded in powers of δ as $\psi = \psi_0 + \delta\psi_1 + \dots$. Then the leading order equation becomes

$$\|\mathbf{S}\|^2 \frac{\partial^2 \psi_0}{\partial \theta^2} + \delta^2 \alpha^2 \psi_0 = 0,$$

suggesting the choice $\|\mathbf{S}\|^2 = \delta^2 \alpha^2$, so that $\|\nabla\theta\|^2 = \alpha^2$, and $\psi_0 = A_0 \exp\{-i\theta\}$. The fast scalar θ is now seen to represent the phase of a wave, with amplitude A_0 . A path everywhere orthogonal to planes of constant θ (i.e. in the direction $\nabla\theta$) is called a *ray*. The amplitude is given by the avoidance of a secular term in the first-order equation. The order $1/\delta$ equation is

$$\|\mathbf{S}\|^2 \frac{\partial^2 \psi_1}{\partial \theta^2} + \delta^2 \alpha^2 \psi_1 = \frac{i}{A_0} \nabla \cdot (\mathbf{S} A_0^2) e^{-i\theta}.$$

The term on the right hand side would resonate and lead to a secular solution, unless the secularity condition $\nabla \cdot (\mathbf{S} A_0^2) = 0$ is satisfied. This represents conservation of flux along a ray tube. The evolution of the direction of the ray is given by taking the gradient of $\|\nabla\theta\|^2 = \alpha^2$, yielding

$$\left(\frac{\nabla\theta}{\|\nabla\theta\|} \cdot \nabla \right) \nabla\theta = \nabla\alpha. \quad (4.29)$$

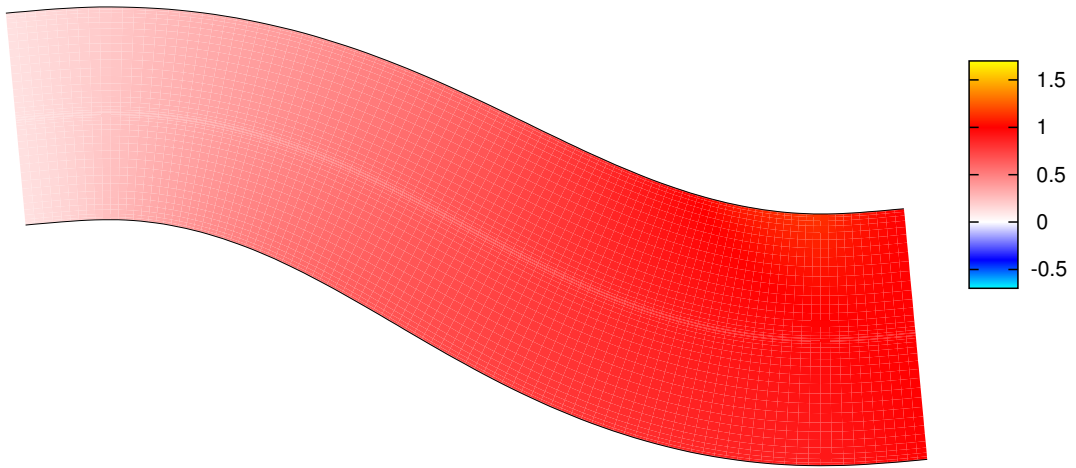


Figure 4.20: The pressure difference from steady state at time $t = -0.7$.

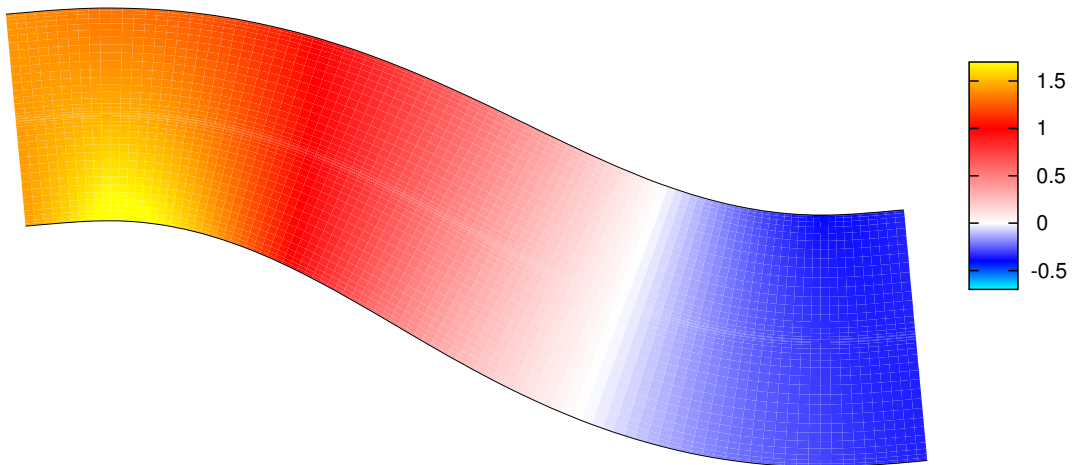


Figure 4.21: The pressure difference from steady state at time $t = 1.0$.

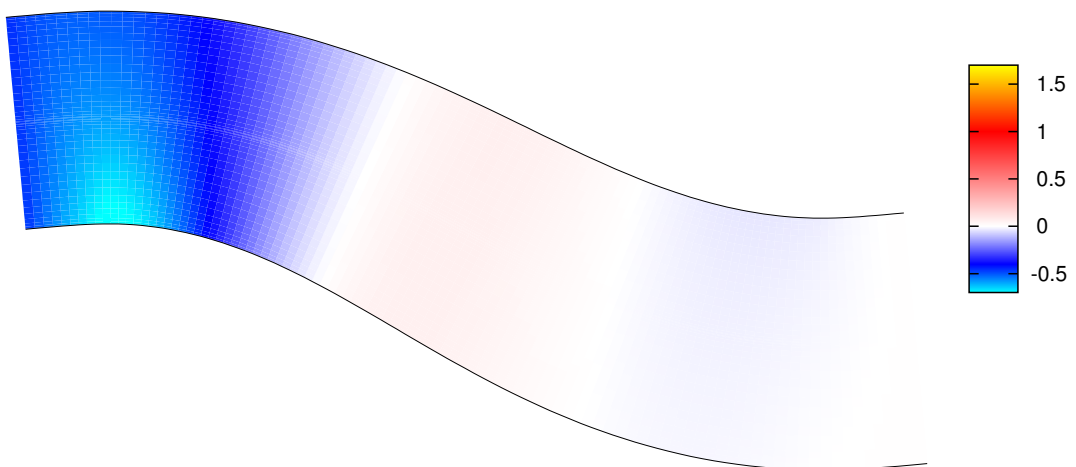


Figure 4.22: The pressure difference from steady state at time $t = 2.7$.

This enables the rays to be traced.

Consider the boundary condition on ψ

$$\frac{\partial\psi}{\partial n} + f(\mathbf{x})\psi = 0, \quad (4.30)$$

where $\partial/\partial n$ denotes the normal derivative at the boundary. Allowing for an inbound ray $A_0^{(1)}e^{-i\theta_1} + O(\delta)$ and an outbound ray $A_0^{(2)}e^{-i\theta_2} + O(\delta)$, this condition becomes

$$-\frac{i}{\delta} \left[A_0^{(1)} \mathbf{n} \cdot \mathbf{S}_1 e^{-i\theta_1} + A_0^{(2)} \mathbf{n} \cdot \mathbf{S}_2 e^{-i\theta_2} \right] + O(1) = 0.$$

For this to hold on the fast lengthscale implies that $\theta_2 - \theta_1$ is constant on the boundary, and without loss of generality it is taken that $\theta_1 = \theta_2$, since this just represents a phase change in $A_0^{(2)}$. Hence, $\nabla\theta_1$ and $\nabla\theta_2$ can only differ in their component perpendicular to the boundary. Since both have magnitude α , $\mathbf{n} \cdot \nabla\theta_1 = \pm \mathbf{n} \cdot \nabla\theta_2$. But if the positive sign were taken, the leading order boundary condition would imply $A_0^{(1)} = -A_0^{(2)}$, and the raytracing equation would enforce $\theta_1 = \theta_2$ everywhere; hence, the two solutions would annihilate. Therefore $\mathbf{n} \cdot \nabla\theta_1 = -\mathbf{n} \cdot \nabla\theta_2$ and $A_0^{(1)} = A_0^{(2)}$; that is, the boundary produces normal reflection (to leading order).

4.7.1 Application of raytracing to curved ducts

An application of the above is to trace the modal shape of the duct modes in a hard-wall curved duct. Note that what follows is two-dimensional raytracing, and is not tracing the real acoustic rays in three dimensions down the duct. Equation (4.7) may be rearranged to give

$$\begin{aligned} \frac{1}{r} \frac{\partial}{\partial r} \left(r \frac{\partial A}{\partial r} \right) + \frac{1}{r^2} \frac{\partial^2 A}{\partial \theta^2} - \frac{\kappa}{h_s} \left(1 + \frac{U_0^2}{C_0^2} \right) \left[\frac{\partial A}{\partial r} \cos \theta - \frac{1}{r} \frac{\partial A}{\partial \theta} \sin \theta \right] \\ + \left[\frac{\omega^2}{C_0^2} - \frac{2\omega U_0 k}{h_s C_0^2} - \frac{k^2}{h_s^2} \left(1 - \frac{U_0^2}{C_0^2} \right) \right] A \\ = \frac{i\varepsilon}{h_s D_0 A} \left[h_s D_0 \mathcal{D} \left(\frac{A^2 \Lambda}{C_0^2} \right) + \frac{\partial}{\partial S} \left(\frac{D_0 k A^2}{h_s} \right) \right], \end{aligned}$$

and then, by making the substitution $\psi = \sqrt{h_s D_0} A$ (to eliminate the first-order derivatives),

$$\begin{aligned} \frac{1}{r} \frac{\partial}{\partial r} \left(r \frac{\partial \psi}{\partial r} \right) + \frac{1}{r^2} \frac{\partial^2 \psi}{\partial r^2} \\ + \left[\frac{\omega^2}{C_0^2} - \frac{2\omega U_0 k}{h_s C_0^2} - \frac{k^2}{h_s^2} \left(1 - \frac{U_0^2}{C_0^2} \right) + \frac{\kappa^2}{4h_s^2} \left(1 + 4 \frac{U_0^2}{C_0^2} + (2\gamma - 3) \frac{U_0^4}{C_0^4} \right) \right] \psi \\ = \frac{i\varepsilon}{\psi} \left[h_s D_0 \mathcal{D} \left(\frac{\psi^2 \Lambda}{h_s D_0 C_0^2} \right) + \frac{\partial}{\partial S} \left(\frac{k \psi^2}{h_s^2} \right) \right]. \quad (4.31) \end{aligned}$$

This is now in the form of a raytracing problem, with parameter

$$\alpha^2 = \frac{\omega^2}{C_0^2} - \frac{2\omega U_0 k}{h_s C_0^2} - \frac{k^2}{h_s^2} \left(1 - \frac{U_0^2}{C_0^2} \right) + \frac{\kappa^2}{4h_s^2} \left(1 + 4 \frac{U_0^2}{C_0^2} + (2\gamma - 3) \frac{U_0^4}{C_0^4} \right),$$

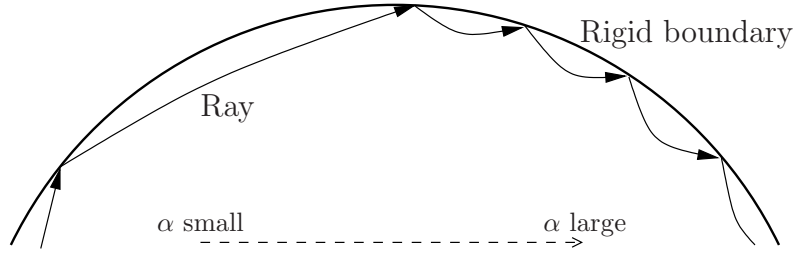


Figure 4.23: Schematic of the rays for a whispering-gallery mode; the rays are reflected with incidence angle equal to reflection angle, and are then refracted by the spatially nonuniform effective sound speed $1/\alpha$. In this case, α increases from left to right, although this is not always the case.

and with the raytracing boundary condition given by (4.30) with

$$f = \frac{\kappa \cos \theta}{2h_s} \left(1 + \frac{U_0^2}{C_0^2} \right).$$

For the raytracing asymptotics to be valid in this case, α needs to be large. This is achieved by requiring both ω and k to be large, in the sense that $k = \mu\omega$ with μ fixed, and letting $\omega \rightarrow \infty$. This leads to

$$\alpha^2 = \left[\frac{1}{C_0^2} - \frac{2\mu U_0}{h_s C_0^2} - \frac{\mu^2}{h_s^2} \left(1 - \frac{U_0^2}{C_0^2} \right) \right] \omega^2 + O(1). \quad (4.32)$$

The small parameter of the raytracing derivation is $\delta = 1/\omega$. Note that the term involving κ^2 in α^2 is neglected. Similarly, the term involving κ in the boundary condition is ignored, since the raytracing derivation above shows that the function f in the boundary condition should be neglected to leading order. However, the curvature is still incorporated, as both the mean flow (U_0 , C_0 , and D_0) and the derivative factor h_s have a strong dependence on the curvature.

Note that α^2 is a function of position only through h_s , which is only a function of $x = r \cos \theta$, the transverse position towards the inside or outside of the curve of the duct. Theoretical rays may be thought of bouncing around inside the cross-section of the duct, being reflected normally by the boundary, subject to a variable wave speed $1/\alpha$ that varies horizontally from the inside to the outside of the bend, but not vertically (as shown in figure 4.23). Figure 4.24 gives some examples of how α^2 varies with transverse position across the duct. The values of μ used for this are for the upstream propagating fundamental mode, a typical cuton–cutoff transition, and the downstream propagating fundamental mode. The fundamental modes contain regions where α^2 goes from being positive to being negative, and hence trap the fundamental modes in one side of the duct. This is examined in detail in the next section.

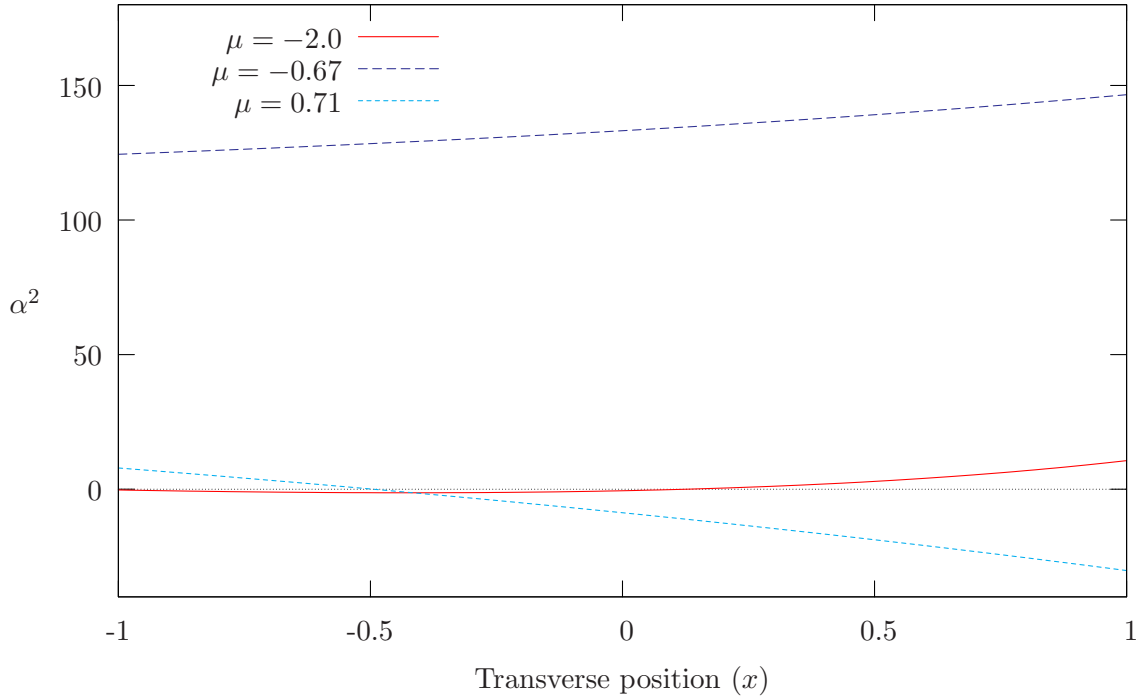


Figure 4.24: Variation in the raytracing parameter α^2 across a cylindrical duct, with $U_\infty = 0.5$, $\kappa = 0.1$, and $\omega = 10$.

4.7.2 Localization of fundamental modes

The plane-wave fundamental modes for a straight duct are uniform across the duct cross-section. For a curved duct, some fundamental modes are shown in figures 4.9(c), 4.10(c), and 4.11(e,f). As mentioned in §4.4.1, for these parameters, the upstream-propagating modes are located on the inside of the bend, while the downstream-propagating modes are localized on the outside. However, this is not always the case: figure 4.25 shows that, for $\kappa = 0.2$, $U_\infty = 0.5$, and $\omega = 31$, there are two upstream-propagating fundamental modes, one localized on the inside of the bend and one on the outside, with the downstream-propagating mode still localized on the outside. The wavenumbers for these modes are shown in figure 4.26, together with a left-right weighting

$$W_x = \frac{\int_0^{2\pi} \int_{a_1}^{a_2} r \cos(\theta) |A_0(r, \theta)|^2 r dr d\theta}{\int_0^{2\pi} \int_{a_1}^{a_2} |A_0(r, \theta)|^2 r dr d\theta}.$$

Modes which are highly localized on the left/right of the duct (i.e. on the outside/inside of the bend) have a value of W_x close to $-1/+1$ respectively. The presence of a few upstream modes localized on the outside is clear in figure 4.26. The question is, therefore, what parameters influence the localization of fundamental modes?

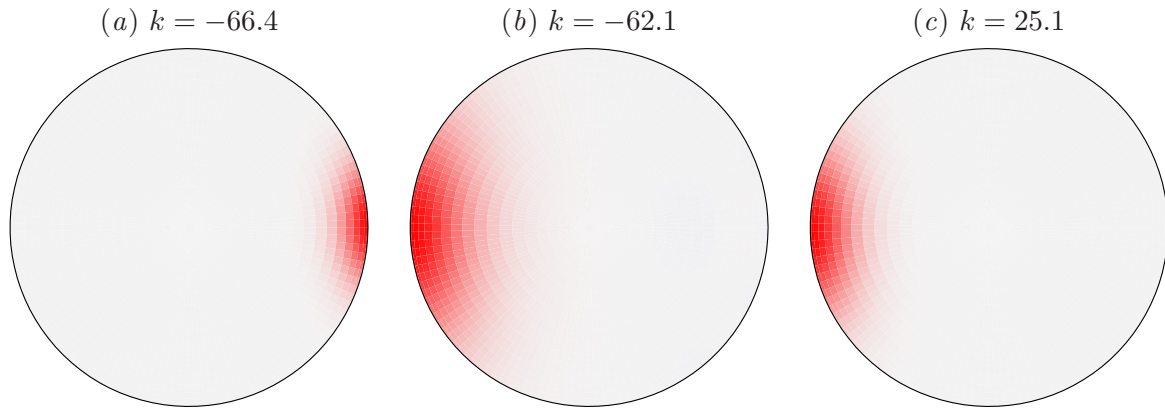


Figure 4.25: Curved-duct equivalents of the plane-wave mode, for $\kappa = 0.2$, $U_\infty = 0.5$, and $\omega = 31$. The inside of the bend is on the right. (a) and (b) are upstream-propagating modes, while (c) is a downstream-propagating mode.

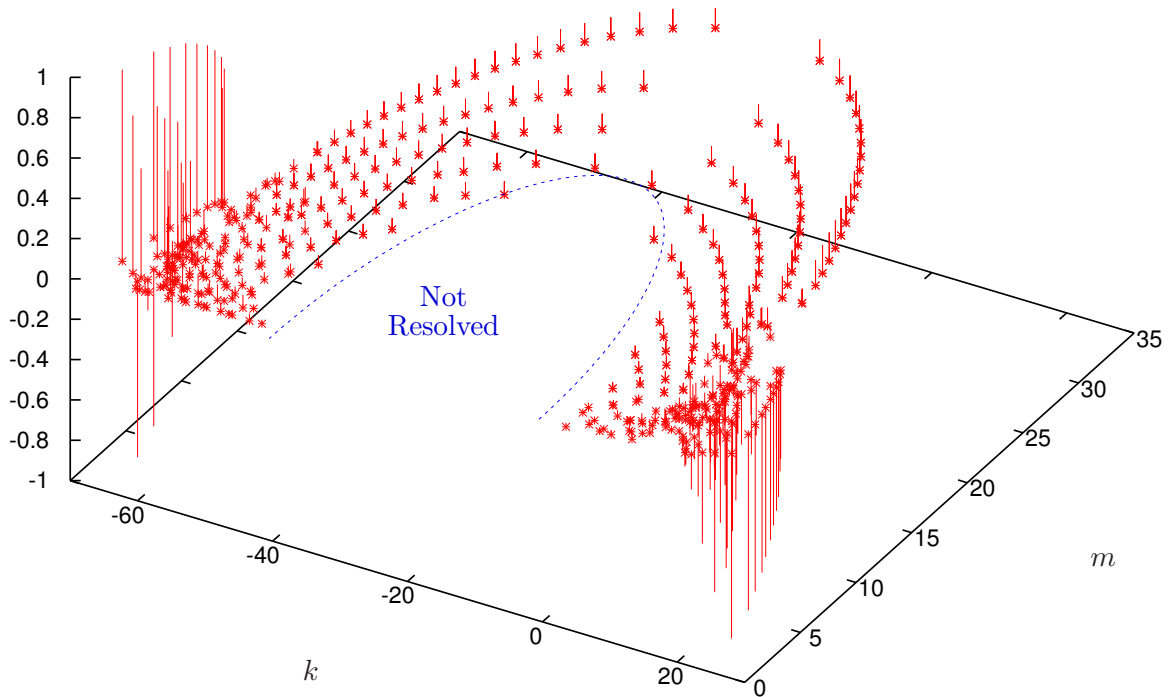


Figure 4.26: The real wavenumbers k for propagating modes against their approximate azimuthal order m , for $\kappa = 0.2$, $U_\infty = 0.5$, and $\omega = 31$. The vertical axis plots W_x , with modes localized on the inside and outside have stalks extending upwards and downwards respectively. Only numerically resolved modes are shown ($n_r = 23$, $n_\theta = 131$); the dashed curve denotes the unresolved region.

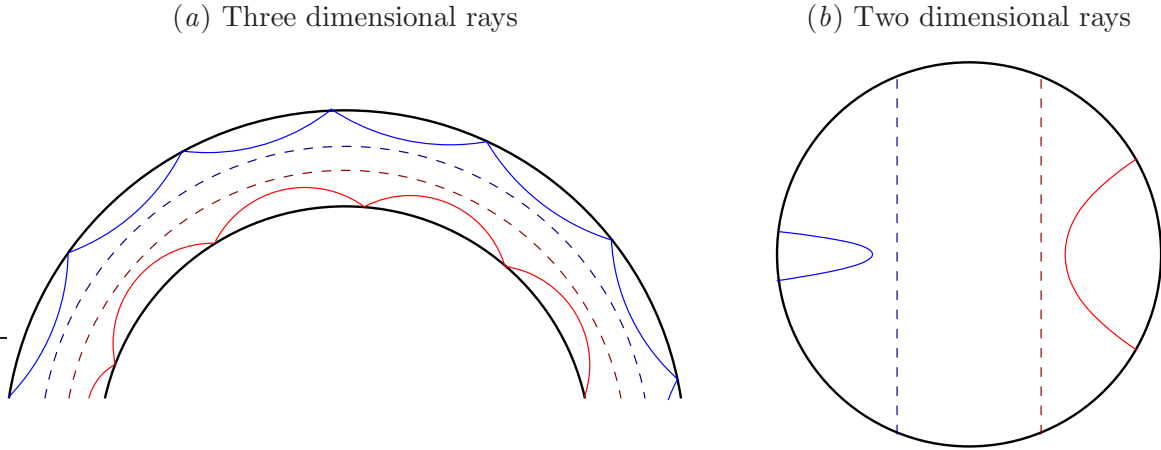


Figure 4.27: Schematic of localized fundamental rays. The dashed lines are where $\alpha^2 = 0$. (a) shows the three-dimensional rays, and (b) shows the two-dimensional representation derived in §4.7.1.

In three dimensions, the fundamental modes may be thought of travelling nearly axially down the duct, reflecting occasionally from the duct boundary. In order to do this, the flow and the geometry must be such that a ray, having just reflected from the boundary, is driven back towards the boundary, as shown in figure 4.27(a). Figure 4.27(b) shows the corresponding two-dimensional rays in the duct cross-section, as derived in §4.7.1. The dashed lines are where α^2 becomes negative, as seen in figure 4.24 for the $\mu = 0.71$ and $\mu = -2.0$ modes, and the rays are restricted to regions where α^2 is positive.

A ray travelling purely axially at the local speed of sound along the duct at a fixed horizontal offset x from the duct centreline would give the raytracing parameter $\mu_{\pm}(x) = h_s/(U_0 \pm C_0)$, with $+$ for downstream and $-$ for upstream. Substituting $\mu_{\pm}(x)$ into (4.32) shows that $\alpha^2 = 0$ at this x position, since such a ray is travelling completely in the axial direction, and therefore has no motion in the duct cross-section. Here, we are concerned with modes localized on the inside or outside of the bend, and so (normalizing such that the duct radius $a_2 = 1$), we are concerned only with $\mu_{\pm}(x)$ at $x = 1$ (for the inside of the bend) and $x = -1$ (for the outside of the bend). Figure 4.28 shows the variation of α^2 across the duct for the four cases in which μ takes one of the values $\mu_+(\pm 1)$, $\mu_-(\pm 1)$. Figure 4.28(b) corresponds to figure 4.10, while figure 4.28(d) corresponds to figure 4.25. By perturbing the value of μ slightly from the values $\mu_{\pm}(\pm 1)$, it is possible that a small pocket of positive α^2 might be created close to the duct wall, and thus (provided the frequency is high enough) a localized mode on that boundary is possible. In order for a small perturbation to μ to lead to a localised mode on the boundary, $\alpha^2(x)$ must decrease away from that boundary. This is also the requirement that a ray having just reflected

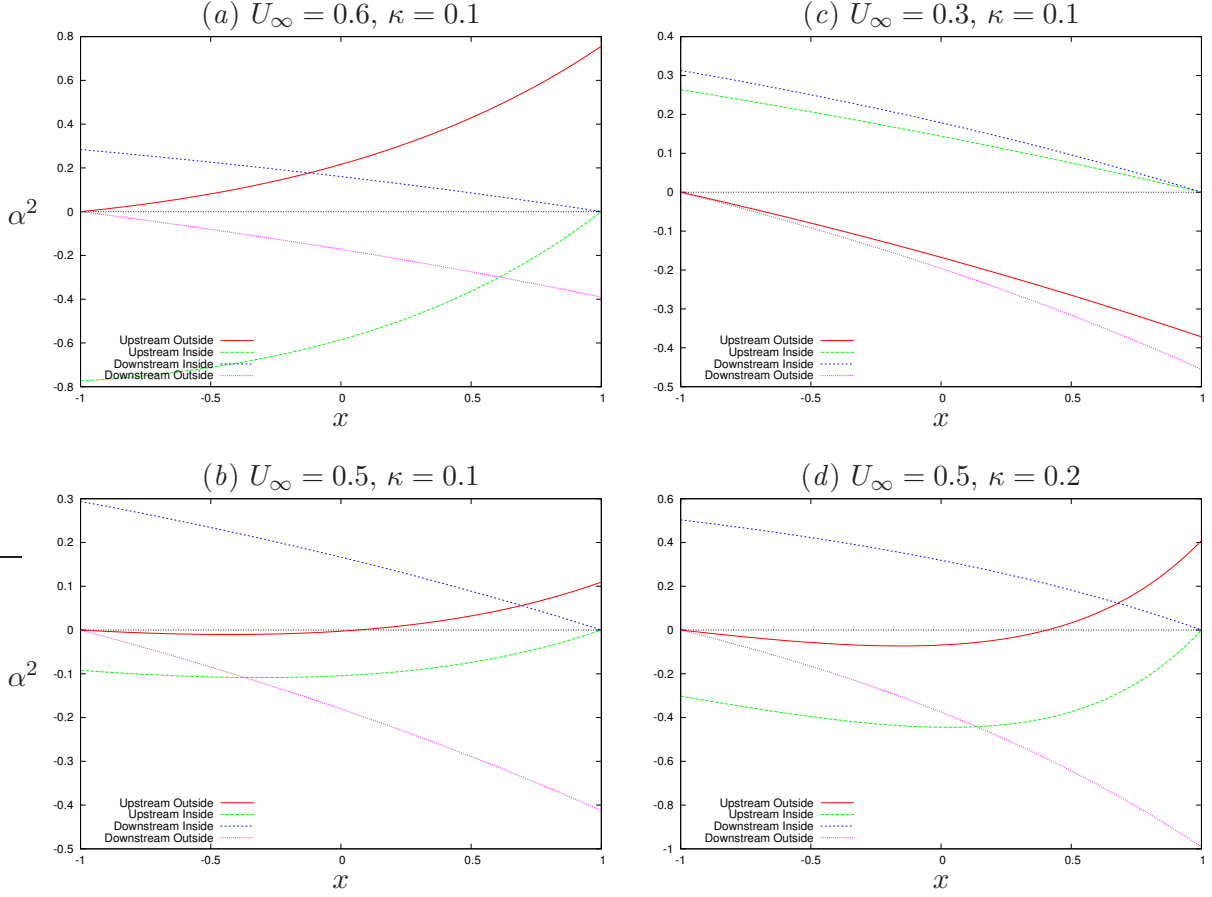


Figure 4.28: The variation in $\alpha^2(x)$, for potential upstream- and downstream-propagating modes localized on the inside and outside of the duct bend.

from the boundary is driven back towards the boundary (see equation 4.29). A change in the number of localized fundamental modes is therefore seen when the derivative of α^2 at $x = \pm 1$ changes sign. As an example, figure 4.28(a) demonstrates the possibility of a downstream fundamental mode localized on the outside of the bend and an upstream fundamental mode localized on the inside. Figure 4.28(c) demonstrates the possibility of both the downstream and upstream fundamental modes being localized on the outside of the bend. Figures 4.28(b,d) both demonstrate the possibility of a downstream fundamental mode localized on the outside, and two upstream fundamental modes, one localized on the inside and one on the outside. Note, however, that for the upstream-propagating outside mode on the outside wall in figure 4.28(b), the derivative of α^2 is very close to zero, implying that a very high frequency would be needed to discover such a mode; this is why such a mode was not seen in figure 4.10.

In order to investigate which values of U_∞ and κ give rise to which types of localization behaviour, we will now look for a change in derivative of α^2 at $x = \pm 1$. Differentiating (4.32)

with respect to x gives

$$\frac{\partial \alpha^2}{\partial x} = \frac{(\gamma - 1)\kappa U_0^2}{C_0^4 h_s} - \frac{2\kappa U_0 H(\gamma - 1)\mu(2h_s - \mu U_0)}{C_0^4 h_s^3} - \frac{2\kappa \mu^2}{h_s^3} \left(1 - \frac{U_0^2}{C_0^2}\right), \quad (4.33)$$

and substituting $\mu = \mu_{\pm}(x) = h_s/(U_0 \pm C_0)$ gives

$$\frac{\partial \alpha^2}{\partial x} = \frac{\kappa}{h_s(U_0 \pm C_0)^2} \left[(\gamma - 1) \frac{U_0^2}{C_0^2} \mp 4 \frac{U_0}{C_0} - 2 \right]. \quad (4.34)$$

A sign change of $\partial \alpha^2 / \partial x$ for a ray propagating axially down the duct is therefore given by a zero of the square brackets in (4.34). After some algebraic manipulation, this gives

$$U_0^2 = H \left(1 \pm \sqrt{\frac{2}{\gamma + 1}} \right). \quad (4.35)$$

Note that the $+$ solution of this (corresponding to a downstream-propagating mode) is very close to $U_0^2 = 2H$, at which point the mean density becomes zero.

Equation 4.35 may be evaluated to give κ in terms of U_{∞} , or U_{∞} in terms of κ , for the critical parameters for which an upstream or downstream propagating mode ($-$ or $+$ in equation 4.35) may be localized on the inside or outside of a bend (evaluating equation 4.35 at $x = 1$ or $x = -1$). Unfortunately, since U_0 depends on both κ and U_{∞} and is calculated numerically, (4.35) must in general be solved numerically. However, as mentioned in §4.1.1, if the duct cross-sectional area is the same as far upstream then $U_{\dagger} = U_{\infty} + O(\kappa^2)$. Hence, if the cross-sectional area is the same as far upstream and κ is small, (4.35) gives

$$\kappa = \frac{1}{x} \left(1 - \frac{U_{\infty}}{\left[H \left(1 \pm \sqrt{\frac{2}{\gamma + 1}} \right) \right]^{1/2}} \right), \quad (4.36)$$

with x being either $+1$ or -1 for the inside or outside of the bend, and H given by (4.1).

Figure 4.29 plots the small-curvature asymptotics given by (4.36) and the numerically calculated solutions of (4.35), assuming the duct cross-sectional area is the same as far upstream. The numerically generated solutions stop around $U_{\infty} = 0.65$, since for these parameters the duct is choked; that is, there is no solution to (4.3) for U_{\dagger} that gives the required mass flow rate.

Interestingly, the boundaries between the different behaviours of the upstream fundamental mode intersect at $\kappa = 0$, as shown in figure 4.29. At this point, the small-curvature asymptotics give the exact answer (assuming the duct cross-sectional area is the same as far upstream), and rearranging (4.36) gives the upstream Mach number for which this occurs as

$$U_{\infty} = \frac{2}{\gamma - 1} \left(\sqrt{\frac{\gamma + 1}{2}} - 1 \right).$$

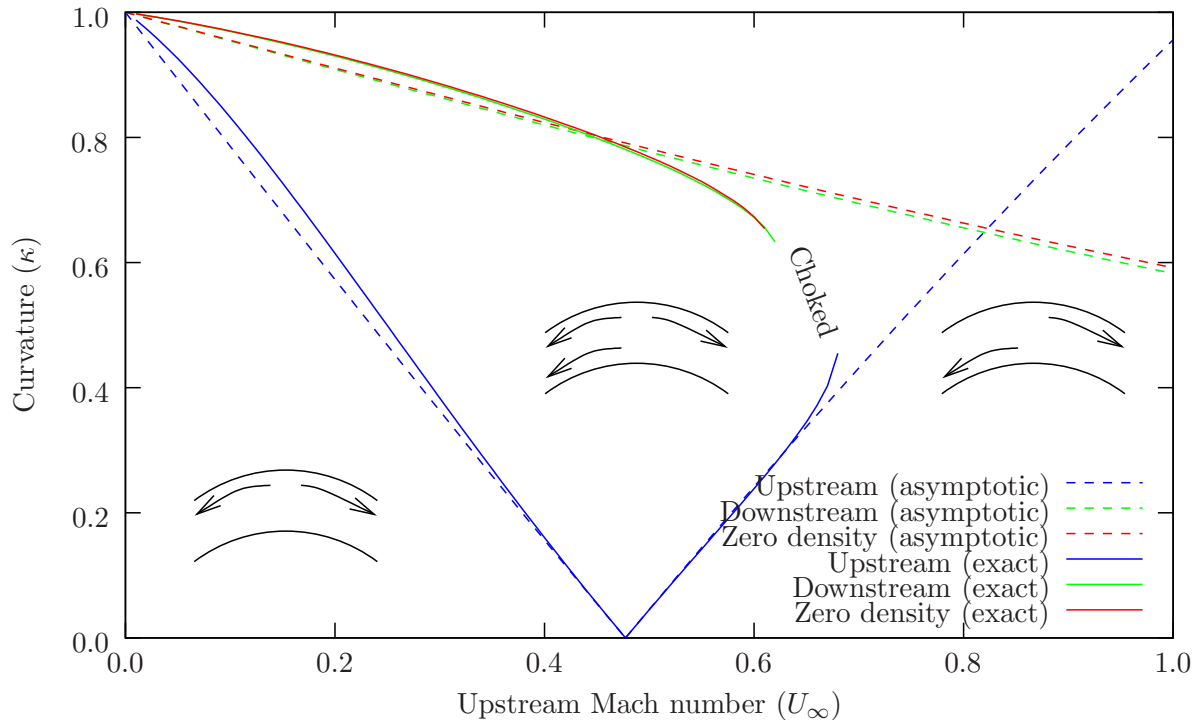


Figure 4.29: The localization of plane waves for varying upstream Mach number (U_∞) and curvature (κ). The sketches show whether modes localized on the inside and outside of the intake are possible, with downstream being the right-facing arrow. Exact results are from (4.35), and asymptotic results from (4.36). The zero-density lines are where $U_0^2 = 2H$ at $x = 1$.

For $\gamma = 1.4$, as used for all the examples presented here, this gives $U_\infty \approx 0.477$. This means that, for U_∞ close to this value (and $U_\infty = 0.5$ has been used for most examples presented here), for all but very small curvatures it is possible for both the upstream localized modes to be present. Indeed, this can be seen in Figure 4.25, where both inside- and outside-localised upstream modes are shown.

For low Mach number flows, the geometry keeps both upstream and downstream modes localized on the outside of the bend, in a similar way to the whispering gallery modes. This is exactly the result seen by Felix & Pagneux (2004). However, different behaviour is seen for larger Mach number flows. For large Mach number flows, the mean flow is fastest on the inside of the bend and slowest on the outside, giving a refraction effect which curves upstream-propagating rays towards the inside of the bend and downstream-propagating rays towards the outside. Hence, as the Mach number is increased from zero, the upstream mode first becomes present on the inner wall, and then disappears from the outside as the Mach number is increased further. Increasing the curvature makes this effect more pronounced.

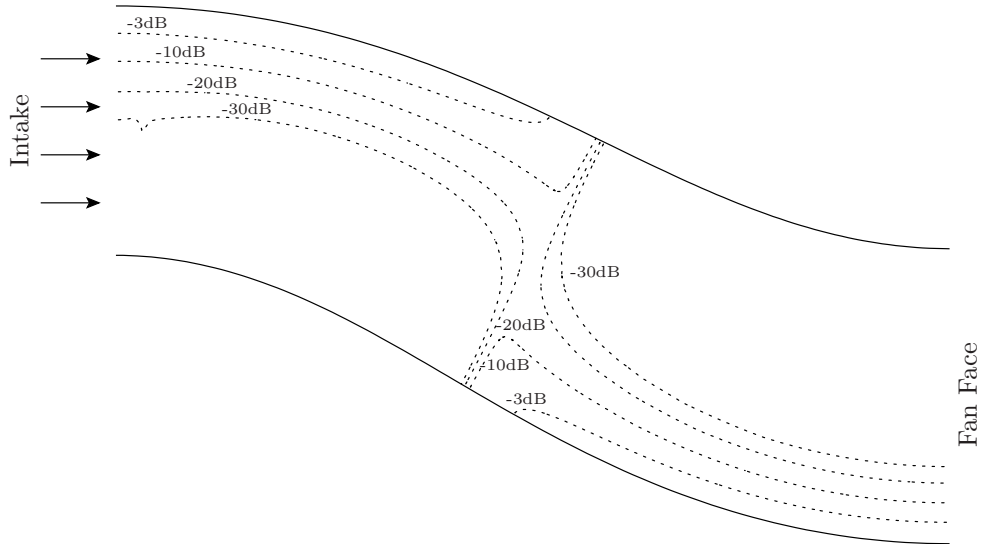


Figure 4.30: SPL for the plane-wave mode propagating from right to left, with a maximum fan-face wall pressure of 0dB. The axial wavenumber k for this mode is shown in figure 4.15 as the bottom of the three solid lines.

Figure 4.30 gives an example of an upstream-propagating plane wave in the RAE 2129 duct, in a similar manner to figure 4.16. In this case, the mode is always localized on the outside of the bends, and becomes a straight-duct plane wave at the midpoint of the intake where the curvature passes through zero. On the right (fan-end) of the duct only this localization is possible. On the left (intake-end) a mode localized on the inside of the bend is also possible, but is not excited.

While figure 4.29 is for a duct with the same cross-section as far upstream, (4.35) is still valid even if this is not the case. The small- κ asymptotics of (4.36) do require this restriction, however. It should also be emphasized that these results, being based on a raytracing approximation, are only valid provided ω is sufficiently large. Presumably, as the boundary between different behaviour is approached, the frequency necessary for these results to be valid will become large. This is why figures 4.9 and 4.10 show only an upstream mode localized on the inside of the bend; the frequency $\omega = 10$ is not high enough for the upstream outside localized mode to develop, even though the results of this section would suggest that an upstream outside localized mode would exist for these parameters.

4.7.3 Whispering gallery asymptotics

Keller & Rubinow (1960) used ray theory to construct a method for determining the eigenvalues of the Helmholtz equation in certain closed domains containing a uniform acoustic

medium. Their procedure was adapted by Babic & Buldyrev (1991) to domains with a varying sound speed. One key step in the Keller & Rubinow procedure is the determination of the shape of a caustic surface inside the domain, which provides an envelope for all possible ray directions. In the case of a circular domain with a uniform medium these caustics are simply concentric circles, whose radii are related to the allowed eigenvalues of the problem. However, for our equivalent variable sound speed it does not appear possible to determine the shape of this caustic in general, but analytical progress can be made for so-called *whispering-gallery* modes. Whispering gallery modes consist of rays running round the perimeter of the boundary, bouncing a large number of times at very short intervals. They are shown schematically in figure 4.23, and an example is shown in figure 4.11(c). We now make use of Babic & Buldyrev's procedure to obtain analytically-based approximations for the eigenvalues of our curved duct at high frequency and high azimuthal order, for the case of hard duct walls.

Babic & Buldyrev (1991, section 5.3, p114–121) determined an asymptotic expression for the eigenvalues of whispering-gallery modes in a circular domain with nonuniform sound speed. The modes are parametrized by two integers: $m \gg 1$, the azimuthal order, and $j = 1, 2, \dots$, the radial order. For the case of a curved duct, with the effective sound speed given by (4.32), their analysis gives

$$k_{jm} = \frac{\pi\mu}{I_1(a_2)} \left\{ 2m + I_2(a_2) \left[\frac{9m}{4I_1(a_2)} (j - 3/4)^2 \right]^{1/3} \right\}, \quad (4.37)$$

where

$$I_1(r) = \int_0^{2\pi} \alpha r d\theta, \quad I_2(r) = \int_0^{2\pi} \alpha^{1/3} \left(\frac{1}{r} + \frac{1}{2\alpha^2} \frac{\partial \alpha^2}{\partial r} \right)^{2/3} r d\theta, \quad \frac{\partial \alpha^2}{\partial r} = \cos \theta \frac{\partial \alpha^2}{\partial x},$$

with $\partial \alpha^2 / \partial x$ given in (4.33). This expression is valid for both annular and hollow ducts; because the rays are bouncing around the outer boundary, the inner boundary plays no part. Note that (4.37) gives $k_{jm}(\mu)$ implicitly as a function of $\mu \equiv k_{jm}/\omega$, and an iterative method was therefore needed to find the axial wavenumber k_{jm} for a specified value of ω . Figure 4.31 shows the results of the raytracing asymptotics against numerically calculated eigenvalues. A frequency of $\omega = 40$ was used for the comparison, so as to allow high azimuthal order modes to be cuton. The results are plotted against the azimuthal order m so the individual modes can be distinguished. The agreement is seen to be reasonable, especially for nearly-cutoff large- m modes, as is to be expected from using large m asymptotics.

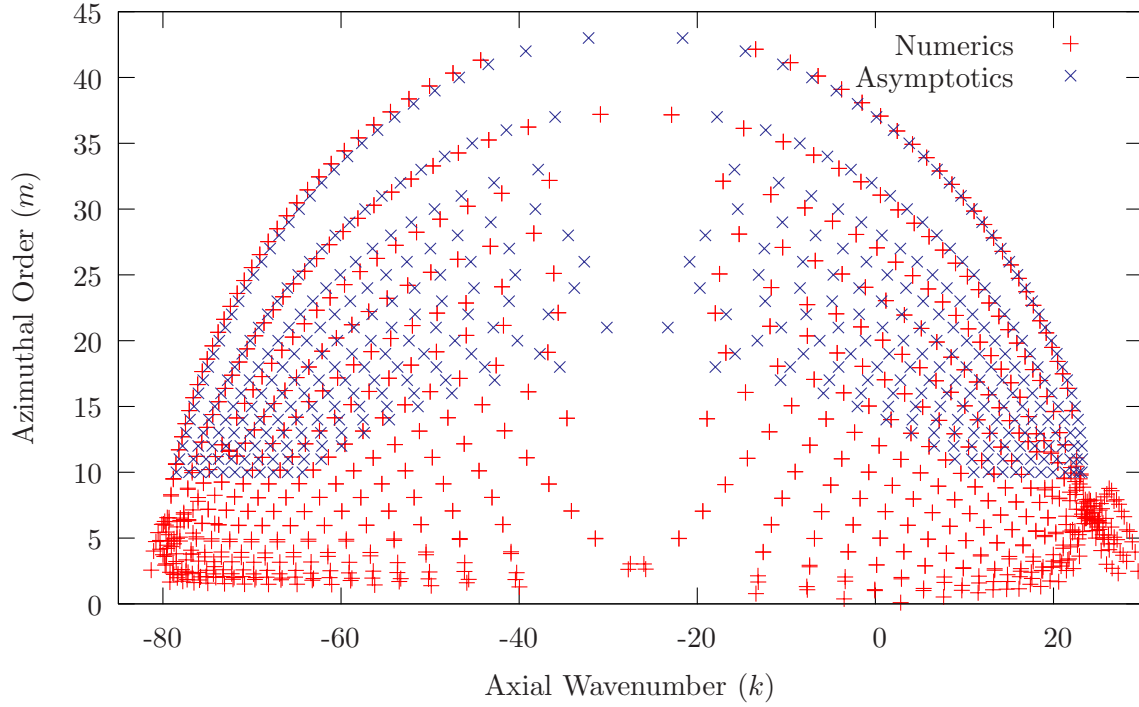


Figure 4.31: Comparison of raytracing asymptotics (\times) against numerical results ($+$). The azimuthal order for the numerics was estimated using a Fourier transform and averaging. $U_\infty = 0.5$, $\kappa = 0.1$, and $\omega = 40$.

4.8 Asymptotics

4.8.1 Smallish curvature limit for a hard-wall duct

Let κ satisfy $\varepsilon^{1/2} \ll \kappa \ll 1/a_2$, so that the leading order acoustic equation (4.9) may be expanded in powers of κ up to κ^2 without the slow variation parameter ε entering. Hence, the

leading order equation (4.9) for A_0 becomes

$$\begin{aligned}
& \frac{1}{r} \frac{\partial}{\partial r} \left(r \frac{\partial A_0}{\partial r} \right) + \frac{1}{r^2} \frac{\partial^2 A_0}{\partial \theta^2} + \left(\frac{\omega^2}{C_{\dagger}^2} - k^2(1 - M_{\dagger}^2) - \frac{2\omega M_{\dagger}^2}{U_{\dagger}} k \right) A_0 \\
& + \kappa \left[-(1 + M_{\dagger}^2) \left(\cos \theta \frac{\partial A_0}{\partial r} - \frac{1}{r} \sin \theta \frac{\partial A_0}{\partial \theta} \right) \right. \\
& \quad \left. + A_0 r \cos \theta \left(\frac{\omega^2}{C_{\dagger}^2} M_{\dagger}^2 (\gamma - 1) - k^2 [2 - 4M_{\dagger}^2 - M_{\dagger}^4 (\gamma - 1)] \right. \right. \\
& \quad \quad \left. \left. - \frac{2k\omega M_{\dagger}^2}{U_{\dagger}} [2 + M_{\dagger}^2 (\gamma - 1)] \right) \right] \\
& + \kappa^2 \left[-r \cos \theta [1 + 3M_{\dagger}^2 + M_{\dagger}^4 (\gamma - 1)] \left(\cos \theta \frac{\partial A_0}{\partial r} - \frac{1}{r} \sin \theta \frac{\partial A_0}{\partial \theta} \right) \right. \\
& \quad \left. + A_0 r^2 \cos^2 \theta \left(\frac{\omega^2}{C_{\dagger}^2} \left[\frac{3}{2} M_{\dagger}^2 (\gamma - 1) + M_{\dagger}^4 (\gamma - 1)^2 \right] \right. \right. \\
& \quad \quad \left. \left. - k^2 \left[3 - 10M_{\dagger}^2 - \frac{11}{2} M_{\dagger}^4 (\gamma - 1) - M_{\dagger}^6 (\gamma - 1)^2 \right] \right. \right. \\
& \quad \quad \left. \left. - \frac{2k\omega M_{\dagger}^2}{U_{\dagger}} \left[3 + \frac{7}{2} M_{\dagger}^2 (\gamma - 1) + M_{\dagger}^4 (\gamma - 1)^2 \right] \right) \right]
\end{aligned}$$

where $C_{\dagger}^2 = (\gamma - 1)(H - U_{\dagger}^2/2)$ and $M_{\dagger} = U_{\dagger}/C_{\dagger}$. Expanding k in powers of κ as $k = k_0 + \kappa k_1 + \kappa^2 k_2 + \dots$ gives

$$\begin{aligned}
& \frac{1}{r} \frac{\partial}{\partial r} \left(r \frac{\partial A_0}{\partial r} \right) + \frac{1}{r^2} \frac{\partial^2 A_0}{\partial \theta^2} + \alpha^2 A_0 \\
& = \kappa \left[(1 + M_{\dagger}^2) \left(\cos \theta \frac{\partial A_0}{\partial r} - \frac{1}{r} \sin \theta \frac{\partial A_0}{\partial \theta} \right) + 2A_0 \left(\frac{\omega M_{\dagger}^2}{U_{\dagger}} + (1 - M_{\dagger}^2) k_0 \right) k_1 + R_1 A_0 r \cos \theta \right] \\
& + \kappa^2 \left[A_0 \left((2k_2 k_0 + k_1^2) (1 - M_{\dagger}^2) + \frac{2\omega M_{\dagger}^2}{U_{\dagger}} k_2 \right) + R_2 r \cos \theta \left(\cos \theta \frac{\partial A_0}{\partial r} - \frac{1}{r} \sin \theta \frac{\partial A_0}{\partial \theta} \right) \right. \\
& \quad \left. + k_1 R_3 A_0 r \cos \theta + R_4 A_0 r^2 \cos^2 \theta \right]
\end{aligned}$$

where

$$\begin{aligned}
\alpha^2 &= \frac{\omega^2}{C_{\dagger}^2} - k_0^2 (1 - M_{\dagger}^2) - \frac{2k_0 \omega M_{\dagger}^2}{U_{\dagger}} \\
R_1 &= -\frac{\omega^2}{C_{\dagger}^2} M_{\dagger}^2 (\gamma - 1) + k_0^2 [2 - 4M_{\dagger}^2 - M_{\dagger}^4 (\gamma - 1)] + \frac{2k_0 \omega M_{\dagger}^2}{U_{\dagger}} [2 + M_{\dagger}^2 (\gamma - 1)] \\
R_2 &= 1 + 3M_{\dagger}^2 + M_{\dagger}^4 (\gamma - 1) \\
R_3 &= 2k_0 [2 - 4M_{\dagger}^2 - M_{\dagger}^4 (\gamma - 1)] + \frac{2\omega M_{\dagger}^2}{U_{\dagger}} [2 + M_{\dagger}^2 (\gamma - 1)] \\
R_4 &= -\frac{\omega^2}{C_{\dagger}^2} \left[\frac{3}{2} M_{\dagger}^2 (\gamma - 1) + M_{\dagger}^4 (\gamma - 1)^2 \right] + k_0^2 \left[3 - 10M_{\dagger}^2 - \frac{11}{2} M_{\dagger}^4 (\gamma - 1) - M_{\dagger}^6 (\gamma - 1)^2 \right] \\
& \quad + \frac{2k_0 \omega M_{\dagger}^2}{U_{\dagger}} \left[3 + \frac{7}{2} M_{\dagger}^2 (\gamma - 1) + M_{\dagger}^4 (\gamma - 1)^2 \right] \tag{4.38}
\end{aligned}$$

We now solve this for A_0 , by expanding $A_0 = A_0^{(0)} + \kappa A_0^{(1)} + \kappa^2 A_0^{(2)} + \dots$ and assuming $A_0^{(0)} = f(r)e^{-im\theta}$. The leading order equation, on multiplication by r , yields the Sturm–Liouville eigenvalue problem

$$(rf')' - \frac{m^2}{r}f = -\alpha^2 rf, \quad \alpha^2 = \frac{\omega^2}{C_\dagger^2} - k_0^2(1 - M_\dagger^2) - \frac{2k_0\omega M_\dagger}{C_\dagger},$$

with weight function $w(r) = r$. This is Bessel’s equation, and the solutions are expressible as Bessel’s functions $f_m(r) = aJ_m(\alpha r) + bY_m(\alpha r)$. The boundary conditions are $\partial f/\partial r = 0$ at $r = a_j$. This yields the dispersion relation for α , and hence for k_0 , for an annular duct as

$$J_m'(\alpha a_2)Y_m'(\alpha a_1) - J_m'(\alpha a_1)Y_m'(\alpha a_2) = 0,$$

and fixes the function f up to multiplication by a constant. In the cylindrical case, $b = 0$, and again f is determined up to multiplication by a constant. In either case, the constant is determined by requiring f to be normalized such that

$$\int_{a_1}^{a_2} f(r)^2 r \, dr = 1.$$

The dispersion relation yields an infinite discrete set of eigenvalues α_{mp} , $p = 1, 2, \dots$, with eigenfunctions $f_{mp}(r)$, exactly as for a straight duct.

Henceforth m and p are considered fixed, and the correction terms to the corresponding mode are considered for small but non-zero curvature. Consider the first order perturbation expanded as a Fourier series,

$$A_0^{(1)} = \sum_{\ell=-\infty}^{\infty} g_\ell(r)e^{-i\ell\theta}.$$

The first order equation is

$$\begin{aligned} \sum_{\ell=-\infty}^{\infty} \left[\frac{1}{r}(rg_\ell)' + \left(\alpha_{mp}^2 - \frac{\ell^2}{r^2} \right) g_\ell \right] e^{-i\ell\theta} \\ = \frac{1}{2r} \left[(1 + M_\dagger^2)(rf'_{mp}(r) - mf_{mp}(r)) + R_1 r^2 f_{mp}(r) \right] e^{-i(m+1)\theta} \\ + \frac{1}{2r} \left[(1 + M_\dagger^2)(rf'_{mp}(r) + mf_{mp}(r)) + R_1 r^2 f_{mp}(r) \right] e^{-i(m-1)\theta} \\ + 2 \left[\frac{\omega M_\dagger^2}{U_\dagger} + (1 - M_\dagger^2)k_0 \right] k_1 f_{mp}(r) e^{-im\theta}, \end{aligned} \quad (4.39)$$

where R_1 is given in (4.38). The final term on the right is exactly the mp -eigenfunction. This term would resonate with the differential equation on the left, and would cause the solution to be unable to satisfy both zero derivative boundary conditions. This may be seen formally by multiplying both sides of equation (4.39) by $f_{mp}(r)e^{im\theta}$ and integrating across the duct cross section; the left hand side would give zero, and the right hand side would give just the coefficient

of this resonant term. In order to eliminate this resonant term, it must be that $k_1 = 0$, so that there is no linear perturbation to the eigenvalue for small κ . This could have been expected, as a sign change in κ corresponds to reversing the bend from (say) left handed to right handed, and should have no effect on the propagation of waves down the duct. It would, however, effect the shape of the modes, and so g_ℓ are expected to be non-zero.

To find the g_ℓ corrections, the orthogonality of $e^{-im\theta}$ and the Bessel functions is used, as in the classic Sturm–Liouville theory. Define the coefficients

$$J_{mp\ell q}^{(n)} = \int_{a_1}^{a_2} f_{mp}(r) f_{\ell q}(r) r^n dr, \quad K_{mp\ell q}^{(n)} = \int_{a_1}^{a_2} f'_{mp}(r) f_{\ell q}(r) r^n dr.$$

Multiplying both sides of the first order equation (4.39) by $f_{\ell q}(r)e^{-i\ell\theta}$ and integrating across the duct gives

$$A_0^{(1)} = g_{m-1}(r)e^{-i(m-1)\theta} + g_{m+1}(r)e^{-i(m+1)\theta}, \quad g_\ell(r) = \sum_{q=1}^{\infty} C_{\ell q} f_{\ell q}(r),$$

where

$$C_{\ell q} = \frac{1}{\alpha_{mp}^2 - \alpha_{\ell q}^2} \left[\frac{1}{2} (1 + M_\dagger^2) (K_{mp\ell q}^{(1)} \mp m J_{mp\ell q}^{(0)}) + \frac{R_1}{2} J_{mp\ell q}^{(2)} \right] \quad \text{for } \ell = m \pm 1.$$

For the second order equation, again consider m and p fixed. Expanding $A_0^{(2)}$ in a similar way to $A_0^{(1)}$,

$$A_0^{(2)} = \sum_{\ell=-\infty}^{\infty} h_\ell(r) e^{-i\ell\theta},$$

gives

$$\begin{aligned} & \sum_{\ell=-\infty}^{\infty} \left[\frac{1}{r} (r h_\ell)' + \left(\alpha_{mp}^2 - \frac{\ell^2}{r^2} \right) h_\ell \right] e^{-i\ell\theta} \\ &= \left[(1 + M_\dagger^2) \left(g'_{m+1}(r) \cos \theta - \frac{i(m+1)}{r} g_{m+1}(r) \sin \theta \right) + R_1 g_{m+1}(r) r \cos \theta \right] e^{-i(m+1)\theta} \\ &+ \left[(1 + M_\dagger^2) \left(g'_{m-1}(r) \cos \theta - \frac{i(m-1)}{r} g_{m-1}(r) \sin \theta \right) + R_1 g_{m-1}(r) r \cos \theta \right] e^{-i(m-1)\theta} \\ &+ \left[2 \left(\frac{\omega M_\dagger^2}{U_\dagger} + (1 - M_\dagger^2) k_0 \right) k_2 f_{mp} + R_2 \left(f'_{mp}(r) \cos \theta - \frac{im}{r} f_{mp}(r) \sin \theta \right) r \cos \theta \right. \\ &\quad \left. + R_3 f_{mp}(r) r^2 \cos^2 \theta \right] e^{-im\theta}, \end{aligned}$$

where R_2 and R_3 are given in (4.38). Multiplying both sides by $f_{mp}(r)e^{-im\theta}$ and integrating

over the duct cross section gives the left hand side as zero, and the right hand side as

$$\begin{aligned} & \frac{1}{2} \sum_{q=1}^{\infty} \left[C_{(m+1)q} \left((1 + M_{\dagger}^2) \left[K_{(m+1)qmp}^{(1)} + (m+1) J_{(m+1)qmp}^{(0)} \right] + R_1 J_{(m+1)qmp}^{(2)} \right) \right. \\ & \quad \left. C_{(m-1)q} \left((1 + M_{\dagger}^2) \left[K_{(m-1)qmp}^{(1)} - (m-1) J_{(m-1)qmp}^{(0)} \right] + R_1 J_{(m-1)qmp}^{(2)} \right) \right] \\ & + \frac{1}{2} R_2 K_{mpmp}^{(2)} + \frac{1}{2} R_3 J_{mpmp}^{(3)} + 2k_2 \left(k_0 (1 - M_{\dagger}^2) + \frac{\omega M_{\dagger}^2}{U_{\dagger}} \right). \end{aligned}$$

Setting this to zero gives an expression for the quadratic eigenvalue correction k_2 .

The equations above giving the first non-zero correction terms $A_0^{(1)}$ and k_2 to the wavefunction and wavenumber are expressed as infinite sums of integrals of products of Bessel's functions of different orders and their derivatives. They were therefore not found helpful in further understanding waves in curved ducts.

4.8.2 Small curvature limit

Consider a duct in which the duct centreline is locally straight, so that $\kappa = \varepsilon \tilde{\kappa} = O(\varepsilon)$. In this case, the cross-duct equation (4.4) becomes

$$\begin{aligned} \frac{1}{r} \frac{\partial}{\partial r} \left(r \frac{\partial A}{\partial r} \right) + \frac{1}{r^2} \frac{\partial^2 A}{\partial \theta^2} + \alpha^2 A = \varepsilon \tilde{\kappa} & \left[(1 + M_0^2) \left(\cos \theta \frac{\partial A}{\partial r} - \frac{\sin \theta}{r} \frac{\partial A}{\partial \theta} \right) \right. \\ & \left. - Ar \cos \theta \left(\frac{\omega^2 M_0^2 (\gamma - 1)}{C_0^2} - k^2 (2 - 4M_0^2 - M_0^4 (\gamma - 1)) - \frac{2\omega k M_0^2}{U_0} (2 + M_0^2 (\gamma - 1)) \right) \right] \\ & + \frac{i\varepsilon}{D_0 A} \left[\mathcal{D} \left(\frac{A^2 \Lambda}{C_0^2} \right) + \frac{\partial}{\partial S} (k D_0 A^2) \right] + O(\varepsilon^2), \end{aligned}$$

where

$$\begin{aligned} \Lambda &= \omega - kU_0, & \alpha^2 &= \omega^2/C_0^2 - k^2(1 - M_0^2) - 2\omega M_0^2 k/U_0, \\ M_0 &= U_0/C_0, & \mathcal{D} &= U_0 \frac{\partial}{\partial S} + V_1 \frac{\partial}{\partial r} + \frac{W_1}{r} \frac{\partial}{\partial \theta}. \end{aligned}$$

The leading order solution is exactly the solution for a straight duct, expressible in terms of Bessel functions. After considerable algebra, the secularity condition becomes

$$\frac{d}{dS} (N^2 (F + I_1 + I_2)) + i\tilde{\kappa} N^2 (H_1 + H_2) = 0$$

where

$$\begin{aligned} F &= \int_0^{2\pi} \int_{a_1}^{a_2} D_0 A_0^2 \left(\frac{\omega U_0}{C_0^2} + k(1 - M_0^2) \right) r dr d\theta \\ I_i &= \int_0^{2\pi} \frac{r D_0^2 U_0 \Lambda A_0^2}{i\omega Z} \Big|_{r=a_i} d\theta \\ H_1 &= \int_0^{2\pi} \left[\frac{1}{2} (1 + M_0^2) D_0 A_0^2 r \right]_{a_1}^{a_2} \cos \theta d\theta \end{aligned}$$

$$H_2 = \int_0^{2\pi} \int_{a_1}^{a_2} D_0 A_0^2 r \cos \theta \left[\frac{\omega^2 M_0^2 (\gamma - 1)}{C_0^2} - k^2 (2 - 4M_0^2 - M_0^4 (\gamma - 1)) - \frac{2\omega k M_0^2}{U_0} (2 + M_0^2 (\gamma - 1)) \right] r dr d\theta$$

However, the leading order solution A_0 has angular dependence $\cos(m\theta)$ or $\sin(m\theta)$. Performing the θ integrals gives $H_1 = H_2 = 0$, so that the solution is exactly that of a straight, slowly varying duct. This result agrees with that of the smallish curvature analysis in §4.8.1, since it predicts the effects of curvature on wave propagation occur at order κ^2 . At order κ , the only effect of curvature is to alter the mode shape, rather than its propagation characteristics.

Chapter 5

Nonlinear two-dimensional surge propagation

For surge in an aeroengine intake, the time-domain signal shown in figure 4.19 is of large amplitude, typically peaking at three times the ambient pressure. In such situations, nonlinear effects become dominant, leading to steepening of wave fronts and shock formation. In order to begin investigating this, a two-dimensional inviscid compressible shock-capturing first-order-accurate Godunov numerical scheme was written. This was then applied to a two-dimensional version of the RAE 2129 intake. The advantage of this numerical scheme is that it is quick to compute and easily parallelizable, requiring about 12 CPU hours to give all the results presented in this chapter.

5.1 Numerical method

The numerical method used here was inspired by Igra *et al.* (2001), who used a second-order-accurate Godunov scheme to predict the behaviour of shocks around sharp corners with remarkable accuracy when compared with experimental results. The equations of motion of a compressible inviscid perfect gas in two dimensions, written in conservative form, are (Landau & Lifshitz,

1987, chapter 1)

$$\frac{\partial \rho}{\partial t} + \frac{\partial \rho u}{\partial x} + \frac{\partial \rho v}{\partial y} = 0 \quad (5.1a)$$

$$\frac{\partial \rho u}{\partial t} + \frac{\partial}{\partial x}(\rho u^2 + p) + \frac{\partial}{\partial y}(\rho uv) = 0 \quad (5.1b)$$

$$\frac{\partial \rho v}{\partial t} + \frac{\partial}{\partial x}(\rho uv) + \frac{\partial}{\partial y}(\rho v^2 + p) = 0 \quad (5.1c)$$

$$\begin{aligned} \frac{\partial}{\partial t} \left(\frac{1}{2} \rho (u^2 + v^2) + \rho \epsilon \right) + \frac{\partial}{\partial x} \left(u \left(\frac{1}{2} \rho (u^2 + v^2) + \rho \epsilon + p \right) \right) \\ + \frac{\partial}{\partial y} \left(v \left(\frac{1}{2} \rho (u^2 + v^2) + \rho \epsilon + p \right) \right) = 0, \end{aligned} \quad (5.1d)$$

where ρ is the density, (u, v) is the velocity, p is the pressure, and ϵ is the specific internal energy. Assuming a perfect gas,

$$\epsilon = c_V T = \frac{1}{\gamma - 1} \frac{p}{\rho},$$

where T is the temperature, c_V and c_P are the specific heats at constant volume and pressure respectively, and $\gamma = c_P/c_V$. The local speed of sound is given by $c = \gamma p/\rho$.

The computational domain is split up into a cartesian grid with spacing Δx , and the average velocity, pressure, and density within each grid square is recorded. The system is time-stepped by computing the fluxes of mass, momentum, and energy across each grid boundary, averaged over the timestep. This type of numerical method is known as a finite volume method, and guarantees that mass, momentum, and energy are all conserved; for example, any energy that is lost by one grid cell is gained by another. For the first-order-accurate Godunov method used here, at the beginning of each timestep the fluid within each grid cell is considered to be uniform in space, so that the pressure is equal to the average pressure everywhere within the grid cell, and so on. This situation is solved exactly for small times; at each grid cell boundary this involves solving the appropriate Riemann problem (see §5.1.1 below). These solutions are only valid for small times, for which the disturbance caused by one cell boundary does not interact with the other cell boundaries. Defining the Courant number $C = (c + |u|)\Delta t/\Delta x$, this requirement means that the timestep Δt must satisfy the Courant–Friedrichs–Lewy (CFL) stability criterion $C < 1$. In implementing this numerical scheme, the timestep was adapted to ensure a specified maximum Courant number was adhered to.

Once the Riemann problem has been solved for a cell boundary, the relevant fluxes across that boundary are calculated from the values of the fluid variable (u, v, p, ρ) that lie on the boundary for $t > 0$, using (5.1). For example, the flux of x -momentum across horizontal

boundaries for a cell centred at x, y gives

$$\begin{aligned} \rho(x, y, t + \Delta t)u(x, y, t + \Delta t) &= \rho(x, y, t)u(x, y, t) \\ &+ \left[\rho(x - \Delta x/2, y, t)u(x - \Delta x/2, y, t)^2 + p(x - \Delta x/2, y, t) \right. \\ &\left. - \rho(x + \Delta x/2, y, t)u(x + \Delta x/2, y, t)^2 - p(x + \Delta x/2, y, t) \right] \Delta t / \Delta x, \end{aligned}$$

where variables evaluated at (x, y) are the cell-averaged values, and variables evaluated at $(x \pm \Delta x/2, y)$ are the solutions of the Riemann problem between cells at (x, y) and $(x \pm \Delta x, y)$ evaluated along the interface between the cells. Due to the nature of the Riemann problem, these values remain constant on the boundary, and so the first-order-accurate Godunov method may be seen as taking flow variables piecewise-constant in space, and fluxes piecewise-constant in time. Note that this is the exact solution to the Riemann problem, and not a piecewise-constant-in-time approximation.

Rather than working out all the boundary fluxes in the x - and y -directions in one go and then updating the average values, here the x - and y -fluxes were calculated separately, the average values being updated after each set of flux calculations. This is known as Strang splitting (Strang, 1968). Let the operation at time t of evolving the system $S(t)$ forward a time Δt be $\mathcal{L}_{\Delta t}(t)$, so that $S(t + \Delta t) = \mathcal{L}_{\Delta t}(t)S(t)$. Denote by $\mathcal{L}_{\Delta t}^x(t)$ and $\mathcal{L}_{\Delta t}^y(t)$ the operations of evolving the system forward a time Δt using only fluxes in the x and y -direction respectively. Then the operation performed here is

$$\mathcal{L}_{2\Delta t}(t) = \mathcal{L}_{\Delta t}^y(t + \Delta t)\mathcal{L}_{\Delta t}^x(t + \Delta t)\mathcal{L}_{\Delta t}^x(t)\mathcal{L}_{\Delta t}^y(t).$$

The reason for using this Strang splitting is that, had the x - and y -flux calculations been second order accurate, this splitting would have guaranteed that the whole update was second order accurate, which would not be the case were all fluxes calculated first and then the average values updated. The decision to use Strang splitting was made before any code was written, to enable second order accuracy to be added relatively painlessly should it be needed; this splitting provides no extra benefit in the present case of a first-order-accurate Godunov scheme.

The method used by Igra *et al.* (2001) was second order accurate. This was accomplished by using a piecewise-linear approximation to the flow within each grid cell (subject to a monotonicity constraint that limited the gradients within each cell), rather than the piecewise-constant approximation of the Godunov scheme. Since Δx and Δt are linked by the CFL condition, it makes no sense to be second-order-accurate in space without being second-order-accuracy in time, and so the Riemann problem must be changed. Rather than solving the solution exactly for spatially uniform flows on either side of a grid boundary, the Generalized Riemann Problem

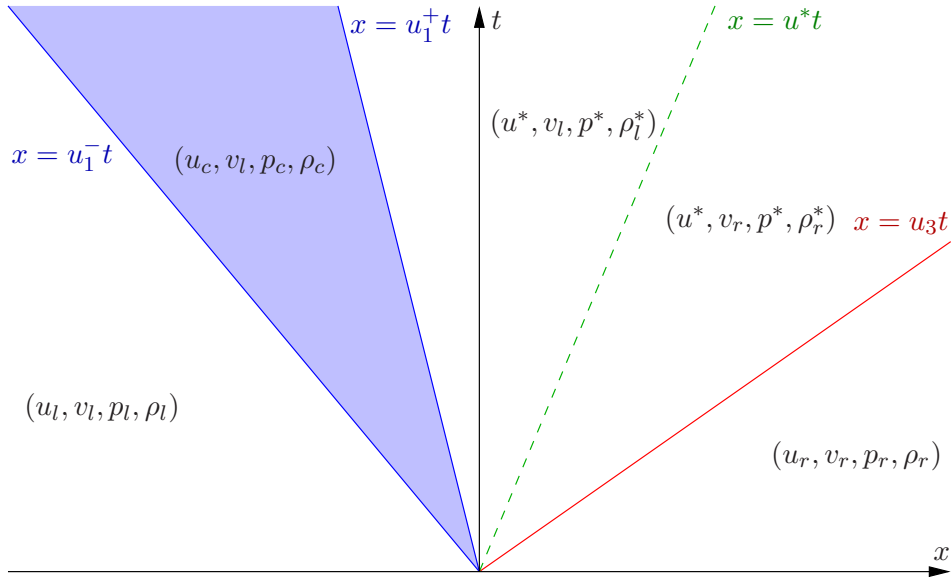


Figure 5.1: A schematic of the general solution to the Riemann problem. On the left is a centred rarefaction wave (CRW). The solid line on the right is a shock wave, while the dashed line is a contact discontinuity.

(GRP) is to solve the flow correct to $O(\Delta x^2 + \Delta t^2)$ for spatially linearly varying flows on either side of a grid boundary (Ben-Artzi & Falcovitz, 1984; Ben-Artzi *et al.*, 2006; Men'shov, 1990). However, as mentioned previously, here only the first-order-accurate Godunov scheme is used.

5.1.1 The Riemann problem

Suppose we have initial conditions that, at time $t = 0$, (u, v, p, ρ) are equal to the constants (u_r, v_r, p_r, ρ_r) for $x > 0$, and equal to the constants (u_l, v_l, p_l, ρ_l) for $x < 0$. The Riemann problem is to derive the solution to this initial condition for $t > 0$ that satisfies (5.1). This solution may, and usually will, be a weak solution, in that it may contain discontinuities. A weak solution to (5.1) would satisfy the integral over any volume of (5.1); it would therefore satisfy (5.1) everywhere that the derivatives are defined, although of course they would not be defined on any discontinuity.

The Riemann problem may be solved using characteristics (Ben-Artzi & Falcovitz, 2003; Landau & Lifshitz, 1987, chapters 9 & 10). The general solution is of the form shown in figure 5.1. The solution is constant in y , and in four distinct regions of the x, t plane. Of the three boundaries between the four constant regions, the central one is always a contact discontinuity, along which v and ρ may jump but through which u and p are continuous, and which moves with the fluid velocity. The left and right boundaries may be either shocks which

move at supersonic speed into the fluid ahead of them, as shown in figure 5.1 along $x = u_3 t$, or a region known as a centred rarefaction wave (CRW, also known as an expansion fan) shown between $x = u_1^- t$ and $x = u_1^+ t$ in figure 5.1, which move at the local speed of sound.

Let us now consider the left boundary of figure 5.1, going from (u_l, v_l, p_l, ρ_l) to $(u^*, v_l, p^*, \rho_l^*)$. The right boundary may be treated similarly. If $p^* > p_l$, this boundary is a shock moving with velocity u_1 , and u^* , ρ_l^* and u_1 are given in terms of p^* and the given initial conditions by

$$\begin{aligned} u_1 &= \frac{u_l \rho_l - u^* \rho_l^*}{\rho_l - \rho_l^*} & u^* &= u_l - c_l \frac{p^*/p_l - 1}{\gamma \sqrt{1 + \frac{\gamma + 1}{2\gamma}(p^*/p_l - 1)}} \\ \rho_l^* &= \rho_l \frac{(\gamma + 1)p^* + (\gamma - 1)p_l}{(\gamma - 1)p^* + (\gamma + 1)p_l}. \end{aligned} \quad (5.2a)$$

where $c_l = \gamma p_l / \rho_l$. Alternatively, if $p^* < p_l$, this boundary is a CRW in the region $u_1^- t < x < u_1^+ t$, and in terms of p^* and the given initial conditions,

$$\begin{aligned} u_1^- &= u_l - c_l & u^* &= u_l - 2c_l / (\gamma - 1) [(p^*/p_l)^{(\gamma-1)/2\gamma} - 1], \\ u_1^+ &= u^* - c^* & \rho^* &= \rho_l (p^*/p_l)^{1/\gamma}, \end{aligned} \quad (5.2b)$$

where $c^* = \gamma p^* / \rho^*$. Within such a CRW, the flow is given by

$$u_c = \frac{\gamma - 1}{\gamma + 1} u_l + \frac{2}{\gamma + 1} \left(c_l + \frac{x}{t} \right) \quad \rho_c = \rho_l \left(\frac{u_c - x/t}{c_l} \right)^{2/(\gamma-1)} \quad p_c = p_l \left(\frac{\rho_c}{\rho_l} \right)^\gamma.$$

The relationships (5.2) above together give $u^*(p^*; u_l, p_l, \rho_l)$; the similar equations for the right boundary may be obtained by changing the sign of the x -direction. The Riemann problem may now be phrased in the following way: given left initial conditions (u_l, v_l, p_l, ρ_l) and right initial conditions (u_r, v_r, p_r, ρ_r) , solve the left and right boundary regions to find the unique value of p^* which is consistent with both the left and right initial conditions. As suggested by Ben-Artzi & Falcovitz (2003), this was implemented numerically using a Newton–Raphson iteration. This procedure is shown schematically in figure 5.2, which shows the first guess for (u^*, p^*) made by the Newton–Raphson iteration with pressure p_{NR} . This procedure is then continued, starting from this value of p_{NR} and the two corresponding values of u^* , until the final solution is found to a given tolerance.

5.1.2 Boundary conditions

The above method gives the flux between two grid cells, both of which are completely filled with fluid. However, at the edge of the computational domain, or at an oblique boundary that cuts through a grid cell, alternative flux calculations are needed. Several sorts of boundary

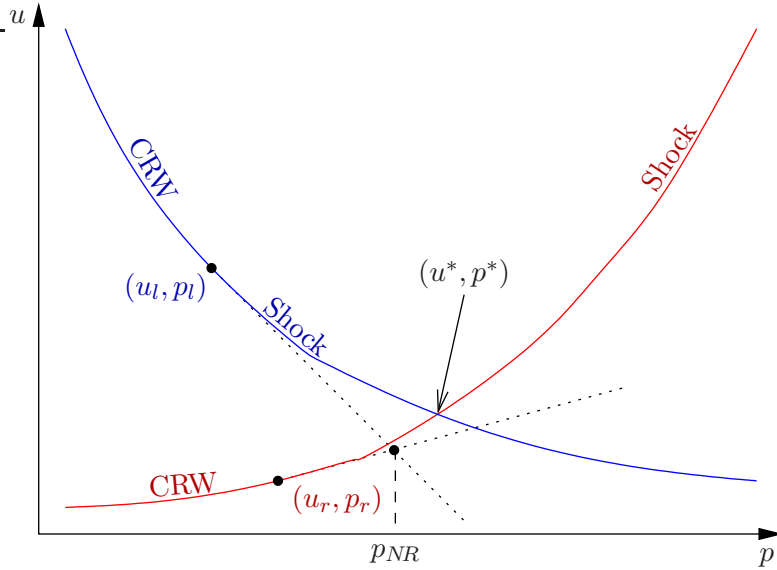


Figure 5.2: Schematic of the Newton–Raphson method of solving the Riemann problem. The first guess of the Newton–Raphson procedure is labelled p_{NR} .

conditions were implemented, all of which still consider a Riemann-like problem in order to give the correct upwinding (see §5.1.3). Oblique hard boundaries are considered last, with all other boundaries aligned along the edge of a grid cell.

Hard-wall boundaries

The condition at a hard-wall boundary along the edge of a grid cell is simply no flow through the boundary, so that $u = 0$ there, while p , ρ , and v are unconstrained. The flux through such a boundary is calculated by specifying $u^* = 0$ in (5.2) and solving for p^* ; this gives the values of the fluid variables on the boundary, from which the fluxes can be calculated, exactly as between two neighbouring grid cells.

Subsonic inflow boundaries

For any inflow or outflow boundary, we have a boundary between a real fluid in the computational domain for which we know (u, v, p, ρ) , and a notional fluid outside the computational domain. We can therefore solve a theoretical Riemann problem, specifying arbitrary jumps across characteristics that lie within the computation domain. For example, imagine in figure 5.1 that $x < 0$ is outside the computational domain and $x > 0$ is the contents of a grid cell. This represents a subsonic ($u_1 < 0$) inflow ($u^* > 0$) from the left, and we may therefore specify, as boundary conditions, the jump across $x = u_3 t$ and $x = u^* t$. We could also specify

the jump across the left-most characteristic, but doing so has no effect on the flux across the boundary, since the flux is calculated along $x = 0$, which in this case involves $(u^*, v_l, p^*, \rho_l^*)$, and is therefore independent of the jump across the left-most characteristic.

For a subsonic inflow boundary, the notional fluid outside the computational domain is given a specified stagnation pressure and temperature. This, in effect, means that we specify upstream (u_0, v_0, p_0, ρ_0) ; within the Riemann problem, we require that the values of the fluid parameters on the boundary $(u^*, p^*, v_l, \rho_l^*)$ be obtainable from (u_0, v_0, p_0, ρ_0) using isentropic Bernoulli,

$$u^* = \sqrt{u_0^2 + \frac{2c_0^2}{\gamma - 1} [1 - (p^*/p_0)^{1-1/\gamma}]} \quad \rho_l^* = \rho_0(p^*/p_0)^{1/\gamma}. \quad (5.3)$$

This is solved using a Newton–Raphson iteration, similar to the Newton–Raphson iteration used to solve the Riemann problem, but with (5.3) replacing either (5.2) or its equivalent in the other direction.

Note that this does not imply that the upstream fluid has parameters (u_0, v_0, p_0, ρ_0) ; it just means that the fluid upstream has the same stagnation pressure and temperature as (u_0, v_0, p_0, ρ_0) .

Subsonic outflow boundaries

At a subsonic outflow boundary, we have one degree of freedom to specify one jump across the only characteristic lying within the computational domain. This is used to specify the static pressure of the fluid outside the computational domain. That is, we specify $p^* = p_0$ in the Riemann problem for some given p_0 , with all the other variables taking the values necessary on the boundary to be consistent with the fluid inside the computational domain and the Riemann problem. This is simpler than the subsonic inflow, since no Newton–Raphson iteration is needed to find the values of the fluid at the boundary.

Supersonic boundaries

These are even more straightforward than their subsonic cases. For a supersonic inflow, we must specify all of the fluid parameters, and then these parameters are the values of the fluid on the boundary used to calculate the fluxes, irrespective of the fluid parameters in the neighbouring grid cell (provided, of course, the parameters in the neighbouring grid cell specify that this boundary is indeed a supersonic inflow). For a supersonic outflow, the fluid parameters at the boundary are just the fluid parameters in the grid cell.

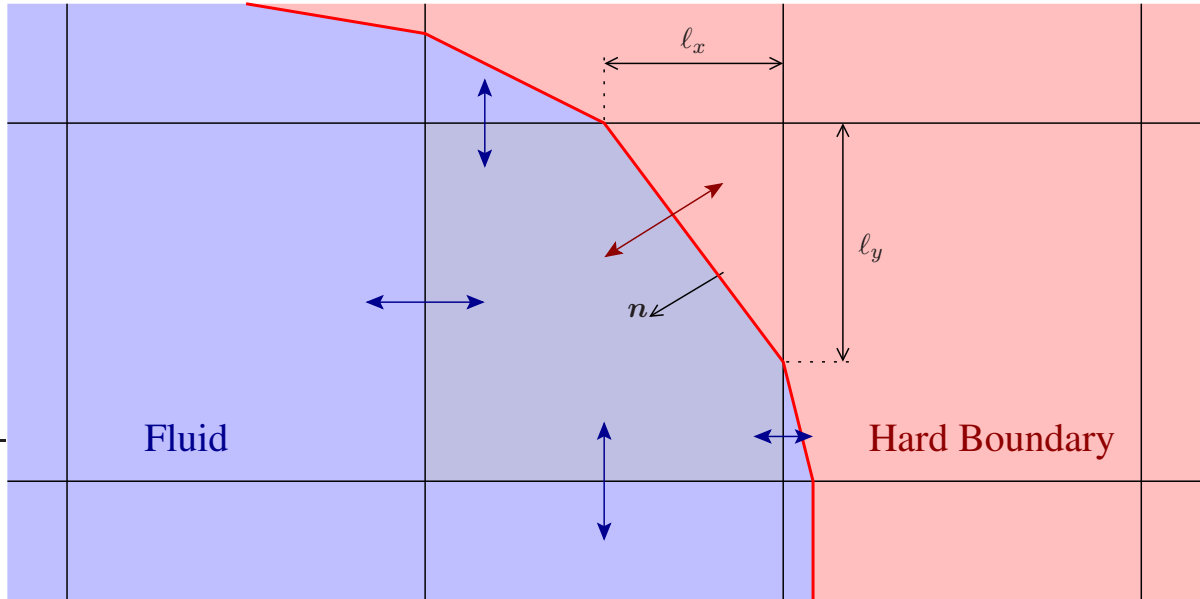


Figure 5.3: Schematic of a grid cell containing an oblique boundary. Double-headed arrows denote fluxes.

Nonreflecting boundaries

The requirement for a non-reflecting boundary is that there is no sudden jump in any of the conserved quantities. This effectively means that the fluid within the computational domain completely specifies the boundary condition, and so the fluid parameters on the boundary are taken to be just the average fluid parameters in the grid cell. This is exactly the same boundary condition as the supersonic outflow, except that the flow does not need to be supersonic, or even an outflow.

Oblique hard boundaries

Here, we allow only a straight boundary that cuts across a grid cell at an oblique angle, and only one such boundary per grid cell, as shown in figure 5.3. For such a cell, the volume of that grid cell is smaller, and so the fluxes into that cell cause a larger effect on the cell average fluid variables. In order to remain stable and allow a large timestep (for a given Courant number), if the volume of a cell becomes too small, that cell is combined with a neighbouring cell to make one larger cell. This is implemented numerically as a post-processing step after all the fluxes have been calculated and the cell averages updated. The volume-weighted averages of the conserved quantities across the two combined cells are then calculated, and these are used to calculate new values for the fluid parameters in the two cells (so that both cells have the

same fluid parameters) whilst still being conservative.

Suppose $\mathbf{n} = (n_x, n_y)$ is the normal to the oblique boundary, pointing into the grid cell, and that the oblique boundary extends a distance ℓ_x in the x direction and ℓ_y in the y direction, as shown in figure 5.3. Given a conservation law

$$\frac{\partial \phi}{\partial t} + \nabla \cdot \mathbf{F} = 0,$$

integrating over the grid cell and using the divergence theorem gives

$$V \frac{d\bar{\phi}}{dt} + \int_B F_x dy - F_y dx = 0$$

where V is the volume of the grid cell, $\bar{\phi}$ is the average of ϕ of the grid cell, B is the boundary of the cell described anticlockwise, and $\mathbf{F} = (F_x, F_y)$. The Strang splitting splits this flux, with the y -integral being the flux in the x -direction and the x -integral being the flux in the y -direction. Note that we could add to \mathbf{F} any arbitrary function provided it were everywhere orthogonal to the boundary normal.

Let us now consider the fluxes in the x -direction. For a grid cell with an oblique boundary running through it, the fluxes across the grid cell boundaries with other cells are calculated as above by solving a Riemann problem. The difficulty is in constructing the fluxes across the oblique boundary. Since $\mathbf{u} \cdot \mathbf{n} = 0$ on a hard boundary, the only non-zero fluxes are those of momentum, (5.1b) and (5.1c). The flux of x -momentum at the oblique boundary is $(p^*, 0)$, while the flux of y -momentum is $(0, p^*)$, where p^* is obtained as for a hard boundary in §5.1.2 by requiring $u^* = 0$ at the wall. Naively, therefore, we might set the x -flux of x -momentum to be $p^* \ell_y$ and the x -flux of y -momentum to be 0 (this will be referred to as boundary type 1). However, recall that, due to the Strang splitting, the x - and y -fluxes are calculated independently, and the fluid parameters updated in between. This means that when calculating the x -fluxes at time t , the cell-averaged fluid parameters may be different to what they were when the y -fluxes were calculated at the same time t . Therefore, this boundary scheme does not enforce that the force exerted by the wall on the fluid be normal to the wall; in other words, it does not conserve momentum parallel to the wall.

An alternative would be to have the x -flux of x -momentum $p^* n_x^2 \ell_y$ and the x -flux of y -momentum $p^* n_x n_y \ell_y$. This is obtained by replacing a flux \mathbf{F} by $(\mathbf{F} \cdot \mathbf{n})\mathbf{n}$, which is a change to \mathbf{F} that is everywhere orthogonal to \mathbf{n} . This has the advantage over the previous boundary scheme that the force exerted by the wall on the fluid is everywhere normal to the wall, but has the disadvantage that a fluid at rest at constant pressure does not remain at rest after a timestep. This will be referred to as boundary type 2.

A third scheme was considered, which first sets $(u^*, v^*) = \mathbf{u} - (\mathbf{u} \cdot \mathbf{n})\mathbf{n}$ as the velocity at the wall, and then gives the x -flux of x -momentum as $\ell_y(\rho^* u^{*2} + p^*)$ and the x -flux of y -momentum as $\ell_y \rho^* u^* v^*$. This third scheme is not conservative, in that it does not enforce that there is no mass or energy flux through the boundary. However, it is the most stable, as it allows for cancellations between the flux in through the fluid boundary on one side and the flux out through the fluid boundary on the other; between the x - and y -timesteps, the boundary acts as a sponge, absorbing flux from one direction before producing it again in the other direction. This will be referred to as boundary type 3.

5.1.3 Properties of the numerical method

One property of this numerical method, and the main reason this method was chosen here, is that it is *shock capturing*, meaning that it can deal comfortably with discontinuities, such as across a shock wave (as demonstrated in §5.2 below). This is obviously the case here, as discontinuities (of arbitrary magnitude) are allowable at all grid-cell boundaries. In fact, higher order Godunov-type schemes tend to smooth over such discontinuities, and special care must be taken to ensure such scheme becomes first order in the neighbourhood of a shock so as to capture the shock correctly; this is usually incorporated into a monotonicity requirement (van Leer, 1979, §3.3).

This scheme is also *conservative*, in that the total mass, momentum, and energy are exactly conserved. This is because conserved quantities are updated by fluxes across grid cell boundaries, and so mass, momentum, and energy may be transferred between grid cells, but never lost. This is, of course, only true provided oblique boundary model 2 is used. Mass, momentum, and energy may also flow in and out of the computational domain through the inflow and outflow boundary conditions.

Another property of this numerical scheme is that it satisfies *upwinding*, meaning that information flows in the correct direction. This is guaranteed by the Riemann problem, or the alternative Riemann-like boundary conditions (and is the reason such boundary conditions were used). For example, if the flow is supersonic, then all the characteristics will lie on the same side of a grid-cell boundary, and so the values for the boundary fluxes will be derived solely from the upstream grid cell.

Finally, as mentioned above, the scheme being piecewise-constant in space and piecewise-steady in time leads to it being first-order-accurate, meaning that the error between the numerical solution and the exact solution decay as $O(\Delta x)$ as $\Delta x \rightarrow 0$, although proof of this

convergence is not given here.

5.2 Test cases

In order to verify the correctness of the numerics, the results generated by this code are compared with some standard testcases.

The first testcase is a one-dimensional one due to Sod (1978), and was used as the first testcase by van Leer (1979). A square domain of unit length and hard walls is filled with a fluid with ratio of specific heats $\gamma = 1.4$. Initially, for $x < 0.5$, $(u, v, p, \rho) = (0, 0, 1, 1)$, while for $x > 0.5$, $(u, v, p, \rho) = (0, 0, 0.1, 0.125)$. This is basically a single Riemann problem. A 100×100 discretization was used with a Courant number of $C = 0.9$, and the solution computed until the shock reached $x = 0.75$. The situation at that time is given in figure 5.4 (c.f. van Leer, 1979, figure 6). The solution is constant in y , and is certainly resolving the analytic solution. The numerical scheme is overly dispersive for the CRW at $0.35 < x < 0.45$ and the contact discontinuity at $x = 0.6$; however, the shock at $x = 0.75$ is sharply resolved, demonstrating the shock-capturing ability.

In order to test the oblique boundary conditions, this testcase was rotated by $\cos^{-1}(3/5)$, so that the square domain now has oblique walls. What was previously the x -direction is now labelled the a -direction, and the same initial conditions as before were used, with different fluid parameters in $a < 0.5$ and $a > 0.5$. Figure 5.5 shows some results for this geometry and a 140×140 numerical grid, which is the equivalent of a 100×100 grid over the interior of the unit square containing the fluid. Lines are drawn between neighbouring grid cells in the x -direction, so that the ends of each line correspond to the edge of the square, and thus lie in grid squares containing an oblique boundary. The results are slightly more dissipative than the one-dimensional case, since both the x and y numerical steps are now needed, rather than just the x step in the one-dimensional version. As can be seen from the ‘hairy’ look of the graphs, the grid cells on the boundary (which are cut by the oblique boundary) are also a source of more noise. This noise can also be seen at $a = 1$. This example uses the oblique boundary model 2.

The different oblique boundary models are compared in figure 5.6. Boundary models 1 and 3, shown in figure 5.6(*b,d*), show far more numerical noise generated by the oblique boundary around $0.5 < a < 0.75$, where there is a significant flow of fluid along the boundary. However, both models also show much less numerical noise at the end boundary $a = 1$. This could have been expected, as boundary model 2 is the most accurate by ensuring conservation of mass,

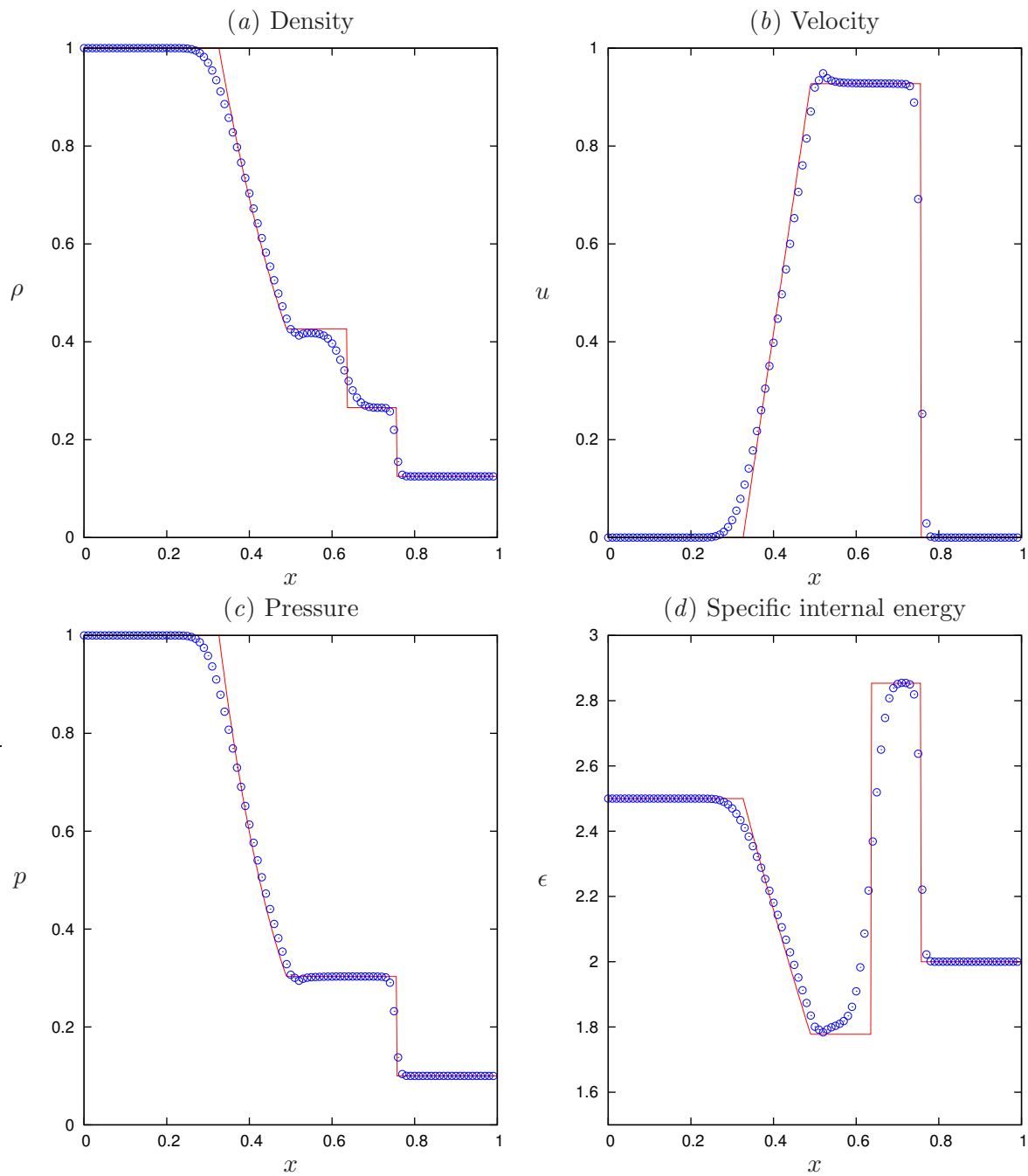


Figure 5.4: Exact solution (solid line) and call averages (circles) for Sod's testcase in one dimension, at $t = 0.147$. Initially $u = 0$, $\rho = p = 1$ for $x < 0$, $\rho = 0.125$ and $p = 0.1$ for $x > 0$. $\gamma = 1.4$, $C = 0.9$, $\Delta x = 0.01$.

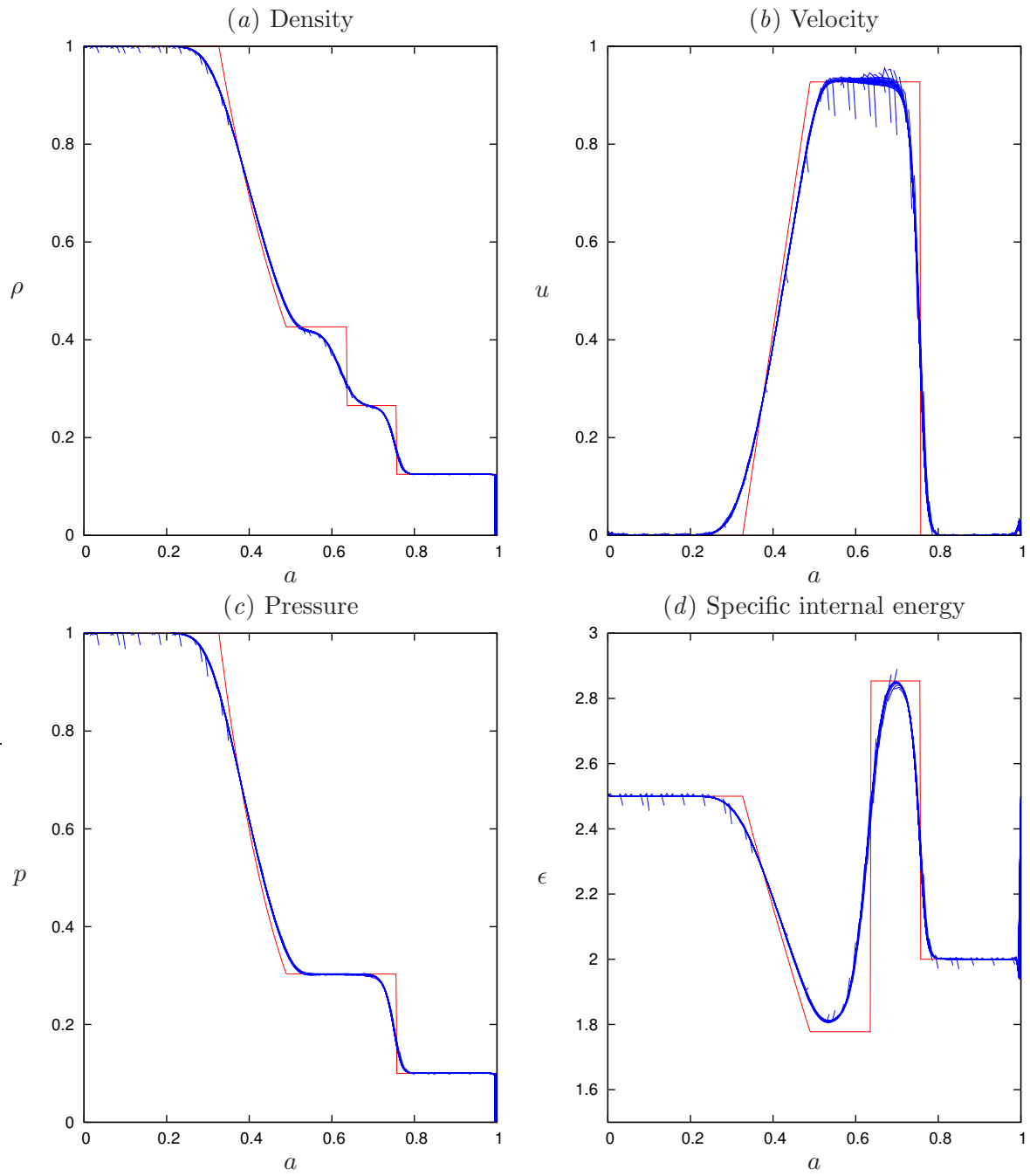


Figure 5.5: Exact solution (red line) and call averages (blue line) for Sod's test case, in two dimensions, at $t = 0.142$. Initially $u = 0$, $\rho = p = 1$ for $a < 0$, $\rho = 0.125$ and $p = 0.1$ for $a > 0$. A 140×140 grid was used, giving $\Delta x = \Delta y = 0.01$. $\gamma = 1.4$ and $C = 0.8$.

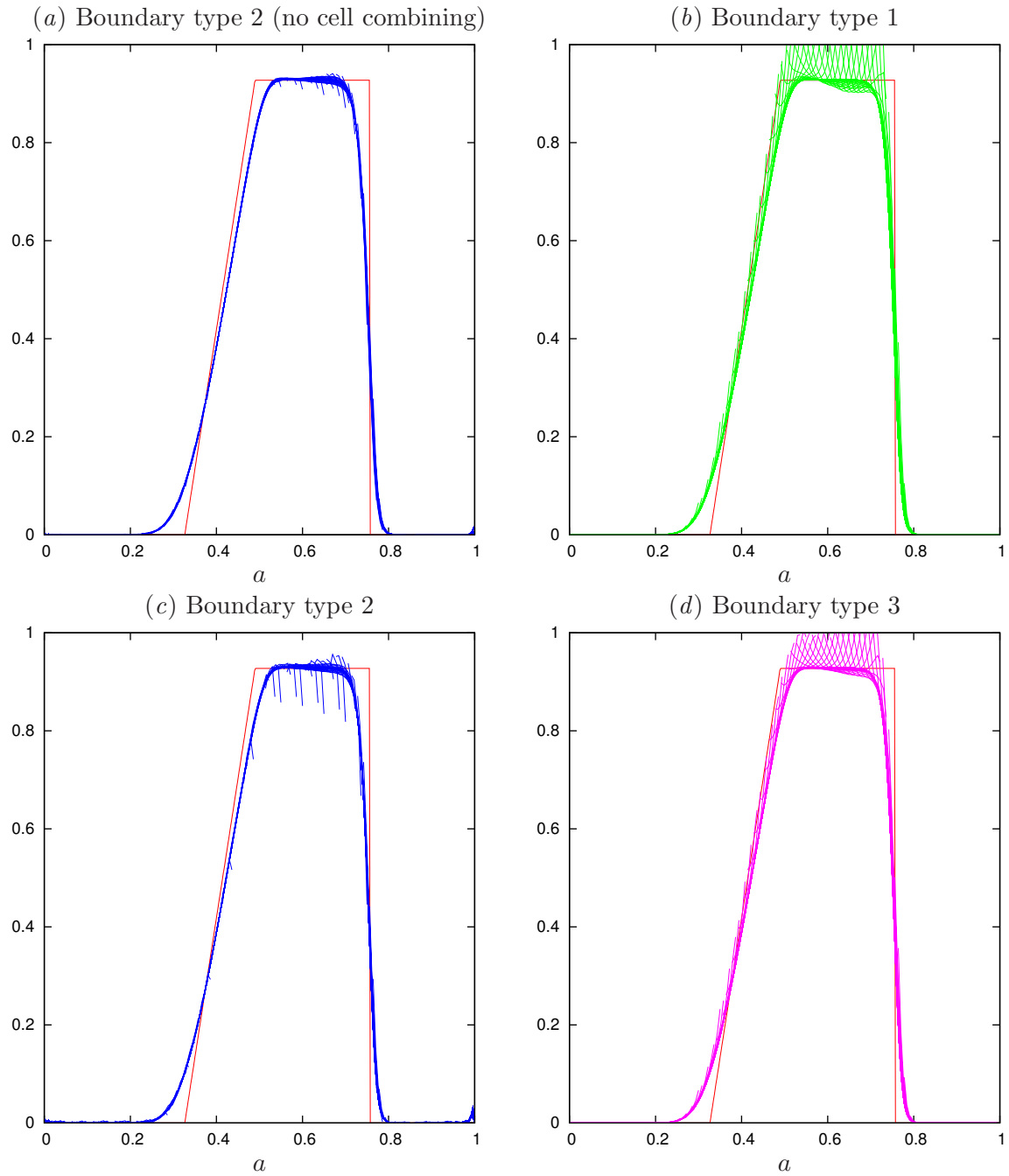


Figure 5.6: The different oblique boundary models for Sod's testcase in two dimensions. Parameters are as for figure 5.5.

energy, and momentum tangent to the wall, while boundary models 1 and 3 allow a cushioning effect by allowing momentum (and, in the case of model 3, energy and mass) to be absorbed and then reproduced by the boundary, yielding better stability when there is a pressure gradient through the boundary.

Figure 5.6(a) shows the results if the cell-combining stage mentioned in §5.1.2 is not performed. This implies that, in order to satisfy the CFL condition, the time step must be taken much smaller, since the minimum distance across a cell is given by the smallest boundary cell. The results are therefore slightly more accurate, but took 3.5 times longer to compute; far more accurate results would have been obtained using the same computational time if instead the cell-combining stage had been performed and the resolution had been increased to 210×210 .

A third test is that of a Mach 3 wind tunnel with a step, which was used as a test case by Woodward & Colella (1984). The domain has height 1 and length 3, and contains a supersonic inflow boundary at $x = 0$ and a supersonic outflow boundary at $x = 3$, while both the top and bottom boundaries are hard. Within the domain, a hard-walled step is located in $0 < y < 0.2$ for $x > 0.6$. The fluid is initially uniformly at $(3, 0, 1, 1.4)$, and $\gamma = 1.4$, giving a uniform horizontal Mach 3 flow. Owing to the step, a shock wave is generated, and the system converges to a steady state with a near-vertical shock in front of the step. Figure 5.7 shows the evolution of the density at different times; by $t = 10.0$ the solution has effectively reached its steady state. The solution at $t = 4$ compares well with Woodward & Colella (1984, figure 3).

These testcases give confidence in the numerical code. We now use this code to look at the propagation of surge through a two-dimensional version of the RAE 2129 intake.

5.3 Surge in a two-dimensional RAE 2129 intake

We consider a two-dimensional version of the cylindrical RAE 2129 intake, by taking the same centreline given in (4.26), with the walls being a distance $\pm a^*$ from the centreline. That is, the two-dimensional duct looks the same as the cross-section through the three-dimensional duct shown in figure 4.14, while the area of the cross-section, and hence the flow, is different. Tests were performed with a variety of oblique boundary conditions, with boundary condition 2 providing the most accurate solution. This is in agreement with the oblique test case in figure 5.6, which indicates boundary condition 2 is the most accurate when there is significant flow parallel to the boundary.

Initially, the duct is filled with fluid of uniform density, pressure, and constant velocity in the

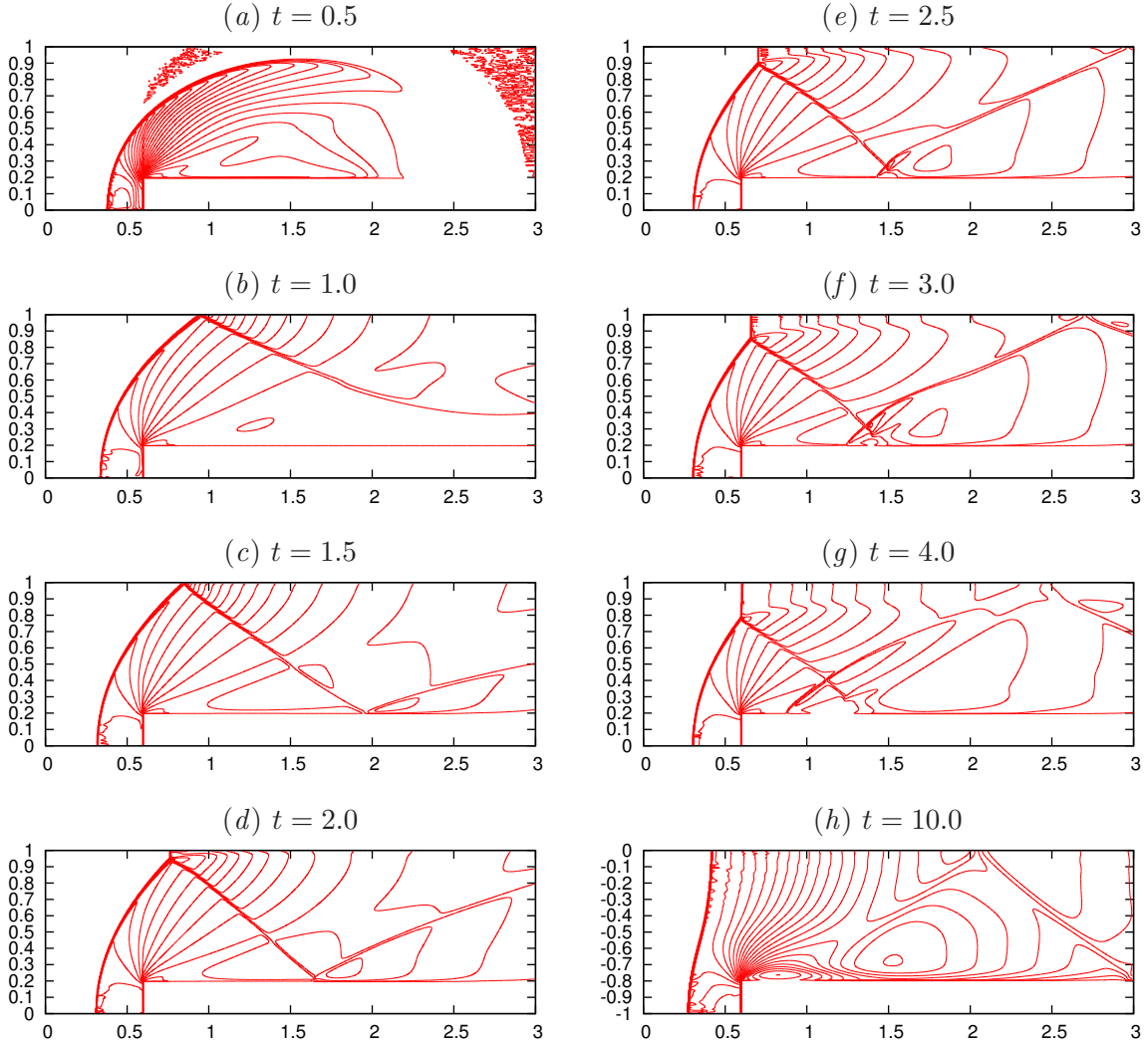


Figure 5.7: Contours of density within the Mach 3 wind tunnel with a step. Initially $(u, v, p, \rho) = (3, 0, 1, 1.4)$ everywhere, with $\gamma = 1.4$. $C = 0.8$, and $\Delta x = \Delta y = 1/200$.

x -direction, which is then allowed to converge to a steady state. The inflow boundary condition prescribes a constant stagnation pressure and temperature, while the outflow boundary condition of a fixed static pressure is tuned to drive the flow at a prescribed upstream Mach number. Once the flow has converged to a steady state, the inflow boundary condition is changed to a nonreflecting one, and the outflow static pressure is varied to give the pressure pulse shown in figure 4.19.

In figures 5.8–5.10, an upstream Mach number of $U_\infty = 0.5$ is prescribed, and the surge in figure 4.19 is scaled to give a peak overpressure ratio of 2, implying a peak underpressure of about 0.6. While the imposed pressure profile is smooth, the overpressure shocks midway through the intake (as shown towards the left in figure 5.8), and the underpressure shocks

almost immediately on entering the duct (as shown towards the right of figure 5.9). The notable feature of figures 5.8–5.10 is that the shock front remains planar, and although the front is not always normal to the duct centreline (especially as the underpressure exits the left-most bend in figure 5.10), nonetheless it exits the curved section as a plane shock without any reflection or mutation due to the curved section.

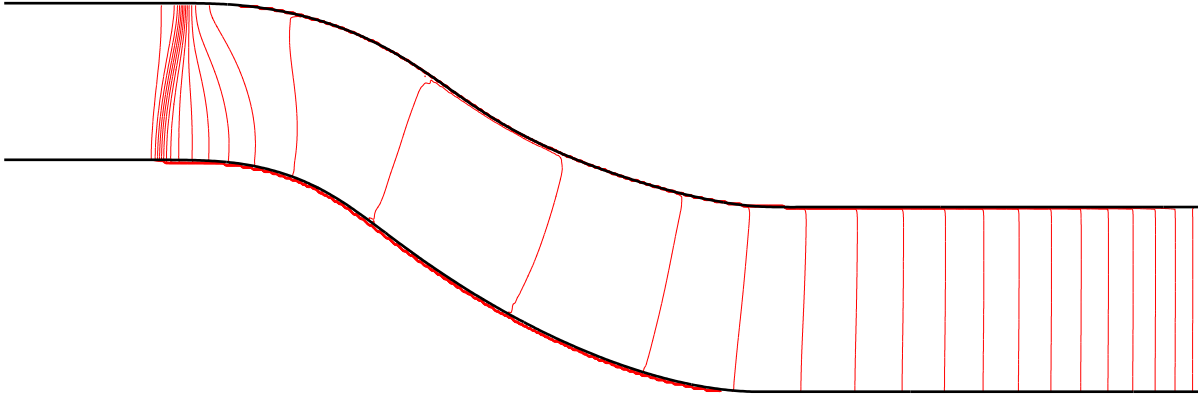


Figure 5.8: Contours of density at $t = 34.75$, equally spaced between 0.6 and 1.8 in steps of 0.05.

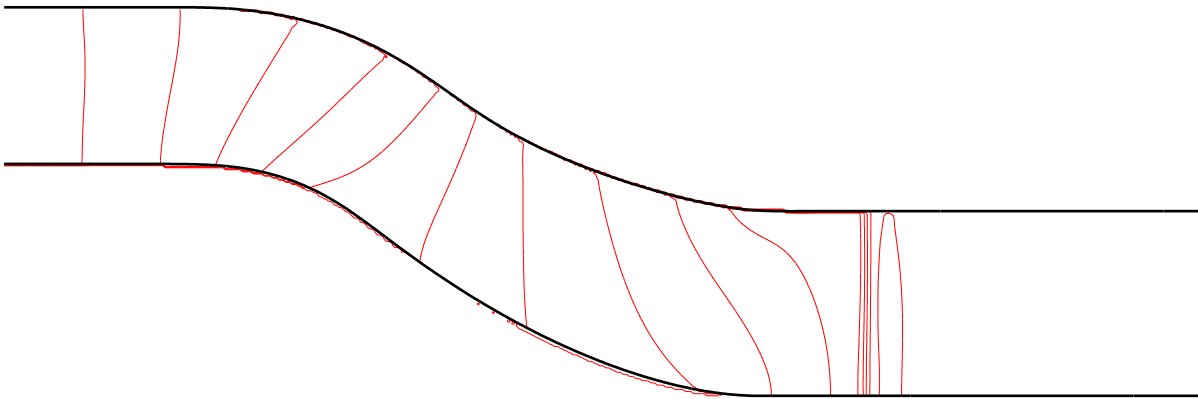


Figure 5.9: Contours of density at $t = 49.75$, equally spaced between 0.6 and 1.8 in steps of 0.05.

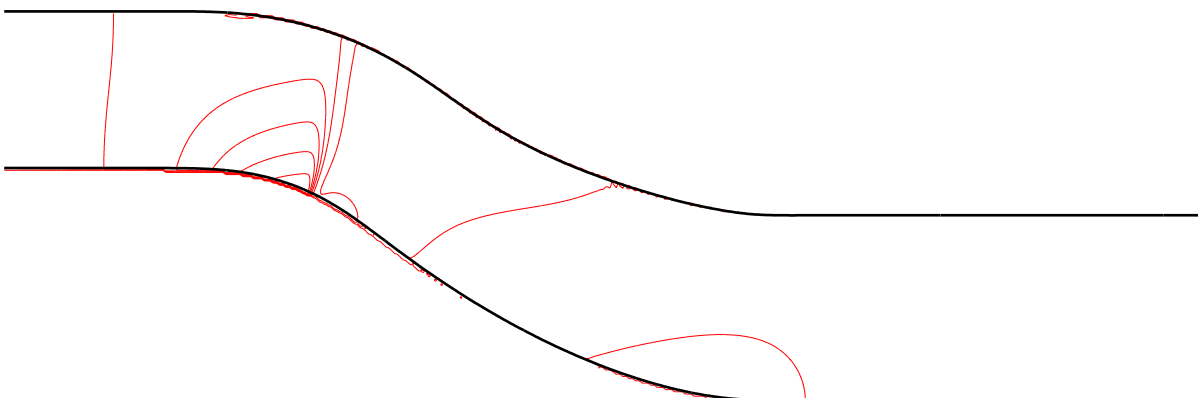


Figure 5.10: Contours of density at $t = 67.25$, equally spaced between 0.6 and 1.8 in steps of 0.05.

Chapter 6

Conclusion

The surface modes discovered by Rienstra (2003*a*) in the high-frequency limit $\omega \rightarrow \infty$ have been generalized to arbitrary azimuthal order m , by considering a similar high-frequency limit. Rienstra's asymptotic dispersion relation for the surface modes is recovered from the generalized dispersion relation (2.2) in a suitable limit. This is unexpected, since (2.2) was derived assuming $m \gg 1$, while Rienstra's dispersion relation is valid for arbitrary m provided $m \ll \omega$, and shows that (2.2) is valid in slightly more generality than might at first have been expected. For realistic parameters for aeroengine intake noise at takeoff, figure 2.3(*b*) shows the generalized dispersion relation to be notably more accurate than Rienstra's. The generalized dispersion relation is utilized for the thin-shell boundary in §3.2, and figure 3.2(*a*) also demonstrates the accuracy of the generalized dispersion relation in this case.

Assuming the impedance boundary to be locally reacting, so that the impedance Z is independent of the axial wavenumber k , up to four surface modes are present for each azimuthal order. The nature of these surface modes, the regions of the complex k -plane they each occupy, and the regions of the complex Z -plane for which they exist, are analysed in a similar manner to Rienstra. These factors are found to depend on the nondimensional number $\lambda = \omega r_0 / (m\sqrt{C^2 - U^2})$, and qualitatively different behaviour is seen for λ in each of four different ranges $[0, \lambda_n]$, $[\lambda_n, \lambda_p]$, $[\lambda_p, 1]$, and $[1, \infty]$, where the critical values λ_n and λ_p correspond to a change in behaviour of the number and position of the surface modes respectively, and are functions of the mean flow Mach number U/C only. Rienstra's asymptotics are recovered in the limit $\lambda \rightarrow \infty$, and so Rienstra predicted only one of these regions. The additional regimes explain, for example, why there are only two surface-mode series in figure 1.2(*b*) for large m , instead of the three predicted by Rienstra, and also why one such series in the lower-right σ -plane for small m crosses into the lower-left as m increases. It was the latter of these that

first highlighted a limitation of Rienstra’s predictions when m is large.

Locally-reacting impedance boundaries such as the mass–spring–damper or Extended Helmholtz Resonator (Rienstra, 2006, §6) models have a subtle mathematical problem; they are illposed, in the sense of that they do not satisfy the conditions of the Hille–Yosida theorem (Rudin, 1991). In summary, given initial conditions \mathbf{x}_0 (living in a suitable normed space), let the operation of evolving these initial conditions forward a time t be \mathcal{L}_t , giving $\mathbf{x}_t = \mathcal{L}_t \mathbf{x}_0$. The operators \mathcal{L}_t are called the *semi-group* for the differential equation being solved. A wellposed problem that satisfies the Hille–Yosida theorem is guaranteed to yield a continuous semi-group, and in particular, $\mathcal{L}_t \rightarrow \mathcal{I}$ as $t \rightarrow 0$ in the operator-norm, where \mathcal{I} is the identity. However, for the mass–spring–damper boundary model, we showed in §3.3 that $\omega \sim -iU\sqrt{k/(\beta d)}$ as $|k| \rightarrow \infty$ for one of the surface modes. This shows that, if arbitrary initial conditions are allowed, arbitrarily quick growth is possible, so that $\mathcal{L}_t \not\rightarrow \mathcal{I}$ as $t \rightarrow 0$, and hence the mass–spring–damper model is illposed. The same also turns out to be true for the Helmholtz resonator boundary model.

This illposedness of the mass–spring–damper boundary manifests itself in various ways. Mathematically, it is an indication that such a model is incorrect and should not be considered. Ignoring this, Rienstra (2003a) considered the stability of the surface waves for a mass–spring–damper boundary. Since the Briggs–Bers stability criterion is inapplicable for exactly the same reasons as the illposedness mentioned above, Rienstra used an alternative stability analysis (Rienstra, 1985). However, in §2.3, we showed this stability analysis to be incorrect. We will comment further on how illposedness manifests itself mathematically below, when we consider the scattering properties in such a system. The illposedness is also very prevalent in computer simulations. It has long been known (e.g. Tam & Auriault, 1996) that time-domain numerical methods with these illposed boundary conditions are unstable, with the instability wavelength comparable with the grid scale, and therefore the instability wavelength changing as the grid is refined. This has led to this instability being interpreted as an artifact of the numerical method, and such instabilities are routinely filtered out using a low-pass filter (Tam & Auriault, 1996; Chevaugeon *et al.*, 2006; Tam & Ju, 2006; Richter & Thiele, 2007). However, we can now see that such an instability is in fact caused by the numerical code attempting to realize the underlying arbitrarily-quick growth rate at arbitrarily-small wavelengths. A regularization of such boundary conditions that is wellposed is obviously needed.

One regularization of the mass–spring–damper boundary is the thin-shell boundary with external spring and damping forces proposed in §3.1. This model is shown to recover the mass–spring–damper model in the limit of the thin-shell thickness $h \rightarrow 0$, while it remains wellposed for all $h > 0$ (see §3.3). Of course, we do not propose that such a model is an appropriate model

for an acoustic lining in an aeroengine. The thin-shell model is, however, useful in pointing out how the illposedness manifests itself mathematically, and demonstrates that modifying the boundary model for large k with the inclusion of bending stiffness, while retaining mass–spring–damper like behaviour for small k , can lead to different conclusions about stability from those reached by Rienstra (2003*a*), even for modes with a small value of k for which these models yield a similar impedance Z . The thin shell boundary is also an interesting problem to consider in its own right.

Since the thin-shell boundary is not locally reacting, the predictions of the existence and behaviour of up to four surface modes in §2.1.2 is not longer relevant. The asymptotic dispersion relation (2.2) remains correct, and using it predicts 18 surface modes (see §3.2). Since the thin-shell problem is wellposed, its stability may be analysed using the Briggs–Bers criterion. We find it to be either stable or absolutely unstable, depending on the parameters of the fluid and the thin shell, although it is only unstable for high mean flow velocities or extremely thin shell thicknesses; examples of these results are given in figure 3.13, and asymptotic predictions of the boundary between stable and unstable behaviour are given in (3.6). This conclusion is interesting, as it differs from the predictions of Peake (1997) for the stability of a thin shell bounding an incompressible fluid. Peake found that convective instabilities were possible, and that absolute instability was not possible provided the mean fluid velocity was below a certain threshold, both of which are different from what is seen here in the compressible case.

We considered the Wiener–Hopf problem of a wave scattering off a sudden boundary change from a hard wall to a thin-shell boundary, in order to regularize the illposed Wiener–Hopf scattering of a sudden change from a hard wall to a mass–spring–damper boundary analysed by Rienstra (2007). Assuming all modes to be stable, Rienstra found the surface streamline to be $O(x^{1/2})$ as $x \rightarrow 0$, where $x = 0$ is the location of the sudden boundary change. Allowing one of the surface modes to be an instability gave Rienstra a degree of freedom, which could be used to satisfy a Kutta-like condition at $x = 0$ and give $O(x^{3/2})$ behaviour of the surface streamline. For the thin-shell boundary (where we consider the thin shell clamped to the hard wall at $x = 0$), the boundary streamline is $O(x^2)$, without any spare degrees of freedom or Kutta-like conditions, and without any ambiguity over the inclusion of an instability. This streamline behaviour is true for any $h > 0$, even for h so small that the boundary impedance Z is locally (in k and ω) indistinguishable from that of the mass–spring–damper boundary. Note that the constants C_1 and C_2 occurring in the Wiener–Hopf solution in §3.4.5 could have been specified (incorrectly) by satisfying the Kutta-like condition of $O(x^4)$ smoothness of the surface streamline as $x \rightarrow 0$. However, as shown in §3.4.6, the correct values for C_1 and C_2 are obtained

by causality, and applying an $O(x^4)$ Kutta-like condition would have necessitated inbound solid waves in the boundary from $x = +\infty$, and would therefore not give the correct causal solution to the problem of a wave inbound from $x = -\infty$ scattering off the sudden boundary change. This demonstrates that Kutta conditions need to be justified by considering additional realistic physics in a suitable limit, rather than being employed to satisfy reasonable-sounding regularity constraints.

All of this discussion so far has been for a cylindrical duct with a straight centreline. In chapter 4, we derived the modal solutions in a duct with a significantly curved centreline, provided the centreline curvature and duct radii varied slowly. One major difference between curved and straight ducts is the asymmetry in curved ducts between upstream- and downstream-propagating modes (see, for example, figure 4.11). Another difference is that the resulting differential equation in the duct cross-section does not admit analytic solutions for a curved duct, and so was solved numerically. Despite this, certain features can at least be explained asymptotically using raytracing.

In §4.7.2, the behaviour of the fundamental modes (the curved-duct equivalent of plane-wave modes) is explained by a competition between the curved geometry and the refraction effect of the mean flow. If the duct is sufficiently curved and the mean flow sufficiently slow, the geometry dominates and the fundamental modes become localized on the outside of the duct bend. If the mean flow is sufficiently fast or the curvature is sufficiently small, it is the refraction effect that dominates and the fundamental modes become localized on the inside of the duct bend. In certain circumstances, both of these possibilities can exist simultaneously. This situation is summarised in figure 4.29.

The curvature also has an effect on the efficiency of an acoustic lining, as shown in figure 4.12, with the low-order modes being more heavily damped than they would be in a straight duct with the same lining. One might have thought this was attributable to the lining on the side of the duct that the mode was localized on, and that therefore savings could be made by lining only that part of the duct. However, by considering a partially-lined duct in §4.4.2, this was shown not to be the case; despite a mode being localized in one part of the duct, the acoustic lining all round the duct is important. Note that the impedance boundary model used in chapter 4 is locally reacting, and so is susceptible to exactly the same problems with stability analysis demonstrated in §2.2. The thin-shell boundary model of chapter 3 assumes a straight centreline, and so is not applicable to the curved-duct problem without further modification.

One feature that is notable for being the same for a straight or a curved duct (with hard-wall

boundaries) is the cuton–cutoff transition of a mode by the slowly-varying geometry. This is surprising, since the asymptotic inner scaling region is of length $s = O(\varepsilon^{-1/3})$, and so is long on the lengthscale of the duct curvature. The duct is therefore significantly curved over this region, albeit with a constant curvature, and so it is surprising that there is no curvature dependence to the transmission or reflection coefficients.

From the asymptotics in §4.8, if the curvature is small, the effects of the curvature on the wavenumber (and hence the effects on the propagation of the wave) occur at $O(\kappa^2)$, while the effects of the curvature on the cross-duct mode shape occur at $O(\kappa)$. This means that, if the duct curvature is small, the duct may be treated as if it were straight, with the equivalent length given by the length measured along the duct centreline.

A major assumption of the multiple scales derivation is that viscosity can be neglected. In real-world applications, this assumption is valid provided the boundary layer along the wall of the curved duct does not separate. The separation of a boundary layer in an aeroengine intake is very disadvantageous, since the flow entering the engine would then be highly asymmetric and cause a very variable load on each fan blade. However, in certain situations the boundary layer does separate, and in these situations the mean flow derived in §4.1 is not correct.

A limitation of the multiple scales method is that it does not model partial reflection by the slow variation of the duct. For example, consider a mode originating in a section of duct with constant parameters. The duct then varies slowly in some arbitrary fashion before returning to these initial parameters. From one side of the varying part of this duct to the other, the mode will either have been totally reflected or will have been perfectly transmitted without any change. Any changes to a transmitted mode would occur as a higher order correction to the leading order solution given here (for example, in A_1). This means that the method presented here would not, for example, be able to predict the difference in sound generated by a curved music instrument compared with a similar straight one.

Whilst the linear multiple scales method was used to demonstrate a surge pulse (as shown in figure 4.19) propagating through the RAE 2129 intake (see figures 4.20–4.22), in reality such a surge pulse has a large amplitude comparable with the mean flow pressure, and so is not modelled by linear theory. In particular, wave steepening and shock waves are not modelled by the linear theory. The results of chapter 5 for a two-dimensional version of the RAE 2129 intake demonstrate such behaviour, with the overpressure shocking midway through the intake and the underpressure shocking almost immediately. The results shown in figures 5.8–5.10 demonstrate that a disturbance introduced at the downstream end of the duct as constant

across the duct cross-section remains practically one-dimensional as it propagates along the curved duct, although the pulse does not necessarily remain constant across the duct cross-section, nor normal to the duct centreline. This suggests the existence of some underlying mathematical one-dimensional model, similar to classical straight shock-tube theory (Lighthill, 1978), that incorporates the effects of curvature and varying duct diameter.

6.1 Further research

There are many possible ways of extending the work presented in this thesis, including:

- Developing a better regularization of the mass–spring–damper impedance boundary that incorporates the relevant physics of the Helmholtz resonator structure used in actual aeroengine linings. The regularizing parameter h might be the thickness of the viscous boundary layer lying above such a lining, with the viscous dissipation, it is hoped, providing the bounded temporal growth rate in a similar way to the bending stiffness for the thin-shell boundary. The presence of this boundary layer may well be the reason that impedance measurements of an acoustic lining with and without flow give different results (Fung *et al.*, 2007). A good starting point for this would be to build on the work of Auregan *et al.* (2001).
- Investigating a one-dimensional mathematical model of a shock tube with a curved centreline and varying diameter. As mentioned above, the results from §5.3 give promising suggestions that such a model exists. For a straight shock tube, the disturbance is implicitly assumed to be constant across the tube, and one difficult question with a curved tube is what form to assume for the cross-duct disturbance. From figures 5.8–5.10, it may well be helpful to consider a retarded time which varies across the duct; for example, $\tilde{t} = t/h_s^2$.
- Modify the pseudospectral method used in chapter 4 to use Bessel functions rather than Chebyshev polynomials as the radial basis, as suggested by Bi (2007). This has the advantage that the basis functions have the correct behaviour at $r = 0$, which is that basis functions with $\exp\{im\theta\}$ dependence must be $O(r^{|m|})$ as $r \rightarrow 0$. Preliminary results suggest that far fewer radial basis functions are needed in this case than for Chebyshev polynomials, and also that far fewer numerically-found eigenfunctions are spurious. This would then enable a much higher azimuthal order to be used, so that, for example, liner

splices could be accurately resolved. Moving to a Galerkin spectral method, rather than the pseudospectral method used here, may also prove advantageous in this regard.

- Allowing for more abrupt changes in the duct parameters, either by considering higher powers of ε in the multiple-scales expansion (Nayfeh *et al.*, 1980; Adamou *et al.*, 2005), or by allowing sudden changes in parameters using the Wiener–Hopf technique. For example, a Wiener–Hopf analysis of a straight duct connected to another section of duct with constant curvature would be interesting.
- Extending the multiple scales analysis by expanding in powers of the unsteady pressure amplitude. Such an approximation is called *weakly nonlinear*, and allows for modelling effects such as buzz-saw noise, which has application in aeroengines.
- Investigating the effects of adding viscosity into the mean flow derived in §4.1. This would enable the treatment of the mean flow boundary layers separating within the curved section of the duct.
- Relaxing the assumption of a cylindrical duct and allowing the duct cross-section to be arbitrary and slowly varying, in a similar way to Rienstra (2003*b*) for a straight duct. This has applications in military aeroengine intakes, which typically distort from nearly rectangular at the cowl lip to cylindrical at the fan face, in addition to being curved.
- Including torsion, allowing the duct to be coiled as well as curved. While this currently has no direct application, it might be found that, for example, the addition of torsion is beneficial to acoustic damping. This is complicated for nonzero mean flow, since the cross-sectional components V and W become $O(1)$ for nonzero torsion, rather than $O(\varepsilon)$ for zero torsion.
- Investigating further the surge signal that is incident on the downstream end of the intake. The pressure profile in figure 4.19 was suggested by J. Longley (2006, private communication) as a generic typical surge profile. Menzies (2002) considered three alternative surge pressure profiles, some of which had already shocked before entering the intake. Other considerations are whether the flow reverses, and if so, what stagnation temperature and pressure are assumed for the incoming fluid from the engine; due to combustion, these need not be the same as atmospheric. Further experimental measurements would be helpful to answer some of these questions.

Appendix A

Bibliography

- ABRAMOWITZ, M. & STEGUN, I. A. 1964 *Handbook of Mathematical Functions*, 9th edn. Dover.
- ADAMOU, A. T. I., GRIDIN, D. & CRASTER, R. V. 2005 Acoustic quasi-modes in slowly varying cylindrical tubes. *Q. J. Mech. Appl. Math.* **58**, 419–438.
- ANDERSON, E., BAI, Z., BISCHOF, C., BLACKFORD, S., DEMMEL, J., DONGARRA, J., DU CROZ, J., GREENBAUM, A., HAMMARLING, S., MCKENNEY, A. & SORENSEN, D. 1999 *LAPACK Users' Guide*. Society for Industrial and Applied Mathematics.
- AUREGAN, Y., STAROBINSKI, R. & PAGNEUX, V. 2001 Influence of grazing flow and dissipation effects on the acoustic boundary conditions at a lined wall. *J. Acoust. Soc. Am.* **109**, 59–64.
- BABIC, V. M. & BULDYREV, V. S. 1991 *Short-Wavelength Diffraction Theory*. Springer.
- BEN-ARTZI, M. & FALCOVITZ, J. 1984 A second-order Godunov-type scheme for compressible fluid dynamics. *J. Comput. Phys.* **55**, 1–32.
- BEN-ARTZI, M. & FALCOVITZ, J. 2003 *Generalized Riemann Problems in Computational Fluid Dynamics*, chap. 3 and app. C. Cambridge.
- BEN-ARTZI, M., LI, J. & WARNECKE, G. 2006 A direct Eulerian GRP scheme for compressible fluid flows **218**, 19–43.
- BERS, A. 1983 Space–time evolution of plasma instabilities — absolute and convective. In *Basic Plasma Physics* (ed. A. A. Galeev & R. N. Sudan), *Handbook of Plasma Physics*, vol. 1, pp. 451–517. North-Holland.

- BI, W. 2007 On the calculations of modes in circumferentially nonuniform lined intakes. *AIAA Paper* 2007-3550.
- BOYD, J. P. 2001 *Chebyshev and Fourier Spectral Methods*, 2nd edn. Dover.
- BRAMBLEY, E. J. & PEAKE, N. 2006a Classification of aeroacoustically relevant surface modes in cylindrical lined ducts. *Wave Motion* **43**, 301–310.
- BRAMBLEY, E. J. & PEAKE, N. 2006b Sound transmission in strongly-curved slowly-varying cylindrical and annular lined ducts with flow. *AIAA Paper* 2006-2582.
- BRAMBLEY, E. J. & PEAKE, N. 2006c Surface-waves, stability, and scattering for a lined duct with flow. *AIAA Paper* 2006-2688.
- BRAMBLEY, E. J. & PEAKE, N. 2007a Sound in curved intakes. *AIAA Paper* 2007-3552.
- BRAMBLEY, E. J. & PEAKE, N. 2007b Sound transmission in strongly-curved slowly-varying cylindrical ducts with flow. *J. Fluid Mech.* (accepted).
- BRAMBLEY, E. J. & PEAKE, N. 2007c Stability and acoustic scattering in a cylindrical thin shell containing compressible mean flow. *J. Fluid Mech.* (submitted).
- BRIGGS, R. J. 1964 *Electron-Stream Interaction with Plasmas*, chap. 2. MIT Press.
- CHEVAUGEON, N., REMACLE, J.-F. & GALLEZ, X. 2006 Discontinuous Galerkin implementation of the extended Helmholtz resonator model in time domain. *AIAA Paper* 2006-2569.
- COLELLA, P. & WOODWARD, P. R. 1984 The piecewise parabolic method (PPM) for gas-dynamical simulations. *J. Comput. Phys.* **54**, 174–201.
- COOPER, A. J. & PEAKE, N. 2000 Trapped acoustic modes in aeroengine intakes with swirling flow. *J. Fluid Mech.* **419**, 151–175.
- COOPER, A. J. & PEAKE, N. 2001 Propagation of unsteady disturbances in a slowly varying duct with mean swirling flow. *J. Fluid Mech.* **445**, 207–234.
- CRIGHTON, D. G. & LEPPINGTON, F. G. 1974 Radiation properties of the semi-infinite vortex sheet: the initial-value problem. *J. Fluid Mech.* **64**, 393–414.
- CRIGHTON, D. G. & OSWELL, J. E. 1991 Fluid loading with mean flow. I. Response of an elastic plate to localized excitation. *Phil. Trans. R. Soc. Lond. A* **335**, 557–592.

- FELIX, S. & PAGNEUX, V. 2001 Sound propagation in rigid bends: A multimodal approach. *J. Acoust. Soc. Am.* **110**, 1329–1337.
- FELIX, S. & PAGNEUX, V. 2002 Multimodal analysis of acoustic propagation in three-dimensional bends. *Wave Motion* **36**, 157–168.
- FELIX, S. & PAGNEUX, V. 2004 Sound attenuation in lined bends. *J. Acoust. Soc. Am.* **116**, 1921–1931.
- FRIGO, M. & JOHNSON, S. G. 2005 The design and implementation of FFTW3. *Proceedings of the IEEE* **93**, 216–231.
- FUNG, K.-Y., JING, X., LU, Z. & YANG, X. 2007 Time-domain in-situ characterization of acoustic liners in a flow duct via impulse response. *AIAA Paper* 2007-3542.
- GERMANO, M. 1982 On the effect of torsion on a helical pipe flow. *J. Fluid Mech.* **125**, 1–8.
- GOLDSTEIN, M. E. 1978 Unsteady vortical and entropic distortions of potential flows round arbitrary obstacles. *J. Fluid Mech.* **89**, 433–468.
- GRIDIN, D. & CRASTER, R. V. 2003 Quasi-modes of a weakly curved waveguide. *Proc. Roy. Soc. Lond. A* **459**, 2909–2931.
- HINCH, E. J. 1991 *Perturbation Methods*. Cambridge.
- IGRA, O., WU, X., FALCOVITZ, J., MEGURO, T., TAKAYAMA, K. & HEILIG, W. 2001 Experimental and theoretical study of shock wave propagation through double-bend ducts. *J. Fluid Mech.* **437**, 255–282.
- JONES, D. S. 1977 The scattering of sound by a simple shear layer. *Phil. Trans. R. Soc. Lond. A* **284**, 287–328.
- JONES, D. S. & MORGAN, J. D. 1972 The instability of a vortex sheet on a subsonic stream under acoustic radiation. *Proc. Camb. Phil. Soc.* **72**, 465–488.
- JONES, D. S. & MORGAN, J. D. 1974 A linear model of a finite amplitude Helmholtz instability. *Proc. Roy. Soc. Lond. A* **338**, 17–41.
- KEEFE, D. H. & BENADE, A. H. 1983 Wave propagation in strongly curved ducts. *J. Acoust. Soc. Am.* **74**, 320–332.
- KELLER, J. B. & RUBINOW, S. I. 1960 Asymptotic solution of eigenvalue problems. *Annals Phys.* **9**, 24–75.

- KHORRAMI, M. R., MALIK, M. R. & ASH, R. L. 1989 Application of spectral collocation techniques to the stability of swirling flows. *J. Comput. Phys.* **81**, 206–229.
- LANDAU, L. D. & LIFSHITZ, E. M. 1987 *Fluid Mechanics*, 2nd edn. Elsevier.
- LAW, T. R. & DOWLING, A. P. 2006 Optimization of traditional and blown liners for a silent aircraft. *AIAA Paper* 2006-2525.
- VAN LEER, B. 1979 Towards the ultimate conservative difference scheme. V. A second-order sequel to Godunov’s method. *J. Comput. Phys.* **32**, 101–136.
- LIGHTHILL, M. J. 1978 *Waves in Fluids*, chap. 2.8–2.10. Cambridge.
- MCALPINE, A. & WRIGHT, M. C. M. 2006 Acoustic scattering by a spliced turbofan inlet duct liner at supersonic fan speeds. *J. Sound Vib.* **292**, 911–934.
- MEN’SHOV, I. S. 1990 Increasing the order of approximation of Godunov’s scheme using solutions of the generalized Riemann problem. *USSR Comput. Maths. Math. Phys.* **30**, 54–65.
- MENZIES, R. D. D. 2002 Investigation of S-shaped intake aerodynamics using computational fluid dynamics. PhD thesis, University of Glasgow.
- MORGAN, J. D. 1975 The interaction of sound with a subsonic cylindrical vortex layer. *Proc. Roy. Soc. Lond. A* **344**, 341–362.
- MUNT, R. M. 1977 The interaction of sound with a subsonic jet issuing from a semi-infinite cylindrical pipe. *J. Fluid Mech.* **83**, 609–640.
- MYERS, M. K. 1980 On the acoustic boundary condition in the presence of flow. *J. Sound Vib.* **71**, 429–434.
- NAYFEH, A. H., SHAKER, B. S. & KAISER, J. E. 1980 Transmission of sound through nonuniform circular ducts with compressible mean flow. *AIAA J.* **18**, 515–525.
- NOBLE, B. 1958 *Methods based on the Wiener–Hopf Technique for the Solution of Partial Differential Equations*. Pergamon.
- OVENDEN, N. C. 2005 A uniformly valid multiple-scales solution for cut-on cut-off transition of sound in flow ducts. *J. Sound Vib.* **286**, 403–416.
- PAGNEUX, V., AMIR, N. & KERGOMARD, J. 1996a A study of wave propagation in varying cross-section waveguides by modal decomposition. Part I. Theory and validation. *J. Acoust. Soc. Am.* **100**, 2034–2048.

- PAGNEUX, V., AMIR, N. & KERGOMARD, J. 1996*b* A study of wave propagation in varying cross-section waveguides by modal decomposition. Part II. Results. *J. Acoust. Soc. Am.* **101**, 2504–2517.
- PAÏDOUSSIS, M. P. 2004 *Fluid-Structure Interactions Vol. 2*. Elsevier.
- PEAKE, N. 1997 On the behaviour of a fluid-loaded cylindrical shell with mean flow. *J. Fluid Mech.* **338**, 387–410.
- RICHTER, C. & THIELE, F. H. 2007 The stability of time explicit impedance models. *AIAA Paper* 2007-3538.
- RIENSTRA, S. W. 1985 Hydrodynamic instabilities and surface waves in a flow over an impedance wall. In *Proc. IUTAM Symposium ‘Aero- and Hydro-Acoustics’* (ed. G. Comte-Bellot & J. E. Ffowcs Williams), pp. 483–490. Springer, Heidelberg.
- RIENSTRA, S. W. 1999 Sound transmission in slowly varying circular and annular lined ducts with flow. *J. Fluid Mech.* **380**, 279–296.
- RIENSTRA, S. W. 2003*a* A classification of duct modes based on surface waves. *Wave Motion* **37**, 119–135.
- RIENSTRA, S. W. 2003*b* Sound propagation in slowly varying lined flow ducts of arbitrary cross-section. *J. Fluid Mech.* **495**, 157–173.
- RIENSTRA, S. W. 2006 Impedance models in time domain, including the extended Helmholtz resonator model. *AIAA Paper* 2006-2686.
- RIENSTRA, S. W. 2007 Acoustic scattering at hard–soft transition with flow. *J. Eng. Math.* (submitted).
- RIENSTRA, S. W. & EVERSMAAN, W. 2001 A numerical comparison between the multiple-scales and finite-element solution for sound propagation in lined flow ducts. *J. Fluid Mech.* **437**, 367–384.
- RIENSTRA, S. W. & HIRSCHBERG, A. 2001 *An introduction to Acoustics*. Eindhoven University of Technology.
- RIENSTRA, S. W. & PEAKE, N. 2005 Modal scattering at an impedance transition in a lined flow duct. *AIAA Paper* 2005-2852.

- RIENSTRA, S. W. & TESTER, B. J. 2005 An analytic Green's function for a lined circular duct containing uniform mean flow. *AIAA Paper* 2005-3020.
- RUDIN, W. 1991 *Functional Analysis*, p. 380. McGraw-Hill.
- SOD, G. A. 1978 A survey of several finite difference methods for systems of non-linear hyperbolic conservation laws. *J. Comput. Phys.* **27**, 1–31.
- STRANG, G. 1968 On the construction and comparison of difference schemes. *SIAM J. Numer. Anal.* **5**, 506–517.
- TAM, C. K. W. & AURIAULT, L. 1996 Time-domain impedance boundary conditions for computational aeroacoustics. *AIAA J.* **34**, 917–923.
- TAM, C. K. W. & JU, H. 2006 Scattering of acoustic duct modes by axial liner splices. *AIAA Paper* 2006-2459.
- TING, L. & MIKSYS, M. J. 1983 Wave propagation through a slender curved tube. *J. Acoust. Soc. Am.* **74**, 631–639.
- WOODWARD, P. R. & COLELLA, P. 1984 The numerical simulation of two-dimensional fluid flow with strong shocks. *J. Comput. Phys.* **54**, 115–173.

Appendix B

Curve-centred coordinate system

B.1 Curvature and torsion

Let $\mathbf{q}(s)$ denote a curve, parameterised by arc length s . Then the Frenet formulae give

$$\begin{aligned}\frac{d\mathbf{q}}{ds} &= \mathbf{t} & \frac{d\mathbf{t}}{ds} &= \kappa\mathbf{n} \\ \frac{d\mathbf{n}}{ds} &= \tau\mathbf{b} - \kappa\mathbf{t} & \frac{d\mathbf{b}}{ds} &= -\tau\mathbf{n}\end{aligned}$$

where \mathbf{t} is the tangent unit vector, \mathbf{n} is the normal unit vector, $\mathbf{b} = \mathbf{t} \wedge \mathbf{n}$ is the binormal, κ is the curvature and τ is the torsion. Hence

$$\kappa = \left\| \frac{d^2\mathbf{q}}{ds^2} \right\| \qquad \tau = \frac{1}{\kappa} \frac{d^3\mathbf{q}}{ds^3} \cdot \mathbf{b}$$

If the curve is given specified by $y(s)$, giving $\mathbf{q}(s) = x(s)\mathbf{e}_x + y(s)\mathbf{e}_y$ in cartesian coordinates x, y, z , then

$$\kappa(s) = \frac{\frac{d^2y}{ds^2}}{\sqrt{1 - \left(\frac{dy}{ds}\right)^2}} \qquad \tau(s) \equiv 0. \qquad (\text{B.1})$$

B.2 Coordinates

For a general vector \mathbf{x} , write

$$\mathbf{x} = \mathbf{q}(s) + r \cos(\theta + \alpha(s))\mathbf{n} + r \sin(\theta + \alpha(s))\mathbf{b}$$

where $\alpha(s)$ is determined below to yield an orthogonal coordinate system (Germano, 1982).

Then

$$\begin{aligned} d\mathbf{x} &= ds \left(\mathbf{t} + r \cos(\theta + \alpha) ((\tau + \alpha')\mathbf{b} - \kappa\mathbf{t}) - r \sin(\theta + \alpha) (\tau + \alpha')\mathbf{n} \right) \\ &\quad + dr \left(\cos(\theta + \alpha)\mathbf{n} + \sin(\theta + \alpha)\mathbf{b} \right) \\ &\quad + d\theta \left(-r \sin(\theta + \alpha)\mathbf{n} + r \cos(\theta + \alpha)\mathbf{b} \right) \end{aligned}$$

where a prime denotes differentiation by s . Setting $\alpha' = -\tau$ yields an orthogonal coordinate system:

$$\begin{aligned} \frac{d\mathbf{x}}{ds} &= h_s \mathbf{e}_s = (1 - \kappa r \cos(\theta + \alpha))\mathbf{t} \\ \frac{d\mathbf{x}}{dr} &= \mathbf{e}_r = \cos(\theta + \alpha)\mathbf{n} + \sin(\theta + \alpha)\mathbf{b} \\ \frac{d\mathbf{x}}{d\theta} &= r \mathbf{e}_\theta = r(-\sin(\theta + \alpha)\mathbf{n} + \cos(\theta + \alpha)\mathbf{b}) \end{aligned}$$

The derivatives of these vectors are

$$\begin{aligned} \frac{d\mathbf{e}_s}{ds} &= \kappa \cos(\theta + \alpha)\mathbf{e}_r - \kappa \sin(\theta + \alpha)\mathbf{e}_\theta \\ \frac{d\mathbf{e}_r}{ds} &= -\kappa \cos(\theta + \alpha)\mathbf{e}_s & \frac{d\mathbf{e}_\theta}{ds} &= \kappa \sin(\theta + \alpha)\mathbf{e}_s \\ \frac{d\mathbf{e}_r}{d\theta} &= \mathbf{e}_\theta & \frac{d\mathbf{e}_\theta}{d\theta} &= -\mathbf{e}_r \\ \frac{d\mathbf{e}_s}{d\theta} &= \frac{d\mathbf{e}_s}{dr} = \frac{d\mathbf{e}_r}{dr} = \frac{d\mathbf{e}_\theta}{dr} = 0 \end{aligned}$$

B.3 Vector calculus

In this new coordinate system,

$$\nabla = \frac{1}{h_s} \mathbf{e}_s \frac{\partial}{\partial s} + \mathbf{e}_r \frac{\partial}{\partial r} + \frac{1}{r} \mathbf{e}_\theta \frac{\partial}{\partial \theta}$$

Consider the vector field $\mathbf{u} = u\mathbf{e}_s + v\mathbf{e}_r + w\mathbf{e}_\theta$. Then

$$\begin{aligned} \nabla \cdot \mathbf{u} &= \frac{1}{h_s} \left[\frac{\partial u}{\partial s} + \frac{1}{r} \frac{\partial}{\partial r} (rvh_s) + \frac{1}{r} \frac{\partial}{\partial \theta} (wh_s) \right] \\ \nabla \wedge \mathbf{u} &= \mathbf{e}_s \left[\frac{1}{r} \frac{\partial}{\partial r} (rw) - \frac{1}{r} \frac{\partial v}{\partial \theta} \right] + \mathbf{e}_r \left[\frac{1}{rh_s} \frac{\partial}{\partial \theta} (h_s u) - \frac{1}{h_s} \frac{\partial w}{\partial s} \right] + \mathbf{e}_\theta \left[\frac{1}{h_s} \frac{\partial v}{\partial s} - \frac{1}{h_s} \frac{\partial}{\partial r} (h_s u) \right] \\ \nabla^2 \phi &= \frac{1}{h_s} \left[\frac{\partial}{\partial s} \left(\frac{1}{h_s} \frac{\partial \phi}{\partial s} \right) + \frac{1}{r} \frac{\partial}{\partial r} \left(rh_s \frac{\partial \phi}{\partial r} \right) + \frac{1}{r^2} \frac{\partial}{\partial \theta} \left(h_s \frac{\partial \phi}{\partial \theta} \right) \right] \end{aligned}$$